Geochemical Self-Organization and Mineral Pattern Formation in Soda Lakes of the Rift Valley

Melese Getenet Dessie

PhD Thesis

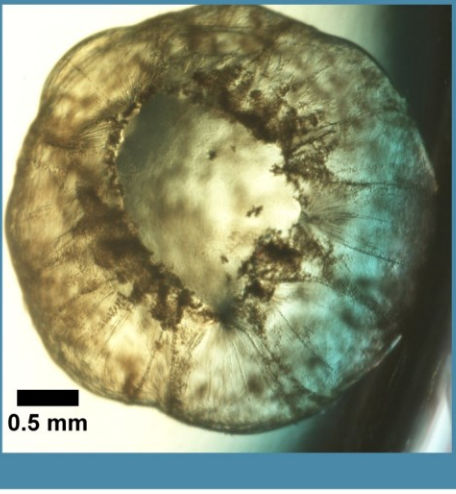

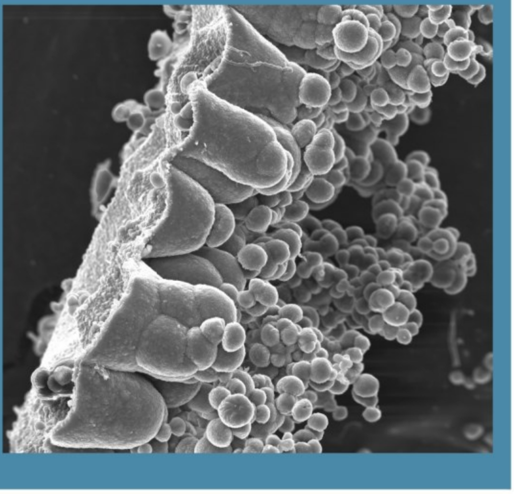

UNIVERSIDAD DE GRANADA

CSIC
Consejo Superior de Investigaciones Científicas

IACT
Instituto Andaluz de Ciencias de la Tierra

lec
Laboratorio de Estudios Cristalográficos

Editor: Universidad de Granada. Tesis Doctorales
Autor: Melese Getenet Dessie
ISBN: 978-84-1117-704-7
URI: https://hdl.handle.net/10481/80343

Geochemical Self-Organization and Mineral Pattern Formation in Soda Lakes of the Rift Valley

MELESE GETENET DESSIE

PhD Thesis – Tesis Doctoral

This dissertation is submitted for the degree of

PhD in Earth Sciences

University of Granada Earth Sciences Doctoral Program

Thesis Supervisor: Prof. Dr. Juan Manuel García-Ruiz

Esta tesis doctoral ha sido dirigida por el Prof. Dr. Juan Manuel García-Ruiz del Instituto Andaluz de Ciencias de la Tierra (Consejo Superior de Investigaciones Científicas-Universidad de Granada)

Granada, October 2022

FUNDING

This thesis was developed within the European Research Council under the European Union’s Seventh Framework Program (FP7/2007-2013)/ERC grant agreement no. 340863, the Spanish Ministerio de Economía y Competitividad (CGL2016-78971-P), and the Spanish government Ministerio de Ciencia, Innovacion y Universidades (BES-2017-081105).

ABSTRACT

The geochemical scenario for the lifeless early Earth is a matter of intense debate. One of the hypotheses is that after the formation of the Moon, water condensed on the Earth's crust, forming alkaline silica and carbonate-rich pools, lakes, and seas resulting from serpentinization of ultramafic rocks and evaporative concentration of solutes. It has been postulated that mineral self-organization could have been a common phenomenon in these geochemical settings. Mineral self-organization is a precipitation phenomenon in which polycrystalline materials self-organize into different complex patterns with non-crystallographic symmetry without the intervention of external directing forces. One of them is a precipitation process by which tubular and filamentous plant-like mineral membranes called chemical gardens form upon the interaction of alkaline silicate/carbonate solution with metal salt (e.g., Ca, Fe, Mn, Co, Mg, etc.) seed/solution because of osmosis, buoyancy, and reaction-diffusion processes. These membranes exhibit staggering physicochemical properties relevant to prebiotic chemistry, the origin of life, and life detection. Owing to the ionic and pH gradients across these tubular membrane walls, chemical gardens behave as fuel cells, generating an electrochemical potential difference (voltage) as high as 550 mV. The voltage across these membranes and their nano-mineralogy were shown to catalyze the formation of amino-/carboxylic acids, RNA nucleobases, and kerogenous products from organic molecules that were available on early Earth (e.g., formamide (CH_3NO), phenol (C_6H_6O), formaldehyde (CH_2O), pyruvate ($CH_3COCO_2^-$)). Moreover, these self-assembled structures grow into tubular, life-like morphologies – reminiscent of biological filaments and fossils. As a result of these remarkable properties, chemical gardens were considered niches for the origin of life and once wrongly considered remnants of life, blurring the boundary between biotic and abiotic structures in geological records.

The extreme conditions required for mineral self-organization reactions had cast doubts on the plausibility of the formation of chemical gardens in natural geochemical settings. To solve these doubts, terrestrial environments analogues to early Earth alkaline oceans were proposed to test the geochemical plausibility of mineral self-assembly. Serpentinization-driven alkaline settings are one of the terrestrial geochemical analogues of early Earth's alkaline oceans. Recent studies by our group have shown that mineral self-assembly is plausible in natural serpentinization-driven alkaline and silica-rich waters of Aqua de Ney (California). In addition, mineral self-assembly was demonstrated during the alteration of granitic rocks by model alkaline solution. Evaporative concentration-driven soda lakes are the other terrestrial geochemical analogues to the alkaline oceans of prebiotic Earth, extraterrestrial planets, and moons such as Enceladus (moon of Saturn) and Europa (moon of Jupiter). Nevertheless, the plausibility of mineral self-assembly in these alkaline carbonate-rich soda lakes is still unknown. Among chemical gardens, carbonate-based gardens are poorly understood systems. Consequently, dynamic diffusion and precipitation processes occurring during the growth and subsequent ripening have not been studied yet in these systems. Hence, the main goal of this thesis was to investigate the implications of mineral self-assembly and pattern formation in soda lakes of the East African Rift Valley to early Earth geochemistry, prebiotic chemistry, and life detection by focusing on a) monitoring the mineral precipitation sequence and the

resulting hydrochemical evolution of soda lake brines, b) testing the plausibility of self-organized mineral structures in natural soda lakes, and c) detail characterization of self-assembled calcium carbonate mineral tubular structures synthesized in model carbonate solutions and soda lake water.

Soda lakes of the East African Rift Valley are hyperalkaline (pH up to 12), hypersaline lakes extremely enriched in Na^+, K^+, Cl^-, CO_3^{2-}, HCO_3^-, and SiO_2 and depleted in Ca^{2+} and Mg^{2+}, where thick evaporite deposits and siliceous sediments form since hundred thousand years. In these lakes, particularly Lake Magadi, Nasikie Engida (southern Kenya), and Natron (northern Tanzania), different hydrates of sodium carbonate/-bicarbonate and other saline minerals precipitate. The precipitation sequence of these minerals is a key to understanding the hydrochemical evolution and the paleoenvironmental conditions of ancient evaporite deposits. However, accurate determination of the precipitation sequence of these minerals was challenging due to the dependency of the different hydrates on temperature, water activity, pH, and pCO_2, which could induce phase transformation and secondary mineral precipitation during sample handling. To shed light on these challenges, we proposed a comprehensive methodology for monitoring evaporitic mineral precipitation and the hydrochemical evolution of saline lakes with a case study on Lake Magadi. This methodology was expanded to investigate the hydrochemical evolution and the production of chemical sediments during the evaporation of Lake Nasikie Engida and Natron and discussed the geochemical and sedimentological perspectives of evaporitic sediments in these lakes. Water samples from tributary springs and Lake Magadi, Nasikie Engida, and Natron have been experimentally studied using in-situ video microscopy and synchrotron X-ray diffraction of acoustically levitated droplets. The mineral patterns were characterized by ex-situ Raman spectroscopy, X-ray diffractions, and scanning electron microscopy. Experiments were coupled with thermodynamic models to understand the evaporation and precipitation-driven hydrochemical evolution of brines.

Major minerals precipitating from the samples were sodium carbonates/bicarbonates and halite. The CO_3/HCO_3 ratio is the main factor defining the Na-carbonates precipitation sequence: in lake brines where $CO_3/HCO_3 > 1$, trona precipitates first, whereas in hot springs, where $CO_3/HCO_3 \ll 1$, nahcolite precipitates instead of trona, which forms later via partial dissolution of nahcolite. Precipitation of nahcolite is possible only at lower pH values (pCO_2 higher than -2.7), explaining the distribution of trona and nahcolite in current lakes and the stratigraphic sequences. Dendritic and acicular trona precipitate via fractional crystallization – reminiscent of grass-like trona layers in the actual settings. Later, during evaporation, thermonatrite precipitates, generally at the same time as halite, at a very high pH (>11.2) after significant depletion of HCO_3^- due to trona precipitation. The precipitation of these soluble minerals increases the pH of the brine and is the main factor contributing to the hyperalkaline and hypersaline character of the lakes. Villiaumite, sylvite, alkaline earth carbonates, fluorapatite, and silica are also predicted to precipitate. Still, most of them have not been observed in evaporation experiments, either because of the small amount of precipitates produced, kinetic effects delaying the nucleation of some phases, or biologically induced effects in the lake chemistry that are not considered in model calculations. The results have

shown that evaporation and mineral precipitation are the major drivers for the formation of hyperalkaline, saline, CO_3^{2-}- and SiO_2-rich brines. Evaporation experiments/simulations up to complete dryness show the entire landscape of plausible evaporitic scenarios. Yet only a fraction of this range of conditions is achieved by actual lake brines in perennial lakes due to the control by the amplitude of seasonal dry/rainy periods, which modulate dilution and evaporative concentration of brines. The synergy of in-situ and ex-situ methods and modelling could be applicable in industrial crystallization and natural brines to reconstruct the hydrogeochemical and hydroclimatic conditions of soda lakes, evaporite settings, and potentially soda oceans of early Earth and extraterrestrial planets.

The second part of the thesis deal with testing mineral self-assembly in soda lakes and characterizing in detail calcium carbonate gardens synthesized in model carbonate solutions and natural carbonate-rich water. Self-assembled tubular and vesicular structures were synthesized by a) pouring saturated metal salt solutions and b) immersing metal salt pellets in Lake Magadi water. The resulting structures were analysed using X-ray diffraction, Raman spectroscopy, and scanning electron microscopy. Ca^{2+}, Mg^{2+}, and Co^{2+} salts could form tubular and vesicular mineral structures, whereas Ba^{2+}, Mn^{2+}, and Fe^{2+} salts formed only vesicular structures. These results suggest that mineral self-assembly could have been a common phenomenon in soda oceans of early Earth and Earth-like planets and moons. These structures formed in natural water have direct implications for life detection on early Earth and other planets. The absence of Ca-phosphate phases in natural $CaCO_3$ structures infers Ca sequestration in carbonate minerals, leaving phosphate in solution for biochemical reactions. This strengthens the suggestion that carbonate-rich lakes could be ideal sites for the “one-pot” synthesis of prebiotic organic compounds and the origin of life.

To further elucidate the dynamic diffusion and precipitation processes occurring during growth and ripening, single macroscopic calcium carbonate tubes were synthesized by controlled addition of model sodium carbonate solution (synthetic/model calcium gardens) and Lake Magadi water (natural calcium gardens) onto calcium salt pellets. The time-dependent behavior of these tubes was monitored by in-situ measurements of pH, ionic concentrations inside and outside the tubular membranes, and voltage. Further, the composition and structure of the tubular membranes were characterized by using ex-situ X-ray diffraction, infrared, and Raman spectroscopy, as well as scanning electron microscopy. The wall of model and natural calcium carbonate tubes is a bilayer of texturally distinct but compositionally similar calcite showing high crystallinity. The interior surface of both types of tubes consists of numerous adjacent cone-like structures, whereas the outer surface is composed of a dense layer of interlocked calcite rhombohedra. Crystalline calcite layers in both types of tubes dramatically reduce the exchange of ionic species between the inner and outer volume, which prevent ion concentration gradients from eliminating in the long term. The densely packed calcite minerals prevent model calcium carbonate gardens from developing significant pH gradients (1.3) and voltage (~10 mV), in contrast to iron, cobalt, and aluminium silica gardens (up to 550 mV).

In contrast, natural carbonate tubes developed a significant pH gradient (5.7) comparable to silica gardens. These tubes developed relatively higher voltage (~30 mV) before the densification of the tube walls. In contrast to model silica gardens, the high pH gradient in natural tubes doesn’t contribute significantly to voltage development, suggesting that pH gradients contribute to voltage only if it co-exists with permeable membranes. This has implications for the proposed role of chemical gardens as catalysers of prebiotic chemistry in soda oceans likely to have formed on the primitive Earth and other planets and moons. Cobalt and iron (II) mineral vesicles and gardens synthesized in Magadi water were less crystalline materials, suggesting that these structures might have developed significant electrochemical voltage required for chemical reactions relevant to prebiotic chemistry and the origin of life in soda oceans of the early Earth.

Overall, the thesis presented the precipitation sequences, the hydrochemical evolution, and self-organized mineral patterns in an environment thought to be analogues to the soda oceans of the early Earth and other extraterrestrial planets and moons. The findings contribute to the knowledge of the geochemistry of soda lakes in which the mineral precipitation sequence in such peculiar hydrochemistry has been explored experimentally for the first time. To this purpose, ex-situ characterization techniques, in-situ synchrotron X-ray diffraction of levitated droplets, and geochemical modelling were integrated. The synergy of these methods could be applicable in industrial crystallization, and natural brines to reconstruct the hydrogeochemical and hydroclimatic conditions of soda lakes, evaporite settings, and potentially soda oceans of early Earth and extraterrestrial planets. In addition, the thesis demonstrated the plausibility of mineral self-assembly in soda oceans of early Earth and Earth-like planets and moons, suggesting direct implications for the origin of life and life detections in geologic records.

RESUMEN

El escenario geoquímico de la Tierra primitiva abiótica es un tema de intenso debate. Una de las hipótesis aceptadas actualmente es que después de la formación de la Luna, el agua se condensó en la corteza terrestre, formando charcas, lagos y mares alcalinos ricos en sílice y carbonato como resultado de la serpentinización de rocas ultramáficas y la concentración evaporativa de solutos. Se ha postulado que la autoorganización mineral podría haber sido un fenómeno común en estos entornos geoquímicos. La autoorganización mineral es un fenómeno de precipitación en el que los materiales policristalinos se autoorganizan en diferentes patrones complejos con simetría no cristalográfica sin la intervención de fuerzas directivas externas. Uno de estos procesos es la precipitación de membranas minerales similares a organismos tubulares y filamentosos, llamadas jardines químicos, por la interacción de una disolución alcalina de silicato/carbonato con semillas/disolución de sales metálicas (p. ej., Ca, Fe, Mn, Co, Mg, etc.) debido a los procesos de ósmosis, flotabilidad y reacción-difusión. Estas membranas exhiben asombrosas propiedades fisicoquímicas relevantes para la química prebiótica, el origen de la vida y la detección de vida. Debido a los gradientes iónicos y de pH a través de estas membranas tubulares, los jardines químicos se comportan como celdas de combustible, generando una diferencia de potencial electroquímico (voltaje) de hasta 550 mV. Se demostró que el voltaje a través de estas membranas y su nanomineralogía catalizan la formación de ácidos amino/carboxílicos, nucleobases de ARN y productos kerógenos de moléculas orgánicas que estaban disponibles en la Tierra primitiva (p.ej., formamida (CH_3NO), fenol (C_6H_6O), formaldehído (CH_2O), piruvato ($CH_3COCO_2^-$)). Además, estas estructuras autoensambladas se convierten en morfologías tubulares que recuerdan a los filamentos biológicos y a los fósiles. Como resultado de estas notables propiedades, los jardines químicos se consideran nichos para el origen de la vida y alguna vez se consideraron erróneamente como restos de vida, desdibujando el límite entre las estructuras bióticas y abióticas en los registros geológicos.

Las condiciones extremas requeridas para las reacciones de autoorganización de los minerales habían arrojado dudas sobre la plausibilidad de la formación de jardines químicos en entornos geoquímicos naturales. Para resolver estas dudas, se propusieron entornos terrestres análogos a los primeros océanos alcalinos de la Tierra para probar la plausibilidad geoquímica del autoensamblaje mineral. Los entornos alcalinos producidos por la serpentinización son uno de los análogos geoquímicos terrestres de los océanos alcalinos de la Tierra primitiva. Estudios recientes realizados por nuestro grupo han demostrado que el autoensamblaje de minerales es plausible en aguas alcalinas y ricas en sílice impulsadas por serpentinización natural en Aqua de Ney (California). Además, se demostró el autoensamblaje mineral durante la alteración de rocas graníticas por solución alcalina modelo. Los lagos de sosa producidos por la concentración evaporativa son los otros análogos geoquímicos terrestres de los océanos alcalinos de la Tierra prebiótica, los planetas extraterrestres y lunas como Encélado (luna de Saturno) y Europa (luna de Júpiter). Sin embargo, aún se desconoce la plausibilidad del autoensamblaje mineral en estos lagos ricos en sodio y carbonato alcalino. Entre los jardines químicos, los jardines basados en carbonato son sistemas poco conocidos. En consecuencia, los procesos dinámicos de difusión y precipitación que ocurren durante el crecimiento y

posterior maduración aún no han sido estudiados en estos sistemas. Por lo tanto, el objetivo principal de esta tesis fue investigar las implicaciones del autoensamblaje mineral y la formación de patrones en los lagos de soda del Valle del Rift de África Oriental para la geoquímica de la Tierra primitiva, la química prebiótica y la detección de vida, centrándose en a) monitorear la secuencia deprecipitación mineral y la evolución hidroquímica resultante de las salmueras de los lagos de soda, b) comprobar la plausibilidad de las estructuras minerales autoorganizadas en los lagos de soda naturales, y c) caracterizar detalladamente las estructuras tubulares minerales de carbonato de calcio autoensambladas sintetizadas en disoluciones de carbonato modelo y agua de lago de soda .

Los lagos de soda del Valle del Rift de África Oriental son hiperalcalinos (pH hasta 12), extremadamente enriquecidos en Na^+, K^+, Cl^-, CO_3^{2-}, HCO_3^- y SiO_2 y empobrecidos en Ca^{2+} y Mg^{2+}, donde se acumulan potentes depósitos de evaporita y silíce. Estos sedimentos se forman desde hace cien mil años. En estos lagos, particularmente en el lago Magadi, Nasikie Engida (sur de Kenia) y Natron (norte de Tanzania), se precipitan diferentes hidratos de carbonato/bicarbonato de sodio y otros minerales salinos. La secuencia de precipitación de estos minerales es clave para comprender la evolución hidroquímica y las condiciones paleoambientales de los antiguos depósitos de evaporitas. Sin embargo, la determinación precisa de la secuencia de precipitación de estos minerales fue un desafío debido a la dependencia de los diferentes hidratos de la temperatura, la actividad del agua, el pH y la pCO_2, lo que podría inducir la transformación de fase y la precipitación mineral secundaria durante el manejo de la muestra. Para arrojar luz sobre estos desafíos, propusimos una metodología integral para monitorear la precipitación mineral evaporítica y la evolución hidroquímica de los lagos salinos con un estudio inicial en el lago Magadi. Esta metodología se amplió para investigar la evolución hidroquímica y la producción de sedimentos químicos durante la evaporación de los lagos Nasikie Engida y Natron y se discutieron las perspectivas geoquímicas y sedimentológicas de los sedimentos evaporíticos en estos lagos. Las muestras de agua de los manantiales tributarios y de los lagos Magadi, Nasikie Engida y Natron se han estudiado experimentalmente utilizando microscopía in situ y difracción de rayos X de sincrotrón en gotas levitadas acústicamente. Los patrones minerales se caracterizaron mediante espectroscopía Raman ex situ, difracción de rayos X y microscopía electrónica de barrido. Los experimentos se combinaron con modelos termodinámicos para comprender la evolución hidroquímica de las salmueras durante la evaporación y la precipitación.

Los principales minerales que precipitaron de las muestras de salmuera fueron carbonatos/bicarbonatos de sodio y halita. La relación CO_3/HCO_3 es el factor principal que define la secuencia de precipitación de los carbonatos de sodio: en las salmueras de los lagos donde $CO_3/HCO_3 > 1$, la trona precipita primero, mientras que, en las aguas termales, donde $CO_3/HCO_3 \ll 1$, precipita la nahcolita en lugar de la trona, que se forma más tarde a través de la disolución parcial de nahcolita. La precipitación de nahcolita es posible solo a valores de pH más bajos (pCO_2 superior a -2,7), lo que explica la distribución de trona y nahcolita en los lagos actuales y en las secuencias estratigráficas. La trona dendrítica y acicular precipita a través de cristalización fraccionada, y recuerda a las capas de trona similares a hierba en los lagos reales. Más tarde, durante la evaporación, la termonatrita precipita, generalmente al mismo tiempo que la halita, a un pH muy alto (>11,2) después de un agotamiento significativo de HCO_3^- debido a la precipitación de trona. La precipitación de estos minerales solubles aumenta el pH de la salmuera y es el principal factor que contribuye al carácter hiperalcalino e hipersalino de los lagos. También se prevé que precipiten viliaumita, silvita, carbonatos alcalinotérreos, fluorapatito y sílice. Pero la mayoría de ellos no se ha observado en los experimentos de evaporación, ya sea por la pequeña cantidad de precipitados producidos, los efectos cinéticos que retrasan la nucleación de algunas fases o los efectos inducidos biológicamente en la química del lago que no se consideran en los cálculos del modelo. Los resultados han demostrado que la evaporación y la precipitación mineral son los principales impulsores de la formación de salmueras hiperalcalinas, salinas, ricas en CO_3^{2-} y SiO_2. Los experimentos/simulaciones de evaporación hasta la sequedad completa muestran todo el panorama de los escenarios evaporíticos plausibles. Sin embargo, solo una fracción de este rango de condiciones se logra a partir de salmueras de lagos prennes reales debido al control de la amplitud de los períodos secos/lluviosos estacionales, que modulan la dilución y la concentración evaporativa de las salmueras. La sinergia de los métodos y el modelado in situ y ex situ podría aplicarse en la cristalización industrial de las salmueras naturales, así como para reconstruir las condiciones hidrogeoquímicas e hidroclimáticas de los lagos de sosa, los entornos evaporíticos y, potencialmente, los océanos de soda de la Tierra primitiva y los planetas extraterrestres.

La segunda parte de la tesis trata de comprobar el autoensamblaje de minerales en lagos de sosa y caracterizar en detalle los jardines de carbonato de calcio sintetizados en soluciones de carbonato modelo y agua natural rica en carbonato. Se sintetizaron estructuras tubulares y vesiculares autoensambladas a) vertiendo disoluciones saturadas de sales metálicas y b) sumergiendo gránulos de sales metálicas en agua del lago Magadi. Las estructuras resultantes se analizaron mediante difracción de rayos X, espectroscopia Raman y microscopía electrónica de barrido. Las sales de Ca^{2+}, Mg^{2+} y Co^{2+} pueden formar estructuras minerales tubulares y vesiculares, mientras que las sales de Ba^{2+}, Mn^{2+} y Fe^{2+} forman solo estructuras vesiculares. Estos resultados sugieren que el autoensamblaje de minerales podría haber sido un fenómeno común en los océanos de soda de la Tierra primitiva y planetas y lunas similares a la Tierra. Estas estructuras formadas en agua natural tienen implicaciones directas para la detección de vida en la Tierra primitiva y otros planetas. La ausencia de fases de Ca-fosfato en las estructuras naturales de $CaCO_3$ sugiere el secuestro de Ca en los minerales de carbonato, dejando el fosfato en disolución para las reacciones bioquímicas. Esto refuerza la propuesta de que los lagos ricos en carbonato podrían ser sitios ideales para la síntesis de compuestos orgánicos prebióticos en un" single-pot" y el origen de la vida.

Para dilucidar aún más los procesos dinámicos de difusión y precipitación que ocurren durante el crecimiento y la maduración, se sintetizaron tubos de carbonato de calcio macroscópicos individuales mediante la adición controlada de una disolución de carbonato de sodio modelo (jardines de calcio sintético/modelo) y agua del lago Magadi (jardines de calcio natural) en gránulos de sal de calcio. El comportamiento dependiente del tiempo de estos tubos se controló mediante mediciones in situ de pH, concentraciones iónicas dentro y fuera de las membranas tubulares y voltaje. Además, la composición y la estructura de las membranas tubulares se caracterizaron mediante difracción de rayos X ex situ, espectroscopia infrarroja y Raman, así como microscopía electrónica de barrido. La pared de los tubos modelo y de carbonato de calcio natural es una bicapa de calcita de textura distinta, pero de composición similar que muestra una alta cristalinidad. La superficie interior de ambos tipos de tubos consta de numerosas estructuras similares a conos adyacentes, mientras que la superficie exterior está compuesta por una densa capa de romboedros de calcita entrelazados. Las capas de calcita cristalina en ambos tipos de tubos reducen drásticamente el intercambio de especies iónicas entre el volumen interior y el exterior, lo que evita que los gradientes de concentración de iones se disipen a largo plazo. Los minerales de calcita densamente empaquetados evitan que los jardines modelo de carbonato de calcio desarrollen gradientes de pH significativos (1,3) y voltaje (~10 mV), en contraste con los jardines de sílice de hierro, cobalto y aluminio (hasta 550 mV).

Por el contrario, los tubos de carbonato a partir de muestras naturales desarrollaron un gradiente de pH significativo (5,7) comparable a los jardines de sílice. Estos tubos desarrollaron un voltaje relativamente más alto (~ 30 mV) antes de la densificación de las paredes del tubo. A diferencia de los jardines de sílice modelo, el alto gradiente de pH en los tubos naturales no contribuye significativamente al desarrollo de voltaje, lo que sugiere que los gradientes de pH contribuyen al voltaje solo si coexisten con membranas permeables. Esto tiene implicaciones para el papel propuesto de los jardines químicos como catalizadores de la química prebiótica en los océanos de sosa que probablemente se formaron en la Tierra primitiva y otros planetas y lunas. Las vesículas y los jardines minerales de cobalto y hierro (II) sintetizados en el agua de Magadi eran materiales menos cristalinos, lo que sugiere que estas estructuras podrían haber desarrollado un voltaje electroquímico significativo requerido para las reacciones químicas relevantes para la química prebiótica y el origen de la vida en los océanos de soda de la Tierra primitiva.

En general, la tesis presenta las secuencias de precipitación, la evolución hidroquímica y los patrones minerales autoorganizados en un entorno que considera análogo a los océanos de soda de la Tierra primitiva y otros planetas y lunas extraterrestres. Los resultados contribuyen al conocimiento de la geoquímica de los lagos de sosa en los que se ha explorado experimentalmente por primera vez la secuencia de precipitación mineral en una hidroquímica tan peculiar. Para ello, se integraron técnicas de caracterización ex situ, difracción de rayos X sincrotrón in situ de gotas levitadas y modelado geoquímico. La sinergia de estos métodos podría ser aplicable en cristalización industrial y en el estudio de salmueras naturales para reconstruir las condiciones hidrogeoquímicas e hidroclimáticas de los lagos de soda, entornos evaporíticos y potencialmente océanos de soda de la Tierra primitiva y planetas extraterrestres. Además, la tesis demuestra la plausibilidad del autoensamblaje mineral en los océanos de soda de la Tierra primitiva y planetas y lunas similares a la Tierra, lo que sugiere implicaciones directas para el origen de la vida y las detecciones de vida en los registros geológicos.

Acknowledgment

First and foremost, I would like to express my sincere gratitude to my supervisor Prof. Juan Manuel García-Ruiz who offered me the opportunity to do the PhD research with him. You were very supportive and kind in helping to achieve the best out of my PhD research. You always encourage me to attend and present at seminars, conferences, courses, and outreach activities that helped me to improve my scientific knowledge and communication skills and meet new people. Your science enthusiasm was an inspiration to happily pursue my PhD research. Your kind support was not limited to supervision and training. I am very grateful for everything you did personally as well, especially during those difficult times. I must use this opportunity to acknowledge your effort to create collaborations between the University of Granada, CSIC, and Bahir Dar University. Similarly, your wife Martha was so kind that she was there for me when I need her help. Thank you very much Juanma and Martha!

The support and guidance of Dr. Fermin Otálora Muñoz were enormous during my PhD research. Your contribution to the accomplishment of my PhD research is boldly reflected in my PhD thesis. I would love to express my sincere gratitude to you. You were always supportive and kind to help me solve scientific and technical puzzles. Not only at work but also your help during my stay in Granada was countless both in administrative and personal matters. Thanks a lot, Fermin! I am also very grateful to your wife Irene for kindly helping me and my wife.

I have received enormous technical, administrative, and personal support from the members of Laboratorio de Estudios Cristalográficos during my stay in Granada. I am very grateful for Cristóbal Verdugo Escamilla, Duane Choquesillo Lazarte, Paqui Espinosa Pérez, Raquel Fernández Penas, Luis Antonio González, Joaquin Criado Reyes, Francisco Javier Acebedo, Emmanouil Giampouras, Alfonso García Caballero, Carmen López Sánchez, Jose Antonio Gavira, and Jaime Gómez Morales. I am thankful to Alicia González Segura, Isabel Guerra Tschuschke, and Isabel Sánchez Almazo from Centro de Instrumentación Científica for training me with scanning electron microscopy and Miryam Rojas Gómez from Estación Experimental del Zaidín for her analytical help. I would like to thank Arsenio Granados Torres, Fernando Palero Fernandez, Antonio Delgado Huertas, and Silbia López de Lacalle for the experience we had and the sampling you thought me during the fieldwork in Dallol (Ethiopia).

I would like to express my sincere gratitude to Dr. Franziska Emmerling from BAM Federal Institute for Materials Research and Testing (Berlin, Germany) for allowing me to work your lab and learn about synchrotron beamline. The wonderful collaboration with you helped me significantly to answer part of the scientific questions of my doctoral research. Your team members, especially Dominik Al-Sabbagh, Maria Heilmann, and Ralf Bienert, were very welcoming, kind, and courageous to teach me about the lab facilities in BAM and BESSY II beamline. Jessica Hennig was very helpful with managing administrative matters for me. Thank you very much, Franziska and your team! I am grateful to Dr. Ángeles Bustillo Revuelta from Museo Nacional de Ciencias Naturales (Madrid) for the practical training on petrographic microscopy.

Special thanks belong to my friends and colleagues Britta Maier, Joti Rouillard, Marievi Papaslioti, Emmanouil Giampouras, Simon Cardinal, Alexander Pérez, Pamela Knoll, Petra Godec, Jelena Mitrić, Rubén Campanero, Adriana Torres, Maria Savchenko, Ayenachew Alemayehou, Tara Barwa, Gan Zhang, and Electra Kotopoulou for the wonderful moments we shared both at work and beyond, and for the wonderful times we spent in Granada. Prof. Abel Moreno, thank you very much for the great times in IACT.

I would love to express my heartfelt gratitude to Kevin Hagmann and his wife Kelly for their kind help when I arrive in Granada for the first time. Thank you very much my friends Davis, Michael, and Sebastian for the great times we had, especially during the COVID lockdown. Thank you very much Tilahun, Shimeles, Ephrem, Zeleke, and Bethlehem for the fun time we spent together in Granada and Addis. I am grateful to my friends and colleagues from the School of Earth Sciences at Bahir Dar University for handling matters on my behalf.

Finally, I have no words to thank my mother, my father, and my siblings. Your presence as a family is always and forever a power that propels me to achieve the highest possible success. I achieved this because you are there carrying my burdens. I owe a special thanks to my hero father, Getenet Dessie, who always stood firm and who never groveled to anyone. No words to thank you, my mother Gelay Awoke: my generous and brave mom. I am indebted forever for the countless prices you paid for me. Alechgn Mamuye, my darling wife, I thank you for everything. You are a wise and kind woman and a blessing to me.

ምስጋና:

በመጀመሪያ ምስጋና ለእግዚአብሔርና ለድንግል ማሪያም ይሁን። በመቀጠል ሳትማሩ ላስተማራችሁኝ፣ በባዶ እግራችሁ እየሄዳችሁ የተሻለ እድል እንዲኖረኝ አስተምራችሁ እዚህ ላደረሳችሁኝ ለባላገሮቹ እናትና አባቴ ገላየ አወቀ እና ጌትነት ደሴ እንዲሁም ሁሌም ጉልበትና ወኔ ለምትሆኑኝ ምርጥ ወንድም እና እህቶቼ ልባዊ ምስጋናዬ ይድረሳችሁ። እኔን አስተምራችሁ እዚህ ለማድረስ የደከማችሁትን አውቃለሁ።

የጀግናውና ለማንም የማይንበረከከው የጌትነት ደሴ ልጆች መሆናችሁን በተግባር አሳይታችሁኛልና፣ ጌትነት ደሴ ከሱ የበለጠ ረመጥ እንጂ አመድ እንዳልወለደ ያሳያችሁኝ ወንድሞቼና እህቶቼ በጣም እኮራባችኋለሁ።እንኳንም የናንተ ወንድም ሆንሁ።

እወዳችኋለሁ!

Table of Contents

Chapter 1

Introduction, Thesis Objectives and Outlines

1. Introduction

This doctoral research has been performed under the framework of PROMETHEUS project (ERC Advanced Grant). PROMETHEUS aims at carrying out an in-depth investigation of the nature of self-assembled mineral structures such as silica biomorphs and chemical gardens, its role in early life detection and origin of life and the plausibility of their formation in natural extreme alkaline geological environments. Extreme environments have a characteristic extremity in one or a combination of pH, temperature, salinity, radiation, oxygen, ionic concentrations, etc. that impose physicochemical limits for life to thrive (Harrison et al., 2013). The extreme geochemical environments have paramount importance to understand the early Earth geochemical environments before life appear and to differentiate abiotic and biologically mediated mineral precipitations. Modern alkaline geochemical environments are natural laboratories where we test the geochemical plausibility of biomimetic inorganic self-assembled mineral structures to help demarcate the boundary between life-like minerals (biomorphs, chemical gardens, and mineral vesicles) and life on early Earth and other planets and moons.

The geochemistry of both alkaline and acidic extreme environments and their role in mineral self-assembly has been studied under the PROMETHEUS project. Kotopoulou et al. (2019) studied the geochemical evolution and the mineral precipitation processes of Dallol hyperacidic hydrothermal brines (Ethiopia) and explained many aspects of the polyextremity in physicochemical conditions. Serpentinization is the main driver of extreme alkalinity and high silica content in some geochemical settings (McCollom and Bach, 2009). Among these settings, García-Ruiz et al. (2017) and Kotopoulou et al. (2020) studied mineral self-organization in serpentinization-driven alkaline springs of Aqua de Ney (California) whereas Giampouras et al. (2020, 2019) explored the mineralogy and geochemistry of alkaline springs of Samail ophiolite (Oman) and Ronda peridotites (Southern Spain) to emulate the early Earth geochemical scenario.

In this doctoral thesis, alkaline environments, other than serpentinization-driven settings, with high alkalinity and silica content have been investigated. Apart from serpentinization, soda lakes that acquire high alkalinity via evaporative concentration of carbonate salts have been proposed as plausible natural settings for mineral self-assembly and the origin of life (García-Ruiz, 2000; García-Ruiz et al., 2020). These environments are considered analogue geochemical settings to soda oceans of early Earth and other extraterrestrial planets and moons such as Enceladus (Kempe and Degens, 1985; Kempe et al., 1989; Kempe and Kazmierczak, 2011). Testing the geochemical plausibility of self-organization in one of the early Earth-analogous environments, soda lakes, is important for prebiotic chemistry and life detection. Hence, this thesis investigates (1) the mineral precipitation processes and the hydrogeochemical evolution of soda lakes of the East African Rift Valley (EARV hereafter) that led to the geochemical conditions (high alkalinity and high silica and carbonate content) proposed as plausible for self-assembly and (2) the actual plausibility of mineral self-organization in these alkaline soda lakes. Before jumping into the detailed overview of the geochemistry of soda lakes and mineral self-organization, I will present first the objectives and the outline of the thesis.

1.1. Thesis Objectives

The thesis aims at advancing our knowledge of soda lakes from the perspective of geochemistry, and early Earth prebiotic chemistry. Hence, it has three main objectives: a) monitoring the mineral precipitation sequence and the resulting hydrochemical evolution of soda lake brines, b) testing the plausibility of self-organized mineral structures in natural soda lakes, and c) detail characterization of self-assembled calcium carbonate mineral tubular structures synthesized in model carbonate solutions and soda lake water.

a) Soda lakes are well-known geochemically analogue environments to the soda oceans of Archean Earth and other extraterrestrial planets and moons such as Enceladus that were thought to provide crucial ingredients for the origin of life. Soda lakes share many of the characteristics of early Earth's ocean geochemistry such as high alkalinities balanced by sodium and potassium, high pH, high silica concentrations, very low calcium, and magnesium concentrations, and high $CaCO_3$ and $MgCO_3$ supersaturations (Kempe and Degens, 1985; Kempe et al., 1989; Kempe and Kazmierczak, 2002, 2011). Owing to the high silica content, abiotic silica precipitation and subsequent chert formation in soda lakes, particularly Lake Magadi, was proposed as a typical model for studying the formation of chert deposits and prebiotic organic matter preservation on modern and Archean Earth (Eugster, 1967; Eugster and Jones, 1968). Evaporative concentration and subsequent mineral precipitation were suggested as the major factors for such geochemistry of the soda lakes (Hardie and Eugster, 1970; Eugster and Hardie, 1978; Eugster and Jones, 1979). However, our knowledge of mineral precipitation in soda lakes depends on either field data or thermodynamic modeling and there is a lack of solid experimental evidence on the precipitation sequence of different minerals.

Under this broad objective, the thesis explored and proposed a comprehensive methodology for monitoring evaporitic mineral precipitation and the hydrochemical evolution of saline lakes by using Lake Magadi as a case study. This methodology was applied in three highly saline soda lakes (Lake Magadi, Nasikie Engida, and Natron) to answer the questions:

- How does evaporation influence the hydrochemical evolution?
- How does mineral precipitation influence the hydrochemistry?
- What are the factors affecting the mineral paragenesis, textures, precipitation sequence, and relative abundance?
- What is the geochemical and sedimentological implication of the observed precipitation sequences and processes?

Observations, experiments, and thermodynamic modelling studies were integrated to answer the above questions by using water samples collected from Lake Magadi, Nasikie Engida (southern Kenya), and Natron (northern Tanzania). Mineralogical, compositional, and textural analyses of the precipitates have been performed to identify phase relations and assemblages by using video microscopy, Raman spectroscopy, X-ray diffraction, and scanning electron microscopy coupled with energy dispersive X-ray analysis. The experimental results were coupled with field observations and thermodynamic modeling to reveal the influence of the initial hydrochemistry on the mineral paragenesis and the influence of the mineral precipitation on the fate of the solutes during evaporation.

b) One of the leading theories of the origin of life on early Earth and extraterrestrial planets and moons is that life emerged in alkaline hydrothermal vents (Russell et al., 1993, 1994; Kempe and Kazmierczak, 2002; Martin and Russell, 2003a; Deamer and Damer, 2017). It is thought that self-assembled membranous mineral gardens and vesicles – reminiscent of hydrothermal chimneys based on the generated pH-Eh gradient – were forming in alkaline oceans enriched in silica and/or carbonate. These structures, both carbonate-based (Angelis et al., 2021) and silica-based chemical gardens (Saladino et al., 2016, 2019; Bizzarri et al., 2018; Barge et al., 2019), are shown to be micro-reactors that could play catalytic roles in prebiotic chemistry and origin of life. Based on synthetic Ca-CO_3 chemical gardens, Cardoso et al. (2019) suggested the plausibility of carbonate-based membranous tubes in soda oceans of Enceladus. Nevertheless, the plausibility of carbonate-based chemical gardens in natural analogue soda lakes was not tested so far. Under the broad objective of testing mineral self-organization, I have performed mineral self-assembly experiments for the first time in purely “natural” soda lake water to answer the following questions:

- Are chemical gardens and mineral vesicles plausible in analogue geochemical settings like soda lakes of the East African Rift Valley?
- If self-assembly is possible, which metal cations can form self-assembled structures?
- What does the composition and the texture of the self-assembled structures look like?
- What are the implications of these mineral structures to prebiotic (geo)chemistry and the origin of life?

c) Recently, carbonate-based chemical gardens received considerable attention in the context of the origin of life. Cardoso et al. (2019) investigated the composition and texture of calcium carbonate chemical gardens grown in synthetic carbonate solution to emulate the conditions in Enceladus’ soda ocean. Iron-based carbonate gardens were shown to catalyze the polymerization of simple prebiotic organic molecules (phenol, formaldehyde, formamide, pyruvate) to kerogens and larger polymers, suggesting the plausible emergence of biochemistry in extraterrestrial soda oceans (Angelis et al., 2021). However, there is a lack of understanding of the ionic diffusions and precipitation processes occurring during the growth and subsequent ripening of carbonate-based chemical gardens. Hence, the thesis also focuses on a detailed study of the spatiotemporal ionic diffusions and precipitation processes in calcium carbonate chemical gardens synthesized in model solution and natural soda lake water. Hence, this section of the thesis aims at

- Detail characterization of the mineralogy and texture of model and natural Ca-carbonate gardens and mineral vesicles
- Monitoring temporal and spatial variations of composition, texture, ionic concentrations, pH, and electrochemical potential across both types of the membranes
- Exploring the difference between the model and natural Ca-carbonate gardens
- Understanding the implication of the texture and physiochemical characteristics of these structures to prebiotic chemistry and origin of life

1.2. Thesis Outlines

The thesis is organized into seven chapters. The first and the last chapters contain the introduction and conclusion of the thesis respectively. Chapters 2 – 6 contain three published articles, one manuscript under review, and a manuscript in preparation. Since each published articles and manuscripts have its materials, methods, and experimental techniques, they are not presented separately as a chapter. Hence, chapters 2 – 6 are structured as prepared and presented for publications with their corresponding abstract (summary), brief introduction, materials and methods, results, and discussion sections. The corresponding references and supplementary materials are presented at the end of each article (chapter). At the end of the thesis, abstracts presented at conferences and hydrochemical data are shown as appendixes.

The first chapter contains the objectives of the thesis and introduces the background knowledge of the geochemistry of soda lakes and mineral self-organization. Chapter two presents a comprehensive methodology for monitoring evaporitic mineral precipitation and hydrochemical evolution of saline lakes with a case study of Lake Magadi soda brines from EARV, which is published in Crystal Growth and Design [1]. Chapter three uses the methodology presented in chapter two to deal with the mineral precipitation and hydrochemical evolution through evaporitic processes in three soda brines of Kenya and Tanzania (Lake Magadi, Nasikie Engida, and Natron). The result presented in this chapter has been submitted to Chemical Geology [2]. This chapter discusses the geochemical and sedimentological aspects of the results presented in chapter two (Lake Magadi) together with new experimental and modeling studies of mineral precipitations in Lake Nasikie Engida and Natron (Kenya – Tanzania border). After understanding the mineral precipitation processes and the hydrochemical evolution of soda lakes that led to the high alkalinity and carbonate content required for mineral self-assembly, the results of mineral self-organization experiments in these alkaline brines, particularly Lake Magadi, are presented in chapters four and six. Chapter four is an article that has been published in Crystals [3]. Chapter five deals with calcium carbonate tubular structures (carbonate gardens) synthesized in model carbonate solutions, their

---

[1] Getenet, M., García-Ruiz, J.M., Otálora, F., Emmerling, F., Al-Sabbagh, D., Verdugo-Escamilla, C., 2022. A comprehensive methodology for monitoring evaporitic mineral precipitation and hydrochemical evolution of saline lakes: the case of Lake Magadi soda brine (East African Rift Valley, Kenya). *Crystal Growth & Design*. https://doi.org/10.1021/acs.cgd.1c01391

[2] Getenet, M., García-Ruiz, J.M., Otálora, F., Emmerling, F., Al-Sabbagh, D., 2022. Mineral Precipitation and Hydrochemical Evolution Through Evaporitic Processes in Soda Brines (East African Rift Valley, Kenya). *Chemical Geology* (under review)

[3] Getenet, M., García-Ruiz, J.M., Verdugo-Escamilla, C., Guerra-Tschuschke, I., 2020. Mineral Vesicles and Chemical Gardens from Carbonate-Rich Alkaline Brines of Lake Magadi, Kenya. *Crystals*. https://doi.org/10.3390/cryst10060467

formation, characterization, and their implications in natural mineral environments. This chapter is an article published in Chemistry – A European Journal [4]. Chapter six is a manuscript in preparation that discusses tubular calcium carbonate gardens synthesized in natural carbonate-rich brines of Lake Magadi to help reveal the similarities and differences between calcium carbonate tubular structures synthesized in model solutions and actual soda lake water. The main conclusions of the thesis, open questions, perspectives, and future works are discussed in chapter seven. In addition to published and submitted articles to scientific journals, the results of the thesis have been disseminated at different national and international conferences as oral and poster presentations. These presentations include a poster presentation at AGU 2020 fall meeting (Virtual) and oral presentations at GE3C 2021 symposium (Vigo, Spain and Online), EGU 2021 General Assembly (Vienna, Austria and Virtual), Goldschmidt 2021 conference (Virtual), IUCr 2021 congress (Prague, Czech Republic and Virtual), AGU 2021 fall meeting (New Orleans, US and Online) and SEM-SEA 2022 meeting (Baeza, Spain). In addition, the thesis was presented to a broad audience in a 3-minute thesis presentation [5] contest organized by CSIC. The abstracts of these presentations are found in appendix 1 at the end of the thesis.

1.3. Geology and Geochemistry of East African Soda Lakes

Direct evidence of rock and fossil records is absent on Hadean Earth, causing a lack of insights into the geochemistry, evolution of life, and preservation of fossils on Precambrian Earth. To fill these knowledge gaps, modern geochemical environments such as soda lakes were brought forward as promising settings due to the analogy between the alkaline geochemistry of these lakes and Precambrian and extraterrestrial oceans, where life is thought to emerged (Kempe and Degens, 1985; Kempe et al., 1989; Kempe and Kazmierczak, 2002, 2011; Glein et al., 2015; Toner and Catling, 2019, 2020). Silica gels and chert deposits from soda lakes, particularly Lake Magadi (Kenya), were proposed as typical models for explaining the origins and mechanisms of the chert deposits and the preservation of cellular structures in siliceous

---

[4] Getenet, M., Rieder, J., Kellermeier, M., Kunz, W., García-Ruiz, J.M., 2021. Tubular structures of calcium carbonate: formation, characterization, and implications in natural mineral environments. *Chemistry – A European Journal*. https://doi.org/10.1002/chem.202101417

[5] Link to 3 minutes thesis presentation https://doi.org/10.6084/m9.figshare.21291483

sediments in Precambrian environments (Eugster, 1967, 1969; Eugster and Jones, 1968; Hay, 1968; Schubel and Simonson, 1990; Behr and Röhricht, 2000; Behr, 2002; Reinhardt et al., 2019; Leet et al., 2021). Identification of these cellular structures and fossils in the Precambrian Earth has been challenged by the formation of self-assembled life-like abiotic mineral structures, which are proposed to form in soda lakes (García-Ruiz, 1994, 1998, 2000; García-Ruiz et al., 2002, 2020). Nevertheless, mineral self-assembly was never tested in "natural" soda lake water. Consequently, we don't know yet whether life-like abiogenic mineral structures are plausible to form in "natural" soda lake water. If these structures were plausible, the texture, mineralogy, physiochemical characteristics, and role in prebiotic geochemistry and life detection of these structures are unknown. Mineral self-assembly will be introduced in detail in section 1.4.

Mineral precipitations and parageneses in soda lakes provide insights into paleo-brine chemistry and paleoenvironmental conditions of mineral deposits in the geological record (Lowenstein and Demicco, 2006; Ma et al., 2011; Jagniecki et al., 2015; Lowenstein et al., 2016; Kolpakova and Gaskova, 2017; Cabestrero and Sanz-Montero, 2018; Demicco and Lowenstein, 2019; Otálora et al., 2020; Renaut et al., 2020; Olson and Lowenstein, 2021). In this context, sodium carbonate mineral assemblages from soda lakes can be used to constrain ancient temperatures and atmospheric CO_2 concentrations (Jagniecki et al., 2015; Demicco and Lowenstein, 2019; Olson and Lowenstein, 2021). Lessons learned about environmental constraints of soda lake deposits can be exported to the study of extra-terrestrial planets, where sodium carbonate minerals characteristic of soda lakes have been reported (McCord et al., 1998; Glein et al., 2015; De Sanctis et al., 2016; Carrozzo et al., 2018). From an economic point of view, soda ash deposits are important resources that have been mined from active and ancient deposits from soda lakes (Smith and Carroll, 2015; Schagerl and Renaut, 2016).

Owing to these scientific and economic values, much work has been carried out on mineral precipitation in soda lakes based either on field data or on thermodynamic modeling (Jagniecki and Lowenstein, 2015; McNulty, 2017; Demicco and Lowenstein, 2019; Renaut et al., 2020; Olson and Lowenstein, 2021). Recent works have proven that a combination of field research, lab experiments, and computer modeling is key to understanding evaporitic brine evolution and mineral precipitation sequences (Rull et al., 2014; Kotopoulou et al., 2019; Otálora et al., 2020). Experimental studies of mineral precipitations are crucial to understanding the full landscape of plausible evaporitic scenarios and the paragenesis of evaporitic minerals, which serve as novel tools to explain modern depositional settings and to reconstruct paleoclimatic and hydrochemical conditions of ancient deposits. Yet, there are no experimental investigations on evaporitic mineral precipitation sequences and hydrochemical evolution of soda lakes of the East African Rift Valley. Therefore, the first part of the thesis presents comprehensive experimental and numerical studies on the evaporitic mineral precipitations and the hydrochemical evolutions in soda lakes of the EARV. To support future works, the thesis provides the scientific community with recent hydrochemical analyses of the spring and lake brines collected in 2016 and 2018 which is after dilution by recent major flooding events of EARV lakes.

The EARV is a series of fault-bounded basins and volcanic centers spanning several thousand kilometers through East Africa in a roughly N-S direction. Each basin is controlled by faults and forms a subsiding graben or trough filled with sediments and/or volcanic rocks. The rift valleys form two main branches: the eastern and western branches of the East African Rift System. The eastern branch, running over 2200 km from Ethiopia in the north, through Kenya, to north Tanzania in the south (Bonavia et al., 1995; Chorowicz, 2005), is dominated by hypersaline alkaline soda lakes dominated by sodium and carbonate species in their dissolved ions (Eugster, 1970; Jones et al., 1977; Deocampo and Renaut, 2016; Renaut et al., 2020). Soda lakes are found widely distributed throughout the world (Grant, 2004; Pecoraino et al., 2015), but they are typically common in regions with volcanic bedrock such as the eastern branch of the EARV and lake basins of the western interior of North America (e.g., Mono Lake, Searles Lake and Owens Lake in California) (Deocampo and Jones, 2014; Schagerl and Renaut, 2016). The endorheic basins on the eastern arm of the EARV are dominated by hypersaline alkaline soda lakes, including Lake Natron, Magadi, Nasikie Engida, Naivasha, Nakuru, Elmenteita, Baringo, and Bogoria from south to north (Figure 1). As shown in Figure 1, the geology of the eastern arm is dominantly occupied by volcanic rocks that control the solute contents of soda lakes. These lakes are characterized by high pH and a large concentration of Na^+, Cl^-, and CO_3^{2-} and a relatively small amount of K^+, HCO_3^-, F^-, SO_4^{2-} and SiO_2 whereas they are depleted in Ca^{2+} and Mg^{2+} (Pecoraino et al., 2015; Deocampo and Renaut, 2016; Schagerl and Renaut, 2016; Renaut et al., 2020; Jones et al., 1977; Eugster, 1970). Among these lakes, the thesis focuses on Lake Magadi, Nasikie Engida (also known as Little Magadi), and Natron, where active precipitation of saline minerals and siliceous gels occurs (Eugster, 1967, 1980; Eugster and Jones, 1968; Jones et al., 1977; Fritz et al., 1987; Manega and Bieda, 1987; Renaut et al., 2020). These lakes are located in the southern lowermost depression of the EARV, near the border between Kenya and Tanzania, occupying an N-S trending axial graben. The precursor paleolake levels were high enough that these lakes were interconnected as a single water body during the Early Holocene (Baker, 1958; Eugster, 1980; Hillaire-Marcel et al., 1986).

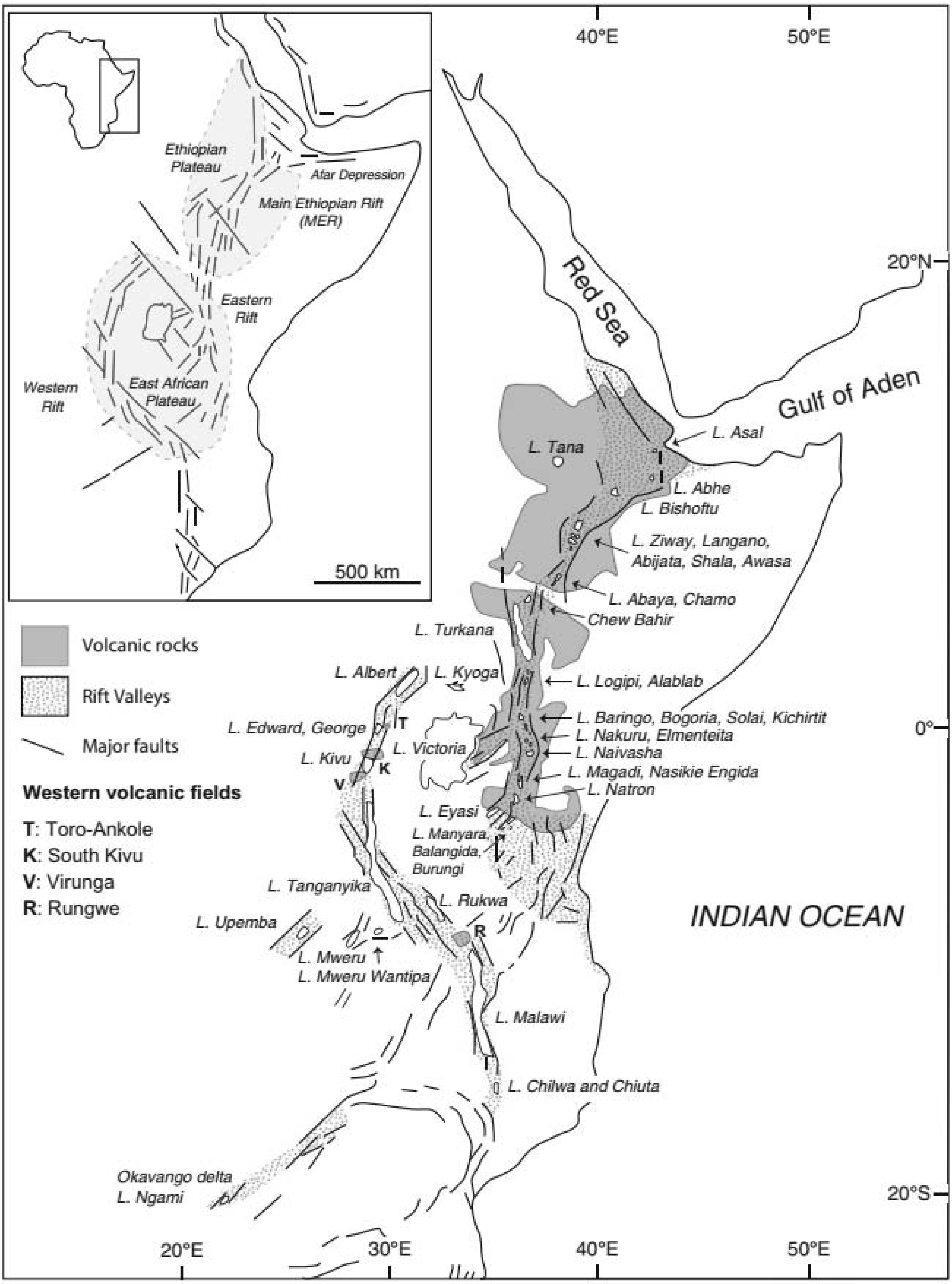

Figure 1. Geological setting of the East African Rift Valley and associated lakes (after Schagerl and Renaut, 2016; Tiercelin and Lezzar, 2002)

1.3.1. Geological Setting of MNN Basins

Lake Magadi and Nasikie Engida lie in the north-south axial Kenya rift depression, floored by faulted Pleistocene alkali trachyte and sediments (Baker, 1958, 1963, 1986; Baker et al., 1977, 1988; Crossley, 1979). Lake Natron, 20 km to the south, is separated from Lake Magadi by extinct Lenderut and Shombole (sometimes referred to as Shompole) volcanoes (Renaut et al., 2020) (Figure 2a). Metamorphic basements to the east and west of boundary faults of Magadi and Nasikie Engida basins are the oldest rocks in the region. Exposed basement rocks were not found along the margins of the Natron basin. The region passed through three stages of rifting namely pre-rifting regional doming, half-graben and full-graben rifting which form different basins filled with volcanic and sedimentary rocks of different compositions (Scoon, 2018). A series of basins, which are occupied by present-day soda lakes, formed during the late-Pleistocene faulting (Baker et al., 1972; Baker, 1987; Dawson, 2008). Alkali trachyte of Magadi and Nasikie Engida regions are overlain by chert deposits that occur in three sedimentary units; from bottom to top, Oloronga Beds, Green Beds, and High Magadi Beds (Baker, 1963; Behr and Röhricht, 2000; Behr, 2002) (Figure 2b). The oldest sediments in and near the trough are indurated silts, clays, and cherts of the Oloronga Beds, which began to be deposited more than 0.78 Ma ago in a weakly alkaline setting. They are capped by a thick caliche layer indicating a period of desiccation (Eugster, 1980; Baker, 1986). Minor faulting of the rift floor affected the Oloronga Beds (Baker, 1958) and led to the deepening of the Natron and Magadi basins during the interval between 0.8 and 0.4 Ma (Baker, 1986).

Green Beds are a series of thinly bedded cherts and greenish laminated or massive, erionite-rich mudstones overlying the Oloronga beds (Baker, 1958; Behr, 2002). These bedded cherts show possible stromatolitic layering, burrows, salt crystal pseudomorphs (calcite and Na-carbonates), and tepee structures consistent with shallow-water sedimentation on playa floors. Soft sediment deformation and crystal casts in these beds suggest precursor soft sediments such as siliceous gel, opaline silica, or magadiite (Hay, 1968; Eugster, 1969; Behr and Röhricht, 2000; Behr, 2002; Buatois et al., 2020). High Magadi Beds, overlying the Green Beds, are dominantly lacustrine sediments exposed up to ~12 m above modern Lake Magadi, that record former high lake levels of Pleistocene to early Holocene age in the Magadi-Nasikie Engida basin. These beds are composed of tuffaceous clays and siltstones, sodium silicates (magadiite ($NaSi_7O_{13}(OH)_3 \cdot H_2O$) and kenyaite ($NaSi_{11}O_{20.5}(OH)_4 \cdot 3H_2O$)), Magadi-type cherts and fine laminae in the lower part containing fossil fish bones (Baker, 1958, 1963; Eugster, 1967, 1969; Hay, 1968; Owen et al., 2018). Magadi and Nasikie Engida regions are well known for these inorganically formed cherts called "Magadi-type cherts", that served as type models for understanding the origins of non-biogenic cherts on Precambrian Earth (Eugster, 1967, 1969; Hay, 1968).

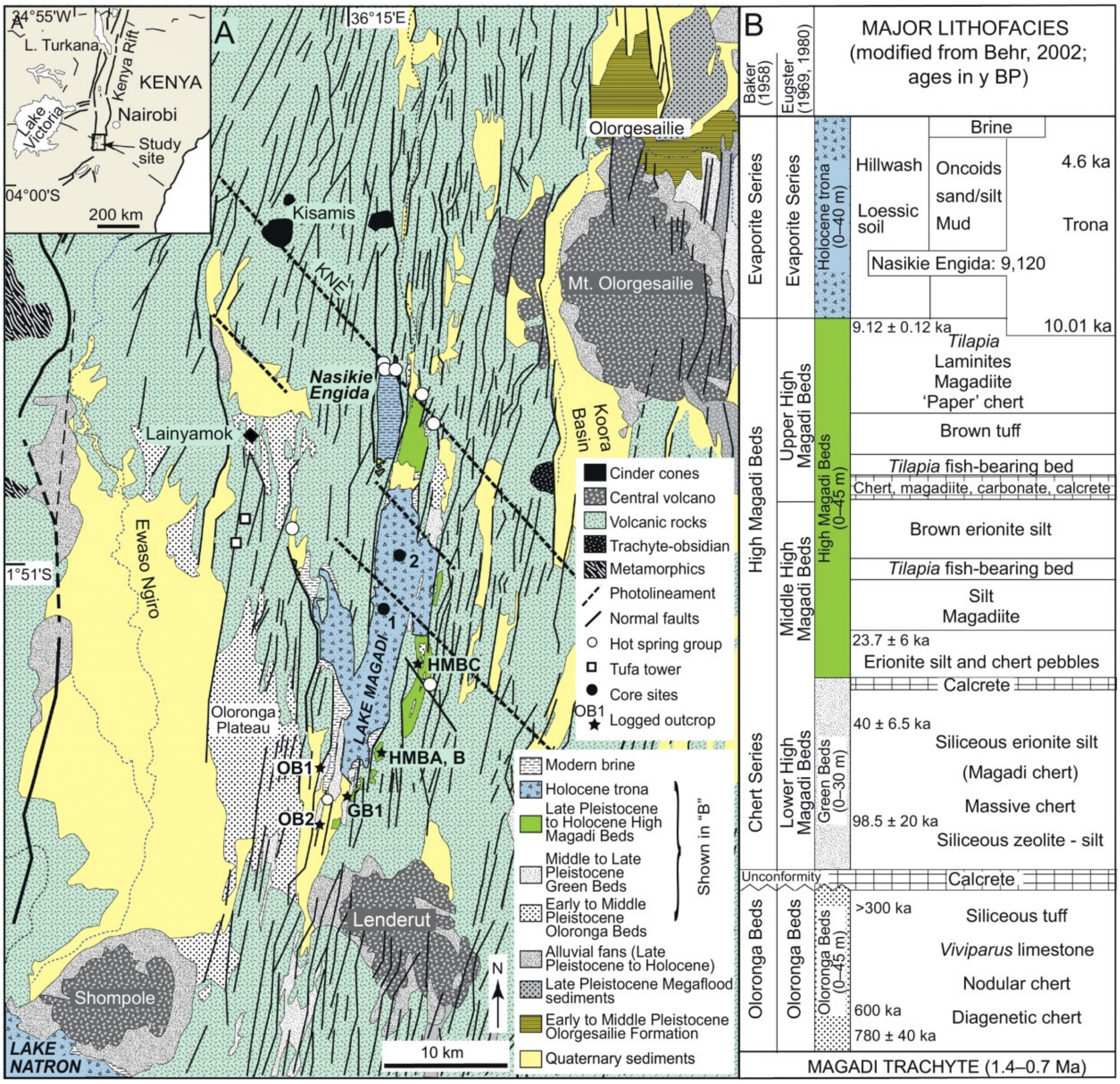

Figure **2**. (A) Geological setting of the Magadi and Nasikie Engida basins. Photolineaments imply subvolcanic NW–SE trends that have locally controlled the morphology of the Magadi and Nasikie Engida basins, drainage, and the alignment of hot-spring groups. KNE = Kisamis-Nasikie Engida-Koora lineament. Outcrops: HMB = High Magadi Beds, GB = Green Beds; OB = Oloronga Beds; (B) Magadi and Nasikie Engida basins stratigraphy modified from Behr (2002) showing evolving terminology and revisions, with earlier schemes to the left. Four informal units are currently recognized based on outcrops: the Oloronga Beds, the Green Beds, the High Magadi Beds, and the Evaporite Series. The stratigraphy and radiometric ages are from Behr (2002). Published dates reported by Behr are from Fairhead et al. (1972), Butzer et al. (1972), Goetz and Hillaire-Marcel (1992) and (Röhricht, 1998) (after Owen et al., 2019)

The sodium silicate minerals, magadiite ($NaSi_7O_{13}(OH)_3{\cdot}H_2O$), and kenyaite ($NaSi_{11}O_{20.5}(OH)_4{\cdot}3H_2O$) which were found in High Magadi Beds were inferred to be the precursor for the formation of inorganic Magadi-type cherts through chemical precipitation of silica from brines of Lake Magadi (Eugster, 1967, 1969; Hay, 1968). Other Pleistocene cherts in these basins, particularly those with soft-sediment deformation features, were formed from a siliceous gel precursor. Modern siliceous gels are currently forming around the hot springs of Nasikie Engida (Eugster and Jones, 1968; De Cort et al., 2019; Renaut et al., 2020). Recently, Leet et al. (2021) presented evidence for the synsedimentary formation of Magadi cherts directly from siliceous gels. Labyrinth patterns preserved in cherts from Lake Magadi cores indicate invasion of air along planes in dewatering gels. These patterns support the precipitation of silica gels in the saline-alkaline Lake Magadi system and syndepositional drying of gels in contact with air as part of chert formation (Leet et al., 2021).

The youngest unit in the Magadi-Nasikie Engida basin is the Evaporite Series on top of the High Magadi Beds, which is a bedded trona ($Na_2CO_3{\cdot}NaHCO_3{\cdot}2H_2O$) evaporitic deposit intercalated by thin beds of tuffaceous clay and muds (Baker, 1958; Eugster, 1967, 1967, 1980; Hay, 1968; Surdam and Eugster, 1976) (see Figure 2b). According to Owen et al. (2019), this unit extends more than 65 m below the lake floor. During Late Pleistocene to Holocene, the High Magadi Beds materials were deposited in a fresh to moderately saline, alkaline lake. The deposition of silicates and cherts was associated with the initial change from a freshwater lake to an alkaline lake (Baker, 1958, 1963; Surdam and Eugster, 1976, 1976; Eugster, 1980, 1986; Behr and Röhricht, 2000; Owen et al., 2019) during the past 12000 years, mainly due to climatic changes and tectonic activity that modified rift morphology, the local hydrology, and climate (Behr and Röhricht, 2000). Currently, mainly trona and nahcolite ($NaHCO_3$) precipitated from highly saline and alkaline brines are being added to the Evaporite Series (Baker, 1958; Owen et al., 2019). In addition to trona and nahcolite, minor thermonatrite ($Na_2CO_3{\cdot}H_2O$), natron ($Na_2CO_3{\cdot}H_2O$), halite (NaCl), and villiaumite (NaF) precipitation occur at some local pools on the lake surface and in the evaporation ponds of TATA chemicals Soda Company (Eugster, 1980; Renaut et al., 2020). The evaporites and brines have been exploited commercially for soda ash and common salt for the last 100 years.

In Natron basin, the footwalls of rift escarpments are composed of thick sequences of layered volcanic, volcaniclastic and lacustrine strata (Figure 3). The oldest volcanic units in Natron basin are the deeply eroded volcanic centers of Mosonik and the Bast hills (Dawson, 1992; Foster et al., 1997). These comprise melanephelinites, melilites, and nephelinite-phonolite pyroclastic deposits with some carbonatite, with ages of 3.1–3.6 Ma (Isaacs and Curtis, 1974; Manega, 1993). Mosonik and the Bast hills are surrounded by a sequence of sub-horizontal basalts, at least 600 m thick, which flowed from Sambu (Isaac, 1967; Isaacs and Curtis, 1974). Sambu basalts are overlain by Hajaro Beds, a set of sandy, clayey, and basaltic materials deposited before the existence of the Peninj River and its drainage network, in about 2 Ma (Thouveny and Taieb, 1987; Diez-Martín et al., 2018). The nephelinites and basalts are overlain by the Plio-Pleistocene Peninj Group (Humbu and Moinik Formations) sediments, fertile layers with paleontological and archaeological remains (Isaac, 1965, 1967; Isaacs and Curtis, 1974; Foster et al., 1997). The Peninj Beds were deposited in the paleo-Lake Natron until the sedimentation was ended by the Natron boundary faulting. These beds are a 100 m thick succession of sediments with interbedded lavas exposed on the west side of modern Lake Natron (Isaac, 1965; Isaacs and Curtis, 1974; Dawson, 2008). The Peninj Group comprises the lower Humbu Formation, sands with clays and reworked tuffs deposited in a freshwater deltaic setting (Figure 3b). The overlying Moinik Formation contains more widespread clays, laminated trachytic tuffs, and evaporite sediments deposited in a saline lake like the modern Lake Natron (Isaac, 1965; Hay, 1968; Dawson, 2008). The age of Peninj beds provides evidence for the formation of an internal drainage basin due to pre-Pleistocene minor faulting and the formation of Natron basin boundary fault that terminated the sedimentation of Peninj Group (Dawson, 2008). Modern Lake Natron is surrounded by zeolitized clays and tuffs with irregular chert nodules containing magadiite and kenyaite, collectively called High Natron Beds (Baker, 1963; Hay, 1968). The High Natron Beds may correlate with the High Magadi Beds, both depositing during the lake high stand that merges Lake Natron and Lake Magadi into a single water body (Baker, 1963; Hillaire-Marcel et al., 1986; Dawson, 2008). Overlying High Natron Beds, the modern evaporites of Natron consist of trona, nahcolite, thermonatrite, and traces of halite and villiaumite interbedded with organic clays. The clays result from the input of volcanic dust into the lake which, combined with organic material from detritus and algal blooms, forms the organic-rich bottom sediments, which also contain gaylussite and pirssonite (Baker, 1986; Manega and Bieda, 1987; Dawson, 2008). Although most of the carbonate salts have been leached out of the sodium-rich volcanic rocks surrounding the lake, there has been some direct volcanic input into the lake during natrocarbonatite eruptions of Oldoinyo Lengai volcano south of Lake Natron (Dawson, 2008). One part of the thesis (chapter 3) discusses the geochemical and sedimentological perspective of evaporitic sediments in MNN lakes based on experimental and geochemical modelling studies.

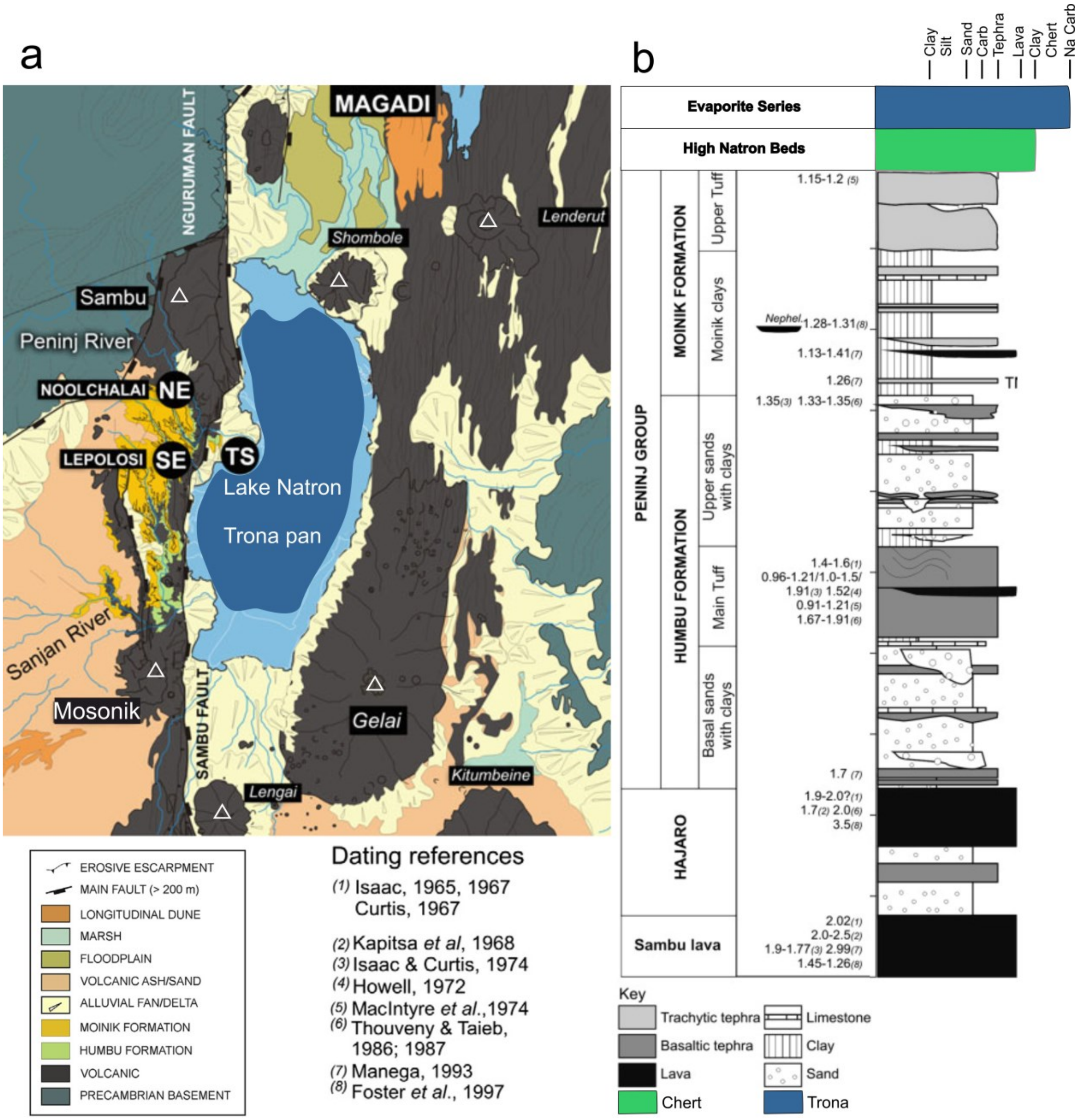

Figure **3**. (a) Geological map of the Lake Natron basin with nearby volcanos (labeled with △) and locations (NE, SE, and TS) where archaeological remains crop out in Peninj sediments; (b) stratigraphic column of Lake Natron basin showing the older volcanics (Sambu and Hajaro), the Peninj Group, High Magadi Beds, and the Evaporite Series. Dates from Isaac (1967, 1965), Curtis (1967), Kapitsa (1968), Howell (1972), Isaacs and Curtis (1974), Macintyre et al. (1974), Thouveny and Taieb (1987, 1986), Manega (1993), and Foster et al. (1997) (modified from Diez-Martín et al. (2014) and McHenry et al. (2011) based on Luque et al. (2009)

1.3.2. Modern Chemical Sediments of MNN Lakes

Since one of the objectives of the thesis is to understand the precipitation sequences and patterns of evaporite minerals in soda lakes, it's worth discussing the modern chemical sediments of the MNN lakes with greater emphasis based on recent field observations. Recently, McNulty (2017) and Renaut et al., (2020) presented a detailed discussion of the modern sodium carbonate and detrital sediments of Lake Magadi and Nasikie Engida. Detailed descriptions of the modern Lake Natron chemical sediments were not found to the best of my knowledge but the works of McNulty (2017) and Renaut et al., (2020) may serve to understand the modern sediments of Lake Natron by analogy in mineralogy and water chemistry with Lake Magadi. Therefore, this section presents the descriptions of the modern chemical sediments and features observed during the different stages of Lake Magadi and Nasikie Engida based on the works of McNulty (2017) and Renaut et al., (2020).

The sediments of Lake Magadi and Nasikie Engida pass through a recurrent cycle of three stages: undersaturation, evaporative concentration, and desiccation (Figure 4). During the evaporative concentration (Figure 4 stage 2), trona grows as thin sheet-like rafts on the surface and as upward radiating needles at the bottom of the lake. After complete evaporation (desiccation stage) (Figure 4 stage 3), continued evaporation of interstitial brines causes expansion and buckling of the crust and precipitation of a variety of efflorescent crusts and intercrystallite cement. During the undersaturation stage (flooding of the lakes) (Figure 4 stage 1), dilute inflows partially dissolve the pre-existing trona or nahcolite, creating layered deposits of upward radiating trona crystals (in Lake Magadi) or nahcolite crystals (in Nasikie Engida) with thin mud layers on top of the dissolution surfaces (Eugster, 1980; McNulty, 2017; Renaut et al., 2020).

During periods of increased inflow, Lake Magadi and Nasikie Engida are both flooded with freshwater that dilutes and undersaturated the brines. Exposure of existing trona (in Magadi and southern Nasikie Engida) and nahcolite (in Nasikie Engida) crusts to dilute floodwaters produces horizontal dissolution surfaces truncating vertically grown crystals. Suspended fine sediments brought by the flood water settle above the dissolution surfaces in trona or nahcolite crusts producing a thin layer of mud (Figure 5a-b) (Eugster, 1980; McNulty, 2017; Renaut et al., 2020). As the lake brine dissolves pre-existing trona crusts and evaporates, it concentrates and eventually reaches trona or nahcolite saturation and starts precipitating (Stage 2: Figure 4).

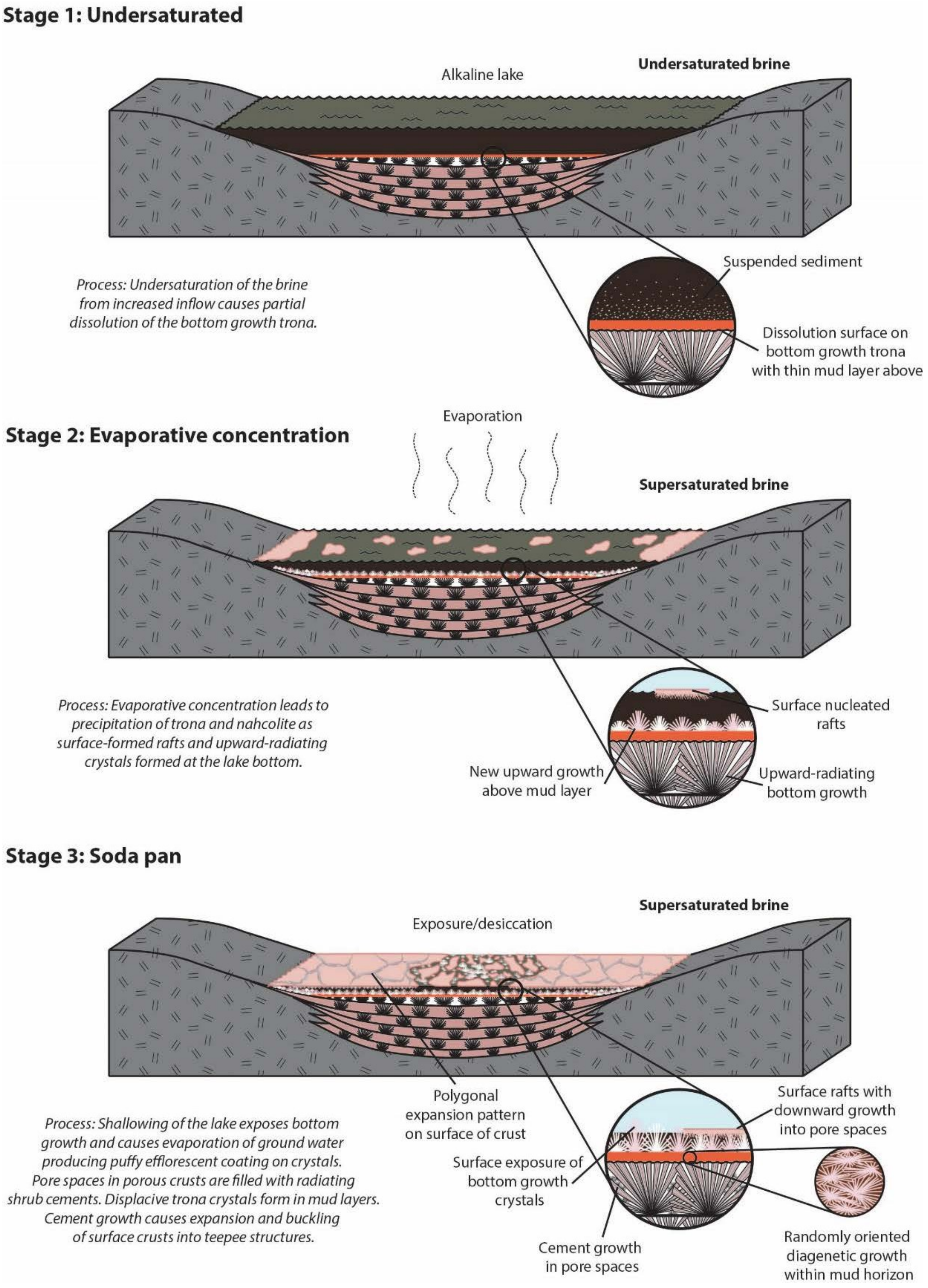

Process: Undersaturation of the brine from increased inflow causes partial dissolution of the bottom growth trona.

Process: Evaporative concentration leads to precipitation of trona and nahcolite as surface-formed rafts and upward-radiating crystals formed at the lake bottom.

Process: Shallowing of the lake exposes bottom growth and causes evaporation of ground water producing puffy efflorescent coating on crystals. Pore spaces in porous crusts are filled with radiating shrub cements. Displacive trona crystals form in mud layers. Cement growth causes expansion and buckling of surface crusts into teepee structures.

Figure 4. Diagram showing the three stages of the Soda Lake Cycle: Stage 1: undersaturated waters are flow into the basin due to increased precipitation reactivating ephemeral streams. This water partially dissolves the surface crust on the soda pan and supplies detrital sediments (mud) that finally deposit on top of the dissolution surface; Stage 2: evaporation concentrates

the brines to supersaturation, leading to precipitation of trona as surface rafts and upward-radiating bottom growth crystals; Stage 3: complete evaporation of the brines exposes trona crystals at the surface. Evaporation of interstitial brines causes the growth of diagenetic trona, leading to expansion and buckling of the surface crust. Diagenetic trona also forms within mud layers (after McNulty, 2017).

Crystallization of trona begins at the air/brine interface, where sub-millimeter to millimeter scale needles precipitate on the surface of the brine. Individual trona crystals coalesce to form larger rafts that vary from centimeter to meter scale in size (Figure 5c-d). The most abundant form of trona at Lake Magadi crystalizes at the brine bottom forming upward radiating needles (Figure 5e). They are commonly overlain by centimeter-scale rafts which came to rest on top of them (Figure 5f). Trona needles are 1-2 cm long near the shore whereas deeper brines near the center of Lake Magadi precipitate larger trona crystals (2-5 cm long) that nucleate from a common point and radiate upwards and outwards (Figure 5e). The upward growth of narrow-bladed nahcolite (Figure 5g) and acicular trona (Figure 5h) occurs at Nasikie Engida far from and near its southern shore respectively. Thin mud layers associated with dissolution surfaces are commonly the site of nucleation of nahcolite as upward radiating crystal shrubs, and larger bladed crystal sprays (Figure 5a) (McNulty, 2017; Renaut et al., 2020).

When the surface brines evaporate to near dryness (desiccated pan stage), early diagenetic features are produced including efflorescent crusts, expansion polygons, and intercrystalline cement. At the south lagoons of Lake Magadi, trona crusts consisting of fine radiating crystal shrubs are observed overlying upward-radiating bottom trona (Figure 5i). Surface rafts rest on the bottom crystals, and as evaporation continues small radiating shrubs of trona grew above the raft, forming a 1-2 cm thick layer. A white puffy efflorescence caps the shrub layer and fills spaces between crystals (Figure 5i). This efflorescence forms during subaerial exposure from the evaporation of interstitial brine. Efflorescent coatings and crusts are produced on almost all surfaces around Lake Magadi during the soda pan stage. Capillary evaporation of supersaturated brines through sediments and pore spaces produces a puffy white microcrystalline coating of trona. The efflorescent crusts may contain thermonatrite, halite, and villiaumite as well. The trona pan surface at Lake Magadi shows evidence of expansive growth following desiccation (Figure 5j). Expansive growth causes the crust to buckle and form polygonal expansion cracks that cover most of the surface of Lake Magadi and the south end of Nasikie Engida during the soda pan stage (Figure 5j) (Eugster, 1980; McNulty, 2017; Renaut et al., 2020).

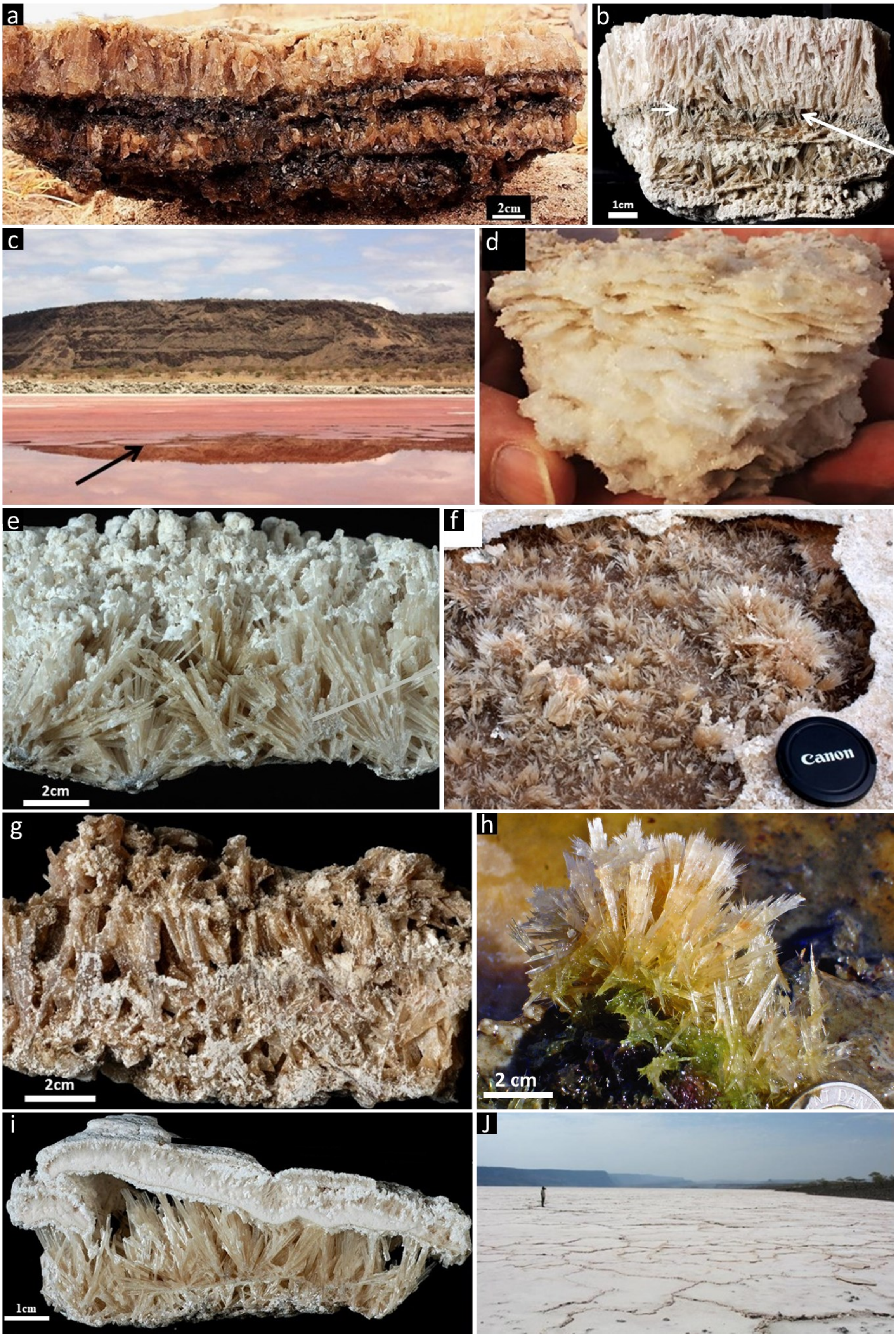

Figure 5. Features of trona and nahcolite produced during different stages of Magadi and Nasikie Engida. (a) Nahcolite from Nasikie Engida showing layers of upward-radiating crystals

with cm thick layers of fine dark mud overlying dissolution surfaces; (b) trona crust from the western shore of Lake Magadi showing upward radiating growth with a thin layer of dark mud showing a dissolution surface; (c) pink trona rafts (arrow) covering lake surface on the northwest shore of Lake Magadi. The pink color is caused by halophilic archaea; (d) imbricated flake-like trona rafts nucleated on the submerged rafts; (e) upward growth of trona from the southern lagoon of Lake Magadi; (f) upward radiating trona from the southwest lagoon of Lake Magadi covered by a layer of interlocking trona rafts that settled on top of the crystals (lens cap 6 cm); (g) nahcolite collected from the lakebed at Nasikie Engida, 500 m off-shore; (h) radial crystal-shrub of acicular trona from shallow (<15 cm) lake floor of the southern margin of Nasikie Engida; (i) trona from the south lagoon of Lake Magadi with ~1 cm thick coating of upward radiating trona shrubs and puffy white trona efflorescence; (j) expansion polygons on the buckled crust formed during desiccation stage of southern Nasikie Engida. Panels a-g, i-j after McNulty (2017); panel h after Renaut et al. (2020)

Near the center of Lake Magadi, where brines remained below the surface for prolonged periods, originally porous trona crusts become compact due to cementation. Trona cements consist of intercrystalline white puffy efflorescence, suggesting rapid growth from interstitial brines following complete evaporation of surface brines. This efflorescent cement is made of fine radiating needles of trona that nucleate from the sides of trona framework crystals. On the margins of the lake, brine levels dropped too rapidly for large volumes of cement to form. Fine crystalline cement didn’t form in the subaqueous nahcolite crusts from perennial Nasikie Engida, which suggests the sub-aqueous nahcolite has not been exposed. The different textures of trona appear to be controlled by water depth. For example, shallow near-shore areas are covered by imbricated rafts or 1-2 cm scale upward-radiating bottom growth crystals whereas deeper more central areas are covered by a crust of 2-5 cm scale bottom growth crystals that could be cemented by trona (Eugster, 1980; McNulty, 2017; Renaut et al., 2020).

Apart from the sodium carbonate minerals, siliceous gels are actively forming in the vicinities of hot springs on the northern shore of Nasikie Engida (Eugster, 1967, p. 196, 1980; Eugster and Jones, 1968; Renaut et al., 2020). Eugster and Jones (1968) proposed that these gels form when Na-CO_3-rich hot spring reacts with alkali trachytic flows and their detritus. During dry seasons, gels might form along the shoreline where evaporating brines react with fine sediments. Alternatively, siliceous gels may form in the water column from fluids supersaturated with amorphous silica via evaporation as observed in Alkali Lake, Oregon (Rooney et al., 1969). Hence, gel formation is not limited by proximity to hot springs (Renaut et al., 2020).

As discussed earlier, much work has been carried out on the mineral precipitation sequences and patterns in soda lakes based either on field data or on thermodynamic modeling (Jagniecki and Lowenstein, 2015; McNulty, 2017; Demicco and Lowenstein, 2019; Renaut et al., 2020; Olson and Lowenstein, 2021). Some recent works have proved that a combination of field research, lab experiments, and computer modeling is key to understanding evaporitic brine evolution and mineral precipitation sequences (Rull et al., 2014; Kotopoulou et al., 2019; Otálora et al., 2020; Renaut et al., 2020). So far, there are no experimental investigations on the mineral precipitation sequences and pattern formations in soda lakes. This part of the thesis presents a comprehensive experimental investigation and geochemical modeling of the mineral precipitation sequence and hydrochemical evolution of MNN brines, using evaporative mineral precipitation experiments monitored by (a) in situ video microscopy and synchrotron X-ray diffraction from acoustically levitated droplets; (b) ex situ Raman spectroscopy, X-ray diffraction, and scanning electron microscopy; and (c) computational modeling. The result of a particular study on Lake Magadi (published in Crystal Growth and Design, chapter 2) closely reproduced the mineral assemblages, patterns, and textural relations observed in the natural setting, as presented earlier in this section. The results have also shown that the synergy of different methods could be applicable in industrial crystallization and natural brines to reconstruct the hydrogeochemical and hydroclimatic conditions of soda lakes, evaporite settings, and potentially soda oceans of early Earth and extraterrestrial planets. The other work (chapter 3) presents a detailed discussion on the geochemical and sedimentological perspective of evaporitic sediments in MNN lakes based on experimental and geochemical modelling studies. The results show that pH, and consequently CO_3^{2-}/HCO_3^- ratios are the major factors determining the precipitation order, relative quantity, and resulting mineral paragenesis in the East African Rift Valley hyperalkaline, hypersaline lakes, and springs.

1.3.3. Hydrochemistry of MNN Lakes

As mentioned in sections 1.3.1 and 1.3.2, siliceous gels, magadiite, kenyaite, sodium carbonate, and other salts from MNN lakes have been precipitating since the Pleistocene time. Understanding the solute sources and the solute acquisition and enrichment mechanisms that led to supersaturation with respect to these minerals play paramount importance in understanding the precipitation processes of evaporites and cherts in MNN basins and other similar geological settings. On the other hand, evaporitic mineral precipitation and redissolution were proposed as one of the mechanisms that led to the formation of saline-alkaline chemistry of soda lakes (Hardie and Eugster, 1970; Jones et al., 1977; Eugster and

Hardie, 1978; Eugster and Jones, 1979). Hence, it's crucial to discuss how evaporation controls hydrochemical evolution and how mineral precipitation in dilute waters led to alkaline and saline-sodic geochemistry of the EARV soda lakes.

East African soda lakes are closed basins with no significant outflow where groundwater and seasonal streams flowing from the surrounding highlands collect to form standing lakes. Some of the lakes are mainly fed by rivers (e.g., Natron, Turkana, Baringo, Nakuru) whereas others receive a considerable part of the inflow from hydrothermal springs (e.g., Magadi, Nasikie Engida, Bogoria, Elmenteita). Due to the aridity of these regions, surface evaporation rates exceed the rate of water inflow allowing the dissolved minerals to concentrate into sodic alkaline brines with a pH up to 12, reaching supersaturation in sodium carbonate and other saline minerals (Deocampo and Jones, 2014; Pecoraino et al., 2015; Deocampo and Renaut, 2016; Schagerl and Renaut, 2016).

General models for the hydrochemical evolution of hydrologically closed basins have been presented by Eugster and Jones (1979), Garrels and Mackenzie (1967), and Hardie and Eugster (1970). The pronounced hydrochemical fractionation between dilute and concentrated brines of closed basins arises from silicate hydrolysis, evaporation, mineral precipitation, selective dissolution, sorption, degassing, and redox reactions (Garrels and Mackenzie, 1967; Hardie and Eugster, 1970; Eugster and Jones, 1979). The evolution of the chemical composition of saline lake waters consists of two steps: (1) solutes are acquired by the dilute inflow waters principally through dissolution, and (2) subsequent evaporative concentration leads to the precipitation of minerals, profoundly affecting the composition of the remaining waters. In continental settings, rivers and groundwaters are the source of most inflow waters and solutes that eventually form concentrated brines and evaporite salt deposits. The composition of the final brines depends on the surrounding lithologies that are leached by the dilute inflows (Garrels and Mackenzie, 1967; Jones et al., 1977; Eugster and Hardie, 1978).

In typical volcanic regions such as EARV, dilute inflow waters such as rivers and seasonal runoff acquire solutes through rainfall and hydrolysis of silicate minerals, pyroclastic, and volcanic glasses, producing Na^+ and HCO_3^--rich waters with high SiO_2 content and leaving alumina behind as clays or residual gels (Eugster and Jones, 1968). Hence, these dilute inflows have $HCO_3^- > Ca^{2+}+Mg^{2+}$. After silicate hydrolysis, these waters are subjected to surface and capillary evaporation, initially increasing the solute concentration but later minerals precipitate as caliche-type films, cement, and efflorescent crusts (Hardie and Eugster, 1970; Jones et al., 1977; Eugster, 1986). Abundant aggregates and veinlets of anhedral calcite in tuffaceous lake beds covered by efflorescent crusts consisting of trona, thermonatrite, and halite evidence Ca^{2+}, and carbonate removal (Surdam and Eugster, 1976). Precipitation of alkaline earth carbonates (calcite, Mg-calcite, dolomite, Magnesite) at the initial stage depletes Ca^{2+}, and Mg^{2+}, leaving excess HCO_3 in the evolving inflows. As HCO_3 is the next most abundant ion in the dilute waters, it combines with Na in the next stages of evaporative concentration, leading to the precipitation of efflorescent crusts of sodium carbonate minerals such as trona, thermonatrite, and halite (Eugster, 1970, 1986; Jones et al., 1977; Eugster and Hardie, 1978; Eugster and Jones, 1979; Deocampo and Renaut, 2016).

The next rainy season dissolves trona, thermonatrite, and halite from the efflorescent crusts and the resulting ions in solution join the groundwater reservoir, leading to highly alkaline water with a lower bicarbonate/carbonate ratio that emerges as springs on the lakeshores. Due to their low solubility, Ca-Mg carbonate minerals remain in the valley floor sediments causing the alkaline groundwater to be depleted in Ca^{2+}, Mg^{2+}, and HCO_3^-. Recurrent formation and fractional dissolution of efflorescent crusts in a high geothermal gradient region give rise to saline groundwater that emerges in the form of warm and hot springs on the shore of MNN lakes, feeding it and evolving, mainly by evaporation, to brines rich in Na^+, Cl^-, CO_3^{2-}, and HCO_3^- that is saturated with respect to trona and/or nahcolite (Eugster, 1980; Jones et al., 1977; Eugster, 1970; Hardie and Eugster, 1970). These springs flow into lagoons on the margins of the lakes, which act as preconcentration basins for the lake brines. These lagoons vary greatly in concentration and are intermediate between spring waters and the fractioned lake brines (Eugster, 1970; Jones et al., 1977). The most important inflow to Magadi and Nasikie Engida comes from the perennial warm and hot springs that emerge on the shores of these lakes. Dilute streams in the western rim of the rift valley and seasonal runoff from the north also fed Magadi and Nasikie Engida (see Figure 6b) (Eugster, 1970; Jones et al., 1977; Renaut et al., 2020). Similarly, warm and hot springs recharge Lake Natron along its shoreline together with four major perennial rivers draining from the western escarpments and the highlands (Figure 6a,c) (Guest and Stevens, 1957; Jones et al., 1977; Manega and Bieda, 1987). After the saline groundwater emerges at the shores of MNN lakes, further evaporative concentration leads to precipitation of very soluble saline minerals forming thick trona and nahcolite deposits (Garrels and Mackenzie, 1967; Jones et al., 1977; Eugster and Hardie, 1978). In addition to evaporative concentration, isotopic studies of evaporites of MNN lakes suggested an important contribution of the Ol Doinyo Lengai volcano to the salinity of these lakes (Bell et al., 1973). This volcano erupts natrocarbonatite lavas and ashes containing soluble sodium-potassium carbonate minerals (Dawson, 1962, 1964), which are leached to give a sodium-rich solution (Bell et al., 1973; Baker, 1986).

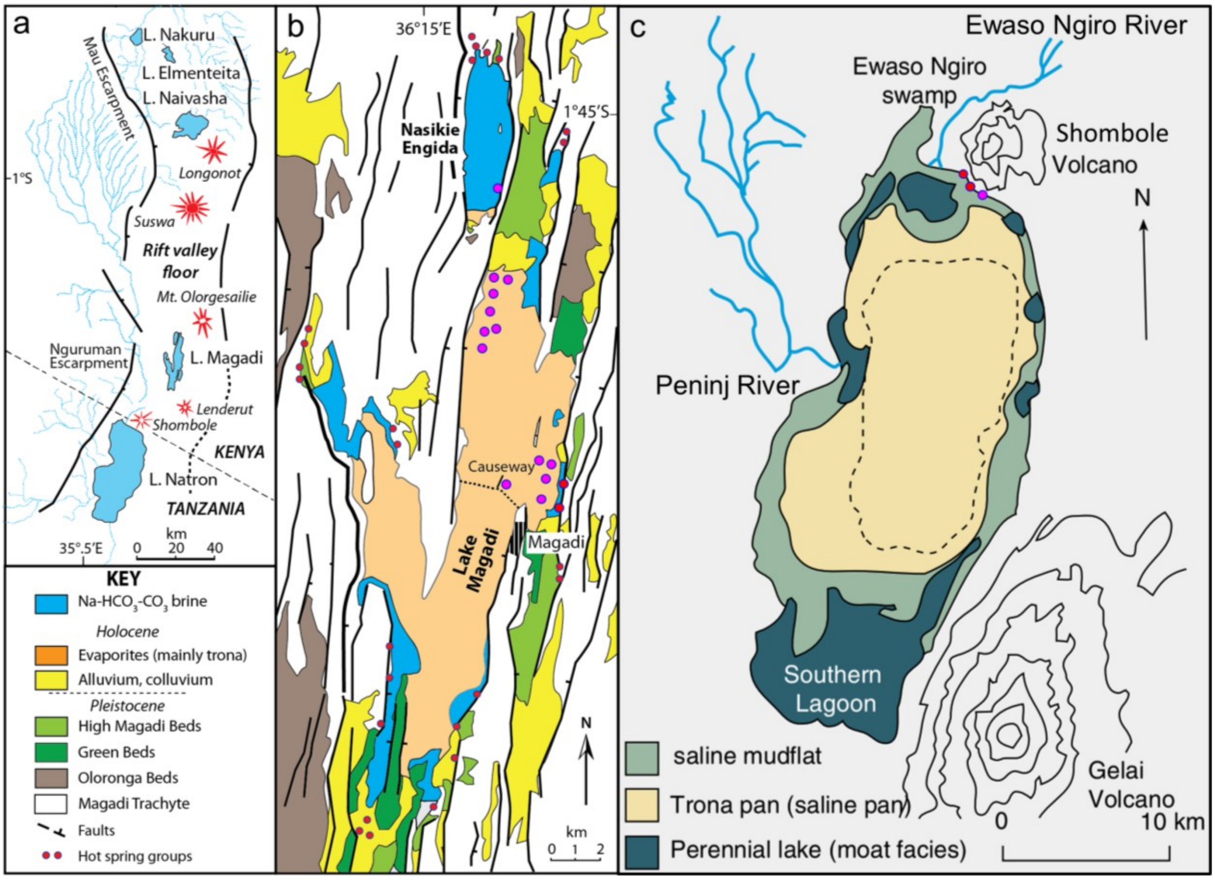

Figure 6. (a) General hydrology of the southern Kenya Rift with major fault trends and volcanos; (b) sampling points and simplified geological setting of the Lake Magadi and Nasikie Engida; (c) simplified geological setting of Lake Natron; (● spring sampling points; ● lake brine sampling points). Maps a-b and c are modified from Renaut et al. (2020) and Warren (2016) respectively.

The evolutionary processes between dilute inflows and concentrated brines presented in previous studies are depicted by the ternary diagram presented in Figure 7, which is a recent hydrochemical data of the MNN lakes collected in 2016 and 2018. The hydrochemical data of samples shown in Figure 6 (sampling points are shown in Figure 6b,c) are presented in appendix 2 to provide the readers with recent data for further works. The cyan arrow (Figure 7) depicts the evolutionary pathway between the dilute rivers and the alkaline groundwater that emerge as warm and hot springs on the lake shores. The river waters which initially contain more than 80% HCO_3^- ions evolve into springs with less than 55% HCO_3^- ions. This evolution is accompanied by significant loss of Ca^{2+} and Mg^{2+} due to precipitation of Ca-Mg carbonates along the flow path. Once the alkaline hot springs emerge to the surface along the lakeshore, the evolution toward lake brines occurs through surface evaporation and mineral precipitation. This evolution is shown by the blue arrow in Figure 7 whereby the relative HCO_3^- content decreases from 50 to 10% whereas CO_3^{2-} content raise from 10 to 50%. Further evaporation causes a decline in the relative CO_3^{2-} content in evaporation ponds due to removal by trona (in Magadi, Natron, southern Nasikie Engida) and HCO_3^- (Northern Nasikie Engida), causing the relative buildup of Cl^- content until halite precipitation sets in, which is possible only in efflorescent crusts and evaporation ponds of TATA chemicals. Chloride in MNN brines behaves conservatively, so it has been used as a brine evolution marker (Eugster, 1970).

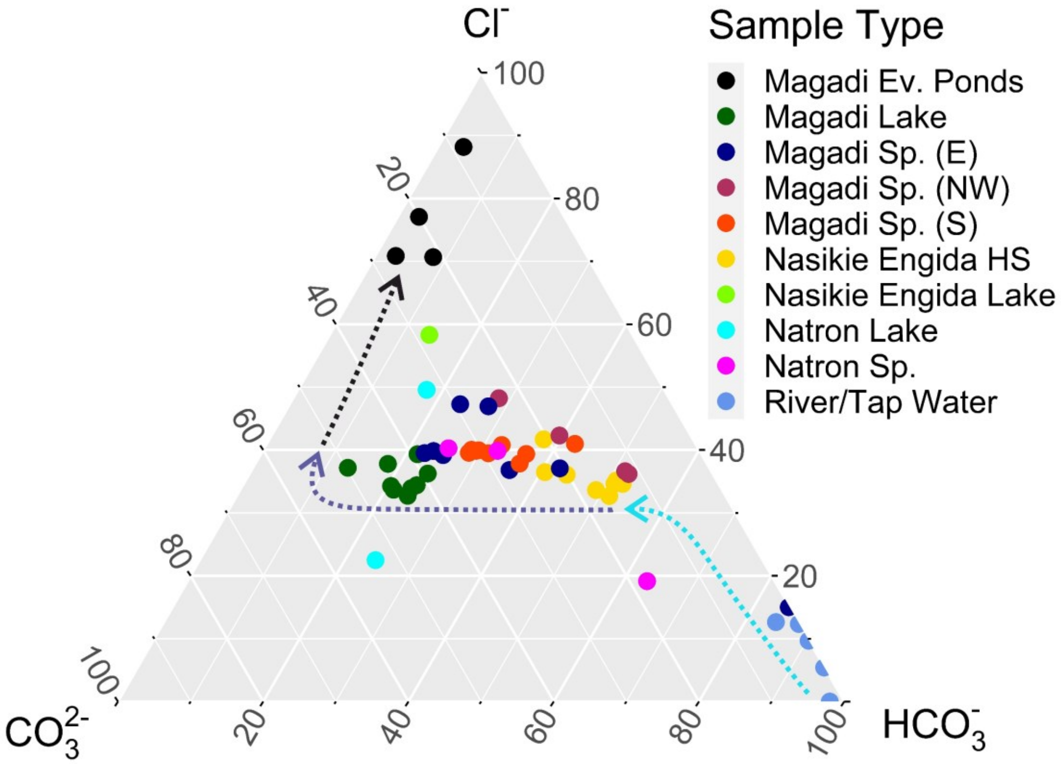

Figure 7. Ternary diagram of water samples collected from MNN lakes and the surrounding during the 2016 and 2018 field campaign

Since the dilute inflows contain relatively lower amounts of K^+, F^-, SiO_2, and SO_4^{2-}, the springs and lake brines contain a relatively smaller amount of these (Jones et al., 1977; Eugster, 1986). In addition, during the evolution of dilute inflows to springs and lake brines, sorption and ion exchange reactions on mineral surfaces may also remove certain solutes (Jones et al., 1977). K^+ loss was observed between streams/dilute groundwater and springs and brines of Magadi and Nasikie Engida due to ion exchange on reactive surfaces such as volcanic glasses or silicate gels and potassium silicate precipitation during subsurface flow (Eugster, 1970; Surdam and Eugster, 1976; Jones et al., 1977). SO_4^{2-} concentration is lowered by sorption and sulfate reduction in earlier evolutionary steps. In concentrated brines, this decline is caused by bacterial sulfate reduction and mirabilite crystallization during cooler nights and conversion to thenardite at midday (Eugster, 1970; Jones et al., 1977; Eugster and Hardie, 1978). The volcanic rocks of East Africa are richer in fluoride than analogous rocks of the world so high fluoride concentrations in the surface waters are the products of weathering reactions (Kilham and Hecky, 1973; Gizaw, 1996). The high fluoride contents of MNN lakes are not caused by unusually high fluoride sources, but rather by the relative paucity of calcium, which is removed as carbonate before fluorite saturation occurs. Elevated Na^+ levels in the concentrated lake brine lead to the precipitation of sodium fluoride salts in the trona crust that include villiaumite (NaF) and kogarkoite (Na_3SO_4F) (Baker, 1958; Eugster, 1970, 1980, 1986; Jones et al., 1977; Nielsen, 1999).

The silica content in rivers, and dilute groundwater arise from the solubility of the trachyte glasses and silicate gels, which rises during evaporative concentration (Eugster, 1980). However, silica loss still occurs along the entire evolutionary steps from dilute rivers to lake brines. The major SiO_2 loss occurred during subsurface flow between dilute rivers and hot springs probably because of precipitation of opaline cements. Siliceous gels are actively forming in the vicinities of hot springs on the northern shore of Nasikie Engida (Eugster, 1967, 1980; Eugster and Jones, 1968; Renaut et al., 2020). The silica content of MNN brines is controlled by the solubility of amorphous silica (Jones et al., 1967; Fritz et al., 1987), which increases rapidly with pH (Figure 8) due to the polymerization of silicic acid (Krauskopf and Bird, 1979). During the evolution of the dilute flows towards the concentrated brine, pH grows logarithmically with the CO_3^{2-}/HCO_3^- ratio (Figure 8). High pH is caused by depletion in HCO_3^- following trona precipitation (see also Figure 7). As shown by the following reaction, CO_2 degassing is essential to explain the pH rise and HCO_3 decline accompanying the evaporative concentration of alkaline brines. Degassing of CO_2 in response to equilibration with the atmosphere or change in temperature leads to a rise in the pH of alkaline waters. It is increased by a decline in the solubility of CO_2 with increasing salinity (Eugster, 1970, 1980; Jones et al., 1977; Eugster and Jones, 1979).

$$2HCO_3^- \rightarrow CO_3^{2-} + CO_2 + H_2O$$

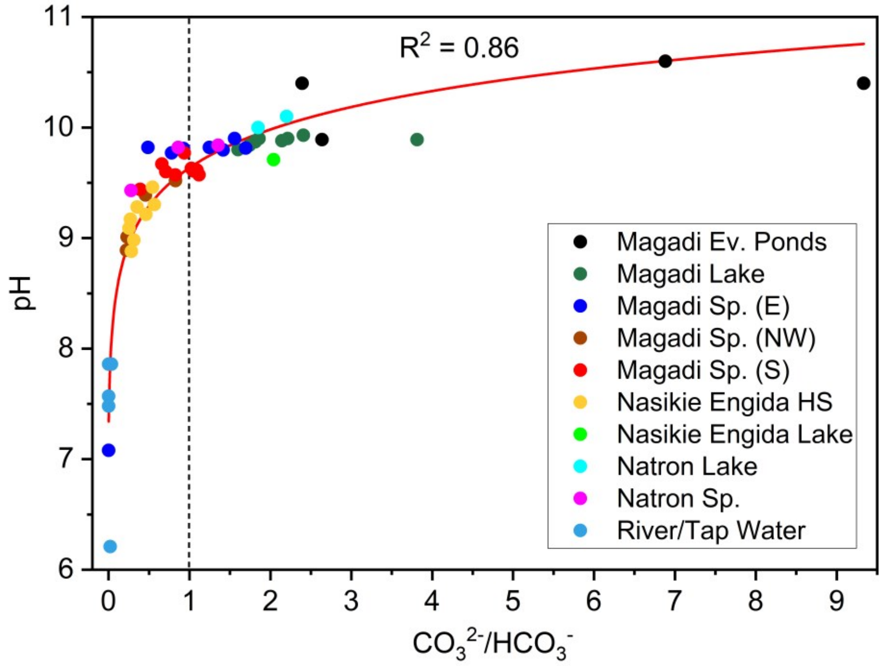

Figure 8. The relation between pH and molar CO_3^{2-}/HCO_3^- ratio of the dilute inflows, springs, lake brines, and evaporation ponds of the MNN lakes presented in Figure 7; The red line is a logarithmic fitting through the data points with a coefficient of determination (R^2) of 0.86

The physicochemical characteristics of the springs of MNN lakes vary depending on their locations, which in turn control the brine chemistry. Mixing between dilute waters and recycled brines could be responsible for the variability in spring chemistry. The hydrochemistry of Lake Natron is more complex and three separate reservoirs are proposed to exist feeding different spring groups (Eugster, 1970). One of the remarkable differences observed in the spring inflows of MNN lakes is the relative CO_3^{2-} and HCO_3^- composition. Nasikie Engida hot springs have the highest temperature (mostly higher than 80 °C) and the lowest CO_3^{2-}/HCO_3^- ratio among the springs (see Figure 8). These hot springs were suggested to emanate from a hot saline groundwater body (100 – 150 °C) recharged by the lower Ewaso Ngiro River and local groundwater (Allen et al., 1989). The CO_3^{2-}/HCO_3^- ratio together with pCO_2 in the atmosphere controls the different mineral assemblages forming in MNN lakes. In northern Nasikie Engida where the hot springs and the lake brines have HCO_3^- content higher than CO_3^{2-} (Figure 8) and there are magmatic CO_2 inputs along the fault fractures (Lee et al., 2016, 2017), nahcolite is the primary precipitate whereas in Magadi, Natron, and southern Nasikie Engida abundant trona forms instead of nahcolite due to the relatively lower pCO_2 level (Jones et al., 1977; Eugster, 1980; Renaut et al., 2020). As discussed earlier in this section, evaporative concentration and mineral precipitation were suggested as the major causes of the alkalinity and salinity of soda lakes of the EARV based on field research, hydrochemical analysis, and modelling. However, there is a lack of experimental evidence on how the stepwise precipitation of different minerals affects the hydrochemistry of these lakes. Chapters 2 and 3 explore the hydrochemical evolution of the brines and the fate of different ions during evaporation by integrating experimental evaporitic mineral precipitation with geochemical modelling of evaporation, and mineral precipitation.

1.3.4. Sodium Carbonate Evaporite Deposits in MNN Lakes

The MNN lakes have mineral assemblages dominated by trona and nahcolite only even though sodium carbonate minerals have other hydrous and anhydrous forms such as natrite (Na_2CO_3), natron ($Na_2CO_3 \cdot 10H_2O$), thermonatrite ($Na_2CO_3 \cdot H_2O$), weigschederite ($Na_2CO_3 \cdot 3NaHCO_3$), and sodium carbonate heptahydrate ($Na_2CO_3 \cdot 7H_2O$). Evaporitic precipitation of different hydrates of the sodium carbonate minerals is favored by different hydrochemical and environmental conditions such as temperature and atmospheric CO_2 levels. Studies of sodium carbonate mineral equilibria allow sedimentological, petrographic, and geochemical interpretations of modern and ancient mineral assemblages (Eugster, 1966; Bradley and Eugster, 1969; Harvie et al., 1984; Monnin and Schott, 1984; Risacher and Clement, 2001; Lowenstein and Demicco, 2006; Liu and Fleet, 2009; Jagniecki et al., 2013, 2015; Lowenstein et al., 2016). Phase relations in the system $NaHCO_3 – Na_2CO_3 – H_2O$ determined in the laboratory (Figure 9a) and using thermodynamic models (Figure 9b) can be used as a guide to interpreting the processes observed in nature at MNN lakes (Eugster, 1966, 1971; Bradley and Eugster, 1969). In the undersaturated solutions, the activity of CO_2 (aCO_2) decreases from right to left (Figure 9b). During evaporation, the compositions of undersaturated solutions move away from the H_2O corner, and along straight lines, if the CO_2 content remains constant. These paths can be used to discuss evaporation under equilibrium conditions in a system closed with respect to all components except H_2O. Path 1 shows evaporation of undersaturated solutions at a constant CO_3/HCO_3 ratio which become saturated with respect to nahcolite at point A (Figure 9b). As evaporation continues, nahcolite precipitates, and the compositions of the bulk solution enter the nahcolite + solution field (Eugster, 1966, 1971; Bradley and Eugster, 1969). This evaporation pathway represents the case of northern Nasikie Engida where dominantly nahcolite forms through contentious removal of water by evaporation while maintaining the bulk composition in the nahcolite + solution field. If evaporation continues passed the boundary between nahcolite + solution and nahcolite + trona + solution, the bulk composition would enter the nahcolite + trona + solution field through conversion of precipitated nahcolite to trona.

Finally, evaporation will be completed when the last remnants of nahcolite convert to trona, and the solution disappears leaving a system consisting of trona only. Nevertheless, the perennial hot spring inflows on the northern lakeshore maintained northern Nasikie Engida in the nahcolite + solution field allowing dominantly subaqueous nahcolite precipitations. These brines were able to maintain the high HCO_3^- content required for nahcolite precipitation from magmatic CO_2 supply (Figure 9a) (Lee et al., 2016, 2017) which otherwise form dominantly trona instead of nahcolite in the southern part of the same lake due to the lower pCO_2 levels (Eugster, 1971, 1980; Renaut et al., 2020).

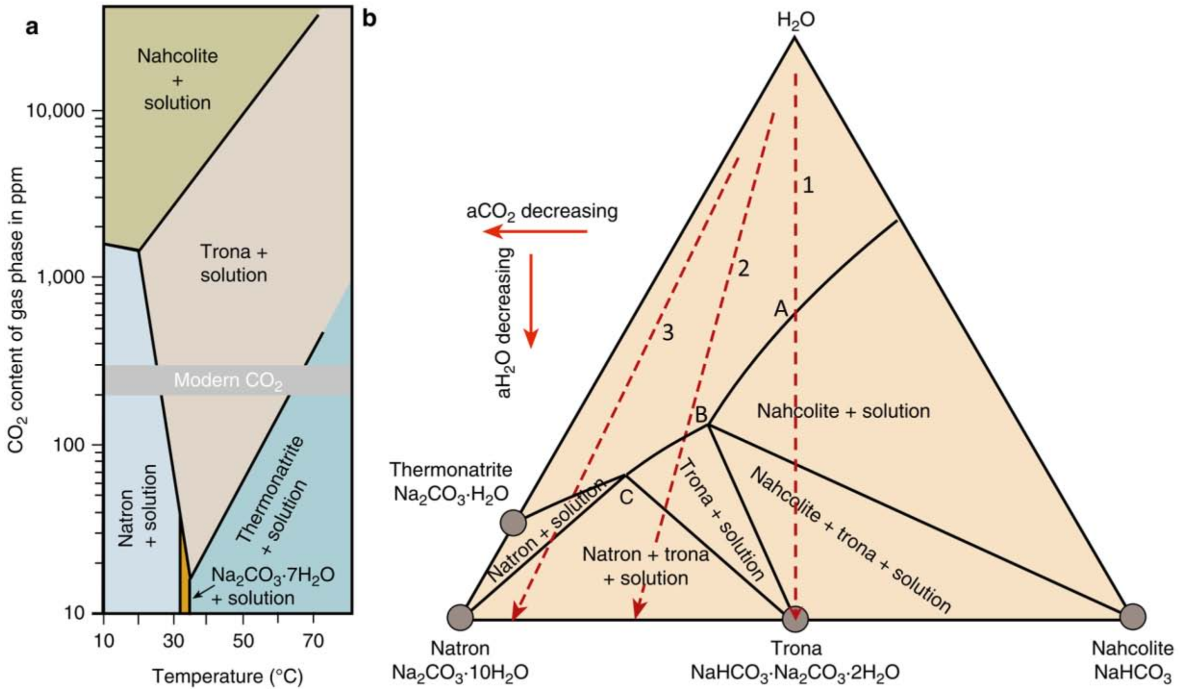

Figure **9**. Phase chemistry of sodium carbonate salts. (a) sodium carbonate phases in equilibrium with a saturated solution as a function of the CO_2 content of the gas phase and temperature. The CO_2 content of today's atmosphere is plotted as a grey band; (b) phase diagram for the sodium carbonate, sodium bicarbonate, and water system at 25 °C (modified from Eugster (1971) and Warren (2016b))

Solutions following evaporation path 2 become saturated with respect to trona at point B (Figure 9b). As trona precipitates and evaporation proceed, the composition of the solution moves towards the trona + solution field and eventually to natron + trona + solution until dryness (Eugster, 1966; Bradley and Eugster, 1969). Path 2 resembles the evaporation pathway followed by Lake Magadi, Natron, and southern Nasikie Engida brines that form dominantly trona deposits, not natron. This implies that these brines follow path 2 until they enter the trona + solution field and remain in this field. In this case, trona precipitates first and evaporation ceases before natron appears. If evaporation proceeds past the trona + solution and natron + trona + solution boundary, the CO_2 level and HCO_3^- the content of the brines would decline and eventually lead to the precipitation of a mixture of trona and natron/thermonatrite depending on temperature (Figure 9a). Nevertheless, an excess supply of atmospheric and biogenic CO_2 maintained precipitation of trona from bicarbonate-poor lake brines and inhibit natron and thermonatrite precipitation (Eugster, 1970, 1971, 1980). Once trona deposition in MNN lakes has begun, the CO_2 resupply from the atmosphere is too slow to allow equilibrium between atmospheric CO_2 levels and levels of CO_2 in the brine. Hence, trona precipitation along with HCO_3^- depletion in increasingly saline brines suggests that fractional crystallization likely controls trona deposition in these lakes (Eugster, 1970; Warren, 2016b).

Path 3 represents the evaporation of bicarbonate-poor solutions in which natron precipitate at point C (Figure 9b). The initial feeder springs are relatively bicarbonate rich. Hence, path 3 cannot lead to the formation of trona deposits of MNN lakes. Path 3 may represent the precipitation of natron from bicarbonate depleted brines on cool nights and thermonatrite during the hot daytime in the artificial ponds of Magadi TATA soda company. When trona precipitation depletes the HCO_3^- content in the residual brines of Magadi, natron crystallizes during cool nights and redissolves during the morning as the brine temperature increase into the trona stability field (Figure 9a). On the other hand, TATA soda company transfer bicarbonate depleted brines from the lake to artificial ponds where dominantly thermonatrite precipitate with some trona due to very rapid H_2O loss in the absence of excess CO_2 input required to replenish HCO_3^- for continuous trona deposition (Eugster, 1970, 1971, 1980).

Lake Magadi and Natron are among the well-known environments in the world where thick Pleistocene and Holocene trona deposits form whereas Lake Nasikie Engida is the only soda lake on modern earth where nahcolite deposits form thanks to the elevated pCO_2 originating from magmatic sources (Eugster, 1980; Lee et al., 2016, 2017; De Cort et al., 2019; Renaut et al., 2020). Nevertheless, Eocene nahcolite deposits are found in the Piceance Creek basin, Colorado, and Anpeng deposit, China due to the elevated atmospheric CO_2 during the Eocene. Trona is the principal sodium carbonate in younger deposits due to the drop in pCO_2 level after the Eocene (Lowenstein and Demicco, 2006; Jagniecki et al., 2015; Lowenstein et al., 2016). Excess concentration of bicarbonate ions in inflow waters is essential to force the hydrochemical evolutions towards alkaline soda composition, typically with pH above 9 (Eugster, 1970, 1971; Jones et al., 1977; Eugster and Hardie, 1978; Eugster and Jones, 1979) whereas excess CO_2 in lake brines is crucial to be able to form thick trona deposits in the geologic record (Earman et al., 2005). Nahcolite precipitations require elevated pCO2 levels (see Figure 9a).

As stated earlier, the mineral paragenesis and assemblages in evaporite settings are controlled by the chemistry of the brines, temperature, and atmospheric CO_2 levels. The control of these parameters on the resulting mineral assemblage and hydrochemistry are explored in chapter 3 by using brine samples with different hydrochemistry collected from different parts of the lakes to represent the full hydrochemical landscape of MNN lakes. Different hydrates of sodium carbonate-bicarbonate minerals may precipitate from soda lakes depending on different hydrochemical and environmental conditions which may lead to transformation between different hydrated forms, e.g., during the isolation of minerals forming in a reservoir of lake brines and further cleaning and drying for ex-situ characterization. To avoid phase transformations and secondary mineral precipitation during sample handling, I opted for droplet evaporation on plane glass surfaces. This method allows in-situ visual inspection of the mineral precipitation process until complete desiccation and analysis of the mineral patterns with Raman spectroscopy and electron microscopy directly, without inducing secondary precipitation. Thermodynamically and/or kinetically controlled mineral phase transformation may occur during evaporation. To examine possible phase transformations between different minerals, I monitored the precipitation process of levitated droplets until complete desiccation by using in-situ X-ray diffractions.

The result of these works (chapters 2 and 3) revealed the importance of integrating experimental and modelling studies in understanding sedimentological, petrographic, and geochemical interpretations of modern and ancient mineral assemblages. On the other hand, hydrochemical models predicting the precipitation sequence, and the relative abundance of evaporitic minerals in the resulting paragenesis are shown to be a novel tool in explaining modern depositional settings and in reconstructing paleoclimatic and hydrochemical conditions during the deposition of ancient evaporite deposits. Experimentally determined and simulated mineral assemblages and parageneses reproduced the various natural mineral assemblages and abundances observed in different parts of the MNN lakes due to the spatial variation of the hydrochemistry, atmospheric pCO_2 levels, and rate of evaporation in springs, lake brines, and evaporation ponds.

1.4. Mineral Self-Organization

Mineral self-organization is a nonequilibrium precipitation process by which minerals self-organize spontaneously into different complex patterns (García-Ruiz, 1985, 1994, 1998, 1999; García-Ruiz et al., 2009; Glaab et al., 2012, 2016; Kellermeier et al., 2013; Barge et al., 2015b; Nakouzi and Steinbock, 2016). Nakouzi and Steinbock (2016) discussed different examples of precipitation systems that couple reaction kinetics and transport to produce nonequilibrium self-assembled materials. Liesegang patterns, discovered in the 19th century by Raphael Edward Liesegang (Liesegang, 1896; Stern, 1954), are prime examples of periodic precipitation forming periodic rings when the outer electrolyte diffuses into the reaction medium (Henisch and García-Ruiz, 1986a, 1986b; Badr et al., 2011; Lagzi, 2012). Other well-known examples of self-assembly are Belousov-Zabotinsky oscillation patterns (Petrov et al., 1993), silica biomorphs (García-Ruiz, 1985, 1994, 1998, 1999; García-Ruiz et al., 2002, 2003, 2009, 2017; Nakouzi et al., 2015; Knoll and Steinbock, 2018), chemical gardens, and mineral vesicles (García-Ruiz, 1985, 1999; Cartwright et al., 2002; Glaab et al., 2012, 2016; Kellermeier et al., 2013; Nakouzi et al., 2014; Bizzarri et al., 2018). These patterns were proposed to form beyond the laboratory in geochemical and mineralogical environments (García-Ruiz, 1994, 1998, 2000; García-Ruiz et al., 2002, 2003, 2009; Kelley et al., 2005; Sultan et al., 2013; Nabika, 2015; McMahon, 2019). Self-assembly opened new avenues for synthesizing advanced functional materials with interesting catalytic, optical, and biomedical applications (Kellermeier et al., 2012; Noorduin et al., 2013; Wang et al., 2015; Nakouzi and Steinbock, 2016; Opel et al., 2016, 2019, 2020; Kaplan et al., 2017; Zhang et al., 2017, 2018; Holtus et al., 2018; Li et al., 2018; Hendrikse et al., 2020, 2021a, 2021b; Bistervels et al., 2022). More importantly, extensive research has been done on mineral self-organization to advance the understanding of plausible pathways to biological self-assembly (Hanczyc et al., 2003), biomineralization (Song and Cölfen, 2010; Bergström et al., 2015; Cardoso et al., 2016), the origin of life, and its implication in life detection and prebiotic geochemistry (García-Ruiz, 1994, 2000; Saladino et al., 2016; Bizzarri et al., 2018; Barge et al., 2019; McMahon, 2019; García-Ruiz et al., 2020). A historical discussion of mineral self-assembly can be found in Cintas (2020)

Among these patterns, biomimetic chemical gardens and silica-carbonate biomorphs received significant attention due to their relevance in life detection (García-Ruiz, 1994, 1998, 2000; García-Ruiz et al., 2002, 2003, 2017, 2020), origin of life, and prebiotic chemistry of early Earth and other planets and moons (Russell et al., 1994; Russell and Hall, 1997; Saladino et al., 2016, 2019; García-Ruiz et al., 2017, 2020; Bizzarri et al., 2018; Barge et al., 2019). Tubular and vesicular chemical gardens are capable of catalyzing prebiotic chemical reactions leading to the synthesis of organic molecules such as carboxylic acids, amino acids, and nucleobases, suggesting the plausible emergence of life in alkaline early Earth soda oceans (Saladino et al., 2016, 2019; Bizzarri et al., 2018; Barge et al., 2019; Angelis et al., 2021). Siliceous sediments and chert deposits of soda lakes, particularly Lake Magadi and Nasikie Engida, were proposed as models to understand the deposition of Precambrian cherts (Eugster, 1967, 1969; Eugster and Jones, 1968; Hay, 1968; Schubel and Simonson, 1990; Behr and Röhricht, 2000; Behr, 2002; Reinhardt et al., 2019) where primitive biological organisms and putative microfossils were reported (Buick, 1990; Schopf, 1993; García-Ruiz, 1994). Self-assembled silica-carbonate biomorphs were proposed as alternative explanations for these primitive organisms and putative microfossils due to morphological reminiscence and the geochemical plausibility of the chemical cocktails used for the synthesis of biomorphs and chemical gardens (García-Ruiz, 1994, 1998, 2000; García-Ruiz et al., 2002, 2003, 2009, 2017, 2020). These chemical cocktails are high pH and silica and carbonate-rich solutions. Soda oceans on Precambrian Earth and other planets and moons such as Enceladus were proposed to contain high pH and high concentration of silica and carbonate species characteristic of modern soda lakes (Kempe and Degens, 1985; Kempe et al., 1989; Kempe and Kazmierczak, 2002, 2011; Glein et al., 2015; Toner and Catling, 2019, 2020).

Beyond laboratory synthesis, mineral self-assembly was proposed as a global phenomenon in alkaline geochemical environments of early Earth and soda oceans of planets and moons (García-Ruiz, 1998, 2000; García-Ruiz et al., 2002, 2003, 2009, 2017, 2020; Saladino et al., 2016; Bizzarri et al., 2018; Barge et al., 2019; Cardoso et al., 2019). Owing to the high pH, and high concentration of silica and carbonate ions, García-Ruiz and colleagues claimed that self-organization could be possible in natural alkaline soda lakes and serpentinization-driven alkaline waters (García-Ruiz, 1994, 1998, 2000; García-Ruiz et al., 2002). This claim was proved by synthesizing silica gardens and biomorphs in natural serpentinization-driven alkaline springs of Ney (California) (García-Ruiz et al., 2017; Kotopoulou et al., 2021). Moreover, silica gardens were synthesized through alteration reactions between model alkaline fluid with granite rocks (Satoh et al., 2014). So far, these two works are the only examples where mineral self-organization was tested by using “natural” waters and rocks, implying the plausibility of self-assembly in early Earth soda oceans. Yet, testing self-assembly in modern soda lakes is still missing. This left us with a lack of the knowledge of plausibility of mineral self-assembly in soda lakes – analogous environments to early Earth alkaline soda oceans – and its implication for the origin of life and life detection on prebiotic Earth and elsewhere in the solar system. To fill these gaps, in the second part of the thesis, I will present the first case of mineral self-organization in “natural soda lake” environments of the East African Rift Valley, which acquire high alkalinity and silica and carbonate content through geochemical processes other than serpentinization.

The East African Rift Valley has been flooded in recent years due to extreme rainfalls in the region (Dong and Sutton, 2015; Kilavi et al., 2018), raising lake levels and diluting the silica content of soda lakes. Consequently, it was not possible to synthesize silica biomorphs in relatively diluted soda lakes. Hence, the thesis focuses on chemical gardens and mineral vesicles based on the carbonate-rich chemistry of soda lakes. Mineral self-assembly experiments were performed in purely “natural” water collected from Lake Magadi soda lake by placing different metal salt pellets and saturated solutions in Magadi water. The result (chapter 4) suggests that mineral self-assembly could have been a common phenomenon in the soda oceans of early Earth and Earth-like planets and moons. The composition of the obtained vesicles and gardens strengthens the proposal that alkaline brines could be ideal sites for the “one-pot” synthesis of prebiotic organic compounds and the origin of life. Furthermore, this part of the thesis provides insights into time-dependent chemical gradients and precipitation processes and the composition and physicochemical characteristics of both synthetic and natural calcium-based chemical gardens synthesized in soda lakes. The results (chapters 5 and 6) have shown that high density of minerals prevents calcium carbonate gardens from developing significant electrochemical potential differences even though significant pH gradients develop across natural calcium carbonate gardens synthesized in soda lake water.

1.4.1. Soda Lakes, Early Earth, and Origin of Life

Earth is 4.5 billion years old and as early as 4.4 billion years ago, water is believed to be condensed on the surface of the Hadean Earth after the solidification of the first ultramafic crust mostly composed of olivine and pyroxenes (Mojzsis et al., 2001; Wilde et al., 2001). The geochemical reactions between the condensed water and the ultramafic rocks – serpentinization – lead to the formation of a reduced atmosphere and H_2 with serpentine and brucite. Later, CH_4 formed upon the reaction of H_2 with CO_2 outgassing from the inner mantle (Sleep et al., 2004; Schulte et al., 2006; Neubeck et al., 2011). The presence of brucite increases the pH leading to alkaline aquatic environments low in silica. When high pH waters derived from serpentinization interact with silica-rich rocks, they will produce silica-rich solutions. Hence, serpentinization was presumed to have created alkaline hydrothermal fluids and high-pH ocean reminiscent of modern earth alkaline water such as Aqua de Ney (García-Ruiz et al., 2017, 2020). On the other hand, Kempe et al. proposed alkaline, silica and bicarbonate-rich geochemical conditions for Precambrian soda oceans similar to modern earth soda lakes (Kempe and Degens, 1985; Kempe et al., 1989) which form mainly through evaporative concentration (Garrels and Mackenzie, 1967; Hardie and Eugster, 1970; Eugster and Hardie, 1978; Eugster and Jones, 1979). The Hadean alkaline oceans are argued to have been widespread allowing the plausible formation of self-assembled chemical gardens and biomorphs (García-Ruiz, 2000; García-Ruiz et al., 2020). Serpentinization along with the Fischer–Tropsch type reactions and evaporative concentration could have produced organic molecules on early Earth (McCollom and Seewald, 2007; Neubeck et al., 2011; Toner and Catling, 2019, 2020). The condensation and polymerization of biologically relevant organic molecules are critical in the emergence of life. However, the synthesis of more complex organic molecules and polymers in aqueous solutions has been challenged by the competition of hydrolysis against polymerization. In the absence of concentrating mechanisms, organic molecules dissolved in primitive Hadean oceans or large terrestrial water bodies would be too diluted to undergo polymerization (Pinto et al., 1980; Stribling and Miller, 1987; Cohn et al., 2001). To address this challenge, prebiotic polymerization via adsorption to mineral surfaces was proposed as a mechanism for the selection and concentration of essential biomolecules (Wächtershäuser, 1988; Ferris et al., 1996; Sowerby et al., 2002; Hanczyc et al., 2003; Schoonen et al., 2004; Hazen and Sverjensky, 2010; Brack, 2013; Dalai et al., 2016). The role of mineral surfaces such as silica, clays, pyrite, and iron oxides/sulfides in polymerization reactions and the synthesis of proto-cellular membranes has been studied by many scholars to understand the geochemical pathway for the transition from inorganic chemistry to biology on early Earth (Ertem and Ferris, 1996; Ferris, 1999, 2005; Martin and Russell, 2003b; Ertem, 2004; Sahai et al., 2017).

In addition to mineral interfaces, gradients were important disequilibrium features of the early Earth contributing to Earth's prebiotic complexity and the emergence of life (Hazen and Sverjensky, 2010). Self-assembled chemical gardens were shown to preserve chemical, pH, and electrochemical potential disequilibrium between the inner and outer solutions for the duration of fluid flow and for some time thereafter (Cartwright et al., 2002; Glaab et al., 2012, 2016; Barge et al., 2015a; Rieder et al., 2022b). Chemical gardens were shown to form in a wide range of ionic solutions such as silicates (Figure 10a-b), carbonates (Figure 10c), phosphates (Figure 10d), and hydroxides when metal salt seeds or metal salt saturated solutions immerse in it (García-Ruiz, 1985; Collins et al., 1999b; Cartwright et al., 2002, 2011a; Barge et al., 2012, 2015b; Glaab et al., 2012, 2016; Kellermeier et al., 2013; Batista and Steinbock, 2015a; Bizzarri et al., 2018; Cardoso et al., 2019). Particularly, the gradients in chemistry, pH, electrochemical potential and mineralogy across silica-based chemical gardens were demonstrated to catalyze the synthesis of biologically relevant organic compounds, suggesting the potential role of chemical gardens in origin of life on early Earth and extraterrestrial bodies (Saladino et al., 2016, 2019; Bizzarri et al., 2018; Barge et al., 2019). A recent study has shown that carbonate-based iron chemical gardens, as well, can catalyze the condensation of simple organic prebiotic molecules to kerogens, suggesting the emergence of elementary biochemical precursors in extraterrestrial soda oceans (Angelis et al., 2021).

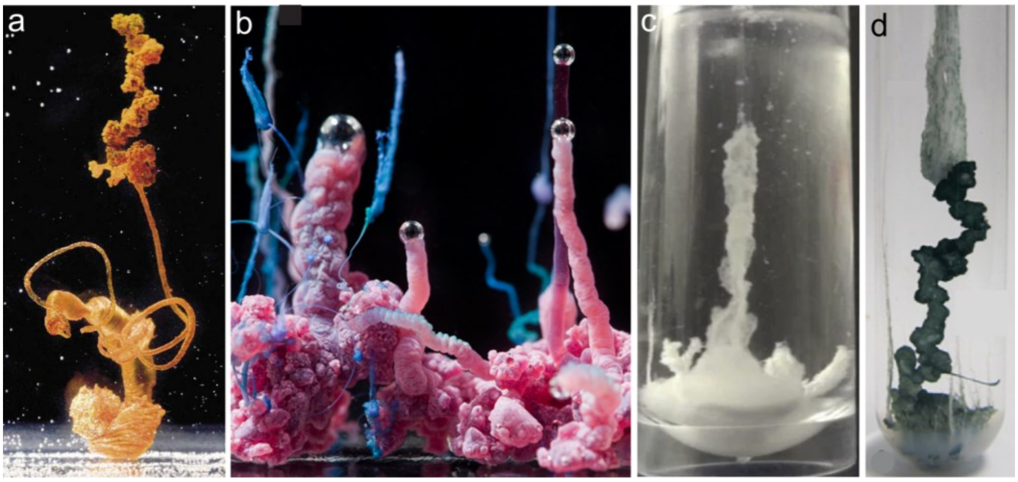

Figure **10**. Chemical gardens formed in (a) sodium silicate solution with an iron(III) chloride seed and (b) cobalt chloride seed; (c) 0.8 M sodium carbonate with calcium chloride seed (taken from Cardoso et al., 2019); (d) 1 M silicate and 0.7 M phosphate with iron (II) chloride (after Barge et al., 2012). Panel a and b images courtesy of Stephane Querbes taken from Barge et al. (2015b).

The relevance of self-assembled mineral structures is not limited to prebiotic geo(chemistry) and origin of life. The precipitation of these inorganic membranes has important implications for life detection in the rock record of early Earth and other planets (Johannessen et al., 2019; McMahon, 2019). Iron (oxy)hydroxide and iron (alumino) silicates filaments and tubes have been reported to form in submarine hydrothermal vents (Grenne and Slack, 2003; Zhou et al., 2015; Dodd et al., 2017). Filaments and tubes from early Earth (Precambrian) have been reported as examples of Earth’s oldest fossils (Bengtson et al., 2017; Dodd et al., 2017). These structures show complex morphological features that look biological, leading to the use of morphology as evidence of biogenicity (Hofmann and Farmer, 2000; Grenne and Slack, 2003; Hofmann et al., 2008; Zhou et al., 2015; Dodd et al., 2017). Nevertheless, abiotic self-assembled mineral structures, mainly chemical gardens and biomorphs, have become alternative explanations for some of these complex morphologies observed in rock records, making the sole use of morphology arguable evidence for biogenicity (García-Ruiz, 1994, 1998; Brasier et al., 2002; García-Ruiz et al., 2002, 2003; McLoughlin et al., 2007; Brasier and Wacey, 2012).

The evidence for the plausibility of mineral self-assembly on early Earth and other planets and moons was based on solely model laboratory solutions until recently. This had casted doubts on the geochemical plausibility of mineral self-assembly due to the extremely high pH and silica content required for mineral self-assembly. It has been proposed that mineral self-assembled structures may have been forming in modern alkaline and silica-rich environments such as soda lakes of the East African Rift Valley and serpentinization-driven alkaline springs of Aqua de Ney (California) (García-Ruiz, 1994, 1998; García-Ruiz et al., 2020). The laboratory synthesis of self-assembled mineral membranes from geological materials was first reported by Satoh et al. (2014). Satoh et al. (2014) synthesized calcium silicate hydrate membranes formed upon the interaction of model alkaline fluids with granites. Recent studies have shown that abiotically self-assembled chemical gardens and biomorphs could form in natural waters collected from serpentinization-driven alkaline springs of Aqua de Ney (California) (García-Ruiz et al., 2017; Kotopoulou et al., 2021).

Generally, mineral self-organization in magmatic-driven acidic and serpentinization-driven alkaline modern environments, mainly hydrothermal systems, has been studied extensively both in the field and in the laboratory with model solutions, mainly silicate, whereas the study of mineral self-assembly in carbonates acquired little attention (Cardoso et al., 2019). Recently, calcium carbonate gardens were synthesized in synthetic sodium carbonate solutions to compare the composition and the microstructures with biominerals of bivalves (Cardoso et al., 2016) and to reproduce the possible conditions of mineral precipitation at hydrothermal vents in the alkaline ocean of Enceladus (Cardoso et al., 2019). Yet, the dynamic diffusion and precipitation processes in model carbonate gardens is not studied. Moreover, the plausibility mineral self-assembly in natural alkaline carbonate-rich soda lakes, which were proposed as ideal settings for self-assembly, is yet unknown. Hence, the second part of the thesis was aimed at filling these gaps.

1.4.2. Metal Silicate Self-Assembled Structures

Classical chemical gardens are synthesized by placing crystals and pellets of metal (Co^{2+}, $Fe^{2+}/^{3+}$, Cu^{2+}, Ni^{2+}, Zn^{2+}, Mn^{2+}, Al^{3+}, $Ba^{2+,}$ and Ca^{2+}) salt into a large volume of aqueous solutions containing anions, for instance, silicates, carbonates, phosphates, and hydroxides (Cartwright et al., 2002; Kellermeier et al., 2013). The aqueous solution dissolves the metal pellets causing mineral precipitation around the pellet at the interface between the two solutions containing the anions and the dissolved metal cations. The mineral osmotic membrane forming around the pellet causes the development of osmotic pressure due to water flow leading to swelling and rupture. Upon rupture of the initial mineral membrane, the lighter acidic metal salt solution ascends vertically through the surrounding anionic solution due to buoyancy followed by spontaneous precipitation. In this manner, tubular tree-like mineral structures form (Cartwright et al., 2002; Kellermeier et al., 2013).

Owing to their relatively robust and stable structures, metal silicate inorganic mineral membranes are among the most studied chemical gardens. Metal-silica membranes form spontaneously via a reaction/diffusion-controlled precipitation process when alkaline silicate-rich solution reacts with concentrated metal solution (Thouvenel-Romans and Steinbock, 2003; Cartwright et al., 2011a, 2011b; Glaab et al., 2012, 2016; Kellermeier et al., 2013; Kotopoulou et al., 2021). Depending on the methods of synthesis, metal salts, and concentration of silica solutions, silica gardens of different morphology and physicochemical properties have been synthesized. In cases metal salt seeds and pellets are used, the diameter of the tubular membranes is controlled by the sizes of the seeds and the pellets. When metal seeds are used bunches of hollow grass-like tubes form (Figure 11a). Glaab et al. (2012, 2016) synthesized silica gardens through the controlled addition of silicate solutions on metal-salt pellets of 16 mm diameter. The resulting tubes had an open end towards the atmosphere with lengths of about 20 mm and diameters of about 6 mm (Figure 11b). The size of the tubes was mainly determined by the dimensions of the used metal salt pellets, with bigger pellets yielding larger tubes (Glaab et al., 2012, 2016).

Chemical gardens are capable of forming in quasi-2D confined geometries as well (Haudin et al., 2014, 2015b, 2015c; Schuszter et al., 2016b, 2016a). Haudin et al. (2014, 2015a, 2015b) presented a detailed account of the effects of variable concentrations and injection rates on the morphology of silica gardens synthesized in confined Hele-Shaw cells. The confined conditions feature a wealth of new patterns including spirals, flowers, worms, and filaments

(Figure 11c). Silica gardens were also synthesized by injecting metal salt solutions into silicate solution to improve the control over the formation of the tubular structures, resulting single tubular membrane (Figure 11d) (Thouvenel-Romans and Steinbock, 2003; Thouvenel-Romans et al., 2005; Pagano et al., 2007). Batista and Steinbock (2015b) grow one-dimensional membranes like chemical gardens in microfluidic devices. Recently, it has been shown that chemical gardens could form by placing droplets of concentrated metal salt solutions into anionic aqueous solutions. In this manner, vesicular minerals precipitate form instead of tubular morphology owing to the shape of the drops (Bizzarri et al., 2018). The chemical gardens synthesized by placing droplets of metal salt solutions on silicate solutions or vice versa give vesicular mineral membranes (Figure 11e) instead of long tubes (Saladino et al., 2016; Bizzarri et al., 2018).

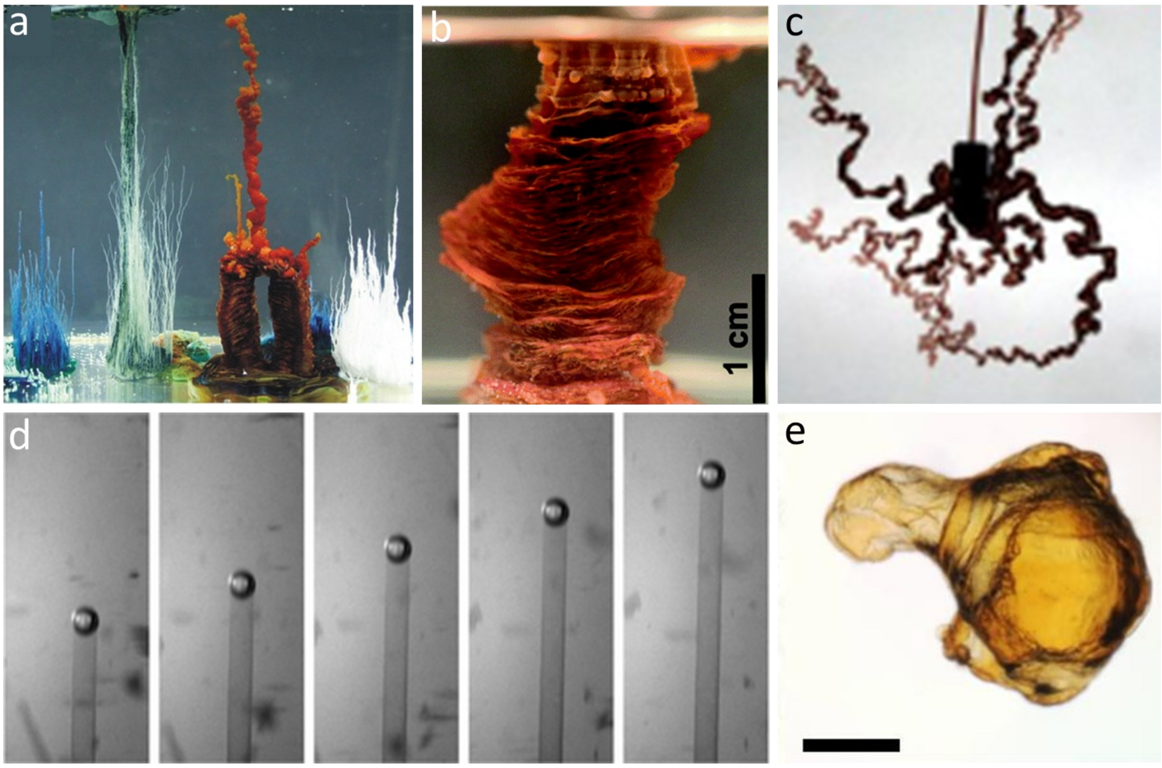

Figure **11**. Metal-silica membranes with different morphologies: (a) silica gardens prepared by addition of concentrated silica sol (pH 11.6) to crystals of (from left to right) $CoCl_2$ (blue), $FeCl_2$ (green), $FeCl_3$ (brown-orange), and $CaCl_2$ (white) (after Glaab, 2011); (b) single macroscopic silica garden tube obtained by controlled addition of sodium silicate solution to pressed pellets of $FeCl_3$ (after Glaab et al., 2016); (c) Filamentous quasi 2D membranes produced by injecting a cobalt chloride sol into sodium silicate solution in a Hele-Shaw cell at a fixed flow rate. Field of view is 15×15 cm (after Haudin et al., 2014); (d) image sequence of tube precipitation in 1 M sodium silicate solution during the injection of 0.5 M cupric sulfate solution at a constant flow rate. Field of view: 3.0 × 7.3 mm (after Thouvenel-Romans et al., 2005); (e) vesicular Fe^{3+}-silica membrane forming by placing a droplet of $FeCl_3$ solutions in alkaline silicate solution, scale 200 mm (after Bizzarri et al., 2018)

Metal-silicate gardens are space-compartmentalized mineral membranes separating two distinct chemical environments in terms of pH and ion concentrations. The precipitation tubes separate the inner acidic metal salt solution from the surrounding outer alkaline silica solution creating chemical gradients across the tubular structure (Glaab et al., 2012, 2016; Kotopoulou et al., 2021; Rieder et al., 2022b). Compositionally, many of the metal silica gardens contain bilayers of amorphous silica on the outer surface and metal hydroxides on the inner surfaces of the tubes. During the tube growth, metal cations trying to penetrate the tube wall from the inner solution oxidize and precipitate as metal oxy/hydroxides once they encounter the high pH outer silicate solution. On the contrary, silicate ions, following the reverse path, polymerize as they experience the low pH of the metal salt solution, and amorphous silica precipitates on the outer wall of the membrane (Jones and Walter, 1998; Collins et al., 1999a; Cartwright et al., 2002; Bormashenko et al., 2006; Pagano et al., 2007; Glaab et al., 2012, 2016, 2017). On the contrary, a recent study has shown that calcium silicate gardens are homogeneous in composition with (hydrated) calcium silicate as the main phase and no detectable differences between the inner and outer surface (Rieder et al., 2022a). On the other hand, a recent study of Fe^{3+} silica gardens synthesized in natural water and commercial silicate argues that iron-silica filamentous membranes are made of amorphous silica layers enclosing an internal layer of nanosized iron-(oxy)hydroxides (Kotopoulou et al., 2021).

Chemical gradients and space compartmentalization of silica gardens allow the study of self-organized natural systems and their implications in materials science and biogeochemistry. Owing to these fascinating features, Glaab et al. (2012) synthesized metal silicate garden tubes with a large enough diameter that allows immersion of electrodes and pipettes for the in situ measurement of pH, electrochemical voltage, and ion concentrations inside the tubes (Figure 12a-b). The electrochemical potential and pH gradient measured across the tubular silicate membranes persisted from hours up to days. The highest voltage of ~550 mV (Figure 12d) and pH difference of ~10 (Figure 12c) were measured across Fe^{3+} silica gardens. Cobalt and Fe^{2+} silica gardens show relatively lower potential and pH gradients, but the gradient persisted longer than that of Fe^{3+} silica gardens (Figure 12c-d). The pH gradient was shown to be the major contributor to the voltage whereas the remaining voltage comes from diffusion and membrane potentials (Glaab et al., 2012, 2016). Similarly, Barge et al. (2015a) measured the electrical potential and current across membranes precipitated by injection and solution interface methods in iron sulfide and iron hydroxide reaction systems. The battery-like nature of chemical gardens was demonstrated by linking multiple experiments in series which produced sufficient electrical energy to light an external light emitting diode (Barge et al., 2015a). These works paved the way for determining relevant properties of chemical gardens that may have played roles in origin of life, and materials sciences that utilize the electrochemical properties of self-organizing chemical systems (Glaab et al., 2012, 2016; Barge et al., 2015a).

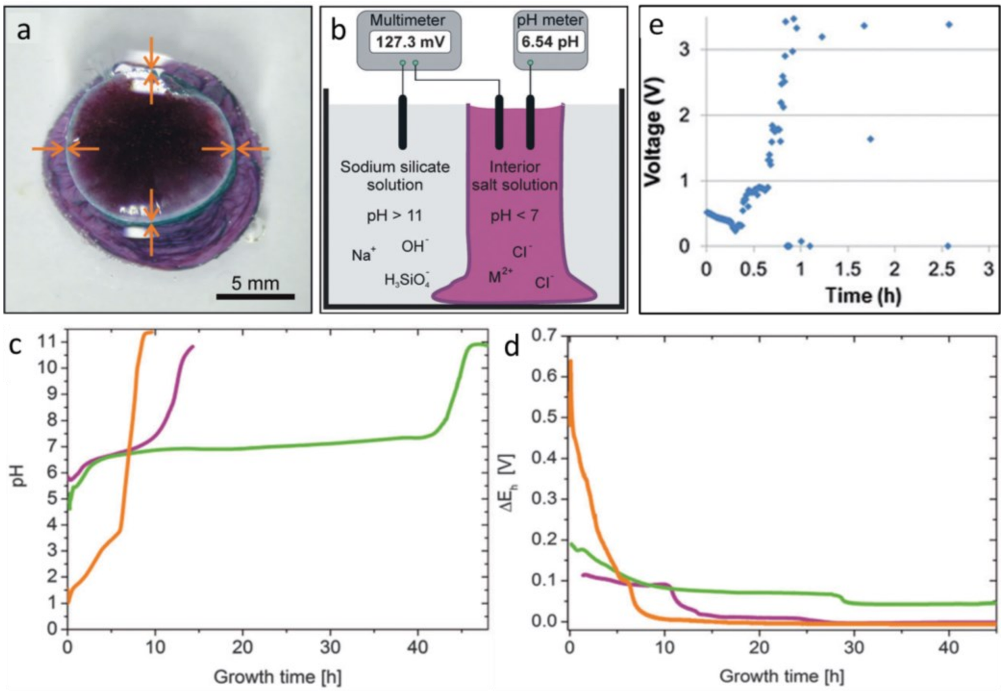

Figure **12**. (a) Top view of the tubular membrane with its open end synthesized by slow addition of silica solution to a tablet of $CoCl_2$ for measuring pH, voltage, and ionic concentrations, arrows mark the tube wall; b) scheme of the experimental setup used for pH and voltage measurements (after Glaab et al., 2012); (c) temporal evolution of the pH inside silica garden tubes prepared with $CoCl_2$ (purple), $FeCl_2$ (green) and $FeCl_3$ (orange); (d) electrochemical potential differences measured across the tube membranes as a function of time (the same colour code as in panel c) (after Glaab et al., 2016); (e) potential difference measured across four electrically connected chemical gardens (after Barge et al., 2015a)

A recent study on Fe^{3+} silica gardens synthesized in silica-rich natural water and commercial silicate solution has shown that the structure and nano-mineralogy of the iron-silica membranes control the catalytic function of the membranes (Kotopoulou et al., 2021). It has been shown that metal silica gardens and mineral vesicles selectively catalyze the synthesis of biologically relevant organic compounds in the presence of formamide (Saladino et al., 2016, 2019; Bizzarri et al., 2018) and pyruvate (Barge et al., 2019). Bilayer membranes, made of amorphous silica and metal oxide/hydroxide nano crystals, catalyze the condensation of formamide, yielding RNA nucleobases, amino acids, and carboxylic acids in a single-pot experiment (Saladino et al., 2016, 2019; Bizzarri et al., 2018). The condensation of formamide is catalyzed during the formation of silica oxyhydroxide membranes of iron, magnesium, manganese, and copper, common metals in the ultramafic and komatiitic rocks of the earliest crust of the planet (Bizzarri et al., 2018). When comparing the reactivities of active versus passive metal silicate chemical gardens, Saladino et al. (2019) did not find significant differences in either the number or the yield of biochemically relevant compounds. This implies that the electrochemical voltage reported in previous silica gardens experiments (Glaab et al., 2012, 2016) does not play a differential role in the catalysis of prebiotic compounds (Saladino et al., 2016). This finding agrees with the finding of Kotopoulou et al. (2021) who attributed the catalytic nature of iron-silica membranes to their structure and nano-mineralogy. Nonetheless, Bizzarri et al. (2018) have shown the higher reactivity of the silica metal oxyhydroxide membranes of the mineral vesicles when compared with metal silicate membranes prepared with classical silica garden experiments (Saladino et al., 2016). Hence, the yield and the variety of synthesized organic molecules were enhanced, resulting in the formation of guanine, hypoxanthine, oxaloacetic acid, and alanine only in the presence of active mineral vesicles. The enhanced catalytic properties of the mineral vesicles obtained with micro drops, compared to silica gardens, might be due to their smaller size (and consequent higher surface area), and the fact that they are actively formed during formamide condensation (Bizzarri et al., 2018). Barge et al. (2019) demonstrated reductive amination of pyruvate in the presence of mixed-valence iron oxyhydroxides to form the amino acid alanine and the reduced product lactate. Gradients of pH, redox, and temperature in iron oxyhydroxide systems were shown to affect product selectivity. Partially oxidized minerals promote amino acid formation whereas purely ferrous hydroxides did not drive reductive amination instead promoted pyruvate reduction to lactate, and ferric hydroxides did not result in any reaction. This finding has shown that geochemical gradients of electrochemical potential, pH, and temperature would strongly affect prebiotic chemistry driven by redox active iron hydroxide minerals on the early Earth (Barge et al., 2019).

1.4.3. Metal Carbonate Self-Assembled Structures

Self-assembled carbonate-based mineral precipitations have implications for biomineralization and bio-inspired materials design (Cardoso et al., 2016; Birkedal and Chen, 2020), origin of life, and prebiotic chemistry (Cardoso et al., 2019; Chin et al., 2020; Angelis et al., 2021), and life detection (García-Ruiz et al., 2002, 2020; McMahon, 2019). Owing to their rich applicability, several studies have reported the formation and characterization of carbonate-based tubular and vesicular structures synthesized by immersion of metal-containing salt seeds and pellets in Na_2CO_3 solutions (Maselko and Strizhak, 2004; Maselko et al., 2005; Cardoso et al., 2016, 2019), by injection of metal salt solutions into carbonate solutions (Kiehl et al., 2015; Takács et al., 2019), by growth on cation exchange membranes (Takiguchi et al., 2006; Igarashi et al., 2008) and gel/liquid interfaces (Steenbjerg Ibsen et al., 2014; Birkedal and Chen, 2020). Metal carbonate membranes have been also produced in quasi-2D confined Hele-Shaw cell by injecting carbonate solution into a solution containing metal salts (Haudin et al., 2015b; Schuszter and De Wit, 2016).

The morphologies of self-assembled tubular and vesicular membranes vary depending on the methods of synthesis, the metal cations, and the concentration of the solutions. Igarashi et al. (2008) and Takiguchi et al. (2006) synthesized tubular agglomerates of vaterite and calcite crystals from calcium chloride and sodium carbonate solutions separated by a cation-exchange membrane (Figure 13a-b). The tubular aggregates form on small spots of the membrane left uncovered with crystals while most of the membrane is covered with small rhombohedral crystals. The length of these tubes reaches 200 – 400 µm with diameters up to 30 µm. Kiehl et al. (2015) injected aluminium chloride into carbonate/hydroxide solution to produce elastic gelatinous tubular, and lumpy membranes by varying the concentration of both solutions (Figure 13c). These membranes grow via self-healing where the pressure-driven stretching is causing chemical bonds to break, and the empty space is filled by molecules from the surrounding solutions. As shown by the image sequences (Figure 13c), in contrast to the silica gardens, the membranes dissolve and disappear after the precipitation process is over. Despite the tubes are synthesized in a mix of hydroxide and carbonate solutions, the carbonate didn’t contribute to the precipitate and the membrane is purely aluminium hydroxide (Kiehl et al., 2015). Maselko and Strizhak (2004) could grow relatively wider tubular calcium-based carbonate tubes by immersing pressed pellets of calcium chloride in sodium carbonate solutions (Figure 13d).

De Wit and colleagues extensively studied the effect of concentration and flow rates on the complex mineral patterns of metal carbonate gardens by injecting carbonate solutions into Ca, Ba, and Co salt solutions in quasi-2D confined Hele-Shaw geometries (Haudin et al., 2015b; Schuszter and De Wit, 2016; Schuszter et al., 2016b, 2016a). Depending on the metal salt types, concentrations, and flow rates, these precipitates show a rather wide range of patterns including flowers, filaments, worms, spirals, and circles (Figure 13e-h). These works discussed the implication of the precipitation patterns of these carbonate minerals from the perspective of

CO_2 sequestration and storage. Particularly, the self-assembly of calcium carbonate minerals has been proposed as a possible pathway for the synthesis of complex hierarchical composite biominerals (Cartwright and Checa, 2007; Cartwright et al., 2009; Checa et al., 2015, 2016). Cardoso et al. (2016) studied the self-assembly of calcium carbonate micro-tubes and nanotubes by comparing the microstructures and compositions of the precipitates with biomineral calcium carbonate tubules that form watering pot shells (Clavagelloidea). The study shows that nature could build calcium carbonate tubes using the self-assembly route observed in chemical gardens and watering pot shell tubules are an example of self-organized mineral tube formation in a biological system (Cardoso et al., 2016).

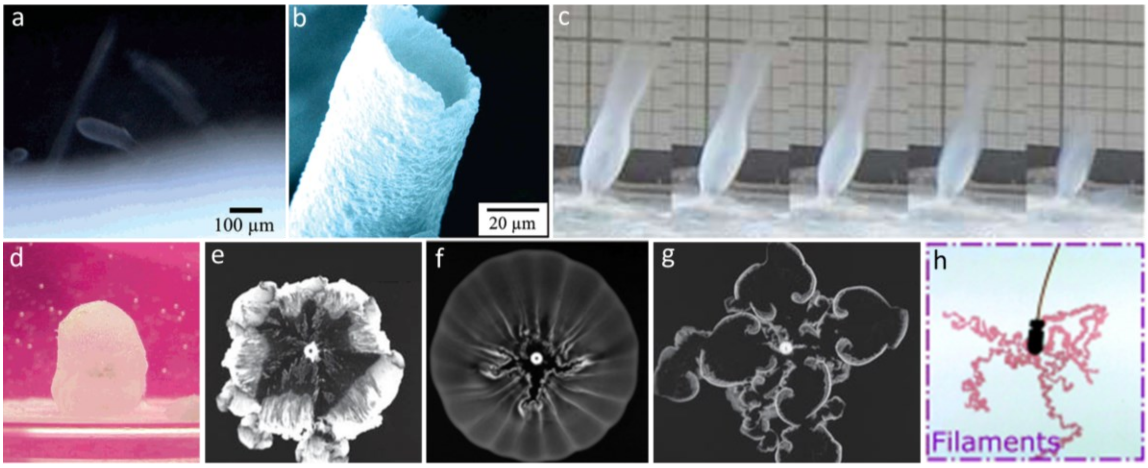

Figure **13**. (a) Calcium carbonate tubes grown on cation-exchange membrane; (b) electron microscope image of tubes grown on cation-exchange membrane (after Takiguchi et al., 2006); (c) time lapse photos of tubes synthesized by injecting saturated $AlCl_3$ into 0.3 M NaOH and 0.22 M Na_2CO_3 (after Kiehl et al., 2015); (d) membrane formed by submerging calcium chloride pellet in 1.5 M of sodium carbonate solution, pellet diameter 6 mm (after Maselko and Strizhak, 2004); (e) $CaCO_3$ patterns obtained by injecting 0.26 M carbonate solution into 0.68 M calcium salt solution, field of view 123 mm×98 mm (after Schuszter and De Wit, 2016); (f) $CaCO_3$ patterns obtained by injecting 1.5 M carbonate solution into 0.5 M Ca solution, field of view 123 mm×98 mm (after Schuszter et al., 2016b); (g) $BaCO_3$ patterns obtained by injecting 0.26 M carbonate solution into 0.68 M barium solution, field of view 123 mm×98 mm (after Schuszter and De Wit, 2016); (h) filaments obtained by injecting 1 M $CoCl_2$ solution into 2.5 M Na_2CO_3, field of view 15 cm×15 cm (taken from Haudin et al., 2015a)

Recently, carbonate-based self-assembled structures attracted the attention of origin of life, prebiotic biogeochemistry, and life detection research mainly for two reasons. One of the reasons is that self-assembled carbonate tubular structures are analogous to submarine serpentinization-driven hydrothermal chimneys which are composed of calcium carbonate minerals and brucite (Kelley et al., 2001; Ludwig et al., 2006) and thought to support the origin and evolution of life (Martin et al., 2008). The second reason is that early Earth and extraterrestrial ocean worlds are thought to be dominated by alkaline carbonate-rich geochemistry that could permit mineral self-organization. This strengthens the significance of understanding carbonate-based mineral self-assembly in natural environments for the accurate detection of life-like abiotic and biotic structures in geologic records (Brasier et al., 2002; García-Ruiz et al., 2002, 2003, 2020; McLoughlin et al., 2007; Brasier and Wacey, 2012; McMahon, 2019). As a result, carbonate chemical gardens are ideal laboratories to investigate the role of mineral self-assembly in origin of life on primitive Earth and other planets and moons and life detection to accurately determine life and life-like patterns.

As a result of these, part of the recent origin of life research focused on exploring chemical gardens synthesized in model carbonate solutions to emulate the conditions on prebiotic Earth and elsewhere in the solar system (Barge et al., 2019; Cardoso et al., 2019; Chin et al., 2020; Angelis et al., 2021). Cardoso et al. (2019) investigated calcium carbonate chemical gardens to reproduce the possible conditions of mineral precipitation at a hydrothermal vent in the alkaline ocean of Saturn's moon Enceladus. This work presents relatively a detailed account of the morphologies, microstructures, and compositions of calcium carbonate chemical gardens formed by immersing calcium chloride salts seeds and pellets into commercial sodium carbonate solution to mimic the geochemistry of the soda ocean of Enceladus. These tubular structures are composed of mainly calcite, vaterite, and gaylussite. The morphological evolution of the tubes may arise from a transformation from amorphous calcium carbonate to vaterite and then to calcite (Rodriguez-Blanco et al., 2011; Bots et al., 2012). These self-assembled structures share similar composition with the serpentinization-driven hydrothermal chimneys of Lost City which are composed of mainly calcium carbonate minerals, calcite, and brucite (Kelley et al., 2001; Ludwig et al., 2006). The mechanical stability of the carbonate tubes is low for two reasons: i) the fast precipitation rate of the carbonate conglomerates that produce clusters of weakly joined particles; and ii) the lack of a scaffold to give greater structural support, which is a polypeptide membrane in biominerals forming stable self-assembled calcium carbonate structures (Cardoso et al., 2019).

Recent studies explored carbonate chemical gardens with respect to their role in catalyzing and polymerization simple organic molecules (Angelis et al., 2021) and in life detection (McMahon, 2019). Angelis et al. (2021) investigated the plausible emergence of biochemistry in Enceladus by using carbonate-based Fe^{2+} and Fe^{3+} chemical gardens as a catalyst to condense phenol-formaldehyde and formamide. In this typical study, the authors added 10 mg of the dried membranes in 200 μL of phenol-formaldehyde solutions. The membrane structures showed catalytic activity enabling the condensation of phenol-formaldehyde that led to the formation of kerogenous products. This study suggested that carbonate-based iron chemical gardens could passively catalyze the condensation of the prebiotic molecule formamide to larger polymers, suggesting that elementary biochemical precursors could have emerged in Enceladus (Angelis et al., 2021). Formamide incubation with these gardens form $C_2N_2H_2$, suggesting the presence of HCN polymers. These polymers differ from nucleobases, amino acids, and carboxylic acids synthesized in previous studies (Saladino et al., 2016; Bizzarri et al., 2018). This difference could be related to the fact that Angelis et al. (2021) used passive chemical gardens as catalysts and these chemical gardens were synthesized in carbonate solution, which is silicate in the case of Saladino et al. (2016) and Bizzarri et al. (2018). From the perspective of detecting fossil records on early Earth and other planets, McMahon (2019) synthesized curving filaments from iron sulfate seed grains in sodium carbonate solution, suggesting that Earth's earliest purported fossils may be iron-mineralized chemical gardens, even though García-Ruiz et al. (2002, 2003) have shown that morphology alone cannot evidence both abiogenicity and biogenicity. These studies on carbonate-based chemical gardens discussed its role in biochemistry and life detection based on morphological studies and ex situ characterizations of synthetic tubes to emulate the geochemical conditions of hydrothermal vents and soda oceans of extraterrestrial planets. Yet, dynamic diffusion and precipitation processes occurring during the growth and subsequent ripening have not been studied in synthetic calcium carbonate tubes. Thus, it's not yet clear where does the catalytic properties in these tubes come from. To shed lights on the characteristics of calcium-carbonate tubes, the second part of the thesis (chapter 5) provides insights into time-dependent chemical gradients and precipitation processes and mineralogical, textural, and physiochemical characteristics of calcium carbonate mineral gardens synthesized in model carbonate solutions. On the other hand, it's crucial to study carbonate tubes synthesized in natural soda lake water to better imitate mineral self-assembly in geochemical conditions of soda oceans of early Earth and other planetary bodies. Considering this, I have studied the time-dependent chemical gradients and precipitation processes and mineralogical, textural, and physiochemical characteristics of calcium carbonate mineral gardens synthesized in natural soda lake water.

1.4.4. Mineral Self-Assembly from Purely Natural Water/Rock Interactions

Mineral self-assembly was thought a plausible scenario in natural geochemical environments on early Earth and other planets and moons. The analogy between these environments and modern geochemical environments such as alkaline soda lakes and serpentinization-driven springs (Kempe et al., 1989; Kempe and Kazmierczak, 2002, 2011) and the potential of these environments in mineral self-assembly was proposed since decades (García-Ruiz, 1994, 1998; García-Ruiz et al., 2002). Despite these facts, laboratory synthesis and characterization of mineral self-assembled structures were focused on using model commercial solutions instead of testing analogue natural waters and rocks. Recently, few studies synthesized mineral self-assembled structures from natural waters and rocks and discussed their implication in prebiotic geochemistry and dissolution/precipitation processes in natural alkaline environments (Satoh et al., 2014; García-Ruiz et al., 2017; Kotopoulou et al., 2021). Satoh et al. (2014) presented the first proof of the formation of silica garden structures because of the alteration of a natural rock by alkaline fluid in flow-through systems. Silica released from the dissolution of sodium-rich plagioclase and quartz reacts with the calcium leached from cementitious buildings to form calcium silicate hydrate phases in the form of hollow tubular structures (Figure 14a,b). These tubular structures form selectively on the surface of plagioclase in a similar way to reverse silica garden structures (Figure 14c). The interior of the tube wall was Si-rich whereas the exterior wall showed a slightly Ca-rich composition (Satoh et al., 2014).

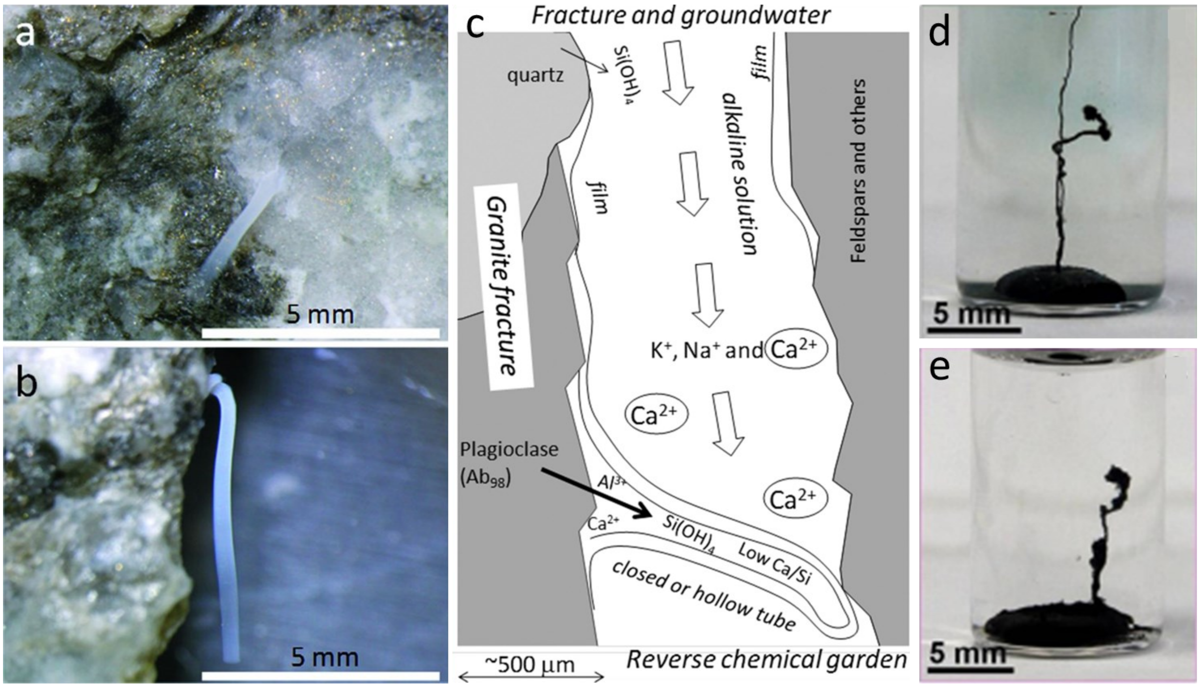

Figure **14**. (a, b) Photomicrographs of the tubular alteration phase on a granite specimen in the reaction cell; (c) schematic illustration of the formation process of the reverse silica garden on the surface of a granite fracture surface by alkaline solution; metal silicate hydrate tubular membranes produced by the reaction of (d) Co and (e) Fe (II) salt pellet with the Ney water. Panels a-c after Satoh et al. (2014) and d-e after García-Ruiz et al. (2017)

García-Ruiz et al. (2017) reported for the first time the synthesis of self-assembled tubular metal silicate hydrates and biomorphs in silica-rich natural alkaline springs (Aqua de Ney, California). The alkaline character and the high pH of the water result from serpentinization processes occurring during the streaming of the water through fractions of the ultramafic rocks of the ophiolite complex (Barnes and O’Neil, 1969; Barnes et al., 1972). The extraordinary enrichment in silica could be explained by the flowing of the alkaline water through the dacitic-andesitic-basaltic rocks, resulting in the dissolution of silica and silica-rich minerals under high pH conditions (García-Ruiz et al., 2017). Hollow tubular Co and Fe (II) metal silicate hydrates, typical of silica gardens produced with model solutions, were synthesized by immersing soluble salt pellets of Co and Fe (II) in Ney water. These structures reproduced a key feature of classical silica gardens: textural and compositional gradients across the membrane (Pagano et al., 2007; Glaab et al., 2016). The outer surface of the metal silicate hydrate membrane was smooth, homogeneous, and rich in silica and metal silicates whereas the inner surface consists of micro rosettes and nano globules enriched in metal (oxy)hydroxides (García-Ruiz et al., 2017). Kotopoulou et al. (2021) studied the nanoscale anatomy of iron-silica self-organized membranes synthesized in these springs by comparing them with the iron-silica membranes synthesized in model silica solutions. This nanoscale study revealed that the anatomy of iron-silica filamentous membranes is made of amorphous silica layers enclosing an internal layer of nanosized iron-(oxy)hydroxides. Membranes grew from natural water show higher micro- and nano porosity and higher specific surface area, suggesting that natural membranes are potentially better catalysts than the model ones (Kotopoulou et al., 2021). Particularly interesting for prebiotic chemistry is the fact that iron nanoparticles catalyze the Fischer–Tropsch synthesis of abiotic organic molecules, which has been shown to take place in submarine hydrothermal vents (Foustoukos and Seyfried, 2004; McCollom and Seewald, 2007; Proskurowski et al., 2008). These findings support the geochemical plausibility of the role of membranes in catalyzing the building blocks of life from simple reactions, such as formamide or pyruvate condensation, or Fischer–Tropsch organics produced in hydrothermal settings. At the same time, these membranes could have provided an inorganic template for the concentration and organization of the organic molecules in a bilayer membrane, under a self-organizing mechanism. Since ferrous iron, silica and carbonate saturated waters and abiotic organics were thought to be widespread in early Earth and Earth-like planets, iron-silica self-organization might have played a universal role in the geochemical origin of life (García-Ruiz et al., 2020; Toner and Catling, 2020; Kotopoulou et al., 2021).

Comparable to the serpentinization-driven alkaline springs of Ney, soda lakes attain high pH, silica, and carbonate content via evaporative concentration relevant to the synthesis of self-assembled tubular structures that may emulate the alkaline hydrothermal chimneys (despite the different mechanisms of formation), e.g., Lost City, Hadean Earth and extra-terrestrial ocean worlds in composition and physiochemical properties. Despite this fact, mineral self-organization was not tested yet in natural soda lakes, which are relevant to the biogeochemistry of early Earth and extraterrestrial ocean worlds. Hence, this thesis aims at investigating the geochemical plausibility of mineral membrane growth from natural aqueous solutions of soda lakes in the presence of different metal cations. Furthermore, the thesis provides insights into time-dependent chemical gradients and precipitation processes of both synthetic and natural calcium carbonate mineral membranes. The composition and physicochemical characteristics of these structures will be characterized in detail and compared with previously reported silicate gardens in terms of roles in prebiotic chemistry, life detection, and origin of life.

References

Allen, D.J., Darling, W.G., Burgess, W.G., 1989. Geothermics and hydrogeology of the southern part of the Kenya Rift Valley with emphasis on the Magadi-Nakuru area (No. SD/89/001), British Geological Survey Research Report SD/89/1. British Geological Survey Research Report SD/89/1, 1–68.

Angelis, G., Kordopati, G.G., Zingkou, E., Karioti, A., Sotiropoulou, G., Pampalakis, G., 2021. Plausible Emergence of Biochemistry in Enceladus Based on Chemobrionics. Chemistry – A European Journal 27, 600–604. https://doi.org/10.1002/chem.202004018

Badr, L., Moussa, Z., Hariri, A., Sultan, R., 2011. Band, target, and onion patterns in Co(OH)2 Liesegang systems. Phys. Rev. E 83, 016109. https://doi.org/10.1103/PhysRevE.83.016109

Baker, B.H., 1987. Outline of the petrology of the Kenya rift alkaline province. Geological Society, London, Special Publications 30, 293–311. https://doi.org/10.1144/GSL.SP.1987.030.01.14

Baker, B.H., 1986. Tectonics and volcanism of the southern Kenya Rift Valley and its influence on rift sedimentation. Geological Society, London, Special Publications 25, 45–57. https://doi.org/10.1144/GSL.SP.1986.025.01.05

Baker, B.H., 1963. Geology of the Area south of Magadi (No. 61). Geol. Surv. Kenya, Nairobi, Kenya, Rep. 61. pp 27.

Baker, B.H., 1958. Geology of the Magadi Area (No. 42). Geol. Surv. Kenya, Nairobi, Kenya, Rep. 42. pp 81.

Baker, B.H., Goles, G.G., Leeman, W.P., Lindstrom, M.M., 1977. Geochemistry and petrogenesis of a basalt-benmoreite-trachyte suite from the southern part of the Gregory Rift, Kenya. Contr. Mineral. and Petrol. 64, 303–332. https://doi.org/10.1007/BF00371759

Baker, B.H., Mitchell, J.G., Williams, L.A.J., 1988. Stratigraphy, geochronology and volcano-tectonic evolution of the Kedong–Naivasha–Kinangop region, Gregory Rift Valley, Kenya. Journal of the Geological Society 145, 107–116. https://doi.org/10.1144/gsjgs.145.1.0107

Baker, B.H., Mohr, P.A., Williams, L. a. J., 1972. Geology of the Eastern Rift System of Africa. https://doi.org/10.1130/SPE136-p1

Barge, L.M., Abedian, Y., Russell, M.J., Doloboff, I.J., Cartwright, J.H.E., Kidd, R.D., Kanik, I., 2015a. From Chemical Gardens to Fuel Cells: Generation of Electrical Potential and Current Across Self-Assembling Iron Mineral Membranes. Angew. Chem. Int. Ed. 54, 8184–8187. https://doi.org/10.1002/anie.201501663

Barge, L.M., Cardoso, S.S.S., Cartwright, J.H.E., Cooper, G.J.T., Cronin, L., De Wit, A., Doloboff, I.J., Escribano, B., Goldstein, R.E., Haudin, F., Jones, D.E.H., Mackay, A.L., Maselko, J., Pagano, J.J., Pantaleone, J., Russell, M.J., Sainz-Díaz, C.I., Steinbock, O., Stone, D.A., Tanimoto, Y., Thomas, N.L., 2015b. From Chemical Gardens to Chemobrionics. Chem. Rev. 115, 8652–8703. https://doi.org/10.1021/acs.chemrev.5b00014

Barge, L.M., Doloboff, I.J., White, L.M., Stucky, G.D., Russell, M.J., Kanik, I., 2012. Characterization of Iron–Phosphate–Silicate Chemical Garden Structures. Langmuir 28, 3714–3721. https://doi.org/10.1021/la203727g

Barge, L.M., Flores, E., Baum, M.M., VanderVelde, D.G., Russell, M.J., 2019. Redox and pH gradients drive amino acid synthesis in iron oxyhydroxide mineral systems. Proceedings of the National Academy of Sciences 116, 4828–4833. https://doi.org/10.1073/pnas.1812098116

Barnes, I., O'Neil, J.R., 1969. The Relationship between Fluids in Some Fresh Alpine-Type Ultramafics and Possible Modern Serpentinization, Western United States. GSA Bulletin 80, 1947–1960. https://doi.org/10.1130/0016-7606(1969)80[1947:TRBFIS]2.0.CO;2

Barnes, I., Rapp, J.B., O'Neil, J.R., Sheppard, R.A., Gude, A.J., 1972. Metamorphic assemblages and the direction of flow of metamorphic fluids in four instances of serpentinization. Contr. Mineral. and Petrol. 35, 263–276. https://doi.org/10.1007/BF00371220

Batista, B.C., Steinbock, O., 2015a. Chemical gardens without silica: the formation of pure metal hydroxide tubes. Chem. Commun. 51, 12962–12965. https://doi.org/10.1039/C5CC04724B

Batista, B.C., Steinbock, O., 2015b. Growing Inorganic Membranes in Microfluidic Devices: Chemical Gardens Reduced to Linear Walls. J. Phys. Chem. C 119, 27045–27052. https://doi.org/10.1021/acs.jpcc.5b08813

Behr, H.-J., 2002. Magadiite and Magadi Chert: A Critical Analysis of the Silica Sediments in the Lake Magadi Basin, Kenya, in: Renaut, R.W., Ashley, G.M. (Eds.), Sedimentation in Continental Rifts. SEPM Society for Sedimentary Geology, pp. 257–273. https://doi.org/10.2110/pec.02.73.0257

Behr, H.-J., Röhricht, C., 2000. Record of seismotectonic events in siliceous cyanobacterial sediments (Magadi cherts), Lake Magadi, Kenya. Int Journ Earth Sciences 89, 268–283. https://doi.org/10.1007/s005319900070

Bell, K., Dawson, J.B., Farquhar, R.M., 1973. Strontium Isotope Studies of Alkalic Rocks: The Active Carbonatite Volcano Oldoinyo Lengai, Tanzania. GSA Bulletin 84, 1019–1030. https://doi.org/10.1130/0016-7606(1973)84<1019:SISOAR>2.0.CO;2

Bengtson, S., Rasmussen, B., Ivarsson, M., Muhling, J., Broman, C., Marone, F., Stampanoni, M., Bekker, A., 2017. Fungus-like mycelial fossils in 2.4-billion-year-old vesicular basalt. Nat Ecol Evol 1, 1–6. https://doi.org/10.1038/s41559-017-0141

Bergström, L., Sturm (née Rosseeva), E.V., Salazar-Alvarez, G., Cölfen, H., 2015. Mesocrystals in Biominerals and Colloidal Arrays. Acc. Chem. Res. 48, 1391–1402. https://doi.org/10.1021/ar500440b

Birkedal, H., Chen, Y., 2020. Mussel inspired self-healing materials: Coordination chemistry of polyphenols, in: Ruiz-Molina, D., van Eldik, R. (Eds.), Advances in Inorganic Chemistry, Nanoscale Coordination Chemistry. Academic Press, pp. 269–298. https://doi.org/10.1016/bs.adioch.2020.03.006

Bistervels, M.H., Kamp, M., Schoenmaker, H., Brouwer, A.M., Noorduin, W.L., 2022. Light-Controlled Nucleation and Shaping of Self-Assembling Nanocomposites. Advanced Materials 34, 2107843. https://doi.org/10.1002/adma.202107843

Bizzarri, B.M., Botta, L., Pérez-Valverde, M.I., Saladino, R., Di Mauro, E., García-Ruiz, J.M., 2018. Silica Metal Oxide Vesicles Catalyze Comprehensive Prebiotic Chemistry. Chemistry – A European Journal 24, 8126–8132. https://doi.org/10.1002/chem.201706162

Bonavia, F.F., Chorowicz, J., Collet, B., 1995. Have wet and dry Precambrian crust largely governed Cenozoic intraplate magmatism from Arabia to East Africa? Geophysical Research Letters 22, 2337–2340. https://doi.org/10.1029/95GL02061

Bormashenko, E., Bormashenko, Y., Stanevsky, O., Pogreb, R., Whyman, G., Stein, T., Barkay, Z., 2006. Template-assisted growth of chemical gardens: Formation of dendrite structures. Colloids and Surfaces A: Physicochemical and Engineering Aspects 289, 245–249. https://doi.org/10.1016/j.colsurfa.2006.06.026

Bots, P., Benning, L.G., Rodriguez-Blanco, J.-D., Roncal-Herrero, T., Shaw, S., 2012. Mechanistic Insights into the Crystallization of Amorphous Calcium Carbonate (ACC). Crystal Growth & Design 12, 3806–3814. https://doi.org/10.1021/cg300676b

Brack, A., 2013. Clay Minerals and the Origin of Life, in: Bergaya, F., Lagaly, G. (Eds.), Developments in Clay Science, Handbook of Clay Science. Elsevier, pp. 507–521. https://doi.org/10.1016/B978-0-08-098258-8.00016-X

Bradley, W.H., Eugster, H.P., 1969. Geochemistry and paleolimnology of the trona deposits and associated authigenic minerals of the Green River Formation of Wyoming (USGS Numbered Series No. Professional Paper 496-B). U.S. Geological Survey.

Brasier, M.D., Green, O.R., Jephcoat, A.P., Kleppe, A.K., Van Kranendonk, M.J., Lindsay, J.F., Steele, A., Grassineau, N.V., 2002. Questioning the evidence for Earth's oldest fossils. Nature 416, 76–81. https://doi.org/10.1038/416076a

Brasier, M.D., Wacey, D., 2012. Fossils and astrobiology: new protocols for cell evolution in deep time. International Journal of Astrobiology 11, 217–228. https://doi.org/10.1017/S1473550412000298

Buatois, L.A., Renaut, R.W., Owen, R.B., Behrensmeyer, A.K., Scott, J.J., 2020. Animal bioturbation preserved in Pleistocene magadiite at Lake Magadi, Kenya Rift Valley, and its implications for the depositional environment of bedded magadiite. Sci Rep 10, 6794. https://doi.org/10.1038/s41598-020-63505-7

Buick, R., 1990. Microfossil recognition in Archean rocks; an appraisal of spheroids and filaments from a 3500 m.y. old chert-barite unit at North Pole, Western Australia. PALAIOS 5, 441–459. https://doi.org/10.2307/3514837

Butzer, K.W., Isaac, G.L., Richardson, J.L., Washbourn-Kamau, C., 1972. Radiocarbon Dating of East African Lake Levels. Science, New Series 175, 1069–1076. https://doi.org/10.1126/science.175.4026.1069

Cabestrero, Ó., Sanz-Montero, M.E., 2018. Brine evolution in two inland evaporative environments: influence of microbial mats in mineral precipitation. J Paleolimnol 59, 139–157. https://doi.org/10.1007/s10933-016-9908-0

Cardoso, S.S.S., Cartwright, J.H.E., Checa, A.G., Sainz-Díaz, C.I., 2016. Fluid-flow-templated self-assembly of calcium carbonate tubes in the laboratory and in biomineralization: The tubules of the watering-pot shells, Clavagelloidea. Acta Biomaterialia 43, 338–347. https://doi.org/10.1016/j.actbio.2016.07.005

Cardoso, S.S.S., Cartwright, J.H.E., Sainz-Díaz, C.I., 2019. Carbonate-hydroxide chemical-garden tubes in the soda ocean of Enceladus: Abiotic membranes and microtubular forms of calcium carbonate. Icarus 319, 337–348. https://doi.org/10.1016/j.icarus.2018.09.020

Carrozzo, F.G., Sanctis, M.C.D., Raponi, A., Ammannito, E., Castillo-Rogez, J., Ehlmann, B.L., Marchi, S., Stein, N., Ciarniello, M., Tosi, F., Capaccioni, F., Capria, M.T., Fonte, S., Formisano, M., Frigeri, A., Giardino, M., Longobardo, A., Magni, G., Palomba, E., Zambon, F., Raymond, C.A., Russell, C.T., 2018. Nature, formation, and distribution of carbonates on Ceres. Science Advances 4, e1701645. https://doi.org/10.1126/sciadv.1701645

Cartwright, J.H.E., Checa, A.G., 2007. The dynamics of nacre self-assembly. Journal of The Royal Society Interface 4, 491–504. https://doi.org/10.1098/rsif.2006.0188

Cartwright, J.H.E., Checa, A.G., Escribano, B., Sainz-Díaz, C.I., 2009. Spiral and target patterns in bivalve nacre manifest a natural excitable medium from layer growth of a biological liquid crystal. Proceedings of the National Academy of Sciences 106, 10499–10504. https://doi.org/10.1073/pnas.0900867106

Cartwright, J.H.E., Escribano, B., Khokhlov, S., Sainz-Díaz, C.I., 2011a. Chemical gardens from silicates and cations of group 2: a comparative study of composition, morphology and microstructure. Phys. Chem. Chem. Phys. 13, 1030–1036. https://doi.org/10.1039/C0CP01093F

Cartwright, J.H.E., Escribano, B., Sainz-Díaz, C.I., 2011b. Chemical-Garden Formation, Morphology, and Composition. I. Effect of the Nature of the Cations. Langmuir 27, 3286–3293. https://doi.org/10.1021/la104192y

Cartwright, J.H.E., García-Ruiz, J.M., Novella, M.L., Otálora, F., 2002. Formation of Chemical Gardens. Journal of Colloid and Interface Science 256, 351–359. https://doi.org/10.1006/jcis.2002.8620

Checa, A.G., Cartwright, J.H.E., Sánchez-Almazo, I., Andrade, J.P., Ruiz-Raya, F., 2015. The cuttlefish Sepia officinalis (Sepiidae, Cephalopoda) constructs cuttlebone from a liquid-crystal precursor. Sci Rep 5, 11513. https://doi.org/10.1038/srep11513

Checa, A.G., Macías-Sánchez, E., Harper, E.M., Cartwright, J.H.E., 2016. Organic membranes determine the pattern of the columnar prismatic layer of mollusc shells. Proceedings of the Royal Society B: Biological Sciences 283, 20160032. https://doi.org/10.1098/rspb.2016.0032

Chin, K., Pasalic, J., Hermis, N., Barge, L.M., 2020. Chemical Gardens as Electrochemical Systems: In Situ Characterization of Simulated Prebiotic Hydrothermal Vents by Impedance Spectroscopy. ChemPlusChem 85, 2619–2628. https://doi.org/10.1002/cplu.202000600

Chorowicz, J., 2005. The East African rift system. Journal of African Earth Sciences, Phanerozoic Evolution of Africa 43, 379–410. https://doi.org/10.1016/j.jafrearsci.2005.07.019

Cintas, P., 2020. Chasing Synthetic Life: A Tale of Forms, Chemical Fossils, and Biomorphs. Angewandte Chemie International Edition 59, 7296–7304. https://doi.org/10.1002/anie.201915853

Cohn, C.A., Hansson, T.K., Larsson, H.S., Sowerby, S.J., Holm, N.G., 2001. Fate of Prebiotic Adenine. Astrobiology 1, 477–480. https://doi.org/10.1089/153110701753593874

Collins, C., Mann, G., Hoppe, E., Duggal, T., Barr, T.L., Klinowski, J., 1999a. NMR and ESCA studies of the ‘silica garden’ Brønsted acid catalyst. Phys. Chem. Chem. Phys. 1, 3685–3687. https://doi.org/10.1039/A904058G

Collins, C., Mokaya, R., Klinowski, J., 1999b. The “silica garden'' as a Brønsted acid catalyst. Phys. Chem. Chem. Phys. 1, 4669–4672. https://doi.org/10.1039/A905296H

Crossley, R., 1979. The Cenozoic stratigraphy and structure of the western part of the Rift Valley in southern Kenya. Journal of the Geological Society 136, 393–405. https://doi.org/10.1144/gsjgs.136.4.0393

Curtis, G., 1967. Notes on some Miocene to Pleistcene potassium/argon result. Calibration of Hominoid Evolution. Scottish Academic Press, Edinburgh 367.

Dalai, P., Kaddour, H., Sahai, N., 2016. Incubating Life: Prebiotic Sources of Organics for the Origin of Life. Elements 12, 401–406. https://doi.org/10.2113/gselements.12.6.401

Dawson, J.B., 2008. The Gregory rift valley and Neogene-recent volcanoes of northern Tanzania, Geological Society of London, Memoirs, 33. Geological Society, London, Memoirs, 33, 102p.

Dawson, J.B., 1992. Neogene tectonics and volcanicity in the North Tanzania sector of the Gregory Rift Valley: contrasts with the Kenya sector. Tectonophysics 204, 81–92. https://doi.org/10.1016/0040-1951(92)90271-7

Dawson, J.B., 1964. Carbonatitic volcanic ashes in Northern Tanganyika. Bull Volcanol 27, 81–91. https://doi.org/10.1007/BF02597513

Dawson, J.B., 1962. The geology of Oldoinyo Lengai. Bull Volcanol 24, 349–387. https://doi.org/10.1007/BF02599356

De Cort, G., Mees, F., Renaut, R.W., Sinnesael, M., Van der Meeren, T., Goderis, S., Keppens, E., Mbuthia, A., Verschuren, D., 2019. Late-Holocene sedimentation and sodium carbonate deposition in hypersaline, alkaline Nasikie Engida, southern Kenya Rift Valley. J Paleolimnol 62, 279–300. https://doi.org/10.1007/s10933-019-00092-2

De Sanctis, M.C., Raponi, A., Ammannito, E., Ciarniello, M., Toplis, M.J., McSween, H.Y., Castillo-Rogez, J.C., Ehlmann, B.L., Carrozzo, F.G., Marchi, S., Tosi, F., Zambon, F., Capaccioni, F., Capria, M.T., Fonte, S., Formisano, M., Frigeri, A., Giardino, M., Longobardo, A., Magni, G., Palomba, E., McFadden, L.A., Pieters, C.M., Jaumann, R., Schenk, P., Mugnuolo, R., Raymond, C.A., Russell, C.T., 2016. Bright carbonate deposits as evidence of aqueous alteration on (1) Ceres. Nature 536, 54–57. https://doi.org/10.1038/nature18290

Deamer, D., Damer, B., 2017. Can Life Begin on Enceladus? A Perspective from Hydrothermal Chemistry. Astrobiology 17, 834–839. https://doi.org/10.1089/ast.2016.1610

Demicco, R.V., Lowenstein, T.K., 2019. When “evaporites” are not formed by evaporation: The role of temperature and pCO2 on saline deposits of the Eocene Green River Formation, Colorado, USA. GSA Bulletin 132, 1365–1380. https://doi.org/10.1130/B35303.1

Deocampo, D.M., Jones, B.F., 2014. Geochemistry of Saline Lakes, in: Holland, H.D., Turekian, K.K. (Eds.), Treatise on Geochemistry (Second Edition). Elsevier, Oxford, pp. 437–469. https://doi.org/10.1016/B978-0-08-095975-7.00515-5

Deocampo, D.M., Renaut, R.W., 2016. Geochemistry of African Soda Lakes, in: Schagerl, M. (Ed.), Soda Lakes of East Africa. Springer International Publishing, Cham, pp. 77–93. https://doi.org/10.1007/978-3-319-28622-8_4

Diez-Martín, F., Sánchez Yustos, P., Gómez de la Rúa, D., Gómez González, J.Á., de Luque, L., Barba, R., 2014. Early Acheulean technology at Es2-Lepolosi (ancient MHS-Bayasi) in Peninj (Lake Natron, Tanzania). Quaternary International, The Evolution of Hominin Behavior during the Oldowan-Acheulian Transition: Recent Evidence from Olduvai Gorge and Peninj (Tanzania) 322–323, 209–236. https://doi.org/10.1016/j.quaint.2013.08.053

Diez-Martín, F., Sánchez-Yustos, P., de Luque, L., 2018. The East African Early Acheulean of Peninj (Lake Natron, Tanzania), in: Gallotti, R., Mussi, M. (Eds.), The Emergence of the Acheulean in East Africa and Beyond: Contributions in Honor of Jean Chavaillon, Vertebrate Paleobiology and Paleoanthropology. Springer International Publishing, Cham, pp. 129–151. https://doi.org/10.1007/978-3-319-75985-2_7

Dodd, M.S., Papineau, D., Grenne, T., Slack, J.F., Rittner, M., Pirajno, F., O’Neil, J., Little, C.T.S., 2017. Evidence for early life in Earth’s oldest hydrothermal vent precipitates. Nature 543, 60–64. https://doi.org/10.1038/nature21377

Dong, B., Sutton, R., 2015. Dominant role of greenhouse-gas forcing in the recovery of Sahel rainfall. Nature Clim Change 5, 757–760. https://doi.org/10.1038/nclimate2664

Earman, S., Phillips, F.M., McPherson, B.J.O.L., 2005. The role of “excess” CO2 in the formation of trona deposits. Applied Geochemistry 20, 2217–2232. https://doi.org/10.1016/j.apgeochem.2005.08.007

Ertem, G., 2004. Montmorillonite, Oligonucleotides, RNA and Origin of Life. Orig Life Evol Biosph 34, 549–570. https://doi.org/10.1023/B:ORIG.0000043130.49790.a7

Ertem, G., Ferris, J.P., 1996. Synthesis of RNA oligomers on heterogeneous templates. Nature 379, 238–240. https://doi.org/10.1038/379238a0

Eugster, H.P., 1986. Lake Magadi, Kenya: a model for rift valley hydrochemistry and sedimentation? Geological Society, London, Special Publications 25, 177–189. https://doi.org/10.1144/GSL.SP.1986.025.01.15

Eugster, H.P., 1980. Lake Magadi, Kenya, and Its Precursors, in: Nissenbaum, A. (Ed.), Developments in Sedimentology, Hypersaline Brines and Evaporitic Environments. Elsevier, pp. 195–232. https://doi.org/10.1016/S0070-4571(08)70239-5

Eugster, H.P., 1971. Origin and deposition of trona. Rocky Mountain Geology 10, 49–55.

Eugster, H.P., 1970. Chemistry and Origin of the Brines of Lake Magadi, Kenya. Mineral. Soc. Amer. Spec. Pap. 3, 213–235.

Eugster, H.P., 1969. Inorganic bedded cherts from the Magadi area, Kenya. Contr. Mineral. and Petrol. 22, 1–31. https://doi.org/10.1007/BF00388011

Eugster, H.P., 1967. Hydrous Sodium Silicates from Lake Magadi, Kenya: Precursors of Bedded Chert. Science 157, 1177–1180. https://doi.org/10.1126/science.157.3793.1177

Eugster, H.P., 1966. Sodium carbonate-bicarbonate minerals as indicators of Pco2. Journal of Geophysical Research (1896-1977) 71, 3369–3377. https://doi.org/10.1029/JZ071i014p03369

Eugster, H.P., Hardie, L.A., 1978. Saline Lakes, in: Lerman, A. (Ed.), Lakes: Chemistry, Geology, Physics. Springer, New York, NY, pp. 237–293. https://doi.org/10.1007/978-1-4757-1152-3_8

Eugster, H.P., Jones, B.F., 1979. Behavior of major solutes during closed-basin brine evolution. American Journal of Science 279, 609–631. https://doi.org/10.2475/ajs.279.6.609

Eugster, H.P., Jones, B.F., 1968. Gels Composed of Sodium-Aluminum Silicate, Lake Magadi, Kenya. Science 161, 160–163.

Fairhead, J.D., Mitchell, J.G., Williams, L. a. J., 1972. New K/Ar Determinations on Rift Volcanics of S. Kenya and their Bearing on Age of Rift Faulting. Nature Physical Science 238, 66–69. https://doi.org/10.1038/physci238066a0

Ferris, J.P., 2005. Mineral Catalysis and Prebiotic Synthesis: Montmorillonite-Catalyzed Formation of RNA. Elements 1, 145–149. https://doi.org/10.2113/gselements.1.3.145

Ferris, J.P., 1999. Prebiotic Synthesis on Minerals: Bridging the Prebiotic and RNA Worlds. Biological Bulletin 196, 311–314. https://doi.org/10.2307/1542957

Ferris, J.P., Hill, A.R., Liu, R., Orgel, L.E., 1996. Synthesis of long prebiotic oligomers on mineral surfaces. Nature 381, 59–61. https://doi.org/10.1038/381059a0

Foster, A., Ebinger, C., Mbede, E., Rex, D., 1997. Tectonic development of the northern Taiizaiiian sector of the East African Rift System. Journal of the Geological Society 154, 689–700. https://doi.org/10.1144/gsjgs.154.4.0689

Foustoukos, D.I., Seyfried, W.E., 2004. Hydrocarbons in Hydrothermal Vent Fluids: The Role of Chromium-Bearing Catalysts. Science 304, 1002–1005. https://doi.org/10.1126/science.1096033

Fritz, B., Zins-Pawlas, M.-P., Gueddari, M., 1987. Geochemistry of silica-rich brines from Lake Natron (Tanzania). Géochimie des saumures riches en silice du lac Natron (Tanzanie). Sciences Géologiques, bulletins et mémoires 40, 97–110. https://doi.org/10.3406/sgeol.1987.1753

García-Ruiz, J.M., 2000. Geochemical Scenarios for the Precipitation of Biomimetic Inorganic Carbonates, in: Grotzinger, J.P., James, N.P. (Eds.), Carbonate Sedimentation and Diagenesis in the Evolving Precambrian World. SEPM Society for Sedimentary Geology, Tulsa, OK, USA, pp. 75–89.

García-Ruiz, J.-M., 1999. Morphological behavior of inorganic precipitation systems, in: Instruments, Methods, and Missions for Astrobiology II. Presented at the Instruments, Methods, and Missions for Astrobiology II, SPIE, pp. 74–82. https://doi.org/10.1117/12.375088

García-Ruiz, J.M., 1998. Carbonate precipitation into alkaline silica-rich environments. Geology 26, 843–846. https://doi.org/10.1130/0091-7613(1998)026<0843:CPIASR>2.3.CO;2

García-Ruiz, J.M., 1994. Inorganic self-organisation in precambrian cherts. Origins Life Evol Biosphere 24, 451–467. https://doi.org/10.1007/BF01582030

García-Ruiz, J.M., 1985. On the formation of induced morphology crystal aggregates. Journal of Crystal Growth 73, 251–262. https://doi.org/10.1016/0022-0248(85)90301-X

García-Ruiz, J.M., Carnerup, A., Christy, A.G., Welham, N.J., Hyde, S.T., 2002. Morphology: An Ambiguous Indicator of Biogenicity. Astrobiology 2, 353–369. https://doi.org/10.1089/153110702762027925

García-Ruiz, J.M., Hyde, S.T., Carnerup, A.M., Christy, A.G., Van Kranendonk, M.J., Welham, N.J., 2003. Self-Assembled Silica-Carbonate Structures and Detection of Ancient Microfossils. Science 302, 1194–1197. https://doi.org/10.1126/science.1090163

García-Ruiz, J.M., Melero-García, E., Hyde, S.T., 2009. Morphogenesis of Self-Assembled Nanocrystalline Materials of Barium Carbonate and Silica. Science 323, 362–365. https://doi.org/10.1126/science.1165349

García-Ruiz, J.M., Nakouzi, E., Kotopoulou, E., Tamborrino, L., Steinbock, O., 2017. Biomimetic mineral self-organization from silica-rich spring waters. Science Advances 3, e1602285. https://doi.org/10.1126/sciadv.1602285

García-Ruiz, J.M., van Zuilen, M.A., Bach, W., 2020. Mineral self-organization on a lifeless planet. Physics of Life Reviews 34–35, 62–82. https://doi.org/10.1016/j.plrev.2020.01.001

Garrels, R.M., Mackenzie, F.T., 1967. Origin of the Chemical Compositions of Some Springs and Lakes, in: Stumm, W. (Ed.), Equilibrium Concepts in Natural Water Systems, Advances in Chemistry. AMERICAN CHEMICAL SOCIETY, WASHINGTON, D.C., pp. 222–242. https://doi.org/10.1021/ba-1967-0067.ch010

Giampouras, M., Garrido, C.J., Bach, W., Los, C., Fussmann, D., Monien, P., García-Ruiz, J.M., 2020. On the controls of mineral assemblages and textures in alkaline springs, Samail Ophiolite, Oman. Chemical Geology 533, 119435. https://doi.org/10.1016/j.chemgeo.2019.119435

Giampouras, M., Garrido, C.J., Zwicker, J., Vadillo, I., Smrzka, D., Bach, W., Peckmann, J., Jiménez, P., Benavente, J., García-Ruiz, J.M., 2019. Geochemistry and mineralogy of serpentinization-driven hyperalkaline springs in the Ronda peridotites. Lithos 350–351, 105215. https://doi.org/10.1016/j.lithos.2019.105215

Gizaw, B., 1996. The origin of high bicarbonate and fluoride concentrations in waters of the Main Ethiopian Rift Valley, East African Rift system. Journal of African Earth Sciences, Hydrogeochemical Studies in Sub-Saharan Africa 22, 391–402. https://doi.org/10.1016/0899-5362(96)00029-2

Glaab, F., 2011. In-situ Examination of Diffusion and Precipitation Processes during the Evolution of Chemical Garden Systems (PhD Thesis). Universität Regensburg, Regensburg, Germany.

Glaab, F., Kellermeier, M., Kunz, W., Morallon, E., García-Ruiz, J.M., 2012. Formation and Evolution of Chemical Gradients and Potential Differences Across Self-Assembling Inorganic Membranes. Angew. Chem. 124, 4393–4397. https://doi.org/10.1002/ange.201107754

Glaab, F., Rieder, J., García-Ruiz, J.M., Kunz, W., Kellermeier, M., 2016. Diffusion and precipitation processes in iron-based silica gardens. Phys. Chem. Chem. Phys. 18, 24850–24858. https://doi.org/10.1039/C6CP02107G

Glaab, F., Rieder, J., Klein, R., Choquesillo-Lazarte, D., Melero-Garcia, E., García-Ruiz, J.-M., Kunz, W., Kellermeier, M., 2017. Precipitation and Crystallization Kinetics in Silica Gardens. ChemPhysChem 18, 338–345. https://doi.org/10.1002/cphc.201600748

Glein, C.R., Baross, J.A., Waite, J.H., 2015. The pH of Enceladus' ocean. Geochimica et Cosmochimica Acta 162, 202–219. https://doi.org/10.1016/j.gca.2015.04.017

Goetz, C., Hillaire-Marcel, C., 1992. U-series disequilibria in early diagenetic minerals from Lake Magadi sediments, Kenya: Dating potential. Geochimica et Cosmochimica Acta 56, 1331–1341. https://doi.org/10.1016/0016-7037(92)90065-Q

Grant, W.D., 2004. Half a Lifetime in Soda Lakes, in: Ventosa, A. (Ed.), Halophilic Microorganisms. Springer, Berlin, Heidelberg, pp. 17–31. https://doi.org/10.1007/978-3-662-07656-9_1

Grenne, T., Slack, J.F., 2003. Bedded jaspers of the Ordovician Løkken ophiolite, Norway: seafloor deposition and diagenetic maturation of hydrothermal plume-derived silica-iron gels. Miner Deposita 38, 625–639. https://doi.org/10.1007/s00126-003-0346-3

Guest, N.J., Stevens, J.A., 1957. Lake Natron, its springs, rivers, brines and visible saline reserves, Geol. Surv. Tanganyika. Mineral Resources Pamphlet, 58.

Hanczyc, M.M., Fujikawa, S.M., Szostak, J.W., 2003. Experimental Models of Primitive Cellular Compartments: Encapsulation, Growth, and Division. Science 302, 618–622. https://doi.org/10.1126/science.1089904

Hardie, L.A., Eugster, H.P., 1970. The Evolution of Closed-Basin Brines. Mineral. Soc. Amer. Spec. Pap. 3, 273–290.

Harrison, J.P., Gheeraert, N., Tsigelnitskiy, D., Cockell, C.S., 2013. The limits for life under multiple extremes. Trends in Microbiology 21, 204–212. https://doi.org/10.1016/j.tim.2013.01.006

Harvie, C.E., Møller, N., Weare, J.H., 1984. The prediction of mineral solubilities in natural waters: The Na-K-Mg-Ca-H-Cl-SO4-OH-HCO3-CO3-CO2-H2O system to high ionic strengths at 25°C. Geochimica et Cosmochimica Acta 48, 723–751. https://doi.org/10.1016/0016-7037(84)90098-X

Haudin, F., Brasiliense, V., Cartwright, J.H.E., Brau, F., Wit, A.D., 2015a. Genericity of confined chemical garden patterns with regard to changes in the reactants. Phys. Chem. Chem. Phys. 17, 12804–12811. https://doi.org/10.1039/C5CP00068H

Haudin, F., Brasiliense, V., E. Cartwright, J.H., Brau, F., Wit, A.D., 2015b. Genericity of confined chemical garden patterns with regard to changes in the reactants. Physical Chemistry Chemical Physics 17, 12804–12811. https://doi.org/10.1039/C5CP00068H

Haudin, F., Cartwright, J.H.E., Brau, F., De Wit, A., 2014. Spiral precipitation patterns in confined chemical gardens. Proceedings of the National Academy of Sciences 111, 17363–17367. https://doi.org/10.1073/pnas.1409552111

Haudin, F., Cartwright, J.H.E., De Wit, A., 2015c. Direct and Reverse Chemical Garden Patterns Grown upon Injection in Confined Geometries. J. Phys. Chem. C 119, 15067–15076. https://doi.org/10.1021/acs.jpcc.5b00599

Hay, R.L., 1968. Chert and its sodium-silicate precursors in sodium-carbonate lakes of East Africa. Contr. Mineral. and Petrol. 17, 255–274. https://doi.org/10.1007/BF00380740

Hazen, R.M., Sverjensky, D.A., 2010. Mineral Surfaces, Geochemical Complexities, and the Origins of Life. Cold Spring Harb Perspect Biol 2, a002162. https://doi.org/10.1101/cshperspect.a002162

Hendrikse, H.C., Aguirre, A., van der Weijden, A., Meeussen, A.S., Neira D'Angelo, F., Noorduin, W.L., 2021a. Rational Design of Bioinspired Nanocomposites with Tunable Catalytic Activity. Crystal Growth & Design 21, 4299–4304. https://doi.org/10.1021/acs.cgd.1c00165

Hendrikse, H.C., Hémon-Charles, S., Helmbrecht, L., van Dam, E.P., Garnett, E.C., Noorduin, W.L., 2021b. Shaping Tin Nanocomposites through Transient Local Conversion Reactions. Crystal Growth & Design 21, 4500–4505. https://doi.org/10.1021/acs.cgd.1c00393

Hendrikse, H.C., van der Weijden, A., Ronda-Lloret, M., Yang, T., Bliem, R., Shiju, N.R., van Hecke, M., Li, L., Noorduin, W.L., 2020. Shape-Preserving Chemical Conversion of Architected Nanocomposites. Advanced Materials 32, 2003999. https://doi.org/10.1002/adma.202003999

Henisch, H.K., García-Ruiz, J.M., 1986a. Crystal growth in gels and Liesegang ring formation: I. Diffusion relationships. Journal of Crystal Growth 75, 195–202. https://doi.org/10.1016/0022-0248(86)90028-X

Henisch, H.K., García-Ruiz, J.M., 1986b. Crystal growth in gels and Liesegang ring formation: II. Crystallization criteria and successive precipitation. Journal of Crystal Growth 75, 203–211. https://doi.org/10.1016/0022-0248(86)90029-1

Hillaire-Marcel, C., Carro, O., Casanova, J., 1986. 14C and Th/U Dating of Pleistocene and Holocene Stromatolites from East African Paleolakes. Quaternary Research 25, 312–239. https://doi.org/10.1016/0033-5894(86)90004-9

Hofmann, B.A., Farmer, J.D., 2000. Filamentous fabrics in low-temperature mineral assemblages: are they fossil biomarkers? Implications for the search for a subsurface fossil record on the early Earth and Mars. Planetary and Space Science, Exobiology in the Solar System 48, 1077–1086. https://doi.org/10.1016/S0032-0633(00)00081-7

Hofmann, B.A., Farmer, J.D., von Blanckenburg, F., Fallick, A.E., 2008. Subsurface Filamentous Fabrics: An Evaluation of Origins Based on Morphological and Geochemical Criteria, with Implications for Exopaleontology. Astrobiology 8, 87–117. https://doi.org/10.1089/ast.2007.0130

Holtus, T., Helmbrecht, L., Hendrikse, H.C., Baglai, I., Meuret, S., Adhyaksa, G.W.P., Garnett, E.C., Noorduin, W.L., 2018. Shape-preserving transformation of carbonate minerals into lead halide perovskite semiconductors based on ion exchange/insertion reactions. Nature Chem 10, 740–745. https://doi.org/10.1038/s41557-018-0064-1

Howell, F.C., 1972. Pliocene/Pleistocene hominidae in eastern Africa: absolute and relative ages. Calibration of hominoid evolution. Scottish Academic Press, Edinburgh 331–368.

Igarashi, K., Takiguchi, M., Ooshima, H., 2008. Growth mechanism of the calcium carbonate tubes on a cation-exchange membrane. J. Ceram. Soc. Japan 116, 111–114. https://doi.org/10.2109/jcersj2.116.111

Isaac, G.L., 1967. The stratigraphy of the Peninj group-early middle Pleistocene formations west of Lake Natron, Tanzania. Background to evolution in Africa 229–257.

Isaac, G.L., 1965. The stratigraphy of the Peninj Beds and the provenance of the Natron Australopithecine mandible. Quaternaria 7, 101–130.

Isaacs, G.L., Curtis, G.H., 1974. Age of early Acheulian industries from the Peninj Group, Tanzania. Nature 249, 624–627. https://doi.org/10.1038/249624a0

Jagniecki, E.A., Jenkins, D.M., Lowenstein, T.K., Carroll, A.R., 2013. Experimental study of shortite (Na2Ca2(CO3)3) formation and application to the burial history of the Wilkins Peak Member, Green River Basin, Wyoming, USA. Geochimica et Cosmochimica Acta 115, 31–45. https://doi.org/10.1016/j.gca.2013.04.005

Jagniecki, E.A., Lowenstein, T.K., 2015. Evaporites of the Green River Formation, Bridger and Piceance Creek Basins: Deposition, Diagenesis, Paleobrine Chemistry, and Eocene Atmospheric CO2, in: Smith, M.E., Carroll, A.R. (Eds.), Stratigraphy and Paleolimnology of the Green River Formation, Western USA, Syntheses in Limnogeology. Springer Netherlands, Dordrecht, pp. 277–312. https://doi.org/10.1007/978-94-017-9906-5_11

Jagniecki, E.A., Lowenstein, T.K., Jenkins, D.M., Demicco, R.V., 2015. Eocene atmospheric CO2 from the nahcolite proxy. Geology 43, 1075–1078. https://doi.org/10.1130/G36886.1

Johannessen, K.C., McLoughlin, N., Vullum, P.E., Thorseth, I.H., 2019. On the biogenicity of Fe-oxyhydroxide filaments in silicified low-temperature hydrothermal deposits: Implications for the identification of Fe-oxidizing bacteria in the rock record. Geobiology 18, 31–53. https://doi.org/10.1111/gbi.12363

Jones, B.F., Eugster, H.P., Rettig, S.L., 1977. Hydrochemistry of the Lake Magadi basin, Kenya. Geochimica et Cosmochimica Acta 41, 53–72. https://doi.org/10.1016/0016-7037(77)90186-7

Jones, B.F., Rettig, S.L., Eugster, H.P., 1967. Silica in Alkaline Brines. Science 158, 1310–1314.

Jones, D.E.H., Walter, U., 1998. The Silicate Garden Reaction in Microgravity: A Fluid Interfacial Instability. Journal of Colloid and Interface Science 203, 286–293. https://doi.org/10.1006/jcis.1998.5447

Kapitsa, A., 1968. Preliminary Report of the Soviet East African Expedition of the Academy of Sciences of the USSR in 1967.

Kaplan, C.N., Noorduin, W.L., Li, L., Sadza, R., Folkertsma, L., Aizenberg, J., Mahadevan, L., 2017. Controlled growth and form of precipitating microsculptures. Science 355, 1395–1399. https://doi.org/10.1126/science.aah6350

Kellermeier, M., Cölfen, H., García-Ruiz, J.M., 2012. Silica Biomorphs: Complex Biomimetic Hybrid Materials from “Sand and Chalk.” European Journal of Inorganic Chemistry 2012, 5123–5144. https://doi.org/10.1002/ejic.201201029

Kellermeier, M., Glaab, F., Melero-García, E., García-Ruiz, J.M., 2013. Experimental Techniques for the Growth and Characterization of Silica Biomorphs and Silica Gardens, in: Methods in Enzymology. Elsevier, pp. 225–256. https://doi.org/10.1016/B978-0-12-416617-2.00011-4

Kelley, D.S., Karson, J.A., Blackman, D.K., Früh-Green, G.L., Butterfield, D.A., Lilley, M.D., Olson, E.J., Schrenk, M.O., Roe, K.K., Lebon, G.T., Rivizzigno, P., 2001. An off-axis hydrothermal vent field near the Mid-Atlantic Ridge at 30° N. Nature 412, 145–149. https://doi.org/10.1038/35084000

Kelley, D.S., Karson, J.A., Früh-Green, G.L., Yoerger, D.R., Shank, T.M., Butterfield, D.A., Hayes, J.M., Schrenk, M.O., Olson, E.J., Proskurowski, G., Jakuba, M., Bradley, A., Larson, B., Ludwig, K., Glickson, D., Buckman, K., Bradley, A.S., Brazelton, W.J., Roe, K., Elend, M.J., Delacour, A., Bernasconi, S.M., Lilley, M.D., Baross, J.A., Summons, R.E., Sylva, S.P., 2005. A Serpentinite-Hosted Ecosystem: The Lost City Hydrothermal Field. Science 307, 1428–1434. https://doi.org/10.1126/science.1102556

Kempe, S., Degens, E.T., 1985. An early soda ocean? Chemical Geology 53, 95–108. https://doi.org/10.1016/0009-2541(85)90023-3

Kempe, S., Kazmierczak, J., 2011. Soda Ocean Hypothesis, in: Reitner, J., Thiel, V. (Eds.), Encyclopedia of Geobiology. Springer Netherlands, Dordrecht, pp. 829–833. https://doi.org/10.1007/978-1-4020-9212-1_192

Kempe, S., Kazmierczak, J., 2002. Biogenesis and Early Life on Earth and Europa: Favored by an Alkaline Ocean? Astrobiology 2, 123–130. https://doi.org/10.1089/153110702753621394

Kempe, S., Kazmierczak, J., Degens, E.T., 1989. The Soda Ocean Concept and Its Bearing on Biotic Evolution, in: Crick, R.E. (Ed.), Origin, Evolution, and Modern Aspects of Biomineralization in Plants and Animals. Springer US, Boston, MA, pp. 29–43. https://doi.org/10.1007/978-1-4757-6114-6_3

Kiehl, M., Kaminker, V., Pantaleone, J., Nowak, P., Dyonizy, A., Maselko, J., 2015. Spontaneous formation of complex structures made from elastic membranes in an aluminum-hydroxide-carbonate system. Chaos 25, 064310. https://doi.org/10.1063/1.4922589

Kilavi, M., MacLeod, D., Ambani, M., Robbins, J., Dankers, R., Graham, R., Titley, H., Salih, A.A.M., Todd, M.C., 2018. Extreme Rainfall and Flooding over Central Kenya Including Nairobi City during the Long-Rains Season 2018: Causes, Predictability, and Potential for Early Warning and Actions. Atmosphere 9, 472. https://doi.org/10.3390/atmos9120472

Kilham, P., Hecky, R.E., 1973. Fluoride: Geochemical and Ecological Significance in East African Waters and Sediments1. Limnology and Oceanography 18, 932–945. https://doi.org/10.4319/lo.1973.18.6.0932

Knoll, P., Steinbock, O., 2018. Inorganic Reactions Self-organize Life-like Microstructures Far from Equilibrium. Israel Journal of Chemistry 58, 682–692. https://doi.org/10.1002/ijch.201700136

Kolpakova, M.N., Gaskova, O.L., 2017. Major ions behaviour during evaporation of different saline type water of Western Mongolian lakes (geochemical modelling). Hydrology Research 49, 163–176. https://doi.org/10.2166/nh.2017.148

Kotopoulou, E., Delgado Huertas, A., Garcia-Ruiz, J.M., Dominguez-Vera, J.M., Lopez-Garcia, J.M., Guerra-Tschuschke, I., Rull, F., 2019. A Polyextreme Hydrothermal System Controlled by Iron: The Case of Dallol at the Afar Triangle. ACS Earth Space Chem. 3, 90–99. https://doi.org/10.1021/acsearthspacechem.8b00141

Kotopoulou, E., Lopez-Haro, M., Calvino Gamez, J.J., García-Ruiz, J.M., 2021. Nanoscale Anatomy of Iron-Silica Self-Organized Membranes: Implications for Prebiotic Chemistry. Angewandte Chemie International Edition 60, 1396–1402. https://doi.org/10.1002/anie.202012059

Krauskopf, K.B., Bird, D.K., 1979. Introduction to Geochemistry, 2nd edition. ed, International Series in the Earth and Planetary Sciences. McGraw-Hill.

Lagzi, I., 2012. Controlling and Engineering Precipitation Patterns. Langmuir 28, 3350–3354. https://doi.org/10.1021/la2049025

Lee, H., Fischer, T.P., Muirhead, J.D., Ebinger, C.J., Kattenhorn, S.A., Sharp, Z.D., Kianji, G., Takahata, N., Sano, Y., 2017. Incipient rifting accompanied by the release of subcontinental lithospheric mantle volatiles in the Magadi and Natron basin, East Africa. Journal of Volcanology and Geothermal Research, Volcano-Hydrothermal Systems 346, 118–133. https://doi.org/10.1016/j.jvolgeores.2017.03.017

Lee, H., Muirhead, J.D., Fischer, T.P., Ebinger, C.J., Kattenhorn, S.A., Sharp, Z.D., Kianji, G., 2016. Massive and prolonged deep carbon emissions associated with continental rifting. Nature Geosci 9, 145–149. https://doi.org/10.1038/ngeo2622

Leet, K., Lowenstein, T.K., Renaut, R.W., Owen, R.B., Cohen, A., 2021. Labyrinth patterns in Magadi (Kenya) cherts: Evidence for early formation from siliceous gels. Geology. https://doi.org/10.1130/G48771.1

Li, L., Fijneman, A.J., Kaandorp, J.A., Aizenberg, J., Noorduin, W.L., 2018. Directed nucleation and growth by balancing local supersaturation and substrate/nucleus lattice mismatch. Proceedings of the National Academy of Sciences 115, 3575–3580. https://doi.org/10.1073/pnas.1712911115

Liesegang, R.E., 1896. Uber einige Eigenschaften von Gallerten. Naturwissensch Wochenschr 11, 353–362.

Liu, X., Fleet, M.E., 2009. Phase relations of nahcolite and trona at high P-T conditions. Journal of Mineralogical and Petrological Sciences 104, 25–36. https://doi.org/10.2465/jmps.080402

Lowenstein, T.K., Demicco, R.V., 2006. Elevated Eocene Atmospheric CO2 and Its Subsequent Decline. Science 313, 1928–1928. https://doi.org/10.1126/science.1129555

Lowenstein, T.K., Dolginko, L.A.C., García-Veigas, J., 2016. Influence of magmatic-hydrothermal activity on brine evolution in closed basins: Searles Lake, California. GSA Bulletin 128, 1555–1568. https://doi.org/10.1130/B31398.1

Ludwig, K.A., Kelley, D.S., Butterfield, D.A., Nelson, B.K., Früh-Green, G., 2006. Formation and evolution of carbonate chimneys at the Lost City Hydrothermal Field. Geochimica et Cosmochimica Acta 70, 3625–3645. https://doi.org/10.1016/j.gca.2006.04.016

Luque, L., Alcalá, L., Domínguez-Rodrigo, M., 2009. The Peninj Group: Tectonics, volcanism, and sedimentary paleoenvironments during the lower Pleistocene in the Lake Natron basin. Peninj. A research project on the archaeology of human origins (1995-2005). Oxbow, Cambridge 15–48.

Ma, L., Lowenstein, T.K., Russell, J.M., 2011. A Brine Evolution Model and Mineralogy of Chemical Sediments in a Volcanic Crater, Lake Kitagata, Uganda. Aquat Geochem 17, 129–140. https://doi.org/10.1007/s10498-010-9108-x

Macintyre, R.M., Mitchell, J.G., Dawson, J.B., 1974. Age of Fault Movements in Tanzanian Sector of East African Rift System. Nature 247, 354–356. https://doi.org/10.1038/247354a0

Manega, P., Bieda, S., 1987. Modern sediments of Lake Natron, Tanzania. Sédimentation récente du lac Natron, Tanzanie. Sciences Géologiques, bulletins et mémoires 40, 83–95. https://doi.org/10.3406/sgeol.1987.1752

Manega, P.C., 1993. Geochronology, geochemistry and isotopic study of the Plio-Pleistocene hominid sites and the Ngorongoro Volcanic Highland in northern Tanzania (Ph.D.). Ann Arbor, United States.

Martin, W., Baross, J., Kelley, D., Russell, M.J., 2008. Hydrothermal vents and the origin of life. Nat Rev Microbiol 6, 805–814. https://doi.org/10.1038/nrmicro1991

Martin, W., Russell, M.J., 2003a. On the origins of cells: a hypothesis for the evolutionary transitions from abiotic geochemistry to chemoautotrophic prokaryotes, and from prokaryotes to nucleated cells.

Philosophical Transactions of the Royal Society of London. Series B: Biological Sciences 358, 59–85. https://doi.org/10.1098/rstb.2002.1183

Martin, W., Russell, M.J., 2003b. On the origins of cells: a hypothesis for the evolutionary transitions from abiotic geochemistry to chemoautotrophic prokaryotes, and from prokaryotes to nucleated cells. Phil. Trans. R. Soc. Lond. B 358, 59–85. https://doi.org/10.1098/rstb.2002.1183

Maselko, J., Borisova, P., Carnahan, M., Dreyer, E., Devon, R., Schmoll, M., Douthat, D., 2005. Spontaneous formation of chemical motors in simple inorganic systems. J Mater Sci 40, 4671–4673. https://doi.org/10.1007/s10853-005-3926-z

Maselko, J., Strizhak, P., 2004. Spontaneous Formation of Cellular Chemical System that Sustains Itself far from Thermodynamic Equilibrium. J. Phys. Chem. B 108, 4937–4939. https://doi.org/10.1021/jp036417j

McCollom, T.M., Bach, W., 2009. Thermodynamic constraints on hydrogen generation during serpentinization of ultramafic rocks. Geochimica et Cosmochimica Acta 73, 856–875. https://doi.org/10.1016/j.gca.2008.10.032

McCollom, T.M., Seewald, J.S., 2007. Abiotic Synthesis of Organic Compounds in Deep-Sea Hydrothermal Environments. Chem. Rev. 107, 382–401. https://doi.org/10.1021/cr0503660

McCord, T.B., Hansen, G.B., Fanale, F.P., Carlson, R.W., Matson, D.L., Johnson, T.V., Smythe, W.D., Crowley, J.K., Martin, P.D., Ocampo, A., Hibbitts, C.A., Granahan, J.C., the NIMS Team, 1998. Salts on Europa’s Surface Detected by Galileo’s Near Infrared Mapping Spectrometer. Science 280, 1242–1245. https://doi.org/10.1126/science.280.5367.1242

McHenry, L.J., Luque, L., Gómez, J.Á., Diez-Martín, F., 2011. Promise and pitfalls for characterizing and correlating the zeolitically altered tephra of the Pleistocene Peninj Group, Tanzania. Quaternary Research 75, 708–720. https://doi.org/10.1016/j.yqres.2010.11.008

McLoughlin, N., Brasier, M.D., Wacey, D., Green, O.R., Perry, R.S., 2007. On Biogenicity Criteria for Endolithic Microborings on Early Earth And Beyond. Astrobiology 7, 10–26. https://doi.org/10.1089/ast.2006.0122

McMahon, S., 2019. Earth’s earliest and deepest purported fossils may be iron-mineralized chemical gardens. Proceedings of the Royal Society B: Biological Sciences 286, 20192410. https://doi.org/10.1098/rspb.2019.2410

McNulty, E., 2017. Lake Magadi and the Soda Lake Cycle: A Study of the Modern Sodium Carbonates and of Late Pleistocene and Holocene Lacustrine Core Sediments (Graduate Dissertations and Theses. 25). Binghamton University, New York, USA.

Mojzsis, S.J., Harrison, T.M., Pidgeon, R.T., 2001. Oxygen-isotope evidence from ancient zircons for liquid water at the Earth’s surface 4,300 Myr ago. Nature 409, 178–181. https://doi.org/10.1038/35051557

Monnin, C., Schott, J., 1984. Determination of the solubility products of sodium carbonate minerals and an application to trona deposition in Lake Magadi (Kenya). Geochimica et Cosmochimica Acta 48, 571–581. https://doi.org/10.1016/0016-7037(84)90285-0

Nabika, H., 2015. Liesegang Phenomena: Spontaneous Pattern Formation Engineered by Chemical Reactions. Current Physical Chemistry 5, 5–20.

Nakouzi, E., Ghoussoub, Y.E., Knoll, P., Steinbock, O., 2015. Biomorph Oscillations Self-organize Micrometer-Scale Patterns and Nanorod Alignment Waves. J. Phys. Chem. C 119, 15749–15754. https://doi.org/10.1021/acs.jpcc.5b04411

Nakouzi, E., Jiménez, Z.A., Biktashev, V.N., Steinbock, O., 2014. Analysis of anchor-size effects on pinned scroll waves and measurement of filament rigidity. Phys. Rev. E 89, 042902. https://doi.org/10.1103/PhysRevE.89.042902

Nakouzi, E., Steinbock, O., 2016. Self-organization in precipitation reactions far from the equilibrium. Science Advances 2, e1601144. https://doi.org/10.1126/sciadv.1601144

Neubeck, A., Duc, N.T., Bastviken, D., Crill, P., Holm, N.G., 2011. Formation of H2 and CH4by weathering of olivine at temperatures between 30 and 70°C. Geochemical Transactions 12, 6. https://doi.org/10.1186/1467-4866-12-6

Nielsen, J.M., 1999. East African magadi (trona): fluoride concentration and mineralogical composition. Journal of African Earth Sciences, Geology and Mineral Resources East Africa 29, 423–428. https://doi.org/10.1016/S0899-5362(99)00107-4

Noorduin, W.L., Grinthal, A., Mahadevan, L., Aizenberg, J., 2013. Rationally Designed Complex, Hierarchical Microarchitectures. Science 340, 832–837. https://doi.org/10.1126/science.1234621

Olson, K.J., Lowenstein, T.K., 2021. Searles Lake evaporite sequences: Indicators of late Pleistocene/Holocene lake temperatures, brine evolution, and pCO2. GSA Bulletin. https://doi.org/10.1130/B35857.1

Opel, J., Brunner, J., Zimmermanns, R., Steegmans, T., Sturm, E., Kellermeier, M., Cölfen, H., García-Ruiz, J.-M., 2019. Symbiosis of Silica Biomorphs and Magnetite Mesocrystals. Advanced Functional Materials 29, 1902047. https://doi.org/10.1002/adfm.201902047

Opel, J., P. Wimmer, F., Kellermeier, M., Cölfen, H., 2016. Functionalisation of silica–carbonate biomorphs. Nanoscale Horizons 1, 144–149. https://doi.org/10.1039/C5NH00094G

Opel, J., Rosenbaum, L.-C., Brunner, J., Staiger, A., Zimmermanns, R., Kellermeier, M., Gaich, T., Cölfen, H., García-Ruiz, J.-M., 2020. Light-switchable anchors on magnetized biomorphic microcarriers. Journal of Materials Chemistry B 8, 4831–4835. https://doi.org/10.1039/C9TB02955A

Otálora, F., Criado-Reyes, J., Baselga, M., Canals, A., Verdugo-Escamilla, C., García Ruiz, J.M., 2020. Hydrochemical and Mineralogical Evolution through Evaporitic Processes in Salar de Llamara Brines (Atacama, Chile). ACS Earth Space Chem. 4, 882–896. https://doi.org/10.1021/acsearthspacechem.0c00085

Owen, R.B., Muiruri, V.M., Lowenstein, T.K., Renaut, R.W., Rabideaux, N., Luo, S., Deino, A.L., Sier, M.J., Dupont-Nivet, G., McNulty, E.P., Leet, K., Cohen, A., Campisano, C., Deocampo, D., Shen, C.-C., Billingsley, A., Mbuthia, A., 2018. Progressive aridification in East Africa over the last half million years and implications for human evolution. PNAS 115, 11174–11179. https://doi.org/10.1073/pnas.1801357115

Owen, R.B., Renaut, R.W., Muiruri, V.M., Rabideaux, N.M., Lowenstein, T.K., McNulty, E.P., Leet, K., Deocampo, D., Luo, S., Deino, A.L., Cohen, A., Sier, M.J., Campisano, C., Shen, C.-C., Billingsley, A., Mbuthia, A., Stockhecke, M., 2019. Quaternary history of the Lake Magadi Basin, southern Kenya Rift: Tectonic and climatic controls. Palaeogeography, Palaeoclimatology, Palaeoecology 518, 97–118. https://doi.org/10.1016/j.palaeo.2019.01.017

Pagano, J.J., Thouvenel-Romans, S., Steinbock, O., 2007. Compositional analysis of copper–silica precipitation tubes. Phys. Chem. Chem. Phys. 9, 110–116. https://doi.org/10.1039/B612982J

Pecoraino, G., D'Alessandro, W., Inguaggiato, S., 2015. The Other Side of the Coin: Geochemistry of Alkaline Lakes in Volcanic Areas, in: Rouwet, D., Christenson, B., Tassi, F., Vandemeulebrouck, J. (Eds.), Volcanic Lakes, Advances in Volcanology. Springer, Berlin, Heidelberg, pp. 219–237. https://doi.org/10.1007/978-3-642-36833-2_9

Petrov, V., Gáspár, V., Masere, J., Showalter, K., 1993. Controlling chaos in the Belousov—Zhabotinsky reaction. Nature 361, 240–243. https://doi.org/10.1038/361240a0

Pinto, J.P., Gladstone, G.R., Yung, Y.L., 1980. Photochemical Production of Formaldehyde in Earth's Primitive Atmosphere. Science 210, 183–185. https://doi.org/10.1126/science.210.4466.183

Proskurowski, G., Lilley, M.D., Seewald, J.S., Früh-Green, G.L., Olson, E.J., Lupton, J.E., Sylva, S.P., Kelley, D.S., 2008. Abiogenic Hydrocarbon Production at Lost City Hydrothermal Field. Science 319, 604–607. https://doi.org/10.1126/science.1151194

Reinhardt, M., Goetz, W., Duda, J.-P., Heim, C., Reitner, J., Thiel, V., 2019. Organic signatures in Pleistocene cherts from Lake Magadi (Kenya) – implications for early Earth hydrothermal deposits. Biogeosciences 16, 2443–2465. https://doi.org/10.5194/bg-16-2443-2019

Renaut, R.W., Owen, R.B., Lowenstein, T.K., Cort, G.D., Mcnulty, E., Scott, J.J., Mbuthia, A., 2020. The role of hydrothermal fluids in sedimentation in saline alkaline lakes: Evidence from Nasikie Engida, Kenya Rift Valley. Sedimentology 68, 108–134. https://doi.org/10.1111/sed.12778

Rieder, J., Nicoleau, L., Glaab, F., E. S. Van Driessche, A., Manuel Garcia-Ruiz, J., Kunz, W., Kellermeier, M., 2022a. Dynamic diffusion and precipitation processes across calcium silicate membranes. Journal of Colloid and Interface Science 618, 206–218. https://doi.org/10.1016/j.jcis.2022.03.042

Rieder, J., Nützl, M., Kunz, W., Kellermeier, M., 2022b. Formation and Dynamic Behavior of Macroscopic Aluminum-Based Silica Gardens. Langmuir 38, 10392–10399. https://doi.org/10.1021/acs.langmuir.2c00971

Risacher, F., Clement, A., 2001. A computer program for the simulation of evaporation of natural waters to high concentration. Computers & Geosciences 27, 191–201. https://doi.org/10.1016/S0098-3004(00)00100-X

Rodriguez-Blanco, J.D., Shaw, S., Benning, L.G., 2011. The kinetics and mechanisms of amorphous calcium carbonate (ACC) crystallization to calcite, viavaterite. Nanoscale 3, 265–271. https://doi.org/10.1039/C0NR00589D

Röhricht, C., 1998. Lithologie und der Chertserien des Magadi Beckens, Lake Magadi, Kenia.

Rooney, T.P., Jones, B.F., Neal, J.T., 1969. Magadiite from Alkali Lake, Oregon. American Mineralogist 54, 1034–1043.

Rull, F., Guerrero, J., Venegas, G., Gázquez, F., Medina, J., 2014. Spectroscopic Raman study of sulphate precipitation sequence in Rio Tinto mining district (SW Spain). Environ Sci Pollut Res 21, 6783–6792. https://doi.org/10.1007/s11356-013-1927-z

Russell, M.J., Daniel, R.M., Hall, A.J., 1993. On the emergence of life via catalytic iron-sulphide membranes. Terra Nova 5, 343–347. https://doi.org/10.1111/j.1365-3121.1993.tb00267.x

Russell, M.J., Daniel, R.M., Hall, A.J., Sherringham, J.A., 1994. A hydrothermally precipitated catalytic iron sulphide membrane as a first step toward life. J Mol Evol 39, 231–243. https://doi.org/10.1007/BF00160147

Russell, M.J., Hall, A.J., 1997. The emergence of life from iron monosulphide bubbles at a submarine hydrothermal redox and pH front. Journal of the Geological Society 154, 377–402. https://doi.org/10.1144/gsjgs.154.3.0377

Sahai, N., Kaddour, H., Dalai, P., Wang, Z., Bass, G., Gao, M., 2017. Mineral Surface Chemistry and Nanoparticle-aggregation Control Membrane Self-Assembly. Sci Rep 7, 43418. https://doi.org/10.1038/srep43418

Saladino, R., Botta, G., Bizzarri, B.M., Di Mauro, E., Garcia Ruiz, J.M., 2016. A Global Scale Scenario for Prebiotic Chemistry: Silica-Based Self-Assembled Mineral Structures and Formamide. Biochemistry 55, 2806–2811. https://doi.org/10.1021/acs.biochem.6b00255

Saladino, R., Di Mauro, E., García-Ruiz, J.M., 2019. A Universal Geochemical Scenario for Formamide Condensation and Prebiotic Chemistry. Chem. Eur. J. 25, 3181–3189. https://doi.org/10.1002/chem.201803889

Satoh, H., Tsukamoto, K., Garcia-Ruiz, J.M., 2014. Formation of chemical gardens on granitic rock: a new type of alteration for alkaline systems. ejm 26, 415–426. https://doi.org/10.1127/0935-1221/2014/0026-2378

Schagerl, M., Renaut, R.W., 2016. Dipping into the Soda Lakes of East Africa, in: Schagerl, M. (Ed.), Soda Lakes of East Africa. Springer International Publishing, Cham, pp. 3–24. https://doi.org/10.1007/978-3-319-28622-8_1

Schoonen, M., Smirnov, A., Cohn, C., 2004. A Perspective on the Role of Minerals in Prebiotic Synthesis. ambi 33, 539–551. https://doi.org/10.1579/0044-7447-33.8.539

Schopf, J.W., 1993. Microfossils of the Early Archean Apex Chert: New Evidence of the Antiquity of Life. Science 260, 640–646. https://doi.org/10.1126/science.260.5108.640

Schubel, K.A., Simonson, B.M., 1990. Petrography and diagenesis of cherts from Lake Magadi, Kenya. Journal of Sedimentary Research 60, 761–776. https://doi.org/10.1306/212F9269-2B24-11D7-8648000102C1865D

Schulte, M., Blake, D., Hoehler, T., McCollom, T., 2006. Serpentinization and Its Implications for Life on the Early Earth and Mars. Astrobiology 6, 364–376. https://doi.org/10.1089/ast.2006.6.364

Schuszter, G., Brau, F., De Wit, A., 2016a. Calcium Carbonate Mineralization in a Confined Geometry. Environ. Sci. Technol. Lett. 3, 156–159. https://doi.org/10.1021/acs.estlett.6b00074

Schuszter, G., Brau, F., Wit, A.D., 2016b. Flow-driven control of calcium carbonate precipitation patterns in a confined geometry. Phys. Chem. Chem. Phys. 18, 25592–25600. https://doi.org/10.1039/C6CP05067K

Schuszter, G., De Wit, A., 2016. Comparison of flow-controlled calcium and barium carbonate precipitation patterns. J. Chem. Phys. 145, 224201. https://doi.org/10.1063/1.4971286

Scoon, R.N., 2018. The Gregory Rift, in: Scoon, R.N. (Ed.), Geology of National Parks of Central/Southern Kenya and Northern Tanzania: Geotourism of the Gregory Rift Valley, Active Volcanism and Regional Plateaus. Springer International Publishing, Cham, pp. 39–57. https://doi.org/10.1007/978-3-319-73785-0_5

Sleep, N.H., Meibom, A., Fridriksson, Th., Coleman, R.G., Bird, D.K., 2004. H2-rich fluids from serpentinization: Geochemical and biotic implications. Proceedings of the National Academy of Sciences 101, 12818–12823. https://doi.org/10.1073/pnas.0405289101

Smith, M.E., Carroll, A.R., 2015. Introduction to the Green River Formation, in: Smith, M.E., Carroll, A.R. (Eds.), Stratigraphy and Paleolimnology of the Green River Formation, Western USA, Syntheses in Limnogeology. Springer Netherlands, Dordrecht, pp. 1–12. https://doi.org/10.1007/978-94-017-9906-5_1

Song, R.-Q., Cölfen, H., 2010. Mesocrystals—Ordered Nanoparticle Superstructures. Advanced Materials 22, 1301–1330. https://doi.org/10.1002/adma.200901365

Sowerby, S.J., Petersen, G.B., Holm, N.G., 2002. Primordial Coding of Amino Acids by Adsorbed Purine Bases. Orig Life Evol Biosph 32, 35–46. https://doi.org/10.1023/A:1013957812213

Steenbjerg Ibsen, C.J., Mikladal, B.F., Bjørnholt Jensen, U., Birkedal, H., 2014. Hierarchical Tubular Structures Grown from the Gel/Liquid Interface. Chem. Eur. J. 20, 16112–16120. https://doi.org/10.1002/chem.201402741

Stern, K.H., 1954. The Liesegang Phenomenon. Chem. Rev. 54, 79–99. https://doi.org/10.1021/cr60167a003

Stribling, R., Miller, S.L., 1987. Energy yields for hydrogen cyanide and formaldehyde syntheses: The hcn and amino acid concentrations in the primitive ocean. Origins Life Evol Biosphere 17, 261–273. https://doi.org/10.1007/BF02386466

Sultan, R.F., Abdel-Fattah, Abdel-Rahman, M., 2013. On dynamic self-organization: examples from magmatic and other geochemical systems. Lat. Am. j. solids struct. 10, 59–73. https://doi.org/10.1590/S1679-78252013000100006

Surdam, R.C., Eugster, H.P., 1976. Mineral reactions in the sedimentary deposits of the Lake Magadi region, Kenya. GSA Bulletin 87, 1739–1752. https://doi.org/10.1130/0016-7606(1976)87<1739:MRITSD>2.0.CO;2

Takács, D., Schuszter, G., Sebők, D., Kukovecz, Á., Horváth, D., Tóth, Á., 2019. Magnetic-Field-Manipulated Growth of Flow-Driven Precipitate Membrane Tubes. Chemistry – A European Journal 25, 14826–14833. https://doi.org/10.1002/chem.201902830

Takiguchi, M., Igarashi, K., Azuma, M., Ooshima, H., 2006. Tubular Structure Agglomerates of Calcium Carbonate Crystals Formed on a Cation-Exchange Membrane. Crystal Growth & Design 6, 1611–1614. https://doi.org/10.1021/cg060045x

Thouvenel-Romans, S., Pagano, J.J., Steinbock, O., 2005. Bubble guidance of tubular growth in reaction–precipitation systems. Phys. Chem. Chem. Phys. 7, 2610–2615. https://doi.org/10.1039/B504407C

Thouvenel-Romans, S., Steinbock, O., 2003. Oscillatory Growth of Silica Tubes in Chemical Gardens. J. Am. Chem. Soc. 125, 4338–4341. https://doi.org/10.1021/ja0298343

Thouveny, N., Taieb, M., 1987. Etude paléomagnétique des formations du Plio-Pléistocène de la région de la Peninj (Ouest du lac Natron, Tanzanie). Limites de l'interprétation magnétostratigraphique. Paleomagnetic study of Plio-Pleistocene formations in the Peninj area (west of Lake Natron, Tanzania). Limits of the magnetostratigraphic interpretation. Sciences Géologiques, bulletins et mémoires 40, 57–70. https://doi.org/10.3406/sgeol.1987.1750

Thouveny, N., Taieb, M., 1986. Preliminary magnetostratigraphic record of Pleistocene deposits, Lake Natron Basin, Tanzania. Geological Society, London, Special Publications 25, 331–336. https://doi.org/10.1144/GSL.SP.1986.025.01.27

Tiercelin, J.-J., Lezzar, K.-E., 2002. A 300 Million Years History of Rift Lakes in Central and East Africa: An Updated Broad Review, in: Odada, E.O., Olago, D.O. (Eds.), The East African Great Lakes: Limnology, Palaeolimnology and Biodiversity, Advances in Global Change Research. Springer Netherlands, Dordrecht, pp. 3–60. https://doi.org/10.1007/0-306-48201-0_1

Toner, J.D., Catling, D.C., 2020. A carbonate-rich lake solution to the phosphate problem of the origin of life. PNAS 117, 883–888. https://doi.org/10.1073/pnas.1916109117

Toner, J.D., Catling, D.C., 2019. Alkaline lake settings for concentrated prebiotic cyanide and the origin of life. Geochimica et Cosmochimica Acta 260, 124–132. https://doi.org/10.1016/j.gca.2019.06.031

Wächtershäuser, G., 1988. Before enzymes and templates: theory of surface metabolism. Microbiological Reviews 52, 452–484. https://doi.org/10.1128/mr.52.4.452-484.1988

Wang, G., Zhao, X., Möller, M., Moya, S.E., 2015. Interfacial Reaction-Driven Formation of Silica Carbonate Biomorphs with Subcellular Topographical Features and Their Biological Activity. ACS Appl. Mater. Interfaces 7, 23412–23417. https://doi.org/10.1021/acsami.5b08493

Warren, J.K., 2016a. Subaqueous Salts: Salinas and Perennial Lakes, in: Warren, J.K. (Ed.), Evaporites: A Geological Compendium. Springer International Publishing, Cham, pp. 303–380. https://doi.org/10.1007/978-3-319-13512-0_4

Warren, J.K., 2016b. Depositional Chemistry and Hydrology, in: Warren, J.K. (Ed.), Evaporites: A Geological Compendium. Springer International Publishing, Cham, pp. 85–205. https://doi.org/10.1007/978-3-319-13512-0_2

Wilde, S.A., Valley, J.W., Peck, W.H., Graham, C.M., 2001. Evidence from detrital zircons for the existence of continental crust and oceans on the Earth 4.4 Gyr ago. Nature 409, 175–178. https://doi.org/10.1038/35051550

Zhang, G., Morales, J., García-Ruiz, J.M., 2017. Growth behaviour of silica/carbonate nanocrystalline composites of calcite and aragonite. J. Mater. Chem. B 5, 1658–1663. https://doi.org/10.1039/C6TB02612E

Zhang, G., Verdugo-Escamilla, C., Choquesillo-Lazarte, D., García-Ruiz, J.M., 2018. Thermal assisted self-organization of calcium carbonate. Nat Commun 9, 5221. https://doi.org/10.1038/s41467-018-07658-0

Zhou, X., Chen, D., Tang, D., Dong, S., Guo, C., Guo, Z., Zhang, Y., 2015. Biogenic Iron-Rich Filaments in the Quartz Veins in the Uppermost Ediacaran Qigebulake Formation, Aksu Area, Northwestern Tarim Basin, China: Implications for Iron Oxidizers in Subseafloor Hydrothermal Systems. Astrobiology 15, 523–537. https://doi.org/10.1089/ast.2014.1234

Chapter 2

2. A Comprehensive Methodology for Monitoring Evaporitic Mineral Precipitation and Hydrochemical Evolution of Saline Lakes: The Case of Lake Magadi Soda Brine (East African Rift Valley, Kenya) [1]

Journal metrics:
JCR 2021 (Clarivate Analytics): Impact Factor: 4.01, Q1 in Crystallography Category

Supporting Information for this article is found at the end of this chapter.

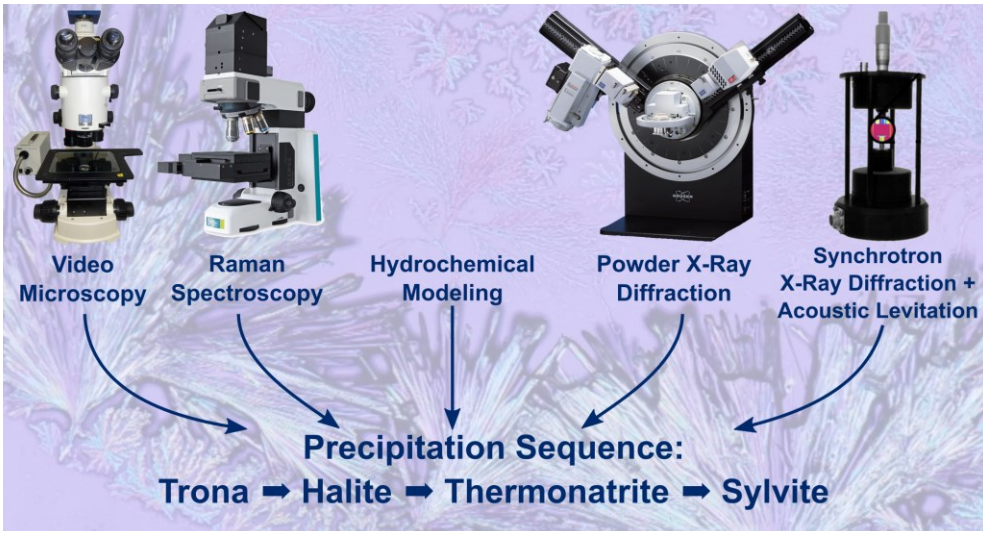

Graphical Abstract Synopsis: We present a comprehensive methodology, with a case study of a saline soda lake, applicable for monitoring evaporitic mineral precipitation and hydrochemical evolution of natural brines. The significance of the synergy of multiple methods in understanding mineral assemblages, precipitation sequences, and textural relations of modern and ancient evaporite deposits is discussed.

---

[1] This chapter has been published in Getenet, M., García-Ruiz, J.M., Otálora, F., Emmerling, F., Al-Sabbagh, D., Verdugo-Escamilla, C. A comprehensive methodology for monitoring evaporitic mineral precipitation and hydrochemical evolution of saline lakes: the case of Lake Magadi soda brine (East African Rift Valley, Kenya). Crystal Growth & Design 2022, 22, 2307 – 2317.
https://doi.org/10.1021/acs.cgd.1c01391

CRYSTAL GROWTH & DESIGN

pubs.acs.org/crystal

Article

A Comprehensive Methodology for Monitoring Evaporitic Mineral Precipitation and Hydrochemical Evolution of Saline Lakes: The Case of Lake Magadi Soda Brine (East African Rift Valley, Kenya)

Published as part of a Crystal Growth & Design virtual special issue in Celebration of the Career of Roger Davey.

Melese Getenet, Juan Manuel García-Ruiz,* Fermín Otálora, Franziska Emmerling, Dominik Al-Sabbagh, and Cristóbal Verdugo-Escamilla

Cite This: *Cryst. Growth Des.* 2022, 22, 2307−2317

Read Online

ACCESS | Metrics & More | Article Recommendations | Supporting Information

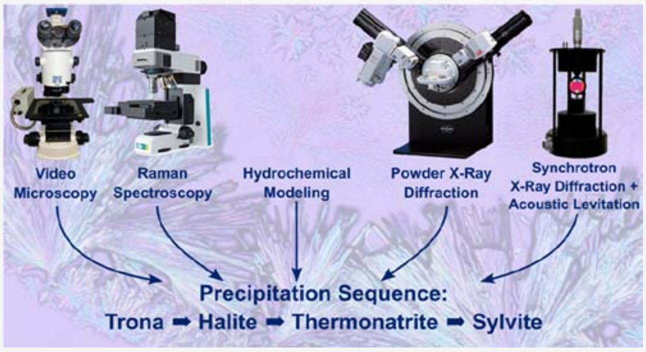

ABSTRACT: Lake Magadi, East African Rift Valley, is a hyperalkaline and saline soda lake highly enriched in Na^{+}, K^{+}, CO$_3^{2-}$, Cl^{-}, HCO$_3^{-}$, and SiO$_2$ and depleted in Ca^{2+} and Mg^{2+}, where thick evaporite deposits and siliceous sediments have been forming for 100 000 years. The hydrogeochemistry and the evaporite deposits of soda lakes are subjects of growing interest in paleoclimatology, astrobiology, and planetary sciences. In Lake Magadi, different hydrates of sodium carbonate/bicarbonate and other saline minerals precipitate. The precipitation sequence of these minerals is a key for understanding the hydrochemical evolution, the paleoenvironmental conditions of ancient evaporite deposits, and industrial crystallization. However, accurate determination of the precipitation sequence of these minerals was challenging due to the dependency of the different hydrates on temperature, water activity, pH and pCO$_2$, which could induce phase transformation and secondary mineral precipitation during sample handling. Here, we report a comprehensive methodology applied for monitoring the evaporitic mineral precipitation and hydrochemical evolution of Lake Magadi. Evaporation and mineral precipitations were monitored by using in situ video microscopy and synchrotron X-ray diffraction of acoustically levitated droplets. The mineral patterns were characterized by ex situ Raman spectroscopy, X-ray diffraction, and scanning electron microscopy. Experiments were coupled with thermodynamic models to understand the evaporation and precipitation-driven hydrochemical evolution of brines. Our results closely reproduced the mineral assemblages, patterns, and textural relations observed in the natural setting. Alkaline earth carbonates and fluorite were predicted to precipitate first followed by siliceous sediments. Among the salts, dendritic and acicular trona precipitate first via fractional crystallization—reminiscent of grasslike trona layers of Lake Magadi. Halite/villiaumite, thermonatrite, and sylvite precipitate sequentially after trona from residual brines depleted in HCO$_3^{-}$. The precipitation of these minerals between trona crystals resembles the precipitation process observed in the interstitial brines of the trona layers. Thermonatrite precipitation began after trona equilibrated with the residual brines due to the absence of excess CO$_2$ input. We have shown that evaporation and mineral precipitation are the major drivers for the formation of hyperalkaline, saline, and SiO$_2$-rich brines. The discrepancy between predicted and actual sulfate and phosphate ion concentrations implies the biological cycling of these ions. The combination of different in situ and ex situ methods and modeling is key to understanding the mineral phases, precipitation sequences, and textural relations of modern and ancient evaporite deposits. The synergy of these methods could be applicable in industrial crystallization and natural brines to reconstruct the hydrogeochemical and hydroclimatic conditions of soda lakes, evaporite settings, and potentially soda oceans of early Earth and extraterrestrial planets.

■ INTRODUCTION

Crystal nucleation and growth usually proceed between narrow compositional or thermal limits and produce a material record of these growth conditions in the form of crystals of a given phase with a given size, morphology, texture, and patterns. In material sciences, we select the growth conditions to produce crystals with some predefined properties. In earth sciences, we

Received: November 26, 2021
Revised: February 23, 2022
Published: March 3, 2022

https://doi.org/10.1021/acs.cgd.1c01391
Cryst. Growth Des. 2022, 22, 2307−2317

Table 1. Results of the In Situ Brine Characterization and the Chemical Analysis of the Sample Used for the Evaporation and Precipitation Experiments[a]

in situ pH	T (°C)	EC (mS/cm)	TDS (g/L)	ORP (mV)	DO (%)	ionic strength (M)
9.8	29.2	68.6	38.1	−464.7	46.2	0.74

Na^+	K^+	Cl^-	CO_3^{2-}	HCO_3^-	SO_4^{2-}	SiO_2	F^-	PO_4^{3-}
12850 ± 1285	228.5 ± 23	5250 ± 788	9600	6100	100.5 ± 15	91.4	208 ± 31	19.4 ± 3.9

Mg^{2+}	Ca^{2+}	Al^{3+}	Fe^{tot}	B^+	Ba^{2+}	Br^-	Sr^{2+}	I^-
12 ± 0.12	4.5 ± 0.45	<0.05	0.1 ± 0.01	5.2 ± 0.52	0.03 ± 0.003	23.3 ± 2.3	0.04 ± 0.004	0.8 ± 0.08

[a] Ionic concentrations are in ppm.

can go in the reverse direction, trying to determine the growth conditions from the properties of natural crystals. This strategy has been previously discussed[1,2] and used, for instance, to constrain the growth conditions of the unique, giant gypsum crystals in Naica, Mexico,[3,4] growth mechanisms of magnesium and sodium salts of playa lakes,[5] or the chemistry of sea 3.5 billion years ago.[6] This crystal growth "reverse engineering" requires a good knowledge of the crystallization processes, typically based on thermodynamic relations between phases. Crystallization of highly soluble salts from evaporating natural brines implies high concentration, chemically complex solutions from which time-dependent, kinetically controlled processes lead to the crystallization of evaporitic minerals. Consequently, an experimental investigation of the crystallization sequence is needed to complement thermodynamic modeling. This would allow the use of evaporites as proxies for the study of ancient water bodies, the paleoclimatology of basins in past arid climates, and the early stages of continental breakup during the movement of tectonic plates.[7]

Crystallization of evaporites from present-day seawater is relatively well understood, but the sequence of minerals crystallizing in closed hydrological system depends on the lithologies leached by the waters contributing to the lake.[8−10] This variability has been roughly classified in five major water types[8] that do not allow the accurate prediction of detailed mineralogical sequences with textural, size, morphological, and pattern information. In this work, we present a methodology for in situ studies of sequential evaporation/crystallization of brines from soda lakes in the African Rift Valley. The knowledge of the mineral precipitation sequence in saline and soda lakes is crucial to understanding the hydrochemical evolution of brines, paleoenvironmental conditions (e.g., temperature, pCO_2) of the evaporite deposits in the geological record, scaling in geothermal power facilities, and implications for industrial crystallization of these materials.[11−17] The assemblage of sodium carbonate minerals precipitated from soda brines are also important for constraining the geochemical conditions of soda oceans in Precambrian Earth, when life is thought to have originated, and other Earth-like planets.[18,19]

Lake Magadi is a saline pan where mainly trona, thermonatrite, and halite precipitate during the dry seasons. Since 1911, soda ash and common salt has been mined by precipitating trona and halite respectively via solar evaporation of the lake brines in artificial pans with further industrial processing.[20] The hypersaline alkaline brines harbor a unique biodiversity relevant to the study of physiological adaption of extremophiles[21] and their biotechnological applications.[22,23] Trace fossils of organisms from the precursor lake of Magadi are also key to understanding depositional environments.[24]

Owing to their scientific and economic values, much work has been carried out on the mineral precipitation in soda lakes based either on field data or on thermodynamic modeling.[15,25−27] Some recent works have proved that a combination of field research, lab experiments, and computer modeling is key to understanding evaporitic brine evolution and mineral precipitation sequences.[16,28,29] So far, there are no experimental investigations on the mineral precipitation sequence in soda lakes. In this work, we present a comprehensive experimental investigation and geochemical modeling of the mineral precipitation sequence and hydrochemical evolution of Lake Magadi brines, using evaporative mineral precipitation experiments monitored by (a) in situ video microscopy and synchrotron X-ray diffraction from acoustically levitated droplets; (b) ex situ Raman spectroscopy, X-ray diffraction, and scanning electron microscopy; and (c) computational modeling.

EXPERIMENTAL SECTION

Solution Chemistry. Brine samples were collected from Lake Magadi during the field campaign in March 2018. All evaporation and precipitation experiments reported in this work use one sample selected for having a composition close to the average of Magadi waters (sampling point located at 36.27° E and 1.84° S, 605 m above sea level). The pH (±0.02), temperature (±0.15 °C), total dissolved solids (TDS; ±1 mg/L), electrical conductivity (EC; ±1 μS/cm), oxidation/reduction potential (ORP; ±1 mV), and saturation percent of dissolved oxygen (DO; ±1%) were measured in situ at the sampling time with a Hanna HI 9829 multiparametric probe.

CO_3^{2-} and HCO_3^- concentrations in the samples were determined by titration with sulfuric acid using methyl orange and phenolphthalein as indicators at the Laboratorio de Estudios Crystalográficos (LEC) of the Instituto Andaluz de Ciencias de la Tierra (IACT) in Granada (Spain). SiO_2 was analyzed by using inductively coupled plasma optical emission spectrometry at the Technical Services of the Estación Experimental del Zaidín (CSIC) in Granada (Spain). All the remaining chemical analyses were performed by ALS Laboratory Group SL: Na^+, K^+, Mg^{2+}, Ca^{2+}, Al^{3+}, Fe (total), Ba^{2+}, B^+, Sr^{2+}, Br^-, and I^- were determined by using inductively coupled plasma mass spectrometry (ICP-MS). The samples were fixed by the addition of nitric acid prior to analysis with ICP-MS. Cl^-, F^-, and SO_4^{2-} were analyzed by using ion liquid chromatography. PO_4^{3-} was determined by a colorimetric method based on molybdenum blue using discrete spectrophotometry.

Table 1 shows the in situ and laboratory measurements of the hydrochemical parameters of the Lake Magadi sample used for the evaporation experiments. The dominant ions are Na^+, K^+, CO_3^{2-}, HCO_3^-, and Cl^- with relatively high levels of SO_4^{2-}, F^-, SiO_2, PO_4^{3-}, and Br^-. However, these brines are depleted in Ca^{2+}, Mg^{2+}, Al^{3+}, and Fe.

Evaporation Experiments. Evaporation and mineral precipitation experiments were performed at 23 ± 1 °C on glass slides. Droplets of about 25 μL (approximate diameter of 1 cm) were poured on glass slides using plastic pipets. Two series of evaporation experiments were implemented: in the first one, droplets were left to evaporate until complete desiccation while in the second the experiment was stopped after the initial stages of precipitation, removing all the liquid with highly absorbent paper to ease the identification of the first precipitates occurring in small amounts. Both series were monitored with optical video microscopy (Nikon AZ100).

Ex Situ Characterization of Precipitates. The mineralogy of the precipitates was characterized after evaporation experiments with the use of X-ray diffraction, Raman spectroscopy, and electron microscopy. For ex situ X-ray diffraction we used a high-resolution Bruker D8 Advance X-ray diffractometer (at the Laboratorio de Estudios Crystalográficos) with monochromatic Cu Kα_1 radiation, primary Ge(111) monochromator, and a Lynxeye PSD detector. Diffractograms were acquired in transmission mode, at 40 kV acceleration voltage and 40 mA current, with 2θ scans spanning from 5 to 80° with a 2θ step of 0.02° s^{-1}. Malvern Panalytical HighScore software (version 4.9) with the ICCD PDF-4+ (2020) database was used for phase identification. Raman spectra were recorded by using a HORIBA Jobin Yvon LabRAM high-resolution Raman spectrometer equipped with an Olympus BX41 optical binocular microscope with Koehler illumination and a CCD detector. An excitation beam with a wavelength of 532 nm (frequency-doubled neodymium-doped yttrium aluminum garnet laser) and output power of 100 mW was used. Spectra were acquired with an exposure time of 5−10 s and accumulation of 10−60 times to improve the signal-to-noise ratio. Electron microscopy was used to characterize the texture and the local elemental composition of the precipitates with a Zeiss Supra 40VP field-emission scanning electron microscope (FESEM) equipped with an Oxford energy-dispersive X-ray analyzer (EDX) at the Centro de Instrumentación Científica (CIC) of the University of Granada (Spain) operating at 5−20 keV. After complete desiccation, glass slides containing the precipitates were directly mounted on the SEM stub by using double-faced conductive carbon tape for electron microscopic analysis.

In Situ Characterization of Precipitates. In situ X-ray powder diffraction data was collected from evaporating, levitated droplets to track the time evolution of mineral precipitation during evaporation. These experiments were performed at the μSpot beamline (see ref 30 for details) at the BESSY II synchrotron (Helmholtz Centre Berlin for Materials and Energy, Berlin, Germany), using the protocol described in ref 31. The beamline features an acoustic levitator used as a containerless sample holder (see the experimental setup in Figure 10a). In a typical experiment, 5 μL of the sample was pipetted in one of the nodes of the standing acoustic wave of the levitator to form a drop with an approximate diameter of 2 mm. The droplets were maintained into the beam during data collection by gradually lowering the reflector of the acoustic wave with decreasing volume of the droplets. An incident beam having a 0.72929 Å wavelength and a 100 μm size was used. Scattered intensities were collected by a two-dimensional detector (Eiger9M, CCD 3072 × 3072) for 5 s exposures. Evaporation was followed for 80 min until complete desiccation. The evolution of the size of the levitated droplet during evaporation was monitored with a video camera. Levitated drop evaporation was performed at 25 ± 1 °C and relative humidity of 35 ± 2%.

Computer Modeling. The PHREEQC version 3.4 code with the Pitzer database was used for thermodynamic hydrochemical speciation, evaporation, and precipitation calculations.[32] In a first step, evaporation was simulated at 25 °C to calculate the saturation index of all mineral phases in the database during the evaporative concentration of the brine. In a second step, we calculated the equilibrium crystallization of all phases that were supersaturated during the first step. The crystallization of minor phases, and the inhibition of phosphate precipitation (due to Ca deficit) has been addressed by our thermodynamic calculations by supplementing the PHREEQC Pitzer database with fluorite, hydroxyapatite, and fluorapatite taken from the llnl.dat database[32] and chlorapatite from the Thermoddem database (version 1.10).[33] For villiaumite (NaF), thermodynamic data was taken from the ThermoChimie database (version 10a).[34] Parameters for $Na(H_2PO_4)$ and its hydrated forms were taken from ref 19.

■ RESULTS

Crystallization during the evaporation of the droplet follows a characteristic sequence and produces distinct mineral patterns. Figure 1 shows the overall sequence of crystallization processes during the evaporation of the drop (the full sequence is presented in Video S1). Mineral precipitation starts on the border of the droplet as dendritic crystals (Figure 1a, white arrows) followed by bunches of thick acicular crystals that nucleate at the tips of the dendrites and grow toward the center of the droplet (Figure 1a (yellow arrows) and 1b). At the center of the drop, within the dashed circle in Figure 1c, precipitates form after the thick acicular crystals have stopped growing (Figure 1c). Crystallization at the center continues until complete desiccation of the brine there, but some liquid is still entrapped between crystals of the external rim, producing the latest precipitation events in the sequence (Figure 1d). The initial crystallization on and near the edge of the drops could be due to pinning of the contact line on the hydrophilic glass surfaces and the outward capillary flow of solutes from the center during evaporation, creating chemical gradients. The wetting property of the glass surface and the emerging crystals, and crystallization-driven flow of solutes may control the subsequent patterns after initial nucleation.[35,36] A relatively higher evaporation rate seems responsible for the patterns observed on the center (Figure 1d), creating tiny outward radiating crystals.

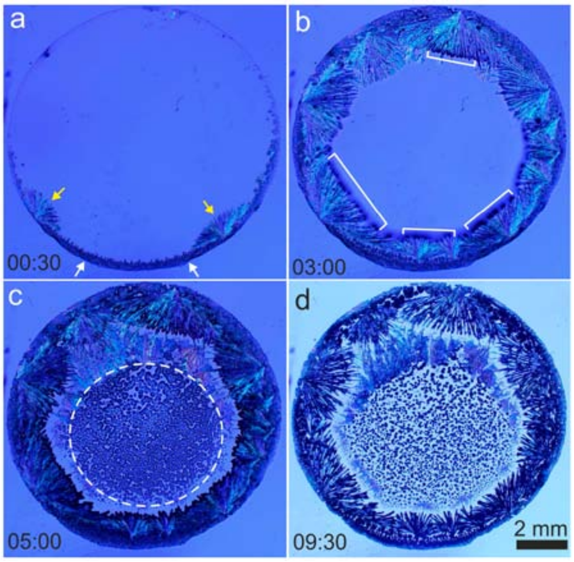

Figure 1. Overall mineral crystallization sequences and patterns formed during the evaporation of a droplet. White arrows, the first dendritic minerals; yellow arrows, thick acicular crystals that form at the second stage; square brackets, crystals that form at the third stage as dark spots. The full sequence is presented in Video S1. Time (bottom left corner of each picture) counts from the beginning of precipitation.

Figure 2 (full sequence in Video S2) shows the details of the precipitation at the border. As shown in Figure 2a and Video S2 (blue arrows), the precipitation process begins on the border of the droplets in the form of dendritic crystals. These dendrites start to precipitate on the liquid/air/glass interface of the droplet, which was clearly observable from top-view images. After the dendrites, bunches of acicular crystals nucleate and grow toward the center of the droplet while

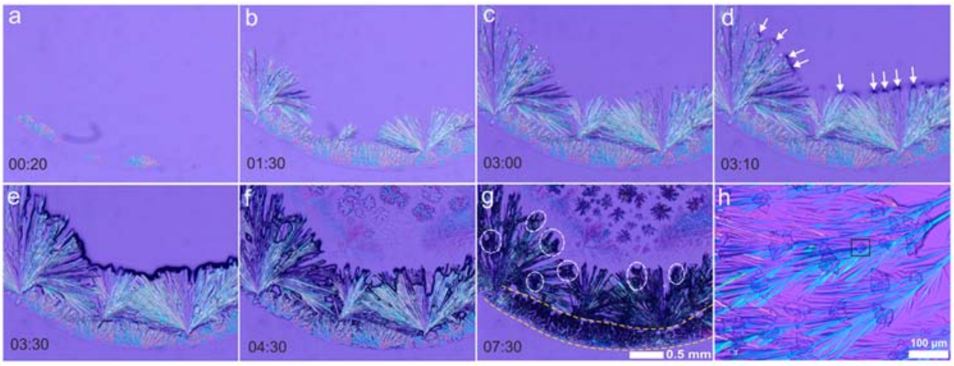

Figure 2. Frames from Video S2 (acquired at the indicated time in minutes since the precipitation began) showing the details of the precipitation sequence of the border dendrites, the acicular minerals, and the irregular dark spots (arrows in panel d and circles in panel g) forming between the acicular minerals. Panel h is a close-up view of the irregular dark spots in panel g showing the aggregates of cubic crystals (note the single cubic crystal inside the black square).

spreading sideways (see Figure 2b,c and Video S2 (blue arrows)). Figure 2c corresponds to the end of the precipitation of the thick acicular crystals and the beginning of a third mineral pattern in the form of irregular dark spots. These irregular-shaped mineral grains are shown in Figure 2d (white arrows) and 2e. Once the irregular-shaped minerals began to form, precipitation at the center of the drop starts (described in the next paragraph). From this time on, the desiccation and precipitation processes in the border advance in a reverse direction (toward the border of the droplet) where the acicular crystals and the border dendrites were already present (see Figure 2f,g and Video S2 (green arrows)). The white dashed ellipses in Figure 2g show the irregular-shaped grains that precipitate between the acicular crystals. High-resolution micrographs show that these irregular dark spots are aggregates of well-developed cubic crystals (see Figure 2h), most probably halite. The last phase of the precipitation process took place beneath the border dendrites as shown in Figure 2g (between the yellow lines). Figure 3 and Video S3 show the details of the precipitation process in this area. Figure 3a shows the area where the first dendrites formed. The transparent bladelike crystals (indicated by the red arrows in Figure 3b) precipitate from the residual water below the dendrites at the end of the evaporation process. In addition, the first precipitated dendrites (Figure 3a) change from transparent to opaque because of the latest precipitation of other minerals from capillary water entrapped between the dendrites. In qualitative terms, the precipitation rate of the minerals from the residual brine held between the dendritic and the acicular trona was the slowest whereas the fastest precipitation rate was observed on the center. The second and third faster rates of precipitation were observed with the dendritic and acicular crystals of trona, respectively.

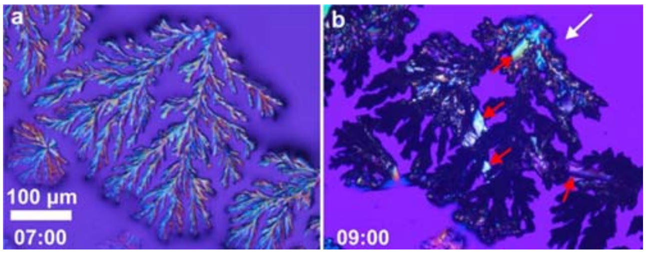

Figure 3. Evolution of border dendrites area during last phases of the precipitation sequence that took place between the branches. The white arrow points from the border to the center of the droplet; red arrows show transparent bladelike crystals beneath the border dendrites.

Figure 4 (full sequence in Video S4) shows the details of the crystallization sequence at the center of the droplets. These precipitates appear later than the cubic crystals on the tips of the acicular crystals (see Figure 2d). Precipitation at the center begins with starlike dendritic minerals that radiate from the center outward (Figure 4a). Once the precipitation of the radiating branches ceases, other crystals (also dendritic) start to precipitate between their branches as shown by the white arrows in Figure 4b. Finally, the residual brine entrapped between the branches of the dendrites evaporates, producing a later precipitate on the preexisting dendrites that darken them (Figure 4c,d).

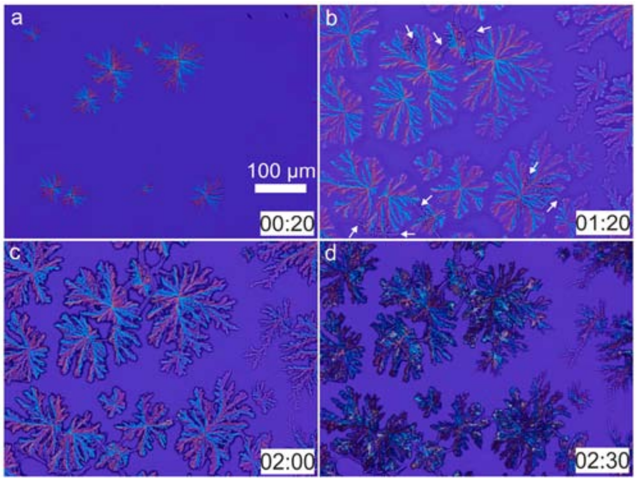

Figure 4. Frames taken from Video S4 showing the precipitation process and mineral patterns on the center of the droplets. The white arrows indicate the crystals forming after the starlike dendritic minerals.

The minerals making these patterns were identified by using X-ray diffraction and Raman spectroscopy. Powder X-ray diffraction of the whole precipitates from dry droplets revealed the presence of trona, thermonatrite, halite, and minor sylvite (Figure 5).

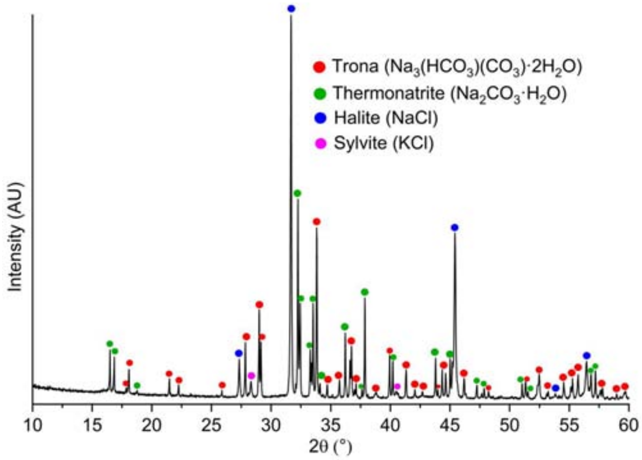

Figure 5. Powder X-ray diffraction patterns of whole precipitates.

Raman spectra of the border dendrites that form first were collected after gentle drying of the drop with absorbent paper to avoid further precipitation. These spectra indicate that these dendrites are made of trona (Figure 6a). In addition, some thermonatrite was detected probably from the evaporation of the water that could not be completely removed. Raman spectra of the last minerals of the precipitation sequence that form beneath and between the dendritic trona (Figure 3 and Video S3) revealed thermonatrite (Figure 6b). The microscopic image in Figure 6a was taken after removal of the water with filter paper, whereas the one in Figure 6b was taken after complete evaporation of the whole solution in the border. The Raman modes between 100 and 300 cm^{-1} are assigned to the lattice modes, whereas the vibration peaks at 1062 and 1067/1068 cm^{-1} represent the symmetric stretching modes of carbonate groups in trona and thermonatrite, respectively.[37,38]

The second type of crystals that precipitate next to the border trona dendrites were thick, and the next were thin, acicular crystals (Figure 2a−g and Video S2). Raman spectra of these acicular crystals show that they are made only of trona (Figure 7). Once the growth of the acicular crystals ceases, aggregates of cubic crystals start to crystallize (Figure 2g (dark spots) and 2h). These cubic crystal aggregates show no Raman signal, suggesting halite or villiaumite.

Raman spectroscopy of the central dendritic minerals revealed a combination of trona and thermonatrite (Figure 8). The crystallization of these dendrites has similarities with the initial crystallization at the border of the droplet. This implies that the first mineral that forms at the center could be trona, whereas thermonatrite comes later due to the later desiccation of the residual water held in the pores between trona crystals.

The distribution of mineral phases and the presence of minor or amorphous precipitates were tested by using EDX elemental composition maps of the precipitates that form on different parts of the droplet. These maps show mainly Na−CO_3 minerals, NaCl (halite), and minor KCl (sylvite) and NaF (villiaumite) (Figure 9, Figures S2 and S3). Figure 9a shows the border precipitates. Raman spectra revealed that these Na−CO_3 minerals are trona and thermonatrite (Figure 6). Halite and sylvite, which are Raman inactive minerals, were identified by EDX analysis. SEM backscattered electron images show that the border dendrites were highly feathery (Figure S1a). The needlelike crystals are trona crystals with smaller halite crystals between them (Figures 2g,h and 9a, and Video S2). These halite crystals were the second mineral in the precipitation sequence (Figure 10b). Semirounded cubic crystals of villiaumite have been observed between the dendritic trona crystals (see Figures S2 and S3). The dendrites at the center are Na−CO_3 minerals (trona and thermonatrite) with halite (Figure 9c). Once the precipitation of the trona dendrites ceases, halite and villiaumite precipitate between their branches (Figure 4b and Video S4). The crystals pointed out by the white arrows in Figure 4b were halite as revealed by the EDX maps (Figure 9c). The dendrites are open-textured aggregates like the initial dendrites at the border (see Figure S1c).

In situ, containerless X-ray diffraction data from evaporating, levitated droplets were collected in the μSpot beamline at BESSY to check for any effect related to the glass substrate or the flat geometry of the drying drop (see Figure 10a). Figure 10b shows eight successive pictures of the levitated drop recorded to track the time evolution of the droplet volume during evaporation. Figure 10c shows the in situ X-ray diffractograms collected during evaporation. Trona precipitates first after 2670 s since evaporation began. Precipitation of halite began 3 min later (after 2855 s; see the green bars). Finally, precipitation of thermonatrite started after 2955 s (red bars). The in situ X-ray diffraction data confirmed the precipitation sequence that was observed in the previously described experiments.

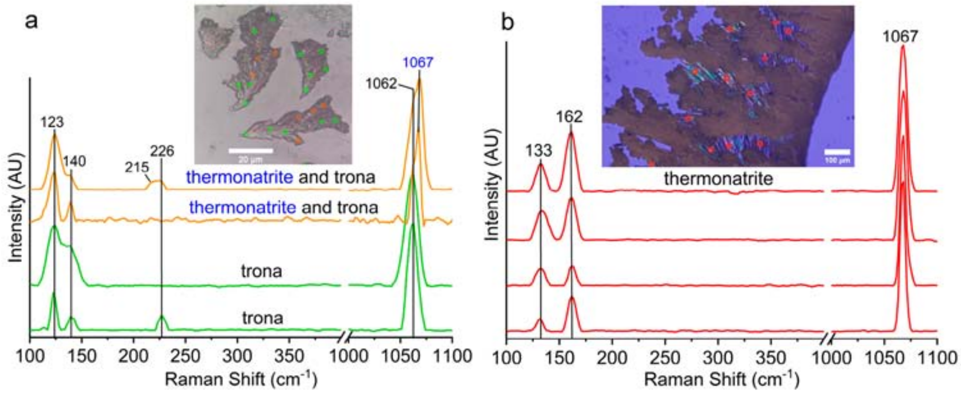

Figure 6. Raman spectra of (a) border branches that form first (green dots, trona; orange dots, trona and thermonatrite) and (b) the last precipitates that form beneath and between the border trona branches (red dots, thermonatrite).

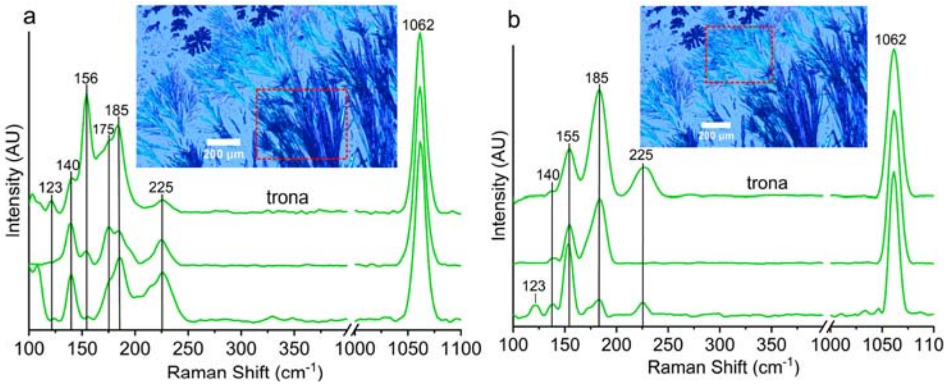

Figure 7. Raman spectra of (a) thick and (b) thin acicular minerals that form next to the border dendrites.

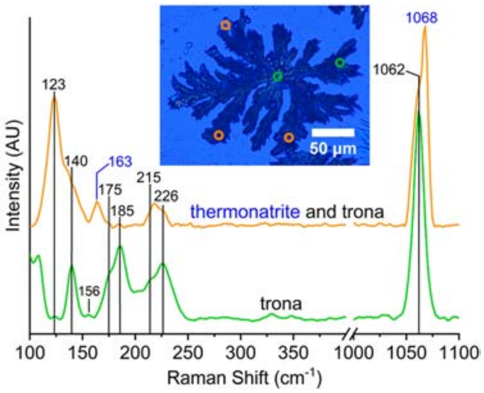

Figure 8. Raman spectra of radiating starlike minerals that form at the center of the droplets (green dots, trona; orange dots, trona + thermonatrite).

Most previous knowledge on the precipitation sequence from soda lake brines comes from thermodynamic modeling.[15,25−27] To set our results in this framework, and to check for any unexpected behavior, mostly large kinetic effects, we have performed a set of hydrochemical modeling runs using the PHREEQC code. These simulations use Pitzer speciation[32] using the pitzer.dat database provided by PHREEQC 3.4 after inclusion of the missing species (alkalinity, Ca, Mg, K, S, Si, and F) and the corresponding speciation and dissolution reactions from different databases as mentioned in the Experimental Section. Evaporation and mineral precipitation simulations compute successive equilibrium states separated by discrete steps of slight water removal. Figure 11 shows the output of this model in terms of the sequence of mineral crystallization (a) and ionic concentration of the relevant species (b) versus concentration factor (CF; the ratio between the initial brine volume and the current volume at each time). The output of the model reproduces very well the experimental observations.

Among the phases identified by in situ and ex situ experiments, trona was predicted to precipitate first at a CF of 9.7, which agrees with the experimental observations. Evaporation linearly raises the concentrations of Na^+ and CO_3^{2-} until the precipitation of trona commences (Figure 11b). Once trona precipitation sets in, sodium and carbonate species start to deplete until the CF reaches a value of 16. Nahcolite is predicted to precipitate for a short period between CFs of 6.2 and 16.4, depleting the HCO_3^- concentration. This depletion continues due to the onset of trona precipitation via the dissolution of nahcolite. After a CF of 30, trona no longer precipitates due to the minimal HCO_3^- concentration, leaving a constant amount of about 114 mmol/kg. However, nahcolite has not been identified in the lab experiments, due to either a short transient presence in the drops or to slow nucleation kinetics.

Halite and villiaumite are predicted to precipitate in the second phase (Figure 11a). The amount of precipitated halite was predicted to be larger than the amount of trona after complete desiccation. Villiaumite precipitates at a CF of 30, almost simultaneously with halite which starts forming at a CF of 32. Thermonatrite crystallization is predicted at a CF of 62.6. Sylvite and glaserite appear near the complete dryness of the brine due to K^+ and SO_4^{2-} evaporative concentrations (Figure 11b). The pH evolution during evaporation was

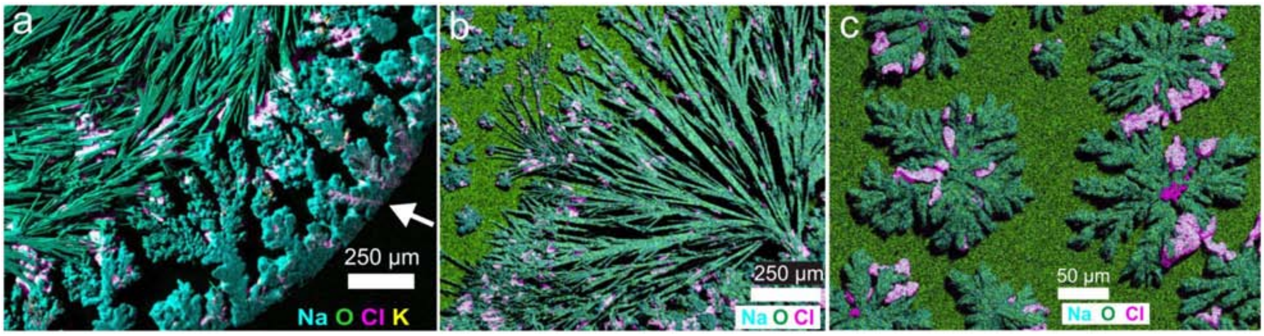

Figure 9. EDX map of (a) border precipitates (white arrow points from the border to the center of the droplet), (b) acicular minerals together with irregular aggregates, and (c) radiating starlike minerals that form on the center.

https://doi.org/10.1021/acs.cgd.1c01391
Cryst. Growth Des. 2022, 22, 2307−2317

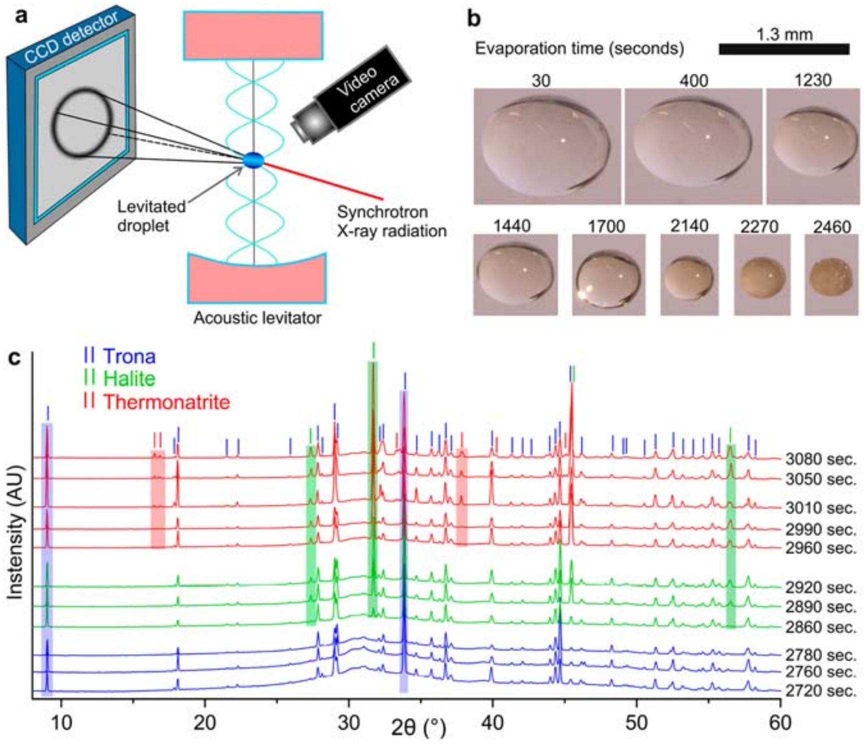

Figure 10. (a) Experimental setup used for in situ X-ray diffraction measurements from levitated drops. (b) Change in the size of the drop during evaporation. (c) X-ray diffractograms collected during the evaporation of levitated droplets of brine. Note that the first diffractograms of the corresponding color are taken a few seconds after precipitation of the corresponding mineral begins so that the characteristic peaks of the given phase are clearly visible. The exact time when each mineral starts to precipitate is reported in the text.

controlled by the CO_3^{2-}/HCO_3^- ratio. Initially, pH decreases slightly from 9.8 to 9.4 until a CF of 6.4 (Figure 11b, blue dotted line). Afterward, pH steeply rises until a CF of 63 due to the steep decline in HCO_3^- concentration following the subsequent onset of nahcolite and trona precipitation. Once thermonatrite precipitation set in (after a CF of 63), pH rises gently with CO_3^{2-} concentration.

On the basis of the thermodynamic model, the initial Lake Magadi brine was supersaturated with respect to fluorapatite and magnesite (see Figure S4a). The amounts of fluorapatite and magnesite predicted to precipitate are about 0.02 and 0.5 mmol, respectively. These minerals were not detected in the lab experiments likely because of their minor amounts. Simulation of evaporation in the absence of fluoride and phosphate ions shows that the initial Lake Magadi brine was supersaturated with respect to calcite and magnesite (see Figure S5a). At a CF of 8.6, calcite starts dissolving and gaylussite begins to form until a CF of 11.5. Pirssonite came to equilibrium with the solution after a CF of 11.5 via dissolution of gaylussite. However, calcite, magnesite, gaylussite, and pirssonite were not detected in the lab experiments most likely because of their trace amounts in the mix of minerals. The amounts of calcite, gaylussite, and pirssonite predicted to precipitate are about 0.12 mmol, whereas that of magnesite was 0.5 mmol. As a result of their trace amounts, precipitation of Ca−Mg carbonate minerals did not deplete the carbonate ions during evaporation simulation (see Figure S5b).

Amorphous silica supersaturates at a CF of 3 (see Figure 11a), reaching a maximum amount of precipitate (1.2 mmol/kg of brine) at a CF of 17. From this point on, it began to redissolve because of the steep pH rise that increases the solubility of SiO_2.[39] Amorphous silica starts to precipitate again when the brine is about to dry, after a CF of 275.

■ DISCUSSION

Deriving conclusions on the natural evaporitic crystallization in Lake Magadi from these drop evaporation experiments requires scaling from the millimeter to the tens of meters spatial scale and from the minutes to the year (seasons) temporal scale. After this scaling, the experimentally observed evaporative precipitation sequence explains many features of the Magadi area deposits and the current precipitation in the lake. Trona has precipitated in Lake Magadi for the past 100 000 years and continues today, forming 65 m thick evaporite deposits.[40] Precipitation occurs at both the bottom and the surface of the lake. Long vertical bladed crystals with sharp points grow upward from the bottom of the water body as stellate groups, forming a firm mesh of crystals. Thin trona crusts precipitate on the water surface[15,41−43] as aggregates of smaller crystals growing at higher supersaturation values under fast evaporation. The experimentally observed initial phase producing dendritic trona and bunches of fast-growing trona needles on the border of the droplets corresponds to the growth of vertical bladed crystals from the bottom of the lake. The third phase of high supersaturation thermonatrite precipitation in the central region of the drop, concomitant with the latest precipitation of trona and halite, is equivalent to the precipitation of thin crusts at the surface of the lake. The upward radiating blades terminate against the trona crust on the surface, which serves as the nuclei of the following generation of crystals for the next year. The successive growth of crystals in this manner gives rise to a layered appearance of trona deposits,[15,41−43] made of 2−5 cm annual bands[41] with a

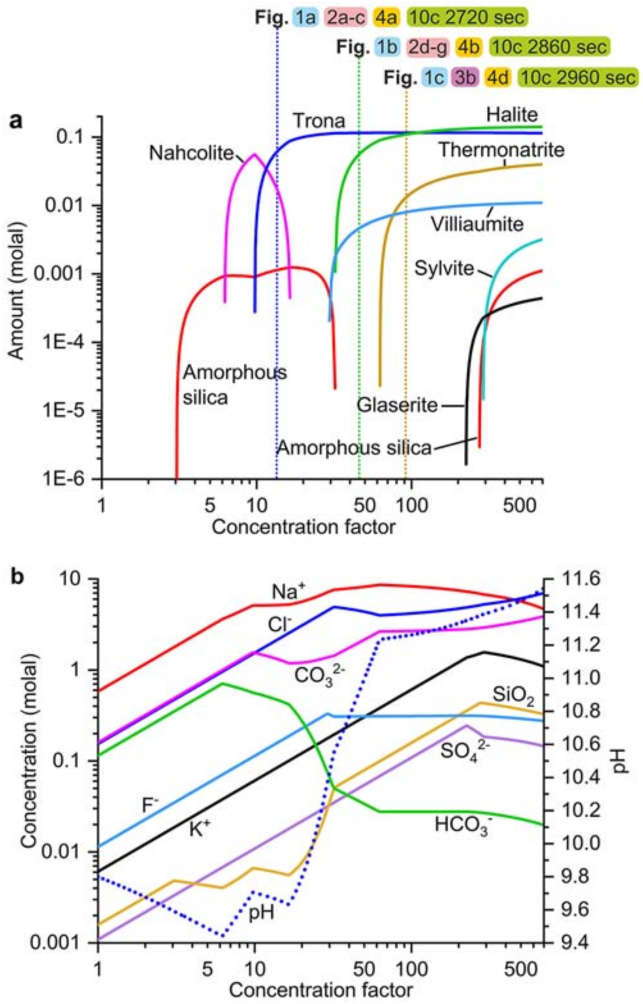

Figure 11. PHREEQC simulation of evaporation and mineral precipitation from Lake Magadi brine at 25 °C: (a) the mineral precipitation sequence and the amount of precipitate and (b) chemical evolution of the brine during mineral precipitation. In panel a, three key points during evaporation are marked by vertical dotted lines labeled with references to previous figures where the status of the brine at this point is shown. Blue, green, and yellow dotted lines represent the time when trona, halite, and thermonatrite precipitation is dominant during the sequence.

content of trona of about 90%.[44] The precipitation of thermonatrite and halite between the dendritic and acicular trona crystals in lab experiments is relevant for the interpretation of the Magadi evaporitic sequence. Thermonatrite and halite form only in the modern evaporite sequence but are not reported in the ancient deposits of Lake Magadi. This must be due to a change in the climatic/hydrologic conditions of the lake; either the paleolake brines did not reach supersaturation required for these minerals to precipitate or they precipitated but redissolved during an episodic freshening of the paleolake brines. In contrast to the natural lake, significant amounts of thermonatrite and halite precipitate respectively at the bottom and on the surface of the artificial pans of TATA Chemicals made for the commercial production of salt by harvesting the top layer of halite.[42,45] The precipitation of significant amounts of thermonatrite and halite in these pans is explained by our results: the company pumps the HCO_3-depleted lake brine (after trona precipitation) into shallow evaporation ponds where evaporation is faster than in the lake, fresher water inputs are absent, and organic production of CO_2 is negligible. Fast evaporation in these HCO_3-depleted ponds, as in the last stage of our experiments, precipitates large amounts of thermonatrite and halite with some trona.[42,45]

Drill cores of the evaporite series also contain nahcolite.[40,41] In our calculations, nahcolite is predicted to appear early during evaporation and then redissolve, but it was not identified during the laboratory experiments. This can be due to kinetic effects, not included in our calculations because no data is available on this kinetics; nahcolite precipitation should be slow with respect to drop evaporation speed. Nahcolite primarily precipitates on the bottom of Nasikie Engida, where there is a higher flux of magmatic CO_2 along the fault zones.[15,46] The opposite trend of the CO_3^{2-}/HCO_3^- ratio after a CF of 15 reflects the precipitation of trona that is limited by the low HCO_3^- content of the brine. The later increase in CO_3^{2-} and decrease in HCO_3^-, and the corresponding increase in pH, lead to the precipitation of thermonatrite and the end of trona precipitation.

The early precipitation of calcium carbonate minerals produces the depletion of calcium, which results in a lack of apatite precipitation[19,47] and the consequent accumulation of phosphate in soda lakes up to levels relevant to the syntheses of prebiotic biomolecules. Lake Magadi samples were supersaturated with respect to fluorapatite since the beginning of evaporation. The amount of fluorapatite was limited by the very low calcium content. As a result, phosphate concentration increases linearly with evaporation (see Figure S4a,b). Apatite precipitation has not been reported in Lake Magadi because of the absence of or a minor amount of Ca in the brines. In the simulation, phosphate concentration was overestimated due to microbial phosphate consumption and deposition with organic matter in the actual environment.[19] Based on the model predictions, there were no $Na(H_2PO_4)$ mineral precipitations until almost complete dryness.

Other consequences of the depletion of Ca in the brines are the lack of fluorite precipitation and the evaporative accumulation of fluoride until villiaumite supersaturation. Once villiaumite precipitation begins at a CF of 30, the fluoride content equilibrates. Villiaumite is a common constituent of the surface deposits of Lake Magadi brines.[41,42]

Calcite, magnesite, gaylussite, and pirssonite are present as efflorescent crusts and pisolites in modern Lake Magadi and drill cores from Lake Magadi and Lake Bogoria.[15,42,48−50] These aggregates form due to the episodic interaction of Ca-rich freshwater with the sodic brine on the lake margin.[15,40,42] Alternatively, as observed in other saline lakes and demonstrated experimentally, Ca−Mg carbonate precipitation could have been mediated by metabolic activities in the lake water.[51−54] Calcite spherule nucleation was observed at the sediment−water interface of highly alkaline lakes with coexisting Ca−Mg-rich hydrochemistry and microbial-driven colloidal substances, forming cemented spherulites in different depositional settings.[53] The precipitation of these phases is predicted by our thermodynamic models in small amounts (less than 0.5 mmol/kg of brine evaporated) at the beginning of evaporation, but only in the absence of phosphate and fluoride (see Figure S5c). Precipitation of these minerals was not observed in our in situ characterization, most probably due to the very low Ca concentration of the sample, which was equilibrated with Ca phases at sampling time and lacks the additional Ca supply to the lake by later freshwater inflow or groundwater input to the lake.

In Lake Magadi, as the pH rises above 9, silica remains concentrating at the same rate as chloride due to the polymerization of silicic acid.[42,44,55] Our thermodynamic model predicted a continuous increase in silica concentration until the initial precipitation and after redissolution of amorphous silica (from CF 6 to 32) up to close to complete dryness. In our experiments, amorphous silica has not been explicitly detected, but some fluffy precipitates can be seen in the drop earlier than trona; for example, see the last frame in Figure 10b (2460 s). However, no diffraction peaks were observed. These precipitates before trona must be amorphous phases, probably amorphous silica, representing the precipitation of siliceous phases such as opal-A, magadiite, or gels in Lake Magadi and Little Magadi.[15] Silica gels precipitate in close proximity to the hot springs of Little Magadi lake and near the shorelines under active evaporation.[15,40,48,56]

Precipitation of sylvite and glaserite is predicted by our model close to complete desiccation, but they have not been reported in the Lake Magadi basin because complete desiccation has never or very seldomly occurred. During the rainy season, freshwater supply reaches the lake before brines reach supersaturation with respect to sylvite and glaserite. These minerals have been reported in other alkaline lakes of the East African Rift Valley, for example, in Lake Katwe (Uganda).[57]

CONCLUSIONS

The evaporitic mineral precipitation sequence in saline and soda brines is challenging to monitor due to concomitant precipitation to many phases and the transformation between different hydrates of sodium carbonate−bicarbonate minerals and secondary mineral precipitation during sample handling under different conditions of pH, temperature, pCO_2, and water activity. In this work, we have presented the synergy of multiple methodologies that allowed accurate determination of the mineral precipitation sequence during laboratory evaporation of Lake Magadi soda brines. The proposed combination of in situ methods used to characterize the evaporative crystallization of salts from Magadi waters shows a high potential to build and check hydrochemical models in earth sciences that can be used in (a) explaining current depositional environments, (b) interpreting the evaporitic deposits appearing in sedimentary records in terms of paleoclimatic indicators, and (c) proposing applied methods for the industrial use of these brines at the optimal time during their natural hydrochemical evolution.

The proposed methodology can be improved if additional in situ information is needed from minor, short-lived metastable or amorphous minerals.[58,59] The most promising method for this type of study is the simultaneous use of synchrotron diffraction and Raman spectroscopy in levitated, containerless evaporation experiments. Exploring this combination will be the next step in our studies in this field.

ASSOCIATED CONTENT

Supporting Information

The Supporting Information is available free of charge at https://pubs.acs.org/doi/10.1021/acs.cgd.1c01391.

Backscattered electron micrographs and elemental maps of mineral precipitates, plots showing amount of minerals predicted to precipitate and resulting hydrochemical evolution during Lake Magadi evaporation in the presence of phosphate and fluoride ions; video microscopy of overall evolution of precipitation during evaporation of a single droplet on glass slide; video microscopy of evaporation and precipitation on the border of a droplet; video microscopy of precipitation process on the border of the droplet marked with red rectangle in Video S2; video microscopy showing details of precipitation process at centers of droplets (ZIP)

AUTHOR INFORMATION

Corresponding Author

Juan Manuel García-Ruiz − *Laboratorio de Estudios Cristalográficos, Instituto Andaluz de Ciencias de la Tierra (CSIC-UGR), Armilla E-18100 Granada, Spain;* orcid.org/0000-0002-4743-8718;
Email: juanmanuel.garcia@csic.es

Authors

Melese Getenet − *Laboratorio de Estudios Cristalográficos, Instituto Andaluz de Ciencias de la Tierra (CSIC-UGR), Armilla E-18100 Granada, Spain;* orcid.org/0000-0002-0733-7277
Fermín Otálora − *Laboratorio de Estudios Cristalográficos, Instituto Andaluz de Ciencias de la Tierra (CSIC-UGR), Armilla E-18100 Granada, Spain;* orcid.org/0000-0003-3753-6071
Franziska Emmerling − *Federal Institute for Materials Research and Testing (BAM), 12489 Berlin, Germany;* orcid.org/0000-0001-8528-0301
Dominik Al-Sabbagh − *Federal Institute for Materials Research and Testing (BAM), 12489 Berlin, Germany*
Cristóbal Verdugo-Escamilla − *Laboratorio de Estudios Cristalográficos, Instituto Andaluz de Ciencias de la Tierra (CSIC-UGR), Armilla E-18100 Granada, Spain;* orcid.org/0000-0003-2345-8359

Complete contact information is available at:
https://pubs.acs.org/10.1021/acs.cgd.1c01391

Funding

This work was supported by European Research Council Grant No. 340863, the Spanish Ministerio de Economía y Competitividad via Project No. CGL2016-78971-P, Junta de Andalucía via Project No. P18-FR-5008, and Spanish Ministerio de Ciencia, Innovacion y Universidades Grant No. BES-2017-081105 (to M.G.).

Notes

The authors declare no competing financial interest.

ACKNOWLEDGMENTS

The authors thank Isabel Guerra-Tschuschke for the support during the scanning electron microscopy analyses at the Centro de Instrumentación Científica (CIC) of the University of Granada. We also thank Francisca Espinosa, Raquel Fernandez-Penas, and Joaquín Criado-Reyes for their technical assistance. We are grateful to Isabel Díaz (Instituto de Catálisis y Petroleoquímica—CSIC) for fluoride analyses. We also thank the National Commission for Science, Technology and Information, National Environmental Management Authority, and Kenya Wildlife Services for research permissions. Magadi Tata Chemicals Ltd. and National Museums of Kenya provided logistic help. The authors gratefully acknowledge Patricia Gitari, Lukas Sossoika, and Tara Barwa for their assistance in fieldwork.

■ REFERENCES

(1) Aquilano, D.; Otálora, F.; Pastero, L.; García-Ruiz, J. M. Three Study Cases of Growth Morphology in Minerals: Halite, Calcite and Gypsum. *Progress in Crystal Growth and Characterization of Materials* **2016**, *62* (2), 227−251.

(2) García-Ruiz, J. M.; Otálora, F. 1 - Crystal Growth in Geology: Patterns on the Rocks. In *Handbook of Crystal Growth*, 2nd ed.; Rudolph, P., Ed.; Elsevier: Boston, 2015; pp 1−43..

(3) Otálora, F.; García-Ruiz, J. Nucleation and Growth of the Naica Giant Gypsum Crystals. *Chem. Soc. Rev.* **2014**, *43* (7), 2013−2026.

(4) García-Ruiz, J. M.; Villasuso, R.; Ayora, C.; Canals, A.; Otálora, F. Formation of Natural Gypsum Megacrystals in Naica, Mexico. *Geology* **2007**, *35* (4), 327−330.

(5) de la P. Blasco, J. A.; García-Ruiz, J. M.; Pérez, R. M.; Rubio, M. P. Growth Features of Magnesium and Salts in a Recent Playa Lake of La Mancha (Spain). *Estudios Geològicos* **1982**, *38* (3), 245−257.

(6) Otálora, F.; Mazurier, A.; Garcia-Ruiz, J. M.; Van Kranendonk, M. J.; Kotopoulou, E.; El Albani, A.; Garrido, C. J. A Crystallographic Study of Crystalline Casts and Pseudomorphs from the 3.5 Ga Dresser Formation, Pilbara Craton (Australia). *J. Appl. Crystallogr.* **2018**, *51* (4), 1050−1058.

(7) Hardie, L. A.; Lowenstein, T. K. Evaporites. In *Encyclopedia of Sediments and Sedimentary Rocks*; Middleton, G. V., Church, M. J., Coniglio, M., Hardie, L. A., Longstaffe, F. J., Eds.; Springer Netherlands: Dordrecht, 2003; pp 257−263..

(8) Eugster, H. P.; Hardie, L. A. Saline Lakes. In *Lakes: Chemistry, Geology, Physics*; Lerman, A., Ed.; Springer: New York, NY, 1978; pp 237−293..

(9) Warren, J. K. Depositional Chemistry and Hydrology. In *Evaporites: A Geological Compendium*; Warren, J. K., Ed.; Springer International Publishing: Cham, Switzerland, 2016; pp 85−205..

(10) Eugster, H. P. Geochemistry of Evaporitic Lacustrine Deposits. *Annual Review of Earth and Planetary Sciences* **1980**, *8* (1), 35−63.

(11) Ma, L.; Lowenstein, T. K.; Russell, J. M. A Brine Evolution Model and Mineralogy of Chemical Sediments in a Volcanic Crater, Lake Kitagata, Uganda. *Aquat Geochem* **2011**, *17* (2), 129−140.

(12) Lowenstein, T. K.; Dolginko, L. A. C.; García-Veigas, J. Influence of Magmatic-Hydrothermal Activity on Brine Evolution in Closed Basins: Searles Lake, California. *GSA Bulletin* **2016**, *128* (9−10), 1555−1568.

(13) Kolpakova, M. N.; Gaskova, O. L. Major Ions Behaviour during Evaporation of Different Saline Type Water of Western Mongolian Lakes (Geochemical Modelling). *Hydrology Research* **2018**, *49* (1), 163−176.

(14) Cabestrero, Ó.; Sanz-Montero, M. E. Brine Evolution in Two Inland Evaporative Environments: Influence of Microbial Mats in Mineral Precipitation. *J. Paleolimnol* **2018**, *59* (2), 139−157.

(15) Renaut, R. W.; Owen, R. B.; Lowenstein, T. K.; de Cort, G.; Mcnulty, E.; Scott, J. J.; Mbuthia, A. The Role of Hydrothermal Fluids in Sedimentation in Saline Alkaline Lakes: Evidence from Nasikie Engida, Kenya Rift Valley. *Sedimentology* **2021**, *68* (1), 108−134.

(16) Otálora, F.; Criado-Reyes, J.; Baselga, M.; Canals, A.; Verdugo-Escamilla, C.; García Ruiz, J. M. Hydrochemical and Mineralogical Evolution through Evaporitic Processes in Salar de Llamara Brines (Atacama, Chile). *ACS Earth Space Chem.* **2020**, *4* (6), 882−896.

(17) Yan, Z.; Xu, W.; Luo, X.; You, Y.; Wen, H. Sedimentation Sequence of a High-Temperature Silica-Rich Hot Spring: Evidence from Isothermal Evaporation Experiments and from Petrology and Mineralogy of Sinters. *Carbonates Evaporites* **2021**, *36* (2), 29.

(18) Kempe, S.; Kazmierczak, J. Biogenesis and Early Life on Earth and Europa: Favored by an Alkaline Ocean? *Astrobiology* **2002**, *2* (1), 123−130.

(19) Toner, J. D.; Catling, D. C. A Carbonate-Rich Lake Solution to the Phosphate Problem of the Origin of Life. *Proc. Natl. Acad. Sci. U.S.A.* **2020**, *117* (2), 883−888.

(20) Schagerl, M.; Renaut, R. W. Dipping into the Soda Lakes of East Africa. In *Soda Lakes of East Africa*; Schagerl, M., Ed.; Springer International Publishing: Cham, Switzerland, 2016; pp 3−24..

(21) Walsh, P. J.; Grosell, M.; Goss, G. G.; Bergman, H. L.; Bergman, A. N.; Wilson, P.; Laurent, P.; Alper, S. L.; Smith, C. P.; Kamunde, C.; Wood, C. M. Physiological and Molecular Characterization of Urea Transport by the Gills of the Lake Magadi Tilapia (Alcolapia Grahami). *Journal of Experimental Biology* **2001**, *204* (3), 509−520.

(22) Grant, W. D.; Mwatha, W. E.; Jones, B. E. Alkaliphiles: Ecology, Diversity and Applications. *FEMS Microbiology Reviews* **1990**, *6* (2−3), 255−269.

(23) Grant, W. D.; Sorokin, D. Yu. Distribution and Diversity of Soda Lake Alkaliphiles. In *Extremophiles Handbook*; Horikoshi, K., Ed.; Springer Japan: Tokyo, 2011; pp 27−54. .

(24) Buatois, L. A.; Renaut, R. W.; Owen, R. B.; Behrensmeyer, A. K.; Scott, J. J. Animal Bioturbation Preserved in Pleistocene Magadiite at Lake Magadi, Kenya Rift Valley, and Its Implications for the Depositional Environment of Bedded Magadiite. *Sci. Rep* **2020**, *10* (1), 6794.

(25) Jagniecki, E. A.; Lowenstein, T. K. Evaporites of the Green River Formation, Bridger and Piceance Creek Basins: Deposition, Diagenesis, Paleobrine Chemistry, and Eocene Atmospheric CO2. In *Stratigraphy and Paleolimnology of the Green River Formation, Western USA*; Smith, M. E., Carroll, A. R., Eds.; Syntheses in Limnogeology; Springer Netherlands: Dordrecht, 2015; pp 1277−312..

(26) Demicco, R. V.; Lowenstein, T. K. When "Evaporites" Are Not Formed by Evaporation: The Role of Temperature and PCO2 on Saline Deposits of the Eocene Green River Formation, Colorado, USA. *GSA Bulletin* **2020**, *132* (7−8), 1365−1380.

(27) Olson, K. J.; Lowenstein, T. K. Searles Lake Evaporite Sequences: Indicators of Late Pleistocene/Holocene Lake Temperatures, Brine Evolution, and PCO2. *GSA Bulletin* **2021**, *133*, 2319.

(28) Rull, F.; Guerrero, J.; Venegas, G.; Gázquez, F.; Medina, J. Spectroscopic Raman Study of Sulphate Precipitation Sequence in Rio Tinto Mining District (SW Spain). *Environ. Sci. Pollut Res.* **2014**, *21* (11), 6783−6792.

(29) Kotopoulou, E.; Delgado Huertas, A.; Garcia-Ruiz, J. M.; Dominguez-Vera, J. M.; Lopez-Garcia, J. M.; Guerra-Tschuschke, I.; Rull, F. A Polyextreme Hydrothermal System Controlled by Iron: The Case of Dallol at the Afar Triangle. *ACS Earth Space Chem.* **2019**, *3* (1), 90−99.

(30) Paris, O.; Li, C.; Siegel, S.; Weseloh, G.; Emmerling, F.; Riesemeier, H.; Erko, A.; Fratzl, P. A New Experimental Station for Simultaneous X-Ray Microbeam Scanning for Small- and Wide-Angle Scattering and Fluorescence at BESSY II. *J. Appl. Crystallogr.* **2007**, *40* (s1), s466−s470.

(31) Wolf, S. E.; Leiterer, J.; Kappl, M.; Emmerling, F.; Tremel, W. Early Homogenous Amorphous Precursor Stages of Calcium Carbonate and Subsequent Crystal Growth in Levitated Droplets. *J. Am. Chem. Soc.* **2008**, *130* (37), 12342−12347.

(32) Parkhurst, D. L.; Appelo, C. A. J. *Description of Input and Examples for PHREEQC Version 3: A Computer Program for Speciation, Batch-Reaction, One-Dimensional Transport, and Inverse Geochemical Calculations*; Techniques and Methods; Report 6-A43; U.S. Geological Survey: 2013; p 497..

(33) Blanc, Ph; Lassin, A.; Piantone, P.; Azaroual, M.; Jacquemet, N.; Fabbri, A.; Gaucher, E. C. Thermoddem: A Geochemical Database Focused on Low Temperature Water/Rock Interactions and Waste Materials. *Appl. Geochem.* **2012**, *27* (10), 2107−2116.

(34) Giffaut, E.; Grivé, M.; Blanc, Ph; Vieillard, Ph; Colàs, E.; Gailhanou, H.; Gaboreau, S.; Marty, N.; Madé, B.; Duro, L. Andra Thermodynamic Database for Performance Assessment: ThermoChimie. *Appl. Geochem.* **2014**, *49*, 225−236.

(35) Shahidzadeh, N.; Schut, M. F. L.; Desarnaud, J.; Prat, M.; Bonn, D. Salt Stains from Evaporating Droplets. *Sci. Rep.* **2015**, *5* (1), 10335.

(36) Efstratiou, M.; Christy, J.; Sefiane, K. Crystallization-Driven Flows within Evaporating Aqueous Saline Droplets. *Langmuir* **2020**, *36* (18), 4995−5002.

(37) Bertoluzza, A.; Monti, P.; Morelli, M. A.; Battaglia, M. A. A Raman and Infrared Spectroscopic Study of Compounds Characterized by Strong Hydrogen Bonds. *J. Mol. Struct.* **1981**, *73* (1), 19−29.

(38) Vargas Jentzsch, P.; Ciobotă, V.; Rösch, P.; Popp, J. Reactions of Alkaline Minerals in the Atmosphere. *Angew. Chem., Int. Ed.* **2013**, *52* (5), 1410−1413.

(39) Krauskopf, K. B.; Bird, D. K. Introduction to Geochemistry, 2nd ed.; *International Series in the Earth and Planetary Sciences*; McGraw-Hill: 1979.

(40) Owen, R. B.; Renaut, R. W.; Muiruri, V. M.; Rabideaux, N. M.; Lowenstein, T. K.; McNulty, E. P.; Leet, K.; Deocampo, D.; Luo, S.; Deino, A. L.; Cohen, A.; Sier, M. J.; Campisano, C.; Shen, C.-C.; Billingsley, A.; Mbuthia, A.; Stockhecke, M. Quaternary History of the Lake Magadi Basin, Southern Kenya Rift: Tectonic and Climatic Controls. *Palaeogeography, Palaeoclimatology, Palaeoecology* **2019**, *518*, 97−118.

(41) Baker, B. H. *Geology of the Magadi Area*; Report No. 42; Geological Survey of Kenya: Nairobi, Kenya, 1958; p 81.

(42) Eugster, H. P. Lake Magadi, Kenya, and Its Precursors. *Developments in Sedimentology* **1980**, *28*, 195−232.

(43) McNulty, E. *Lake Magadi and the Soda Lake Cycle: A Study of the Modern Sodium Carbonates and of Late Pleistocene and Holocene Lacustrine Core Sediments*. M.S. Thesis, Binghamton University, 2017.

(44) Eugster, H. P. Chemistry and Origin of the Brines of Lake Magadi, Kenya. *Mineral. Soc. Am. Spec. Pap.* **1970**, *3*, 213−235.

(45) Eugster, H. P. Origin and Deposition of Trona. *Rocky Mountain Geology* **1971**, *10* (1), 49−55.

(46) Lee, H.; Muirhead, J. D.; Fischer, T. P.; Ebinger, C. J.; Kattenhorn, S. A.; Sharp, Z. D.; Kianji, G. Massive and Prolonged Deep Carbon Emissions Associated with Continental Rifting. *Nature Geosci* **2016**, *9* (2), 145−149.

(47) Getenet, M.; García-Ruiz, J. M.; Verdugo-Escamilla, C.; Guerra-Tschuschke, I. Mineral Vesicles and Chemical Gardens from Carbonate-Rich Alkaline Brines of Lake Magadi, Kenya. *Crystals* **2020**, *10* (6), 467.

(48) Surdam, R. C.; Eugster, H. P. Mineral Reactions in the Sedimentary Deposits of the Lake Magadi Region, Kenya. *GSA Bulletin* **1976**, *87* (12), 1739−1752.

(49) Eugster, H. P. Lake Magadi, Kenya: A Model for Rift Valley Hydrochemistry and Sedimentation? *Geological Society, London, Special Publications* **1986**, *25* (1), 177−189.

(50) Renaut, R. W.; Tiercelin, J. J.; Owen, R. B. Mineral Precipitation and Diagenesis in the Sediments of the Lake Bogoria Basin, Kenya Rift Valley. *Geological Society, London, Special Publications* **1986**, *25* (1), 159−175.

(51) Mercedes-Martín, R.; Rao, A.; Rogerson, M.; Sánchez-Román, M. Effects of Salinity, Organic Acids and Alkalinity on the Growth of Calcite Spherulites: Implications for Evaporitic Lacustrine Sedimentation. *Depositional Record* **2022**, *8*, 143.

(52) Mercedes-Martín, R.; Rogerson, M. R.; Brasier, A. T.; Vonhof, H. B.; Prior, T. J.; Fellows, S. M.; Reijmer, J. J. G.; Billing, I.; Pedley, H. M. Growing Spherulitic Calcite Grains in Saline, Hyperalkaline Lakes: Experimental Evaluation of the Effects of Mg-Clays and Organic Acids. *Sedimentary Geology* **2016**, *335*, 93−102.

(53) Mercedes-Martín, R.; Brasier, A. T.; Rogerson, M.; Reijmer, J. J. G.; Vonhof, H.; Pedley, M. A Depositional Model for Spherulitic Carbonates Associated with Alkaline, Volcanic Lakes. *Marine and Petroleum Geology* **2017**, *86*, 168−191.

(54) Bischoff, K.; Sirantoine, E.; Wilson, M. E. J.; George, A. D.; Mendes Monteiro, J.; Saunders, M. Spherulitic Microbialites from Modern Hypersaline Lakes, Rottnest Island, Western Australia. *Geobiology* **2020**, *18* (6), 725−741.

(55) Jones, B. F.; Eugster, H. P.; Rettig, S. L. Hydrochemistry of the Lake Magadi Basin, Kenya. *Geochim. Cosmochim. Acta* **1977**, *41* (1), 53−72.

(56) Eugster, H. P.; Jones, B. F. Gels Composed of Sodium-Aluminum Silicate, Lake Magadi, Kenya. *Science* **1968**, *161* (3837), 160−163.

(57) Kasedde, H.; Kirabira, J. B.; Bäbler, M. U.; Tilliander, A.; Jonsson, S. Characterization of Brines and Evaporites of Lake Katwe, Uganda. *Journal of African Earth Sciences* **2014**, *91*, 55−65.

(58) Davey, R. J.; Liu, W.; Quayle, M. J.; Tiddy, G. J. T. In Situ Monitoring of Crystallization Processes Using Synchrotron X-Ray Diffraction: The Search for Structural Precursors. *Cryst. Growth Des.* **2002**, *2* (4), 269−272.

(59) Radnik, J.; Bentrup, U.; Leiterer, J.; Brückner, A.; Emmerling, F. Levitated Droplets as Model System for Spray Drying of Complex Oxides: A Simultaneous in Situ X-Ray Diffraction/Raman Study. *Chem. Mater.* **2011**, *23* (24), 5425−5431.

Supporting Information

A comprehensive methodology for monitoring evaporitic mineral precipitation and hydrochemical evolution of saline lakes: the case of Lake Magadi soda brine (East African Rift Valley, Kenya)

Melese Getenet, Juan Manuel García-Ruiz, Fermín Otálora, Franziska Emmerling, Dominik Al-Sabbagh, Cristóbal Verdugo-Escamilla

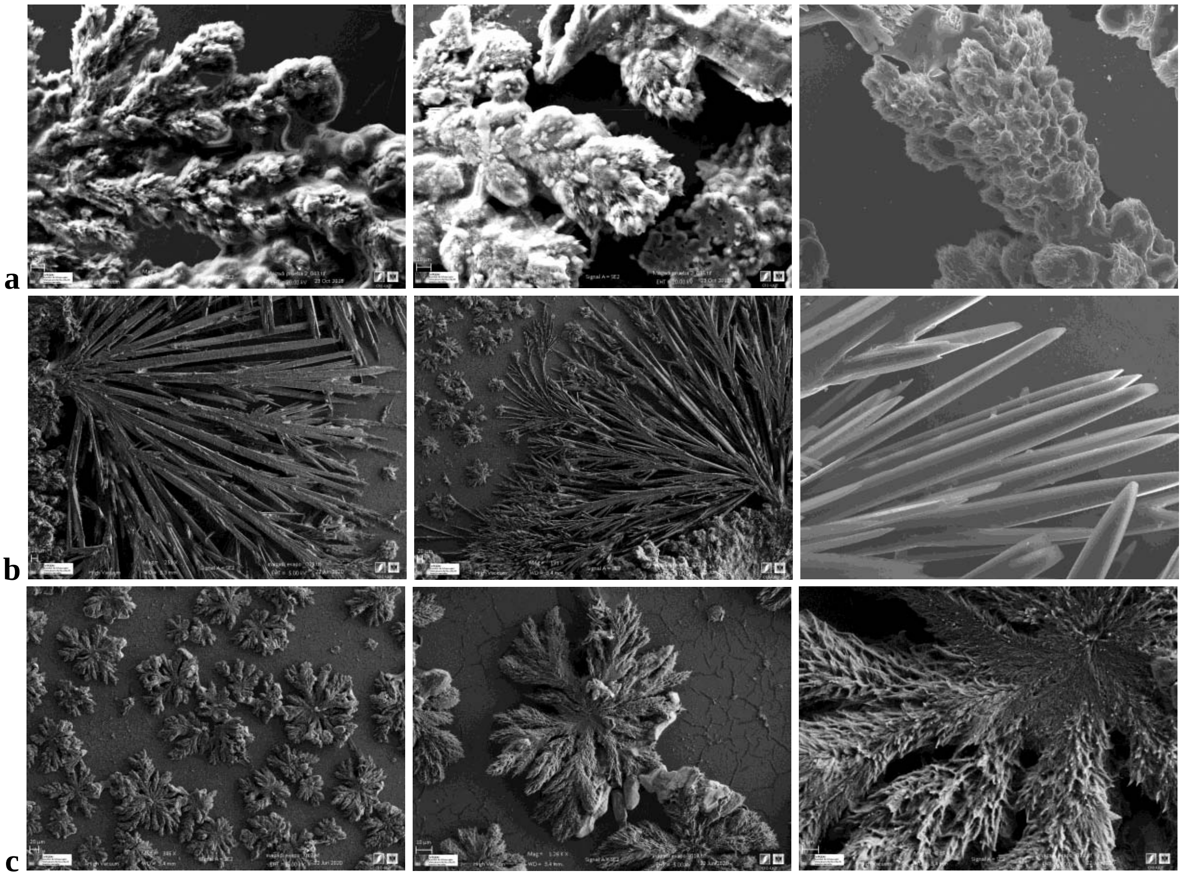

Figure S1: (a) feathery border dendritic minerals, (b) acicular trona, (c) star-like central precipitates with similar feathery texture as shown in panel a

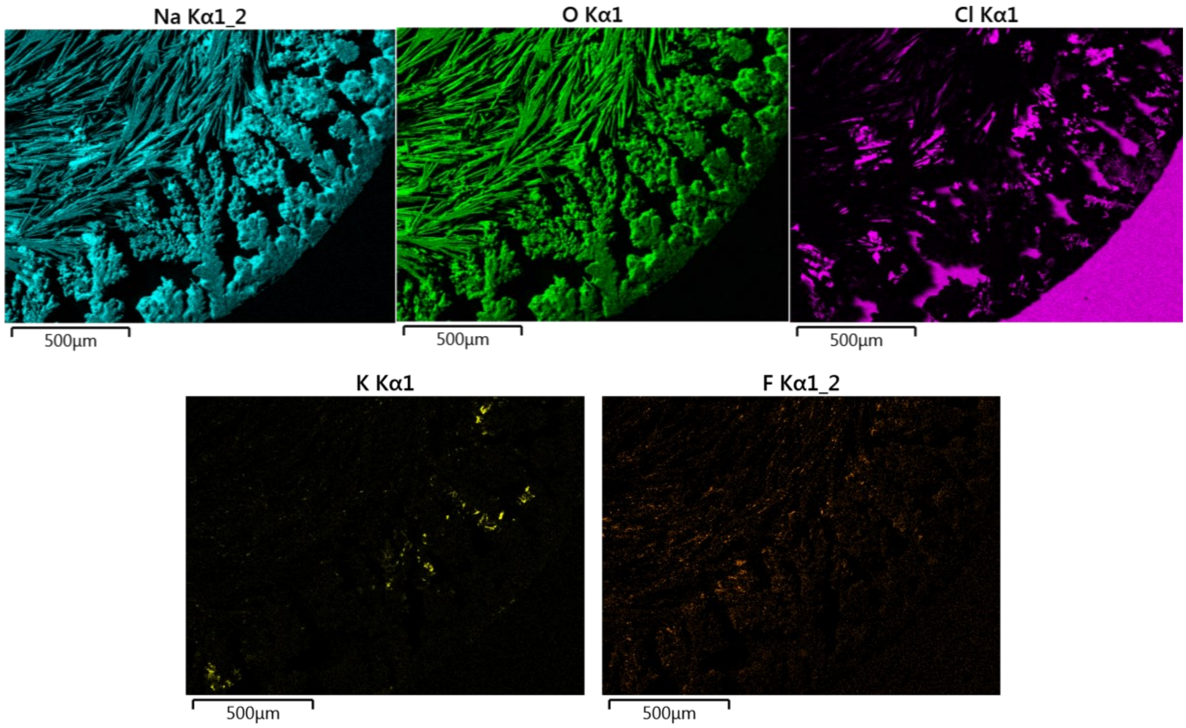

Figure S2: Separate elemental map of the EDX analysis presented in Figure 9a in the main text

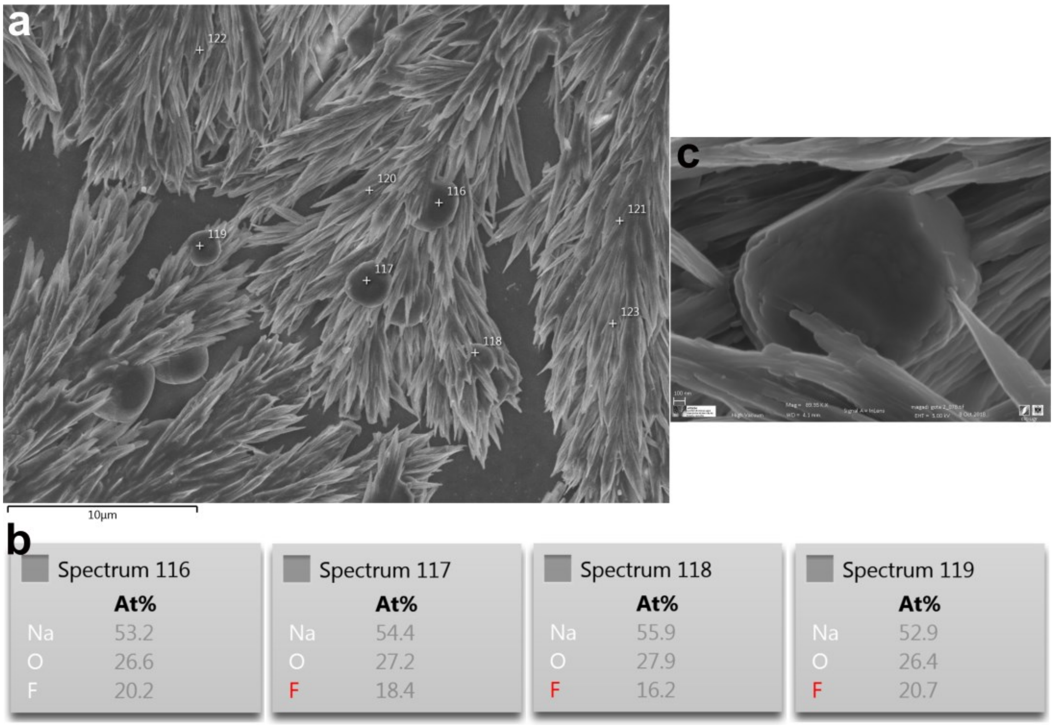

Spectrum 116	At%
Na	53.2
O	26.6
F	20.2

Spectrum 117	At%
Na	54.4
O	27.2
F	18.4

Spectrum 118	At%
Na	55.9
O	27.9
F	16.2

Spectrum 119	At%
Na	52.9
O	26.4
F	20.7

Figure S3: (a) Electron micrograph of rounded and cubic crystals of villiaumite (NaF) between the dendritic trona crystals; (b) EDX elemental analysis of the villiaumite crystals; (c) high-resolution micrograph of semi-rounded cubic villiaumite crystal embedded between trona dendrites

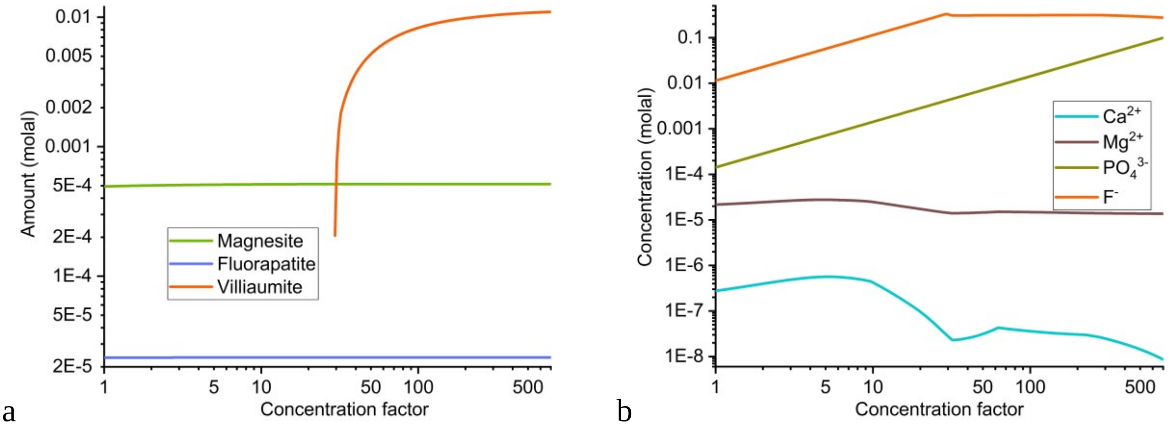

a b

Figure S4: PHREEQC simulation of evaporation and mineral precipitation from Lake Magadi brine at 25 °C in the presence of phosphate and fluoride ions. (a) the mineral precipitation sequence of minor phases and villiaumite and the amount precipitated; (b) chemical evolution of the brine during mineral precipitation

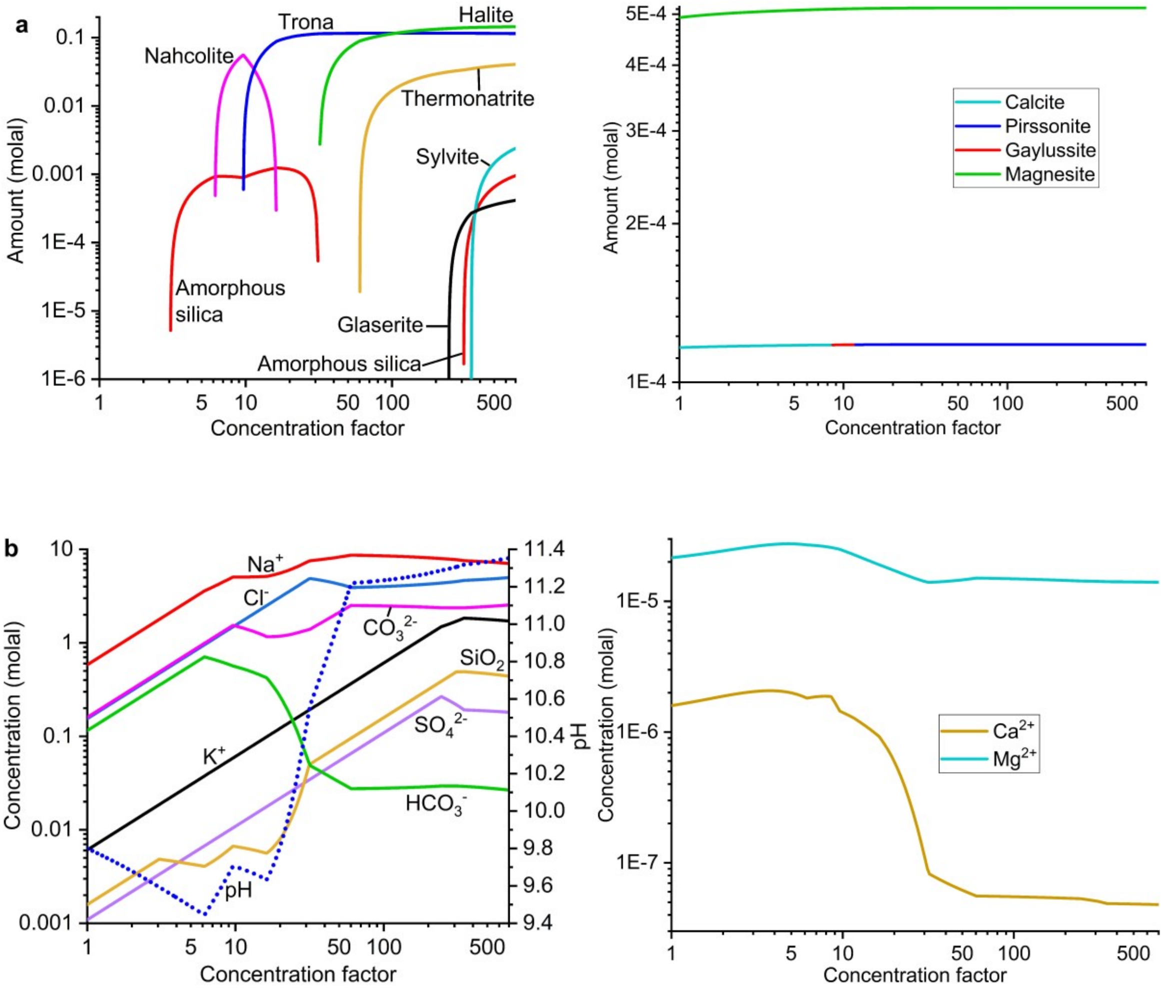

Figure S5: PHREEQC simulation of evaporation and mineral precipitation from Lake Magadi brine at 25 °C in the absence of phosphate and fluoride ions. (a) the mineral precipitation sequence and the precipitated amount of major phases (left) and minor phases (right); (b) chemical evolution of the brine during mineral precipitation

Description of supporting videos presented under
https://doi.org/10.6084/m9.figshare.21077029

Video S1: Video microscopy of the overall evolution of the precipitation during the evaporation of a single droplet on glass slide. The precipitation process begins on the border of the droplet and progress towards the center (speed 8×, MP4)

Video S2: Detail video microscopy of evaporation and precipitation on the border of a droplet. The precipitation process begins on the border of the droplet and progress towards the center (speed 8×, MP4)

Video S3: Video microscopy of the precipitation process on the border of the droplet marked with red rectangle in Video S2 (speed 4×, MP4)

Video S4: Video microscopy showing the details of the precipitation process at the center of the droplets (speed 2×, MP4)

Chapter 3

3. Mineral Precipitation and Hydrochemical Evolution Through Evaporitic Processes in Soda Brines (East African Rift Valley) [1]

---

[1] This chapter is under review in Chemical Geology journal as Getenet, M., Otálora, F., Emmerling, F., Al-Sabbagh, D, García-Ruiz, J.M. Mineral Precipitation and Hydrochemical Evolution Through Evaporitic Processes in Soda Brines (East African Rift Valley, Kenya)

Journal metrics:
JCR 2021 (Clarivate Analytics): Impact Factor: 4.685, Q1 in Geochemistry & Geophysics Category

Supplementary Materials for this article are found at the end of this chapter.

Mineral precipitation and hydrochemical evolution through evaporitic processes in soda brines (East African Rift Valley)

Melese Getenet [a], Fermín Otálora [a], Franziska Emmerling [b], Dominik Al-Sabbagh [b], Juan Manuel García-Ruiz [a,]*

[a] *Laboratorio de Estudios Cristalográficos, Instituto Andaluz de Ciencias de la Tierra (CSIC-UGR), Avenida de las Palmeras 4, Armilla, E-18100 Granada, Spain*

[b] *Federal Institute for Materials Research and Testing (BAM), Richard-Willstätter-Straße 11, 12489 Berlin, Germany*

** Corresponding author: juanmanuel.garcia@csic.es*

Keywords:

Crystallization sequence
Hydrochemical evolution
Alkaline brines
Soda lakes
Sodium carbonate minerals
Evaporite deposits

ABSTRACT

Soda lakes of the East African Rift Valley are hyperalkaline, hypersaline lakes extremely enriched in Na^+, K^+, $Cl^–$, $CO_3^{2–}$, $HCO_3^–$, and SiO_2. In this paper, we investigate the chemical evolution in these lakes and the production of chemical sediments by salt precipitation via evaporation. Water samples from tributary springs and three lakes (Magadi, Nasikie Engida and Natron) have been experimentally studied by in-situ X-ray diffraction during evaporation experiments to characterize the sequence of mineral precipitation. These data are complemented by ex-situ diffraction studies, chemical analyses and thermodynamic hydrochemical calculations producing detailed information on the activity of all solution species and the saturation state of all minerals potentially generated by the given composition. Major minerals precipitating from these samples are sodium carbonates/bicarbonates as well as halite. The CO_3/HCO_3 ratio, controlled by pH, is the main factor defining the Na-carbonates precipitation sequence: in lake brines where $CO_3/HCO_3 > 1$, trona precipitates first whereas in hot springs, where $CO_3/HCO_3 \ll 1$, nahcolite precipitates instead of trona, which forms later via partial dissolution of nahcolite. Precipitation of nahcolite is possible only at lower pH values (pCO_2 higher than -2.7) explaining the distribution of trona and nahcolite in current lakes and the stratigraphic sequences. Later, during evaporation, thermonatrite precipitates, normally at the same time as halite, at a very high pH (>11.2) after significant depletion of HCO_3^- due to trona precipitation. The precipitation of these soluble minerals increases the pH of the brine and is the main factor contributing to the hyperalkaline and hypersaline character of the lakes. Villiaumite, sylvite, alkaline earth carbonates, fluorapatite and silica are also predicted to precipitate, but most of them have not been observed in evaporation experiments, either because of the small amount of precipitates produced, kinetic effects delaying the nucleation of some phases, or by biologically induced effects in the lake chemistry that are not considered in our calculations. Even in these cases, the chemical composition in the corresponding ions allows for discussion on their accumulation of them and the eventual precipitation of these phases. The coupling of in-situ and ex-situ experiments and geochemical modeling is key to understanding the hydrogeochemical and hydroclimatic conditions of soda lakes, evaporite settings, and potentially soda oceans of early Earth and other extraterrestrial bodies.

1. Introduction

Soda lakes are saline lakes mostly found in endorheic basins dominated by volcanic terrains, like the tectonic depressions of the East African Rift valley. They are characterized by high pH and large concentration of Na^+, Cl^-, CO_3^{2-} and HCO_3^- (Deocampo and Renaut, 2016; Pecoraino et al., 2015; Schagerl and Renaut, 2016), leading to active evaporitic precipitation. Lake Magadi, Nasikie Engida (also known as Little Magadi), and Natron, hereafter MNN lakes, are among the highly saline and alkaline soda lakes in the East African Rift Valley where active precipitation of saline minerals and silica gels occurs (Fritz et al., 1987; Jones et al., 1977; Manega and Bieda, 1987). These lakes are located in the southern lowermost depression of the East African Rift valley, near the border between Kenya and Tanzania, occupying a N-S trending axial graben. These basins are formed during the late-Pleistocene faulting of the metamorphic basements to the east and west (Baker, 1987; Baker et al., 1972; Dawson, 2008), when the region passed through three stages of rifting namely pre-rifting regional doming, half-graben and full graben rifting which formed different basins filled with volcanic rocks of different composition, mainly alkali trachyte in the Magadi and Nasikie Engida region.

Three sedimentary units are defined in the region, from bottom to top, Oloronga Beds, Green Beds, and High Magadi Beds (Behr, 2002; Behr and Röhricht, 2000). The youngest sediments in the High Magadi Beds (named Evaporite Series) contains bedded trona deposit intercalated by thin beds of tuffaceous clay and muds (Baker, 1958; Eugster, 1980, 1967, 1967; Hay, 1968; Surdam and Eugster, 1976), and extend more than 65 m below the lake floor (Owen et al., 2019). During Late Pleistocene to Holocene, the High Magadi Beds materials were deposited in a fresh to moderately saline, alkaline lake. Paleolake levels during the Early Holocene were high enough to allow the interconnection of these lakes as a single water body (Baker, 1958; Eugster, 1980; Hillaire-Marcel et al., 1986). Modern Lake Natron is surrounded by zeolitized clays and tuffs collectively called High Natron Beds (Baker, 1963; Hay, 1968); they contain irregular chert nodules with magadiite and kenyaite. The High Natron Beds may correlate with the High Magadi Beds, both depositing during the high stand periods that connected Lake Natron and Lake Magadi (Baker, 1963; Dawson, 2008; Hillaire-Marcel et al., 1986). The modern evaporites of Natron consist of trona, nahcolite, thermonatrite and traces of halite and villiaumite interbedded with clays (Baker, 1986; Dawson, 2008; Manega and Bieda, 1987).

The dominant contributors to the solute content of the lake brines are springs (Eugster, 1980; Jones et al., 1977; Renaut et al., 2020). Nasikie Engida hot springs emanate from a hot saline groundwater body (100-150 °C) recharged by the lower Ewaso Ngiro River and local groundwater (Allen et al., 1989). Apart from springs, Lake Natron is fed by four perennial rivers draining from the western escarpments and the highlands (Manega and Bieda, 1987). Diluted inflows reach the lake through streams in the western rim of the rift valley and seasonal runoff from the north of Lake Magadi (Eugster, 1970; Jones et al., 1977). These inflows are rich in HCO_3^- and silica due to the rapid hydrolysis of volcanic rocks, but poor in Al^{3+} due to precipitation of clays and gels. Furthermore, before reaching the lake, dilute inflows and runoff waters undergo surface evaporation, producing efflorescent precipitation of alkaline earth carbonate crusts (Eugster, 1980), which reduce the concentration of Ca^{2+}, Mg^{2+} and HCO_3^- (Eugster, 1980, 1970; Jones et al., 1977). During the next rainy season, the most soluble fraction of these crusts (halite and thermonatrite) is redissolved by rain and runoff water, increasing groundwater salinity, and leaving behind alkaline earth carbonates and silicates in the lake beds and alluvial flats. Recurrent precipitation and fractional dissolution of these crusts in a high geothermal gradient region give rise to saline groundwater that emerges in the form of warm and hot springs on the shore of Lake Magadi and northern Nasikie Engida, feeding it and evolving, mainly by evaporation, to brines rich in Na^+, Cl^-, CO_3^{2-}, and HCO_3^- that are saturated with respect to trona and/or nahcolite. Isotopic studies of evaporites of MNN lakes suggested an important contribution of Oldoinyo Lengai volcano to the salinity of these lakes (Bell et al., 1973). This volcano has been erupting natrocarbonatite lavas and ashes containing soluble sodium-potassium carbonate minerals (Dawson, 1964, 1962), which are leached to give sodium-rich solution (Baker, 1986; Bell et al., 1973).

The brines of Lake Magadi and Nasikie Engida pass through a recurrent cycle of three stages: undersaturation, evaporative concentration, and desiccation. During the evaporative concentration, trona grows as thin sheet-like rafts on the surface and as upward radiating needles at the bottom of the lake. After complete evaporation (desiccation stage), continued evaporation of interstitial brines causes expansion and buckling of the crust and precipitation of a variety of efflorescent crusts and intercrystallite cement. During the undersaturation stage (flooding of the lake), dilute inflows partially dissolve the pre-existing trona or nahcolite, creating layered deposits of upward radiating trona crystals (in Lake Magadi) or mainly nahcolite crystals (in Nasikie Engida) with thin mud layers on top of the dissolution surfaces (Eugster, 1980; McNulty, 2017). In addition to trona/nahcolite, thermonatrite and halite precipitation occur at some local pools on the lake surface and in the evaporation ponds of TATA Chemicals Soda Company (Eugster, 1980; Renaut et al., 2020). Recently, McNulty (2017) presented a detailed discussion of the present sodium carbonate deposits of Lake Magadi and Nasikie Engida, comparing them with Late Pleistocene and Holocene lacustrine core sediments from Lake Magadi. A detailed discussion on the role of hydrothermal fluids in evaporite sedimentation of Nasikie Engida can be found in Renaut et al. (2020).

Many studies on saline lakes have shown the importance of understanding the mineral precipitation sequence to reveal the hydrochemical evolution of brines, and the paleoenvironmental conditions of ancient mineral deposits (Cabestrero and Sanz-Montero, 2018; Kolpakova and Gaskova, 2017; Lowenstein et al., 2016; Ma et al., 2011; Otálora et al., 2020; Renaut et al., 2020). The mechanisms of solute transport and the active precipitation of sodium carbonate minerals in soda lakes provide important insights into the depositional environment, paleo-brine chemistry, and diagenesis of evaporite deposits in the geological record. In this context, the assemblage of sodium carbonate minerals precipitated from brines can be used to constrain ancient temperatures and atmospheric CO_2 concentrations during deposition and, therefore in understanding the environmental and geochemical conditions of the past (Demicco and Lowenstein, 2019; Jagniecki et al., 2015; Olson and Lowenstein, 2021).

The extrapolations of the knowledge gained on the evaporite precipitation sequence from alkaline waters are also relevant for Precambrian studies and planetary sciences. Soda lakes have geochemistry close to that of the soda oceans in early Earth and other Earth-like planets and this geochemical context has been proposed for the origin of life on Earth (Kempe and Kazmierczak, 2004; Toner and Catling, 2020). Recently, we have demonstrated that self-assembled chemical gardens and vesicles can form from soda lake waters, suggesting the plausibility of their formation in the soda oceans of early Earth and other planets (Getenet et al., 2020). These mineral gardens and vesicles (specifically silica-based) have been shown to play an active catalytic role in the synthesis of prebiotically relevant compounds so they could have contributed to a planetary-scale transition from inorganic geochemistry to prebiotic organic chemistry (García-Ruiz et al., 2020, 2017; Mattia Bizzarri et al., 2018; Saladino et al., 2016).

Silica gels and chert deposits, like those in Lake Magadi and Nasikie Engida, are known to facilitate the accumulation and preservation of organic matter, so their study is expected to help in decoding the information on the early steps of life available within hydrothermal cherts of the Archean Earth (Behr, 2002; Behr and Röhricht, 2000; Eugster, 1967; Eugster and Jones, 1968; Hay, 1968; Reinhardt et al., 2019; Schubel and Simonson, 1990). This motivation for the study of Magadi deposits can be extended to planetary science. Sodium carbonate minerals characteristic of soda lakes have been reported to exist on extraterrestrial planets. Lessons learned about the environmental constraints of these lakes can therefore be exported to the investigation of these planets (Carrozzo et al., 2018; De Sanctis et al., 2016; Glein et al., 2015; McCord et al., 1998). It has been also reported recently that phosphate accumulates in carbonate-rich soda lakes (Toner and Catling, 2020). The co-existence of high silica, carbonate, and phosphate content and the plausibility of mineral self-assembly in modern soda lakes implies that these lakes could be the “one-pot” geochemical environments containing all the important ingredients for the synthesis of prebiotically relevant molecules and plausible settings for the origin of life (García-Ruiz et al., 2020; Getenet et al., 2020).

Soda ash deposits are also economically important. They have been mined from active and ancient deposits from soda lakes (Schagerl and Renaut, 2016; Smith and Carroll, 2015). At Lake Magadi, trona has been mined since 1911 to produce soda ash. Halite is also being produced in ponds where the brine has been evaporated beyond trona saturation (Schagerl and Renaut, 2016). Owing to their scientific and economic values, much work has been carried out on the mineral precipitation in soda lakes. Most of these studies are based either on field data or on thermodynamic modelling (Demicco and Lowenstein, 2019; Jagniecki and Lowenstein, 2015; Olson and Lowenstein, 2021; Renaut et al., 2020). Recent works have proven that a combination of field research, lab experiments and computer modelling is key to understanding evaporitic brine evolution and mineral precipitation sequences (Kotopoulou et al., 2019; Otálora et al., 2020; Rull et al., 2014). Recently, we have presented, and applied to Lake Magadi, a comprehensive methodology for monitoring evaporitic mineral precipitation and hydrochemical evolution of saline lakes (Getenet et al., 2022). Here, we expand this methodology and use it for the study of Lake Nasikie Engida and Lake Natron, discussing the geochemical and sedimentological perspective of evaporitic sediments in soda lakes based on experimental and geochemical modelling studies.

2. Methods and Materials

2.1. Sampling and hydrochemical analysis

Lake brines and hot spring samples were collected from the three lakes during a field campaign in March 2018. The locations of the sampling are shown in Figure 1. We have collected samples from both the hot spring and the lake brine of Nasikie Engida due to a significant spatial variation in hydrochemistry. The samples from the northern shore of Nasikie Engida were collected from one of the perennial hot springs that directly recharge the lake. During sampling, in-situ pH (±0.02), temperature (±0.15 °C), total dissolved solids (TDS; ±1 mg/L), electrical conductivity (EC; ±1 µS/cm), oxidation/reduction potential (ORP; ±1 mV), and saturation percent of dissolved oxygen (DO; ±1%) were recorded by using Hanna HI 9829 multiparametric probe.

CO_3^{2-} and HCO_3^- concentrations were determined by potentiometric titration at the Laboratorio de Estudios Cristalográficos (LEC) of the Instituto Andaluz de Ciencias de la Tierra (IACT) in Granada (Spain) and ALS Laboratory Group (Czech Republic). Cl^-, F^- and SO_4^{2-} were analysed using ion liquid chromatography and ion selective electrode at ALS and Instituto de Catálisis y Petroleoquímica-CSIC (Spain). SiO_2 was analyzed by using inductively coupled plasma optical emission spectrometry and discrete spectrophotometry at the Technical Services of the Estación Experimental del Zaidín-CSIC (Spain) and ALS. All the remaining chemical analyses were performed by ALS laboratory: Na^+, K^+, Mg^{2+}, Ca^{2+}, Al^{3+}, Fe (total), B^+, and Br^- were determined using inductively coupled plasma mass spectrometry (ICP-MS). The samples were fixed by the addition of nitric acid prior to analysis with ICP-MS. PO_4^{3-} was determined by a colorimetric method based on molybdenum blue using discrete spectrophotometry.

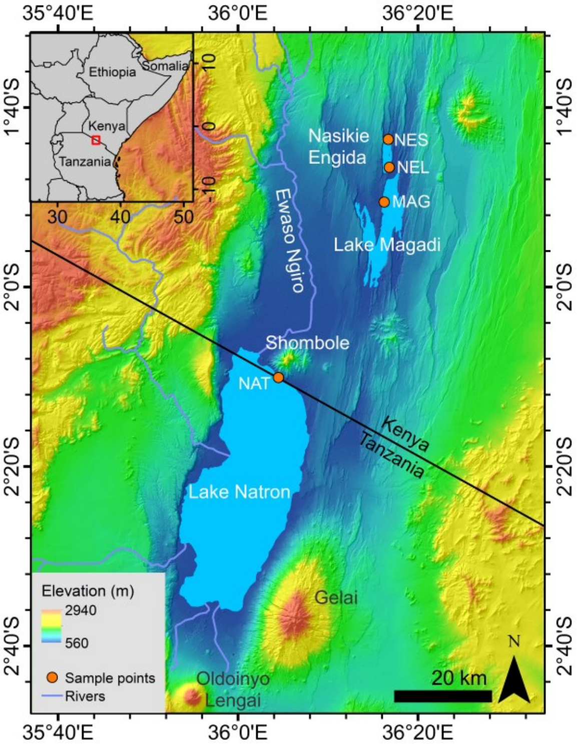

Figure 1. Digital elevation model map of the MNN basin, the sampling points (NES: Nasikie Engida hot spring, NEL: Lake Nasikie Engida brine, MAG: Lake Magadi brine, NAT: Lake Natron brine), and the volcanos in its vicinity. Digital elevation data © NASA Shuttle Radar Topography Mission

2.2. Evaporation experiments and ex-situ characterization of precipitates

Ex-situ evaporation and mineral precipitation experiments were performed at 30 ± 1 °C on glass slides except for Lake Magadi brine which are performed at 25 ± 1 °C. Relative humidity was maintained at 35 ± 2% by using a climate chamber (Memmert, Germany). Droplets of about 25 µL (approximate diameter 1 cm) were poured on glass slides using plastic pipettes. After complete evaporation of the droplets, the mineralogy of the precipitates was characterized by using powder X-ray diffraction. For ex-situ X-ray diffraction, we used a high-resolution Bruker D8 Advance X-ray diffractometer (at the Laboratorio de Estudios Cristalográficos) with monochromatic Cu $K_{\alpha 1}$ radiation, primary Ge(111) monochromator and a Lynxeye PSD detector). Diffractograms were acquired in transmission mode, at 40 kV acceleration voltage, and 40 mA current, 2θ scans spanning from 5° to 80° with a 2θ step of 0.02° per second. Malvern Panalytical HighScore software (version 4.9) with the ICCD PDF-4+ (2020) database was used for phase identification.

2.3. In-situ characterization of precipitates

Transformation between different hydrates of sodium carbonate-bicarbonate minerals, along with secondary precipitation, can happen even during sample handling for ex-situ characterization, which will challenge the accurate determination of the precipitation sequence. To overcome these problems, we have performed in-situ X-ray diffractions of containerless levitated droplets. In situ X-ray diffraction data was collected from evaporating levitated droplets to track the time evolution of mineral precipitation during evaporation. These experiments were performed at the µSpot beamline (see Paris et al., 2007 for detail) at the BESSY II synchrotron (Helmholtz Centre Berlin for Materials and Energy, Berlin, Germany), using the protocol described in Wolf et al. (2008). The beamline features an acoustic levitator used as a containerless sample holder (see the experimental setup in Getenet et al. (2022). In a typical experiment, 5 µl of the sample were pipetted in one of the nodes of the standing acoustic wave of the levitator to form a drop with an approximate diameter of 2 mm. A 0.72929 Å wavelength, 100 µm size incident beam was used. Scattered intensities were collected by a two-dimensional detector (Eiger9M, CCD 3072 × 3072). The exposure time was 5 seconds. Evaporation was followed for 30–80 minutes until complete desiccation. The obtained diffraction images were processed in DPDAK (Benecke et al., 2014) and converted to scattering vector q. The scattering vector was converted to the interplanar distance d by using pre-processing Python script. The evolution of the size of the levitated droplet during evaporation was monitored with a video camera. Levitated drop evaporation was performed at 30 ± 1 °C except for the Lake Magadi sample which was evaporated at 25 ± 1 °C and relative humidity of 35 ± 2 %.

2.4. Computer modelling

We used the PHREEQC version 3.4 code and an updated Pitzer database for thermodynamic hydrochemical speciation, evaporation, and precipitation calculations (Parkhurst and Appelo, 2013). The standard PHREEQC pitzer.dat database was updated with data for fluorite, hydroxyapatite, and fluorapatite taken from the llnl.dat database (Parkhurst and Appelo, 2013) and chlorapatite from Thermoddem database (v1.10) (Blanc et al., 2012). For villiaumite (NaF), thermodynamic data was taken from ThermoChimie database (v10a) (Giffaut et al., 2014). Parameters for thermonatrite, $Na(H_2PO_4)$ and its hydrated forms were taken from Toner and Catling (2020). Evaporation was simulated at 30 °C. In the case of Lake Magadi, simulations were performed at 25 °C (the temperature at which experiments of this specific sample performed) and 30 °C to compare with the rest of the lakes.

3. Results

3.1. Hydrochemistry

Table 1 shows the in-situ and laboratory measurements of the hydrochemical parameters of the MNN brines used for the evaporation experiments. Figure 2 shows the relative composition of major anions (CO_3^{2-}, HCO_3^- and Cl^-), the concentration of Na^+ and the pH of the four samples. The pH was very alkaline, varying between 9.1 (in the Nasikie Engida hot spring) and 10 (in Lake Natron). These samples are considerably rich in SO_4^{2-}, F^-, SiO_2, PO_4^{3-} and Br^-. However, they are highly depleted in Ca^{2+}, Mg^{2+}, Al^{3+}, B^+ and Fe contents.

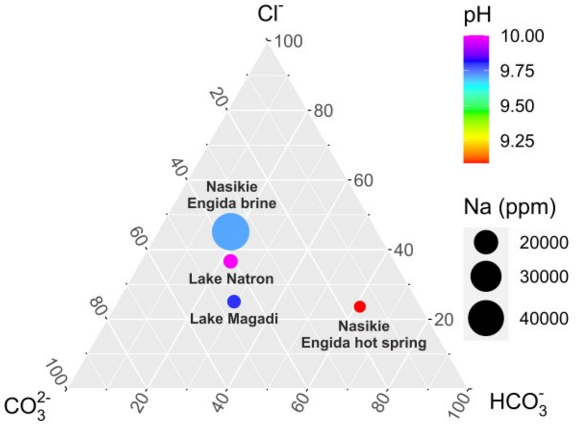

Figure 2. Composition of the four samples shown in Table 1. Point positions in the triangular plot correspond to the relative anionic composition. The size of the points corresponds to the concentration of Na (roughly proportional to TDS). The colour of the points corresponds to the in-situ measured pH at sampling time.

Lake Nasikie Engida brine have the highest concentration of major ions. It is evident from the total dissolved solids and the ionic strength that Lake Nasikie Engida brines are relatively the most enriched in solute contents (Table 1). Lake Nasikie Engida brines are mainly recharged by hot springs on its northern shoreline. Hence, the lake brine is the result of the hydrochemical evolution of the hot springs waters, which give rise to the significant enrichment in major ions except for HCO_3^- (Figure 2). Despite this fact, Lake Nasikie Engida brine contains nearly equivalent amounts of HCO_3^- ions to the hot spring in absolute terms. Lake Natron brine contains the second highest concentration of Na^+, Cl^-, CO_3^{2-}, K^+ and SO_4^{2-} whereas its HCO_3^- and SiO_2 content was the lowest (Figure 2 and Table 1). The hot spring contains the highest HCO_3^- because of its lower pH and shows the lowest K^+, F^- and CO_3^{2-} concentrations (see Figure 2 and Table 1). Lake Magadi brine contains an intermediate concentration of solutes among the three lakes while its Cl^- and SO_4^{2-} ions are relatively the lowest among all samples.

Table 1. Results of the in-situ brine characterization and the laboratory chemical analysis of samples used for the evaporation and precipitation experiments. Ionic concentrations are in ppm.

	Lake Magadi	Nasikie Engida	Nasikie Engida	Lake Natron
Sample type	lake	lake	hot spring	lake
Sample label[a]	MAG	NEL	NES	NAT
In-situ pH	9.8	9.7	9.1	10
Temperature (°C)	29.2	24.7	79.4	40.1
EC (mS/cm)	68.6	104.8	39.04	43.05
TDS (g/L)	38.1	52.42	19.51	21.52
ORP (mV)	-464.7	18	-36.6	-39.6
DO (%)	46.2	72	127.2	143.2
Ionic strength (M)	0.74	2.65	0.64	0.79
Na^+	12850 ± 1285	43300 ± 4330	12700 ± 1270	13000 ± 1300
K^+	228.5 ± 23	1145 ± 115	196 ± 20	364 ± 36
Cl^-	5250 ± 788	37600 ± 5640	6060 ± 909	8700 ± 1305
CO_3^{2-}	9600	30500 ± 3660	3910 ± 469	9710 ± 1165
HCO_3^-	6100	15200 ± 1824	15700 ± 1884	5340 ± 641
SO_4^{2-}	100.5 ± 15	451 ± 67.6	334 ± 50	375 ± 56.3
SiO_2	91.4	193 ± 38.6	65.8 ± 13.2	51.2 ± 10.2
F^-	208 ± 31	434.6	120.5	163.2
PO_4^{3-}	19.4 ± 3.9	26.5 ± 5.3		40.1 ± 8
Mg^{2+}	12 ± 0.12	1.25 ± 0.13	0.072 ± 0.0072	3.02 ± 0.3
Ca^{2+}	4.5 ± 0.45	5.1 ± 0.51	0.501 ± 0.05	19 ± 1.9
Al^{3+}	<0.05	0.62 ± 0.062	<0.02	8.5 ± 0.85
Fe^{tot}	0.1 ± 0.01	0.16 ± 0.016	0.05 ± 0.005	7.3 ± 0.73
B^+	5.2 ± 0.52		9.5 ± 0.95	
Br^-	23.3 ± 2.3		30.2 ± 3	

[a] Sample label refers to the labels of the sampling points in Figure 1

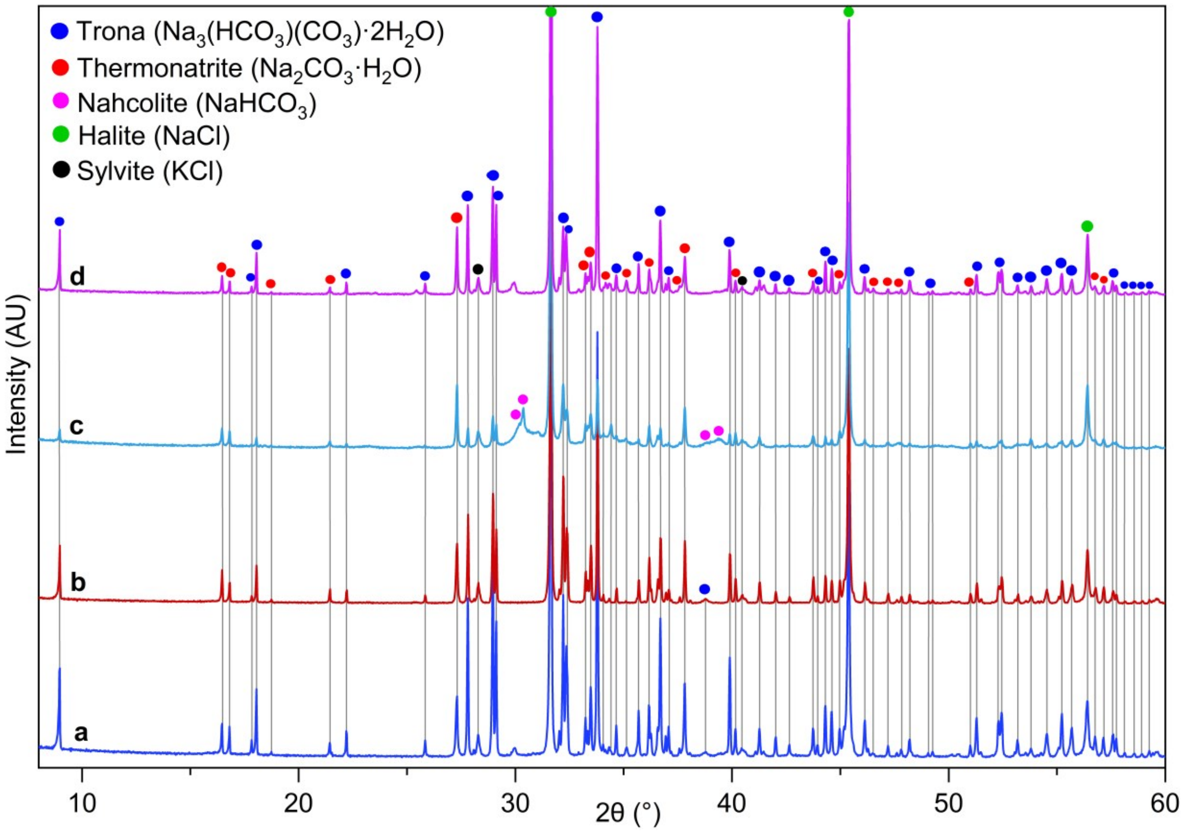

Figure 3. Powder X-ray diffraction of the whole precipitates obtained by evaporation of (a) Lake Magadi brine, (b) Lake Nasikie Engida brine, (c) Nasikie Engida hot spring and (d) Lake Natron brine

3.2. Ex-situ powder X-ray diffraction

Powder X-ray diffraction of the whole precipitates obtained from the evaporation of droplets revealed the presence of trona, thermonatrite, halite, and sylvite in all samples studied (Figure 3a-d). In addition to these phases, nahcolite was detected in Nasikie Engida hot spring (see Figure 3c). The diffraction peaks of nahcolite are broad whereas that of trona are weak relative to the diffraction patterns from lake brines (Figure 3c), most likely due to a phase transition from trona to nahcolite.

3.3. In-situ evaporation of levitated droplets

Figure 4a-d shows the in-situ X-ray diffraction measurements collected during evaporation of acoustically levitated droplets of MNN lakes and hot spring brines. Trona precipitates first after 2670, 1595, and 1725 seconds of evaporation of Magadi, Nasikie Engida and Natron lake brines respectively (see Figure 4a-b,d; the blue bars). In Nasikie Engida hot spring, nahcolite and amorphous silica simultaneously appear first after 1630 seconds of evaporation (Figure 4c; magenta bars). Halite was the second phase to appear in all samples. Precipitation of halite began after 2855, 1645, 1805 and 1790 seconds in Magadi, Nasikie Engida lake and hot spring and Natron respectively (see Figure 4a-d; the green bars). Thermonatrite appeared in a third place after 2955, 1950 and 1970 seconds in Magadi, Nasikie Engida hot spring and Natron respectively (Figure 4a,c,d; the red bars). Finally, precipitation of sylvite starts after 1990 and 2100 seconds in Nasikie Engida hot spring and Lake Natron respectively (Figure 4c-d; grey bars). The phases observed in in-situ evaporation are in good agreement with the ex-situ experiments except for a few discrepancies: sylvite and/or thermonatrite didn’t appear in the in-situ evaporation of Lake Magadi and Nasikie Engida brines while these phases were detected in ex-situ experiments (Figure 3a-b). Trona, which was not detected during in-situ evaporation of Nasikie Engida hot spring bine, was observed in ex-situ evaporation (Figure 3c). These differences are most likely related to the smaller volume of the levitated drops and the resulting smaller volume of precipitated minerals. In the case of Nasikie Engida hot spring, trona observed in the ex-situ diffraction could be the result of partial transformation of nahcolite during sample handling (Figure 3c), which would not happen in the real-time diffraction measurements.

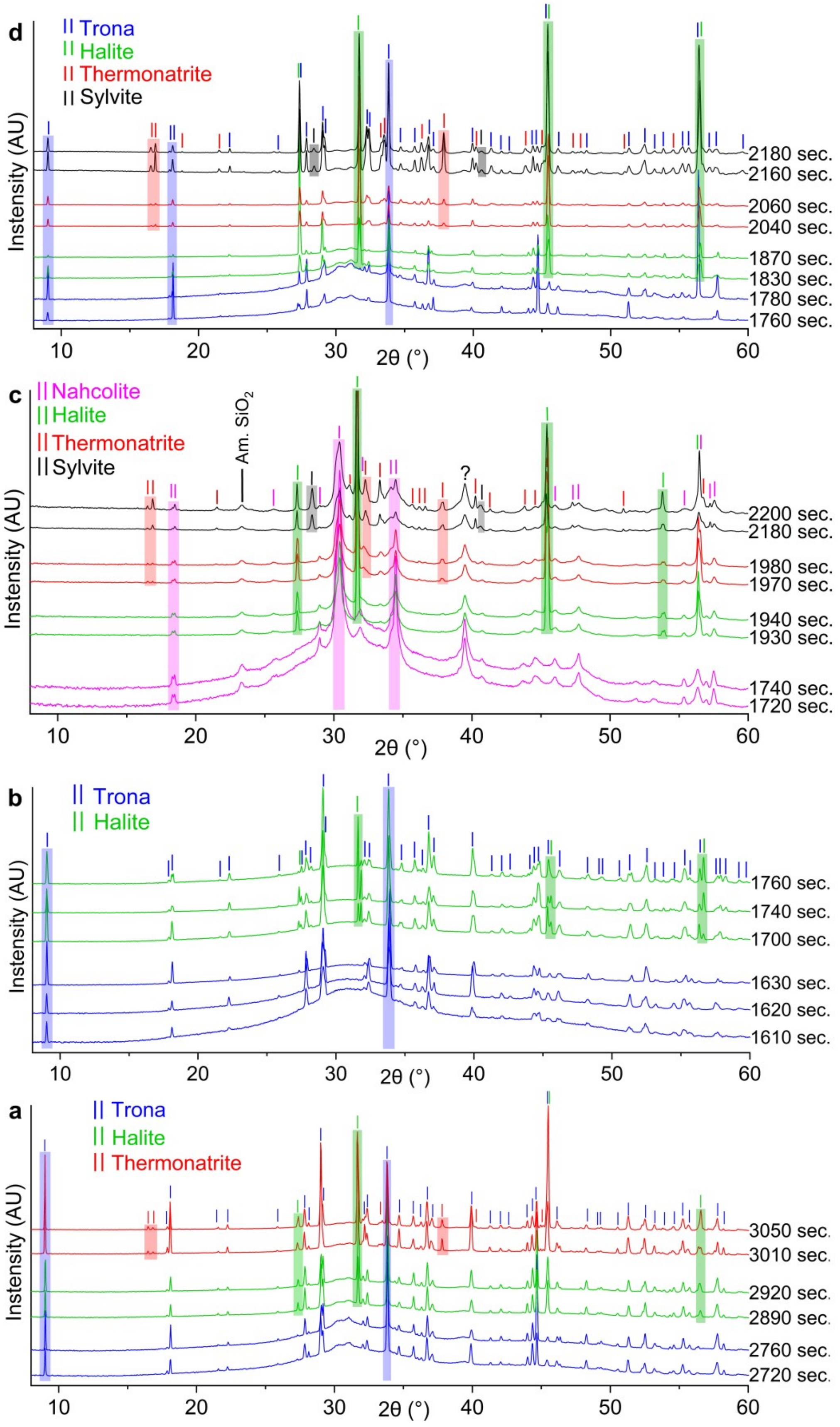

Figure 4. X-ray diffractograms collected during the evaporation of levitated droplets of (a) Lake Magadi brine (modified from Getenet et al. (2022)), (b) Lake Nasikie Engida brine, (c) Nasikie Engida hot spring and (d) Lake Natron brine. Note that the first diffractograms of the corresponding colour are taken a few seconds after the characteristic peaks of the given phase are clearly visible. The exact time when each mineral starts to precipitate is reported in the text.

3.4. Thermodynamic modelling of evaporation

Thermodynamic models are valuable not only for predicting the phase assemblages and the relative amount of the phases precipitated but also for the resulting hydrochemical evolution during evaporitic mineral precipitation. To test our experimental results, we have performed a set of geochemical modelling simulations using the PHREEQC code. Evaporation and mineral precipitation were simulated by computing successive equilibrium states separated by discrete, small removals of water from the solution. Figure 5 shows the output of these models in terms of the precipitation sequence of different minerals (left), and ionic concentration (right) versus concentration factor (CF; the ratio between the initial brine volume and the "current" volume at this point). The output of the model reproduces very well the experimental observations of major phases precipitation.

3.4.1. Sodium carbonates

The precipitation sequence of sodium carbonate phases shows two clearly distinct trends. In the sample from the Nasikie Engida hot spring, nahcolite is the first phase to precipitate (CF=3.4) and the dominant one during the evaporation process (Figure 5e). Precipitation of nahcolite stops after reaching a peak amount of 0.2 mol/kg at a CF=14, but the dissolution of nahcolite after this point is small and this phase stays stable upon subsequent evaporation. Nahcolite and trona are the only sodium carbonate phases precipitating during evaporation of Nasikie Engida hot spring waters. In contrast, the three samples from the different lakes produce, during evaporation, first a short, transient period of nahcolite precipitation starting at CFs of 6 (Lake Magadi), 1.9 (Nasikie Engida) and 7.2 (Lake Natron) (Figure 5a,c,g). Shortly after this event, trona starts to precipitate at CFs of 9.7 (Lake Magadi), 2.2 (Nasikie Engida) and 8.2 (Lake Natron), which ends the precipitation of nahcolite and initiates its dissolution, causing the quick disappearance of this phase. At CFs of 62.6 (Lake Magadi), 8.8 (Nasikie Engida) and 27.6 (Lake Natron), thermonatrite starts precipitating. Trona precipitation is already negligible at this stage during evaporation; after reaching CFs of 30 (Lake Magadi), 5 (Nasikie Engida), and 20 (Lake Natron), trona no longer precipitates leaving a constant amount of trona. The brine from Lake Nasikie Engida shows a sudden transformation of thermonatrite into natron at a CF of 17.8.

In summary, after complete dissolution, the hot spring sample produces a mix of nahcolite (roughly 65%) and trona (roughly 35%), while samples from lake waters produce a mix of trona and thermonatrite (in Lake Magadi and Lake Natron) or trona and natron (in Lake Nasikie Engida). Trona is always dominant in the lake samples with ratios depending on the initial chemistry. The ionic concentration follows the precipitation of the different phases. All ions increase linearly (in a logarithmic scale) with the concentration factor until a phase that contains that ion starts precipitating (Figure 5b,d,f,h). pH initially decreases linearly with evaporation until sodium carbonate phases start precipitating. From this point on, pH is controlled by the precipitation of these phases. CO_3^{2-} is the dominant C species in lake brines during evaporation while HCO_3^- is dominant at the beginning in the hot spring sample. The precipitation of nahcolite and trona depletes the concentration of HCO_3^- and increases the pH of the brine. The subsequent reduction of HCO_3^- concentration slows down the precipitation of trona and eventually undersaturate the brine with respect to nahcolite that starts dissolving. At higher pH values and with slow precipitation of trona, other carbonates, especially thermonatrite, start precipitating except in the case of the hot spring, where the HCO_3^- concentration is higher (although CO_3^{2-} is dominant for CFs higher than 9). This, along with the lower pH, hinders the precipitation of thermonatrite (Figure 5e-f). In all cases, Na^+ is, by far, the dominant cation during the whole evaporation/precipitation process although its concentration is reduced significantly by the end of the evaporation due to the precipitation of sodium carbonate minerals and halite.

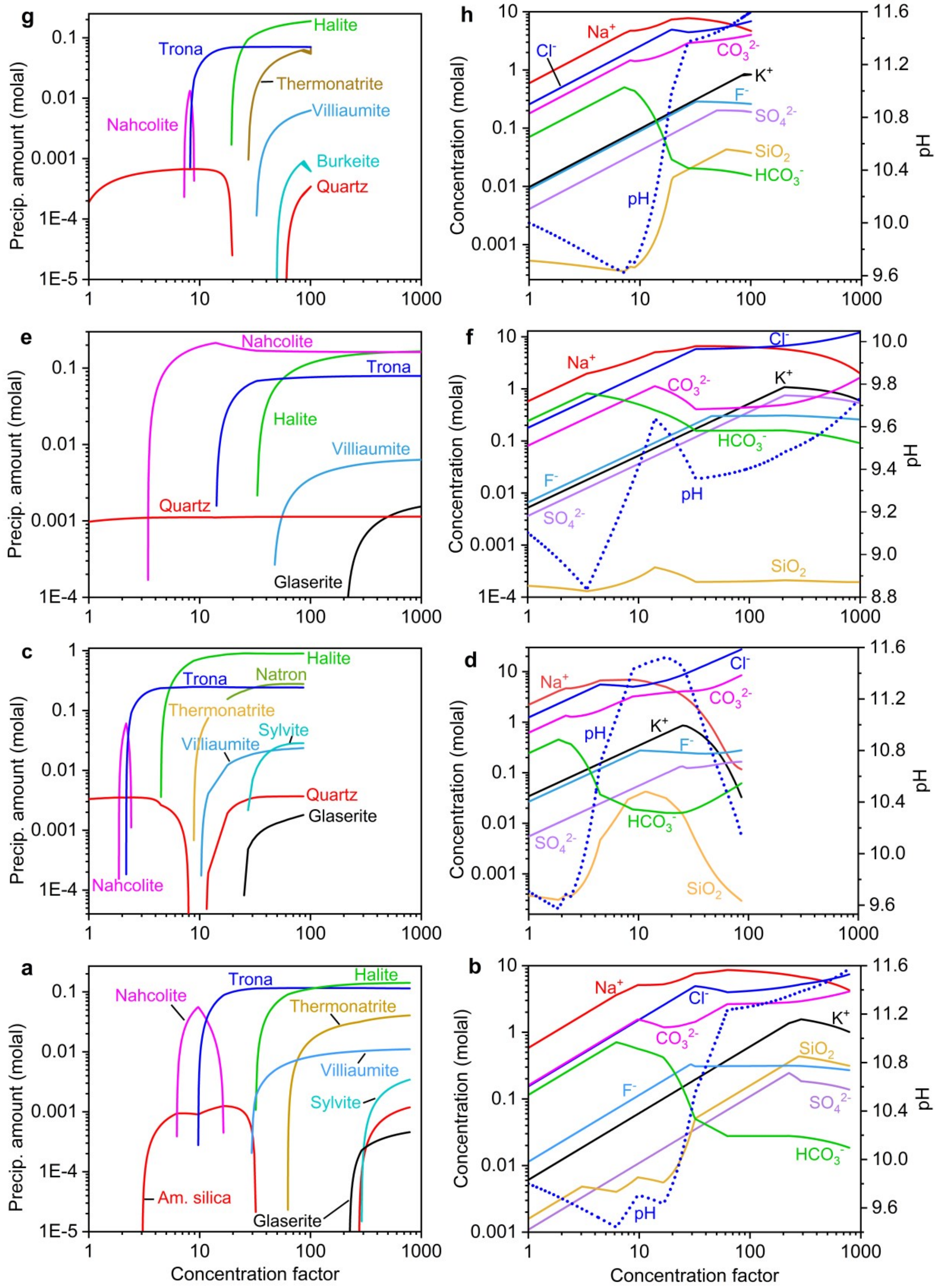

Figure 5. PHREEQC simulation of evaporation and mineral precipitation from Lake Magadi brine at 25 °C (a–b), Lake Nasikie Engida brine (c–d), Nasikie Engida hot spring (e–f), and Lake Natron brine (g–h) at 30 °C: the mineral precipitation sequence and the amount of precipitates (left panels) and hydrochemical evolution of the brines during mineral precipitation (right panels). Note: the simulation of Lake Magadi brine at 30 °C gave similar results to panels a and b except for quartz precipitation instead of amorphous silica (see Figure S1). The maximum CFs vary across samples depending on the point of divergence of the numerical equations during simulation.

3.4.2. Halides

Halite is the main chloride predicted to precipitate, and the only one in samples from Lake Natron and Nasikie Engida hot spring. Precipitation of halite starts at CFs of 31 (Lake Magadi), 4.5 (Nasikie Engida lake), 33.2 (Nasikie Engida hot spring) and 19.3 (Lake Natron) and lasts till the end of the evaporation (Figure 5a,c,e,g). The highest predicted amount of halite (895 mmol/kg) was obtained from Lake Nasikie Engida brine. In Lake Magadi and Nasikie Engida brines, sylvite starts precipitating at CF of 300 (Lake Magadi) and 27.3 (Lake Nasikie Engida), reaching a maximum amount of roughly 3% of halite.

Villiaumite is the only fluoride predicted to precipitate from these brines with high F^-, but low Ca^{2+}. Precipitation starts at a CF=30 (Lake Magadi), 10.3 (Nasikie Engida lake), 47.6 (Nasikie Engida hot spring) and 32.6 (Lake Natron). The concentration of F^- increases linearly until villiaumite starts precipitating and then stays almost constant at around 0.25 molal (Figure 5b,d,f,h).

3.4.3. Silica

Silica precipitation also shows a clearly different trend in lakes and hot spring waters. In lake samples, there are two silica precipitation periods during evaporation, one at the beginning, CF value 3-17 (Lake Magadi), 1-8 (Nasikie Engida) and 1-20 (Lake Natron), and the other to the end, close to complete evaporation, after CF=275 (Lake Magadi), 11.6 (Lake Nasikie Engida) and 60 (Lake Natron). In between, there is a period of silica dissolution related to a sudden increase in pH during evaporation (Figure 5a,c,g). In contrast, silica precipitates continuously during all the evaporation of the hot spring brine (Figure 5e). Silica species in solution closely follow the evolution of pH, controlled by the precipitation of sodium carbonate minerals, increasing when pH increases and decreasing elsewhere because higher pH values increase the solubility of SiO_2 (Krauskopf and Bird, 1979). The dependency on pH is even higher than the dependency on evaporation.

3.4.4. Other minerals

Owing to the low sulphate and calcium content of the brines, sulphate precipitation is scarce and restricted to very small amounts of glaserite ($(Na,K)_3Na(SO_4)_2$) and burkeite ($Na_6(CO_3)(SO_4)_2$). The second is predicted to precipitate only in samples from Lake Natron at high CF values (higher than 50) (Figure 5g) while glaserite is expected to precipitate from the remaining brines at CF of 205 (Lake Magadi), 25.2 (Lake Nasikie Engida) and 220 (Nasikie Engida hot spring) (Figure 5a,c,e). The final amount of these precipitates goes from 0.5 to 3 mmol/kg.

The initial lake brines were supersaturated with respect to fluorapatite, magnesite, and talc (see Figure S1,S3,S5,S7,S8). In the absence of phosphate ions, the lake brines were initially supersaturated with calcite instead of fluorapatite (Figure S3,S5,S8). Nasikie Engida hot spring brine was initially supersaturated with respect to calcite, followed by subsequent precipitation of a minor amount of dolomite, pirssonite, fluorite and borax after a CF of 1.4 (Figure S6a). Fluorapatite and pirssonite precipitation is coupled due to the competition for Ca^{2+}, the precipitation of one of them being triggered by the dissolution of the other (Figure S4a, S7a). Gaylussite is also predicted to precipitate as evaporation of Lake Magadi and Nasikie Engida waters advance (Figure S3, S5). Neither of these phases was observed in the experimental results possibly due to their minor contribution (less than 1 mmol/kg). The precipitation of these phases kept Ca^{2+} and Mg^{2+} species below 20 μmol/kg (Figure S1-S8b). Phosphate, boron, and bromine rise linearly with evaporation (Figure S1-S8b). Boron concentration rises with evaporation until a CF of 306 in Nasikie Engida hot spring and then is predicted to precipitate as borax, depleting the boron concentration (Figure S6).

4. Discussion

4.1. Major phases

The main variability found in our study corresponds to the different precipitation sequences from lake brines and hot springs, the later having a lower pH and CO_3/HCO_3 concentration ratio. From lake brines, the precipitation sequence trona > halite > thermonatrite is consistently predicted and observed (both in-situ and ex-situ). The brine from Lake Nasikie Engida also follows this sequence, but thermonatrite is only observed in the ex-situ experiments. Furthermore, the transformation of thermonatrite into natron is predicted by simulation, but natron was not observed in the experiments. The sequence for the hot-spring brine is clearly different. Its starts with the precipitation of nahcolite, which is the dominant phase during the whole evaporation process. Next, a smaller amount of trona is predicted to precipitate, and was observed in the ex-situ experiments, but not in the in-situ ones. Halite is the next phase predicted and observed. No further Na-carbonate phases are predicted to precipitate, but a small amount of thermonatrite was detected in both the in-situ and ex-situ diffraction experiments. This discrepancy could be due to a kinetic effect; the equilibrium calculation predicts the precipitation of trona after nahcolite, but in the relatively fast evaporation experiments we may reach the precipitation of halite before trona actually precipitates even if the brine is supersaturated with respect to trona. This lack of trona precipitation drives out the fast decrease in pH at CF=11, which finally produces the precipitation of thermonatrite. A similar effect of delayed nucleation is most likely the reason for not observing neither thermonatrite in the in-situ experiments of Lake Nasikie Engida nor the short, transient nahcolite precipitation at the beginning of evaporation.

Full evaporation sequences are not expected to be observed in the lakes, but only in efflorescent crusts. The composition of lake brines reflects the seasonal evolution of incoming waters upon recurring hydrologic cycles and the seasonal variation of outcoming water by evaporation. During rainy seasons, the water income increases and the evaporative outcome decreases, driving the brine composition closer to the hot-spring waters. The reverse process happens during dry seasons. Mixed saline and freshwater diatoms, dissolution surfaces and muddy layers found in the evaporite sequences of Lake Magadi evidence seasonal/periodic flooding of the paleolake brine with dilute water (Buatois et al., 2020; Owen et al., 2019), which apparently happens in the modern deposits. Depending on the amplitude and duration of these periods as well as on the lake volume, the resulting evaporitic sequence can show different combinations of sodium carbonate minerals, although the careful study is required for this because nahcolite may also form during diagenesis through bacterial CO_2 addition to the interstitial brines (Eugster, 1980). Lowenstein et al. (2017) suggested CO_2 input from the decay of organic matter in Green River lakes (USA), leading to precipitation of trona and nahcolite.

Lake Magadi, the southern section of Nasikie Engida and Natron are covered by mainly trona crust and efflorescent thermonatrite and halite (Dawson, 2008; Renaut et al., 2020), which corresponds to the "lake precipitation sequence". Trona has been forming for the last hundred thousand years, forming a 65 m sequence in Lake Magadi (Owen et al., 2019), but drill cores on Lake Magadi (uppermost 65 m of the core) contain nahcolite as well (Baker, 1958; Owen et al., 2019), indicating periods of higher spring inflow in the past. Nahcolite was observed in southern Nasikie Engida, but it is dominantly forming in the northern part of the lake where perennial saline hot springs fed the lake and where magmatic CO_2 emanate via deep faults (Lee et al., 2017, 2016; Renaut et al., 2020). The evaporite sediments of the northern Nasikie Engida are dominated by nahcolite (De Cort et al., 2019; Renaut et al., 2020). Nahcolite was more widespread in the past. Drill cores on the lakebed revealed that the uppermost 374 cm sediments are composed of intercalations of laminated mud with scattered nahcolite crystals and distinct beds of nahcolite resulting from abrupt precipitation at the sediment-water interface or within the water column (De Cort et al., 2019). Towards the centre of the southern Nasikie Engida, layers of up to 3 cm long nahcolite crystals were found beneath the trona beds (Renaut et al., 2020), indicating periods of higher HCO_3 concentration in the past. Hot spring brines are mostly contributed to the lake, but part of them end up gathered around hot spring vents and their outflow channel. There a full evaporation sequence from nahcolite to thermonatrite is expected. Renaut et al. (2020) reported efflorescent crusts of trona, nahcolite, thermonatrite and halite around spring vents on the northern shore of Nasikie Engida.

In Lake Natron we found the opposite situation, with no nahcolite in the evaporitic record. Here trona was reported both in ancient and modern evaporite deposits. The modern surface of Lake Natron is composed of 10-20 cm thick trona, thermonatrite and halite crust (Fritz et al., 1987; Manega and Bieda, 1987). Sediments collected on the lake bottom have shown alternating layers of black clay and trona (Hay, 1966). Trona moulds and casts were found in a horizon of mid-Pleistocene lacustrine sediments of Peninj beds on the west side of Lake Natron. These beds were deposited in a highly saline sodium-carbonate rich lake, which was analogous to the modern Lake Natron (Hay, 1968, 1966; Isaac, 1967, 1965). These differences are most likely due to the much larger water volume, which makes larger the volumetric ratio between evolved lake brines and the relatively fresh spring brines.

Thermonatrite and halite form only in the modern evaporite sequence of MNN lakes as efflorescent crusts and some local pools where there is intense evaporation (Eugster, 1980; Renaut et al., 2020). These minerals were not reported in the ancient deposits due to either the paleolake brines did not reach supersaturation or they precipitated but re-dissolved during an episodic freshening of the paleolake brines. In contrast to the natural lakes, a significant amount of thermonatrite and halite precipitate respectively at the bottom and on the surface of the artificial pans of TATA chemicals company, made for the commercial production of salt by harvesting the top layer of halite (Eugster, 1980, 1971). This fact is explained by our results: the company pumps the HCO_3-depleted lake brine (after trona precipitation) into shallow evaporation ponds where evaporation is very rapid and organic production of CO_2 is negligible. Fast evaporation in these ponds, as in our experiments, precipitate a large amount of thermonatrite and halite with some trona (Eugster, 1980, 1971).

In the natural settings, trona and nahcolite precipitate as thick layers whereas thermonatrite and halite were minor components. However, our experimental observations show that a considerable amount of thermonatrite and halite form in addition to trona. Moreover, the predicted final amount of halite was greater than that of trona and nahcolite in all cases (Figure 5 a,c,g). The difference in the relative amount of the minerals among the experiments and models and the natural setting arises from the difference in partial CO_2 pressure (pCO_2). It has been shown that excess CO_2 input is a crucial pre-condition for the formation of thick deposits of trona and nahcolite to replenish the depleting HCO_3^- and CO_3^{2-} ions (Bradley and Eugster, 1969; Earman et al., 2005; Eugster, 1980, 1966; Jagniecki et al., 2015; Lowenstein and Demicco, 2006). Owing to the fast evaporation and the slow dissolution rate of atmospheric CO_2 into the brines, the depletion of HCO_3^- ions limits nahcolite, trona and thermonatrite precipitates to an amount lower than that of halite in the simulations. Trona deposits with minor thermonatrite could have been possible in Lake Magadi and Natron due to biogenic CO_2 input, which otherwise would form a significant amount of thermonatrite in addition to trona (Eugster, 1980, 1971). The pCO_2 level required for nahcolite stability is higher than that required for trona precipitation, which could happen under current atmospheric conditions ($pCO_2 \approx -3.4$) (Bradley and Eugster, 1969; Eugster, 1980, 1966; Jagniecki et al., 2015; Lowenstein and Demicco, 2006). Our simulations show that precipitation and stability of nahcolite is possible only at $pCO_2 > -2.7$. In lake brines, the pCO_2 was higher than -2.7 only until the onset of nahcolite precipitation. Hence, the early precipitated nahcolite dissolves almost completely (Figure 5 a,c,g). Only the hot spring was able to form a detectable amount of nahcolite after complete evaporation (Figure 3c, Figure 4c). The transformation from nahcolite to trona seems evident from the poor crystallinity of nahcolite and the weak peaks of trona in ex-situ diffractions (see Figure 3c). Natron was predicted to form in southern Nasikie Engida brine (Figure 5c) but was not observed in our experiments nor reported in Nasikie Engida studies. Eugster (1980) observed natron crystallization in Lake Magadi during cool nights which convert to trona in the morning when the temperature increase.

Our results show a lower variety of precipitated phases in the X-ray diffraction experiments than in the simulations. This fact is clearly due to the diffraction detection limit. In addition to sodium carbonate phases and halite, the next more abundant mineral predicted by simulations is villiaumite, with amounts in the range of 6–20 mmol/kg of brine. Since the typical volumes of droplets are 25 μL for ex-situ experiments and 5 μL for the in-situ ones, the maximum expected amount of villiaumite would be around 0.021 μg for the ex-situ experiments and 0.0042 μg for the in-situ ones. These small amounts explain the lack of detection of minerals predicted to precipitate at levels close to or below 20 mmol/kg.

4.2. Phosphates and fluorides

Phosphate accumulates in soda lakes due to calcium sequestration by carbonate minerals precipitation, which results in a lack of apatite precipitation (Toner and Catling, 2020). This accumulation can reach levels relevant to the synthesis of prebiotic biomolecules. MNN samples were supersaturated with respect to fluorapatite since the beginning of evaporation. The amount of fluorapatite eventually precipitated is limited to very low amounts by the extremely low calcium content so this phase has not been reported in these lakes. As a result, phosphate concentration increases linearly with evaporation (Figure S2, S4, S7). Thermodynamic simulations, which don't include biological processes, seem to overestimate the actual phosphate concentration, which is actually lower after microbial phosphate consumption and deposition with organic matter (Toner and Catling, 2020). Based on the model predictions, there was no $Na(H_2PO_4)$ minerals precipitation until complete dryness. In prebiotic carbonate-rich lakes (soda ocean), the situation is expected to be closer to our simulations. There, the coupling of evaporative phosphate accumulation and the absence of living organisms, consuming phosphate has been postulated, rendering these water bodies as plausible settings for the origin of life (Toner and Catling, 2020). In a previous work, we have shown that phosphate minerals were absent during the precipitation of $CaCO_3$ mineral vesicles formed by pouring drops of concentrated $CaCl_2$ solution into Lake Magadi brines (Getenet et al., 2020).

Villiaumite (NaF) precipitation was predicted near the final stages of the evaporation process in all samples but wasn't detected in X-ray diffractions probably due to their small amount. However, micrographs of the precipitates revealed rounded cubic crystals of villiaumite between acicular trona crystals obtained from evaporation of Lake Magadi water droplets (Getenet et al., 2022). Villiaumite is a common constituent of the surface deposits of Lake Magadi brines (Baker, 1958; Eugster, 1980). Trona collected from Lake Magadi and Natron, which serve as cooking salt, is reported to also contain kogarkoite or villiaumite (Nielsen, 1999; Nielsen and Dahi, 2002). Fluorite is common in drill cores on the southern Lake Natron (Manega and Bieda, 1987). Fluorite in outcrops and core sediments of Lake Magadi and Natron form via redissolution of calcite and/or gaylussite (Eugster, 1980; Surdam and Eugster, 1976) whereas fluorite in efflorescent crusts of the Nasikie Engida hot springs forms due to mixing with relatively Ca-rich dilute water (Renaut et al., 2020).

4.3. Calcium phases

The precipitation of calcite, dolomite, gaylussite and pirssonite in small amounts (less than 0.5 mmol/kg of brine evaporated) is predicted by our thermodynamic models, but not observed in experiments due to the small amount. Records of these minerals in the stratigraphic sequence are due to the undersaturation–evaporation–supersaturation cycles that tend to concentrate minerals having lower solubility like these. In rainy seasons when freshwater replenishes the lake and supplies additional Ca and Mg, trona, thermonatrite and halite may dissolve, leaving behind the less soluble mineral phases. This cyclic process may have taken place on the lakeshore, accumulating alkaline earth carbonate deposits, and leading to the formation of Lake Magadi brines which are depleted in Ca and Mg and enriched in Na-Cl-CO_3-HCO_3 ions (Eugster, 1980, 1970; Jones et al., 1977). Calcite, dolomite, magnesite, gaylussite and pirssonite are present as efflorescent crusts and pisolites in modern sediments and drill cores of Lake Magadi and Nasikie Engida (Eugster, 1986, 1980; Renaut et al., 2020; Surdam and Eugster, 1976). Similarly, the core sediments on Lake Natron show interbed trona and mud with disseminated crystals of calcite, gaylussite and pirssonite. The mid-Pleistocene Peninj sediments contain horizons with dolomite and casts of trona, pirssonite and gaylussite, suggesting that these lacustrine beds were deposited in sodium-carbonate rich lake resembling modern Lake Natron (Hay, 1968, 1966; Isaac, 1967; Manega and Bieda, 1987). Calcite and aragonite precipitation was observed in hydrothermal springs along the shorelines of Lake Natron (Manega and Bieda, 1987). Alkaline earth carbonate and Na-Ca carbonate minerals may form due to the episodic interaction of Ca- and Mg-rich freshwater with Na-rich brine on the lake margins (Eugster, 1980; Owen et al., 2019; Renaut et al., 2020). Alternatively, gaylussite may form via the reaction of Na-rich brines with detrital calcite (Eugster and Hardie, 1978; Surdam and Eugster, 1976). Chert deposits of the Green Beds of Lake Magadi contain open crystal moulds, which are suggested to be calcite, gaylussite or pirssonite (Eugster, 1980, 1969; Owen et al., 2019). Eugster (1969) found calcite rosettes in magadiite horizons of the lower High Magadi beds and proposed that they are the source of the carbonate casts. Calcite in these casts may have formed by sodium leaching during the transformation of magadiite to chert (Eugster, 1969). These Ca-Na-carbonate crystals and casts in the chert deposits imply that the paleolake brines may have encountered dilute water with higher Ca concentration (Eugster, 1969, 1967; Schubel and Simonson, 1990). This has been supported by the presence of burrows in High Magadi beds (Buatois et al., 2020) and the finding of calcite, Mg-calcite, and dolomite in drill cores of Lake Magadi at depths below 102 m. The cores above 102 m lack calcite or Mg-calcite reflecting the increasing salinity and alkalinity of the paleolake (Owen et al., 2019). Dilution of the brines during events of high freshwater input lowers the phosphate and fluoride content below that of Ca input. In this case, there could be sufficient calcium remaining for calcite, gaylussite and pirssonite to precipitate after fluorite and apatite.

4.4. Silicates and minor phases

The thermodynamic model predicted an initial brine supersaturation with respect to quartz except for Lake Magadi brine which reaches supersaturation in amorphous silica after a CF of 3 (Figure 5). Silica concentration rises until the initial precipitation of amorphous silica or during the redissolution of amorphous silica and quartz. In Lake Magadi, as the pH rises above 9, silica remains concentrating at the same rate as chloride due to the polymerization of silicic acid (Eugster, 1980, 1970; Jones et al., 1977). The control of pH on the precipitation and dissolution of amorphous silica and quartz is clearly visible in the output of the thermodynamic models due to the pH-dependent silica solubility, which dramatically increases beyond pH 8.3 (Krauskopf and Bird, 1979). In our experiments, amorphous silica was detected only in hot spring samples (see Figure 4c). In Lake Magadi precipitates, it seems that there were visible precipitates without resulting in diffraction peaks, which may indicate the precipitation of amorphous silica (Getenet et al., 2022). In Natron and Nasikie Engida lake brines, neither amorphous silica nor quartz was detected experimentally. Silica gels precipitate in close proximity to the hot springs of Nasikie Engida and near the shorelines under active evaporation (Eugster and Jones, 1968; Renaut et al., 2020; Surdam and Eugster, 1976). A recent study of cherts from drill cores revealed the near-surface synsedimentary formation of Magadi cherts directly from siliceous gels (Leet et al., 2021).

Precipitation of sylvite, glaserite and burkeite is predicted by our model close to complete desiccation. Sylvite was detected by ex-situ X-ray diffractions in all samples and by in-situ diffractions from Lake Natron brine and Nasikie Engida hot spring. However, these phases were not reported in MNN lakes because freshwater supply to the lakes during the rainy season dilutes the brines before they reach supersaturation in sylvite, burkeite and glaserite. However, these minerals have been reported in other alkaline lakes of the East African rift valley, for example, in Lake Katwe (Uganda) (Kasedde et al., 2014; Nielsen, 1999). Borax was predicted to form from the hot spring brine, but not observed in the experiments nor the natural environment of MNN lakes. Borax was reported in other evaporite settings comparable to soda lakes such as the Pleistocene trona deposits of Searles Lake (California) (Smith and Stuiver, 1979).

In summary, the precipitation sequence Ca-Mg carbonates and siliceous sediments, Ca-Na carbonates, Na-carbonates, and halides show the gradual increase of paleolake salinity in geological time scale. Similar precipitation sequence in Lonar Lake (Central India) from calcite through gaylussite to trona evidenced progressive brine evaporation and the onset of drought events in the Holocene (Anoop et al., 2013). The observed and predicted mineral precipitation sequence of Lake Magadi is comparable with the precipitation sequence proposed for the Pleistocene/Holocene evaporites of Searles Lake (USA) (Olson and Lowenstein, 2021).

The impact of biological activity is not included in this model, which may be an additional cause of some differences. For example, bacterial sulphate reduction has been reported to effectively deplete the sulphate content in Lake Magadi (Eugster, 1980, 1970; Jones et al., 1977). Hence, the predicted SO_4^{2-} concentration seems higher than the actual ones, explaining the absence of sulphate-containing minerals. Pyrite, found in the drill cores from Lake Magadi (see Owen et al., (2019)), may indicate this sulphate reduction (García-Veigas et al., 2013). Phosphate concentration and precipitation, as discussed above, is also largely controlled by biological activity (Toner and Catling, 2020).

5. Conclusions

In this work, we have determined the mineral precipitation sequence from different rift valley soda lakes and hot spring tributaries to the lakes. Our experiments and calculations show that pH, and consequently CO_3^{2-}/HCO_3^- ratios are the major factors determining the precipitation order, relative quantity, and resulting mineral paragenesis in the East African Rift Valley hyperalkaline, hypersaline lakes and springs. The precipitation of major phases (Na carbonates/bicarbonates) increases the pH of the brines, so the hyperalkaline nature of the lake brines is due to this precipitation while the hypersaline character is due to the high solubility of Na-CO_3^{2-}/HCO_3^- salts.

The sequence of precipitating minerals depends on the starting composition of the brine. Nahcolite deposits form only from the northern segment of Nasikie Engida and its feeder hot springs due to the lower pH that makes available enough HCO_3^- for nahcolite precipitation. However, in southern Nasikie Engida, Magadi and Natron lakes, nahcolite precipitates only for a short, transient period during evaporation and re-dissolves when pH increases, leading to the precipitation of trona, which is the main precipitated phase. Thermonatrite and halite form dominantly in local pools and efflorescent crust subjected to intense and fast evaporation that limits the dissolution of atmospheric CO_2. In these conditions, the pH rises significantly after trona and nahcolite precipitation. Lake brines are rich in Si, which precipitates as silica during the first stages of evaporation at relatively lower pH values but gets redissolved due to the pH increase induced by the precipitation of trona or nahcolite. This redissolution does not happen in the less alkaline waters from the contributing springs. Silica accumulation in the stratigraphic sequence, therefore, requires either low evaporation levels or a relatively lower pH of the brines.

Full range evaporation experiments/simulations up to complete dryness, like the ones presented in this work, show the full landscape of plausible evaporitic scenarios, but only a fraction of this range of conditions is achieved by actual lake brines in perennial lakes. This range of conditions is controlled by the amplitude of seasonal dry/rainy periods, which modulate the balance between the dilution of brines by the inflow of relatively fresh water and the concentration of them by evaporation. The development of hydrochemical models predicting, within this window of conditions, the precipitation sequence, and the relative abundance of evaporitic minerals in the resulting paragenesis is expected to be a novel tool in explaining modern depositional settings and in reconstructing paleoclimatic and hydrochemical conditions during the deposition of ancient evaporite deposits. This approach could also be adapted to investigate the industrial crystallization of economic minerals from natural brines or even the conditions for the formation of evaporites in extraterrestrial environments using model and analogue brines.

Acknowledgements

The authors thank Isabel Guerra-Tschuschke for the support during the scanning electron microscopy analyses at the Centro de Instrumentación Científica (CIC) of the University of Granada, Francisca Espinosa, Raquel Fernandez-Penas, Cristóbal Verdugo-Escamilla and Joaquín Criado-Reyes for their technical assistance. We are grateful to Isabel Díaz (Instituto de Catálisis y Petroleoquímica-CSIC) for fluoride analyses. We also thank National Commission for Science Technology and Information, National Environmental Management Authority, and Kenya Wildlife Services for research permissions. Magadi Tata Chemicals Ltd. and National Museums of Kenya provide logistic help. The authors gratefully acknowledge Patricia Gitari, Lukas Sossoika, and Tara Barwa for their assistance in fieldwork.

Funding

This work was supported by the European Research Council (grant number 340863); the Spanish Ministerio de Economía y Competitividad via the project CGL2016-78971-P; Junta de Andalucía via the project P18-FR-5008 and the Spanish Ministerio de Ciencia, Innovacion y Universidades (grant number BES-2017-081105) (to M.G.).

Conflicts of Interest

The authors declare that they have no known competing financial interests or personal relationships that could have appeared to influence the work reported in this paper.

Appendix A. Supplementary Materials

Supplementary materials contain figures showing the Lake Magadi simulation results at 30 °C and minor ions and phases of the simulation of Lake Nasikie Engida, its feeder hot spring and Lake Natron brines.

References

Allen, D.J., Darling, W.G., Burgess, W.G., 1989. Geothermics and hydrogeology of the southern part of the Kenya Rift Valley with emphasis on the Magadi-Nakuru area (No. SD/89/001), British Geological Survey Research Report SD/89/1. British Geological Survey Research Report SD/89/1, 1–68.

Anoop, A., Prasad, S., Plessen, B., Basavaiah, N., Gaye, B., Naumann, R., Menzel, P., Weise, S., Brauer, A., 2013. Palaeoenvironmental implications of evaporative gaylussite crystals from Lonar Lake, central India. Journal of Quaternary Science 28, 349–359. https://doi.org/10.1002/jqs.2625

Baker, B.H., 1987. Outline of the petrology of the Kenya rift alkaline province. Geological Society, London, Special Publications 30, 293–311. https://doi.org/10.1144/GSL.SP.1987.030.01.14

Baker, B.H., 1986. Tectonics and volcanism of the southern Kenya Rift Valley and its influence on rift sedimentation. Geological Society, London, Special Publications 25, 45–57. https://doi.org/10.1144/GSL.SP.1986.025.01.05

Baker, B.H., 1963. Geology of the Area south of Magadi (No. 61). Geol. Surv. Kenya, Nairobi, Kenya, Rep. 61. pp 27.

Baker, B.H., 1958. Geology of the Magadi Area (No. 42). Geol. Surv. Kenya, Nairobi, Kenya, Rep. 42. pp 81.

Baker, B.H., Mohr, P.A., Williams, L. a. J., 1972. Geology of the Eastern Rift System of Africa. https://doi.org/10.1130/SPE136-p1

Behr, H.-J., 2002. Magadiite and Magadi Chert: A Critical Analysis of the Silica Sediments in the Lake Magadi Basin, Kenya, in: Renaut, R.W., Ashley, G.M. (Eds.), Sedimentation in Continental Rifts. SEPM Society for Sedimentary Geology, pp. 257–273. https://doi.org/10.2110/pec.02.73.0257

Behr, H.-J., Röhricht, C., 2000. Record of seismotectonic events in siliceous cyanobacterial sediments (Magadi cherts), Lake Magadi, Kenya. Int Journ Earth Sciences 89, 268–283. https://doi.org/10.1007/s005319900070

Bell, K., Dawson, J.B., Farquhar, R.M., 1973. Strontium Isotope Studies of Alkalic Rocks: The Active Carbonatite Volcano Oldoinyo Lengai, Tanzania. GSA Bulletin 84, 1019–1030. https://doi.org/10.1130/0016-7606(1973)84<1019:SISOAR>2.0.CO;2

Benecke, G., Wagermaier, W., Li, C., Schwartzkopf, M., Flucke, G., Hoerth, R., Zizak, I., Burghammer, M., Metwalli, E., Müller-Buschbaum, P., Trebbin, M., Förster, S., Paris, O., Roth, S.V., Fratzl, P., 2014. A customizable software for fast reduction and analysis of large X-ray scattering data sets: applications of the new DPDAK package to small-angle X-ray scattering and grazing-incidence small-angle X-ray scattering. J Appl Cryst 47, 1797–1803. https://doi.org/10.1107/S1600576714019773

Blanc, Ph., Lassin, A., Piantone, P., Azaroual, M., Jacquemet, N., Fabbri, A., Gaucher, E.C., 2012. Thermoddem: A geochemical database focused on low temperature water/rock interactions and waste materials. Applied Geochemistry 27, 2107–2116. https://doi.org/10.1016/j.apgeochem.2012.06.002

Bradley, W.H., Eugster, H.P., 1969. Geochemistry and paleolimnology of the trona deposits and associated authigenic minerals of the Green River Formation of Wyoming (USGS Numbered Series No. Professional Paper 496-B). U.S. Geological Survey.

Buatois, L.A., Renaut, R.W., Owen, R.B., Behrensmeyer, A.K., Scott, J.J., 2020. Animal bioturbation preserved in Pleistocene magadiite at Lake Magadi, Kenya Rift Valley, and its implications for the depositional environment of bedded magadiite. Sci Rep 10, 6794. https://doi.org/10.1038/s41598-020-63505-7

Cabestrero, Ó., Sanz-Montero, M.E., 2018. Brine evolution in two inland evaporative environments: influence of microbial mats in mineral precipitation. J Paleolimnol 59, 139–157. https://doi.org/10.1007/s10933-016-9908-0

Carrozzo, F.G., Sanctis, M.C.D., Raponi, A., Ammannito, E., Castillo-Rogez, J., Ehlmann, B.L., Marchi, S., Stein, N., Ciarniello, M., Tosi, F., Capaccioni, F., Capria, M.T., Fonte, S., Formisano, M., Frigeri, A., Giardino, M., Longobardo, A., Magni, G., Palomba, E., Zambon, F., Raymond, C.A., Russell, C.T., 2018. Nature, formation, and distribution of carbonates on Ceres. Science Advances 4, e1701645. https://doi.org/10.1126/sciadv.1701645

Dawson, J.B., 2008. The Gregory rift valley and Neogene-recent volcanoes of northern Tanzania, Geological Society of London, Memoirs, 33. Geological Society, London, Memoirs, 33, 102p.

Dawson, J.B., 1964. Carbonatitic volcanic ashes in Northern Tanganyika. Bull Volcanol 27, 81–91. https://doi.org/10.1007/BF02597513

Dawson, J.B., 1962. The geology of Oldoinyo Lengai. Bull Volcanol 24, 349–387. https://doi.org/10.1007/BF02599356

De Cort, G., Mees, F., Renaut, R.W., Sinnesael, M., Van der Meeren, T., Goderis, S., Keppens, E., Mbuthia, A., Verschuren, D., 2019. Late-Holocene sedimentation and sodium carbonate deposition in hypersaline, alkaline Nasikie Engida, southern Kenya Rift Valley. J Paleolimnol 62, 279–300. https://doi.org/10.1007/s10933-019-00092-2

De Sanctis, M.C., Raponi, A., Ammannito, E., Ciarniello, M., Toplis, M.J., McSween, H.Y., Castillo-Rogez, J.C., Ehlmann, B.L., Carrozzo, F.G., Marchi, S., Tosi, F., Zambon, F., Capaccioni, F., Capria, M.T., Fonte, S., Formisano, M., Frigeri, A., Giardino, M., Longobardo, A., Magni, G., Palomba, E., McFadden, L.A., Pieters, C.M., Jaumann, R., Schenk, P., Mugnuolo, R., Raymond, C.A., Russell, C.T., 2016. Bright carbonate deposits as evidence of aqueous alteration on (1) Ceres. Nature 536, 54–57. https://doi.org/10.1038/nature18290

Demicco, R.V., Lowenstein, T.K., 2019. When "evaporites" are not formed by evaporation: The role of temperature and pCO2 on saline deposits of the Eocene Green River Formation, Colorado, USA. GSA Bulletin 132, 1365–1380. https://doi.org/10.1130/B35303.1

Deocampo, D.M., Renaut, R.W., 2016. Geochemistry of African Soda Lakes, in: Schagerl, M. (Ed.), Soda Lakes of East Africa. Springer International Publishing, Cham, pp. 77–93. https://doi.org/10.1007/978-3-319-28622-8_4

Earman, S., Phillips, F.M., McPherson, B.J.O.L., 2005. The role of "excess" CO2 in the formation of trona deposits. Applied Geochemistry 20, 2217–2232. https://doi.org/10.1016/j.apgeochem.2005.08.007

Eugster, H.P., 1986. Lake Magadi, Kenya: a model for rift valley hydrochemistry and sedimentation? Geological Society, London, Special Publications 25, 177–189. https://doi.org/10.1144/GSL.SP.1986.025.01.15

Eugster, H.P., 1980. Lake Magadi, Kenya, and Its Precursors, in: Nissenbaum, A. (Ed.), Developments in Sedimentology, Hypersaline Brines and Evaporitic Environments. Elsevier, pp. 195–232. https://doi.org/10.1016/S0070-4571(08)70239-5

Eugster, H.P., 1971. Origin and deposition of trona. Rocky Mountain Geology 10, 49–55.

Eugster, H.P., 1970. Chemistry and Origin of the Brines of Lake Magadi, Kenya. Mineral. Soc. Amer. Spec. Pap. 3, 213–235.

Eugster, H.P., 1969. Inorganic bedded cherts from the Magadi area, Kenya. Contr. Mineral. and Petrol. 22, 1–31. https://doi.org/10.1007/BF00388011

Eugster, H.P., 1967. Hydrous Sodium Silicates from Lake Magadi, Kenya: Precursors of Bedded Chert. Science 157, 1177–1180. https://doi.org/10.1126/science.157.3793.1177

Eugster, H.P., 1966. Sodium carbonate-bicarbonate minerals as indicators of Pco2. Journal of Geophysical Research (1896-1977) 71, 3369–3377. https://doi.org/10.1029/JZ071i014p03369

Eugster, H.P., Hardie, L.A., 1978. Saline Lakes, in: Lerman, A. (Ed.), Lakes: Chemistry, Geology, Physics. Springer, New York, NY, pp. 237–293. https://doi.org/10.1007/978-1-4757-1152-3_8

Eugster, H.P., Jones, B.F., 1968. Gels Composed of Sodium-Aluminum Silicate, Lake Magadi, Kenya. Science 161, 160–163.

Fritz, B., Zins-Pawlas, M.-P., Gueddari, M., 1987. Geochemistry of silica-rich brines from Lake Natron (Tanzania). Géochimie des saumures riches en silice du lac Natron (Tanzanie). Sciences Géologiques, bulletins et mémoires 40, 97–110. https://doi.org/10.3406/sgeol.1987.1753

García-Ruiz, J.M., Nakouzi, E., Kotopoulou, E., Tamborrino, L., Steinbock, O., 2017. Biomimetic mineral self-organization from silica-rich spring waters. Science Advances 3, e1602285. https://doi.org/10.1126/sciadv.1602285

García-Ruiz, J.M., van Zuilen, M.A., Bach, W., 2020. Mineral self-organization on a lifeless planet. Physics of Life Reviews 34–35, 62–82. https://doi.org/10.1016/j.plrev.2020.01.001

García-Veigas, J., Gündoğan, İ., Helvacı, C., Prats, E., 2013. A genetic model for Na-carbonate mineral precipitation in the Miocene Beypazarı trona deposit, Ankara province, Turkey. Sedimentary Geology 294, 315–327. https://doi.org/10.1016/j.sedgeo.2013.06.011

Getenet, M., García-Ruiz, J.M., Otálora, F., Emmerling, F., Al-Sabbagh, D., Verdugo-Escamilla, C., 2022. A Comprehensive Methodology for Monitoring Evaporitic

Mineral Precipitation and Hydrochemical Evolution of Saline Lakes: The Case of Lake Magadi Soda Brine (East African Rift Valley, Kenya). Crystal Growth & Design 22, 2307–2317. https://doi.org/10.1021/acs.cgd.1c01391

Getenet, M., García-Ruiz, J.M., Verdugo-Escamilla, C., Guerra-Tschuschke, I., 2020. Mineral Vesicles and Chemical Gardens from Carbonate-Rich Alkaline Brines of Lake Magadi, Kenya. Crystals 10, 467. https://doi.org/10.3390/cryst10060467

Giffaut, E., Grivé, M., Blanc, Ph., Vieillard, Ph., Colàs, E., Gailhanou, H., Gaboreau, S., Marty, N., Madé, B., Duro, L., 2014. Andra thermodynamic database for performance assessment: ThermoChimie. Applied Geochemistry, Geochemistry for Risk Assessment: Hazardous waste in the Geosphere 49, 225–236. https://doi.org/10.1016/j.apgeochem.2014.05.007

Glein, C.R., Baross, J.A., Waite, J.H., 2015. The pH of Enceladus' ocean. Geochimica et Cosmochimica Acta 162, 202–219. https://doi.org/10.1016/j.gca.2015.04.017

Hay, R.L., 1968. Chert and its sodium-silicate precursors in sodium-carbonate lakes of East Africa. Contr. Mineral. and Petrol. 17, 255–274. https://doi.org/10.1007/BF00380740

Hay, R.L., 1966. Zeolites and Zeolitic Reactions in Sedimentary Rocks, in: Geological Society of America Special Papers. Geological Society of America, pp. 1–122. https://doi.org/10.1130/SPE85-p1

Hillaire-Marcel, C., Carro, O., Casanova, J., 1986. 14C and Th/U Dating of Pleistocene and Holocene Stromatolites from East African Paleolakes. Quaternary Research 25, 312–239. https://doi.org/10.1016/0033-5894(86)90004-9

Isaac, G.L., 1967. The stratigraphy of the Peninj group-early middle Pleistocene formations west of Lake Natron, Tanzania. Background to evolution in Africa 229–257.

Isaac, G.L., 1965. The stratigraphy of the Peninj Beds and the provenance of the Natron Australopithecine mandible. Quaternaria 7, 101–130.

Jagniecki, E.A., Lowenstein, T.K., 2015. Evaporites of the Green River Formation, Bridger and Piceance Creek Basins: Deposition, Diagenesis, Paleobrine Chemistry, and Eocene Atmospheric CO2, in: Smith, M.E., Carroll, A.R. (Eds.), Stratigraphy and Paleolimnology of the Green River Formation, Western USA, Syntheses in Limnogeology. Springer Netherlands, Dordrecht, pp. 277–312. https://doi.org/10.1007/978-94-017-9906-5_11

Jagniecki, E.A., Lowenstein, T.K., Jenkins, D.M., Demicco, R.V., 2015. Eocene atmospheric CO2 from the nahcolite proxy. Geology 43, 1075–1078. https://doi.org/10.1130/G36886.1

Jones, B.F., Eugster, H.P., Rettig, S.L., 1977. Hydrochemistry of the Lake Magadi basin, Kenya. Geochimica et Cosmochimica Acta 41, 53–72. https://doi.org/10.1016/0016-7037(77)90186-7

Kasedde, H., Kirabira, J.B., Bäbler, M.U., Tilliander, A., Jonsson, S., 2014. Characterization of brines and evaporites of Lake Katwe, Uganda. Journal of African Earth Sciences 91, 55–65. https://doi.org/10.1016/j.jafrearsci.2013.12.004

Kempe, S., Kazmierczak, J., 2004. Biogenesis and Early Life on Earth and Europa: Favored by an Alkaline Ocean? Astrobiology 2, 123–130. https://doi.org/10.1089/153110702753621394

Kolpakova, M.N., Gaskova, O.L., 2017. Major ions behaviour during evaporation of different saline type water of Western Mongolian lakes (geochemical modelling). Hydrology Research 49, 163–176. https://doi.org/10.2166/nh.2017.148

Kotopoulou, E., Delgado Huertas, A., Garcia-Ruiz, J.M., Dominguez-Vera, J.M., Lopez-Garcia, J.M., Guerra-Tschuschke, I., Rull, F., 2019. A Polyextreme Hydrothermal System Controlled by Iron: The Case of Dallol at the Afar Triangle. ACS Earth Space Chem. 3, 90–99. https://doi.org/10.1021/acsearthspacechem.8b00141

Krauskopf, K.B., Bird, D.K., 1979. Introduction to Geochemistry, 2nd edition. ed, International Series in the Earth and Planetary Sciences. McGraw-Hill.

Lee, H., Fischer, T.P., Muirhead, J.D., Ebinger, C.J., Kattenhorn, S.A., Sharp, Z.D., Kianji, G., Takahata, N., Sano, Y., 2017. Incipient rifting accompanied by the release of subcontinental lithospheric mantle volatiles in the Magadi and Natron basin, East Africa. Journal of Volcanology and Geothermal Research, Volcano-Hydrothermal Systems 346, 118–133. https://doi.org/10.1016/j.jvolgeores.2017.03.017

Lee, H., Muirhead, J.D., Fischer, T.P., Ebinger, C.J., Kattenhorn, S.A., Sharp, Z.D., Kianji, G., 2016. Massive and prolonged deep carbon emissions associated with continental rifting. Nature Geosci 9, 145–149. https://doi.org/10.1038/ngeo2622

Leet, K., Lowenstein, T.K., Renaut, R.W., Owen, R.B., Cohen, A., 2021. Labyrinth patterns in Magadi (Kenya) cherts: Evidence for early formation from siliceous gels. Geology. https://doi.org/10.1130/G48771.1

Lowenstein, T.K., Demicco, R.V., 2006. Elevated Eocene Atmospheric CO2 and Its Subsequent Decline. Science 313, 1928–1928. https://doi.org/10.1126/science.1129555

Lowenstein, T.K., Dolginko, L.A.C., García-Veigas, J., 2016. Influence of magmatic-hydrothermal activity on brine evolution in closed basins: Searles Lake, California. GSA Bulletin 128, 1555–1568. https://doi.org/10.1130/B31398.1

Lowenstein, T.K., Jagniecki, E.A., Carroll, A.R., Smith, M.E., Renaut, R.W., Owen, R.B., 2017. The Green River salt mystery: What was the source of the hyperalkaline lake waters? Earth-Science Reviews 173, 295–306. https://doi.org/10.1016/j.earscirev.2017.07.014

Ma, L., Lowenstein, T.K., Russell, J.M., 2011. A Brine Evolution Model and Mineralogy of Chemical Sediments in a Volcanic Crater, Lake Kitagata, Uganda. Aquat Geochem 17, 129–140. https://doi.org/10.1007/s10498-010-9108-x

Manega, P., Bieda, S., 1987. Modern sediments of Lake Natron, Tanzania. Sédimentation récente du lac Natron, Tanzanie. Sciences Géologiques, bulletins et mémoires 40, 83–95. https://doi.org/10.3406/sgeol.1987.1752

Mattia Bizzarri, B., Botta, L., Pérez-Valverde, M.I., Saladino, R., Di Mauro, E., García-Ruiz, J.M., 2018. Silica Metal Oxide Vesicles Catalyze Comprehensive Prebiotic Chemistry. Chemistry – A European Journal 24, 8126–8132. https://doi.org/10.1002/chem.201706162

McCord, T.B., Hansen, G.B., Fanale, F.P., Carlson, R.W., Matson, D.L., Johnson, T.V., Smythe, W.D., Crowley, J.K., Martin, P.D., Ocampo, A., Hibbitts, C.A., Granahan, J.C., Team, the N., 1998. Salts on Europa's Surface Detected by Galileo's Near Infrared Mapping Spectrometer. Science 280, 1242–1245. https://doi.org/10.1126/science.280.5367.1242

McNulty, E., 2017. Lake Magadi and the Soda Lake Cycle: A Study of the Modern Sodium Carbonates and of Late Pleistocene and Holocene Lacustrine Core Sediments (Graduate Dissertations and Theses. 25). Binghamton University, New York, USA.

Nielsen, J.M., 1999. East African magadi (trona): fluoride concentration and mineralogical composition. Journal of African Earth Sciences, Geology and Mineral Resources East Africa 29, 423–428. https://doi.org/10.1016/S0899-5362(99)00107-4

Nielsen, J.M., Dahi, E., 2002. Fluoride exposure of East African consumers using alkaline salt deposits known as magadi (trona) as a food preparation aid. Food Additives and Contaminants 19, 709–714. https://doi.org/10.1080/02652030210145900

Olson, K.J., Lowenstein, T.K., 2021. Searles Lake evaporite sequences: Indicators of late Pleistocene/Holocene lake temperatures, brine evolution, and pCO2. GSA Bulletin. https://doi.org/10.1130/B35857.1

Otálora, F., Criado-Reyes, J., Baselga, M., Canals, A., Verdugo-Escamilla, C., García Ruiz, J.M., 2020. Hydrochemical and Mineralogical Evolution through Evaporitic Processes in Salar de Llamara Brines (Atacama, Chile). ACS Earth Space Chem. 4, 882–896. https://doi.org/10.1021/acsearthspacechem.0c00085

Owen, R.B., Renaut, R.W., Muiruri, V.M., Rabideaux, N.M., Lowenstein, T.K., McNulty, E.P., Leet, K., Deocampo, D., Luo, S., Deino, A.L., Cohen, A., Sier, M.J., Campisano, C., Shen, C.-C., Billingsley, A., Mbuthia, A., Stockhecke, M., 2019. Quaternary history of the Lake Magadi Basin, southern Kenya Rift: Tectonic and climatic controls. Palaeogeography, Palaeoclimatology, Palaeoecology 518, 97–118. https://doi.org/10.1016/j.palaeo.2019.01.017

Paris, O., Li, C., Siegel, S., Weseloh, G., Emmerling, F., Riesemeier, H., Erko, A., Fratzl, P., 2007. A new experimental station for simultaneous X-ray microbeam scanning for small- and wide-angle scattering and fluorescence at BESSY II. J Appl Cryst 40, s466–s470. https://doi.org/10.1107/S0021889806045444

Parkhurst, D.L., Appelo, C.A.J., 2013. Description of input and examples for PHREEQC version 3: a computer program for speciation, batch-reaction, one-dimensional transport, and inverse geochemical calculations (Report No. 6-A43), Techniques and Methods. Reston, VA. https://doi.org/10.3133/tm6A43

Pecoraino, G., D’Alessandro, W., Inguaggiato, S., 2015. The Other Side of the Coin: Geochemistry of Alkaline Lakes in Volcanic Areas, in: Rouwet, D., Christenson, B., Tassi, F., Vandemeulebrouck, J. (Eds.), Volcanic Lakes, Advances in Volcanology. Springer, Berlin, Heidelberg, pp. 219–237. https://doi.org/10.1007/978-3-642-36833-2_9

Reinhardt, M., Goetz, W., Duda, J.-P., Heim, C., Reitner, J., Thiel, V., 2019. Organic signatures in Pleistocene cherts from Lake Magadi (Kenya) – implications for early Earth hydrothermal deposits. Biogeosciences 16, 2443–2465. https://doi.org/10.5194/bg-16-2443-2019

Renaut, R.W., Owen, R.B., Lowenstein, T.K., Cort, G.D., Mcnulty, E., Scott, J.J., Mbuthia, A., 2020. The role of hydrothermal fluids in sedimentation in saline alkaline lakes: Evidence from Nasikie Engida, Kenya Rift Valley. Sedimentology 68, 108–134. https://doi.org/10.1111/sed.12778

Rull, F., Guerrero, J., Venegas, G., Gázquez, F., Medina, J., 2014. Spectroscopic Raman study of sulphate precipitation sequence in Rio Tinto mining district (SW Spain). Environ Sci Pollut Res 21, 6783–6792. https://doi.org/10.1007/s11356-013-1927-z

Saladino, R., Botta, G., Bizzarri, B.M., Di Mauro, E., Garcia Ruiz, J.M., 2016. A Global Scale Scenario for Prebiotic Chemistry: Silica-Based Self-Assembled Mineral Structures and Formamide. Biochemistry 55, 2806–2811. https://doi.org/10.1021/acs.biochem.6b00255

Schagerl, M., Renaut, R.W., 2016. Dipping into the Soda Lakes of East Africa, in: Schagerl, M. (Ed.), Soda Lakes of East Africa. Springer International Publishing, Cham, pp. 3–24. https://doi.org/10.1007/978-3-319-28622-8_1

Schubel, K.A., Simonson, B.M., 1990. Petrography and diagenesis of cherts from Lake Magadi, Kenya. Journal of Sedimentary Research 60, 761–776. https://doi.org/10.1306/212F9269-2B24-11D7-8648000102C1865D

Smith, G.I., Stuiver, M., 1979. Subsurface stratigraphy and geochemistry of late Quaternary evaporites, Searles Lake, California, with a section on radiocarbon ages of stratigraphic units (Report No. 1043), Professional Paper. U.S. Geological Survey Professional Paper 1043, 130 p. https://doi.org/10.3133/pp1043

Smith, M.E., Carroll, A.R., 2015. Introduction to the Green River Formation, in: Smith, M.E., Carroll, A.R. (Eds.), Stratigraphy and Paleolimnology of the Green River Formation, Western USA, Syntheses in Limnogeology. Springer Netherlands, Dordrecht, pp. 1–12. https://doi.org/10.1007/978-94-017-9906-5_1

Surdam, R.C., Eugster, H.P., 1976. Mineral reactions in the sedimentary deposits of the Lake Magadi region, Kenya. GSA Bulletin 87, 1739–1752. https://doi.org/10.1130/0016-7606(1976)87<1739:MRITSD>2.0.CO;2

Toner, J.D., Catling, D.C., 2020. A carbonate-rich lake solution to the phosphate problem of the origin of life. PNAS 117, 883–888. https://doi.org/10.1073/pnas.1916109117

Wolf, S.E., Leiterer, J., Kappl, M., Emmerling, F., Tremel, W., 2008. Early Homogenous Amorphous Precursor Stages of Calcium Carbonate and Subsequent Crystal Growth in Levitated Droplets. J. Am. Chem. Soc. 130, 12342–12347. https://doi.org/10.1021/ja800984y

Supplementary Materials

Mineral Precipitation and Hydrochemical Evolution Through Evaporitic Processes in Soda Brines (East African Rift Valley)

Melese Getenet, Fermín Otálora, Franziska Emmerling, Dominik Al-Sabbagh, Juan Manuel García-Ruiz

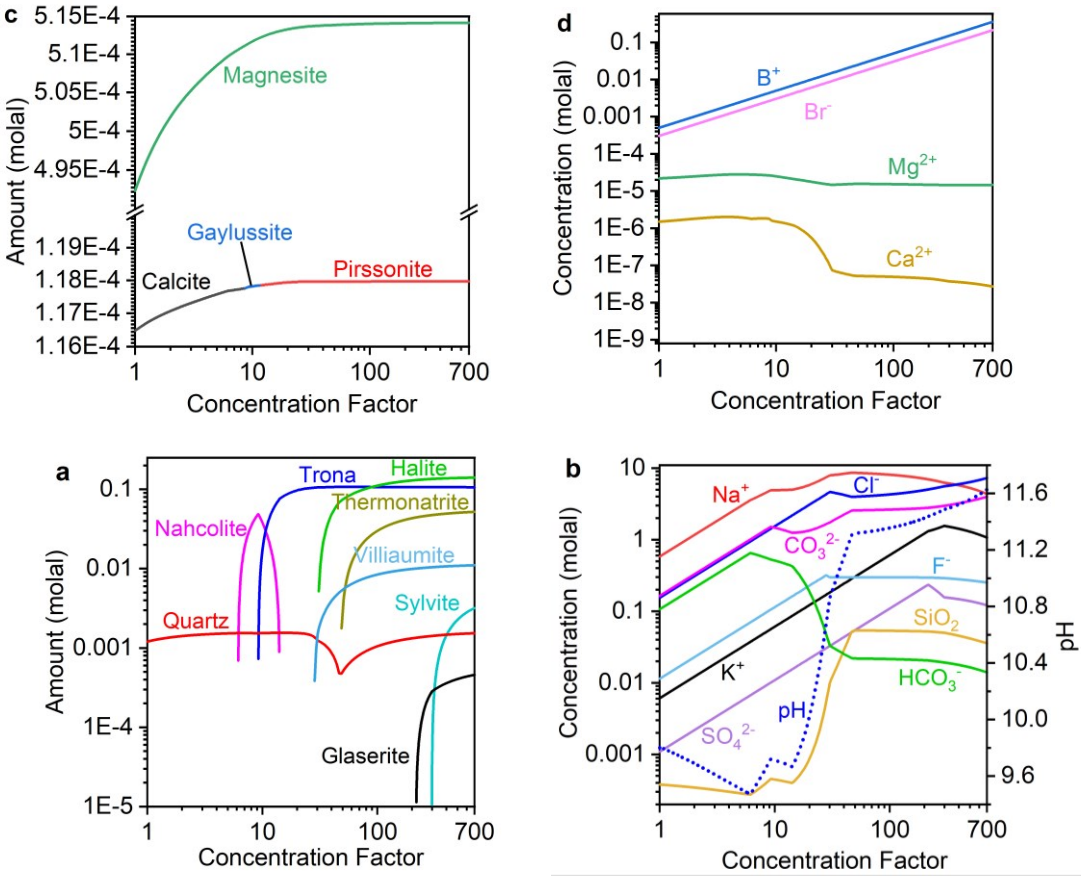

Figure S1. PHREEQC simulation of evaporation and mineral precipitation from Lake Magadi brine at 30 °C. (a,c) the mineral precipitation sequence of phases and the amount precipitated; (b,d) evolution of ionic concentrations

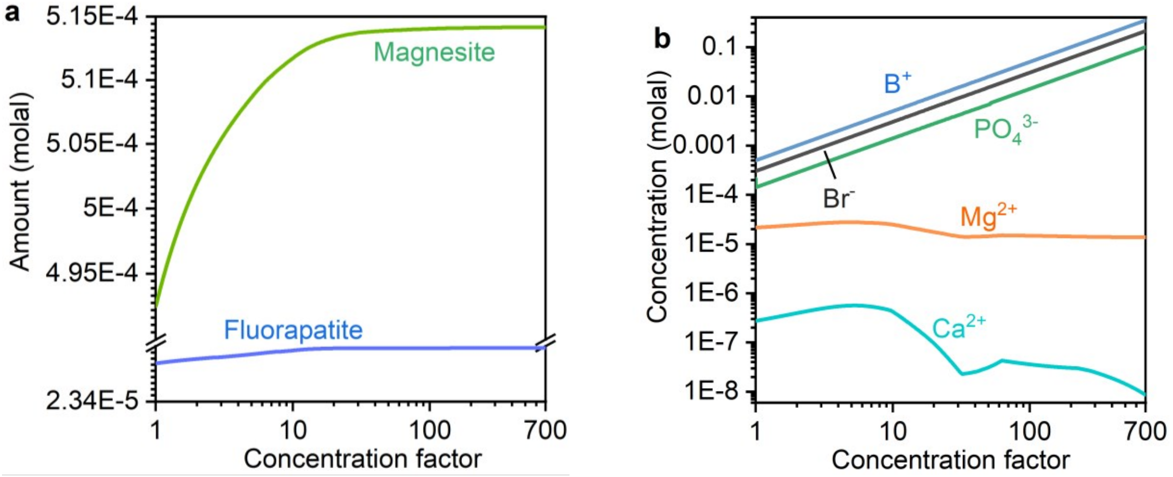

Figure S2. PHREEQC simulation of evaporation and mineral precipitation from Lake Magadi brine at 25 °C in the presence of phosphate ion. (a) the mineral precipitation sequence of minor phases and the amount precipitated; (b) evolution of minor ions concentrations.

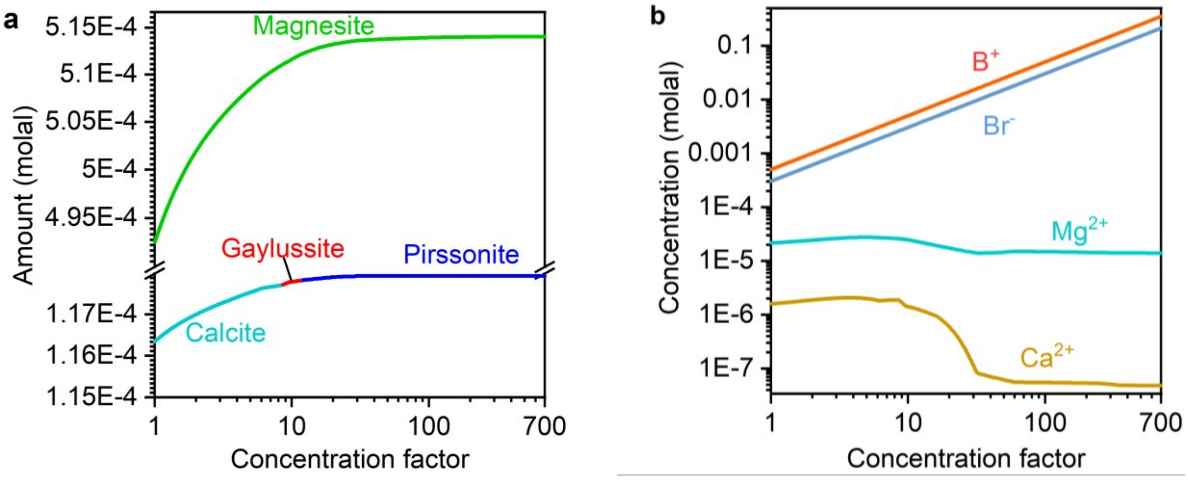

Figure S3. PHREEQC simulation of evaporation and mineral precipitation from Lake Magadi brine at 25 °C in the absence of phosphate ion. (a) the mineral precipitation sequence of minor phases and the amount precipitated; (b) evolution of minor ions concentrations.

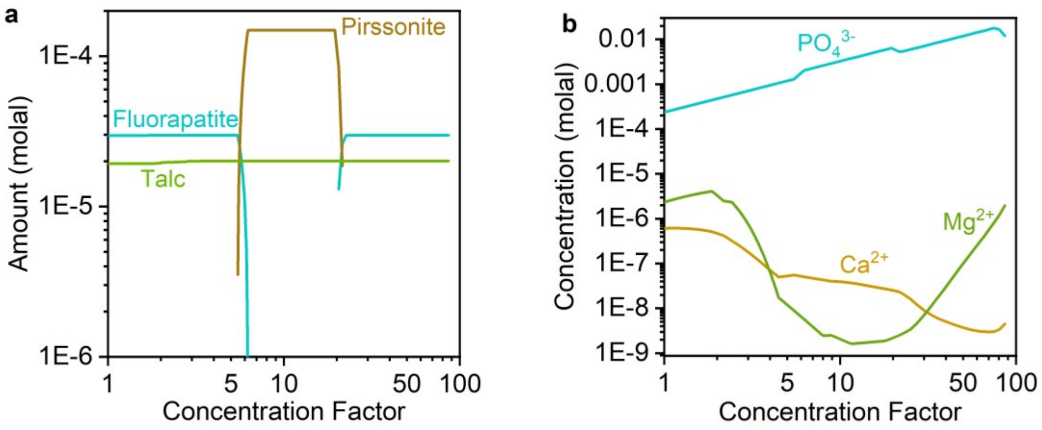

Figure S4. PHREEQC simulation of evaporation and mineral precipitation from Nasikie Engida brine at 30 °C in the presence of phosphate ion. (a) the mineral precipitation sequence of minor phases and the amount precipitated; (b) evolution of minor ions concentrations.

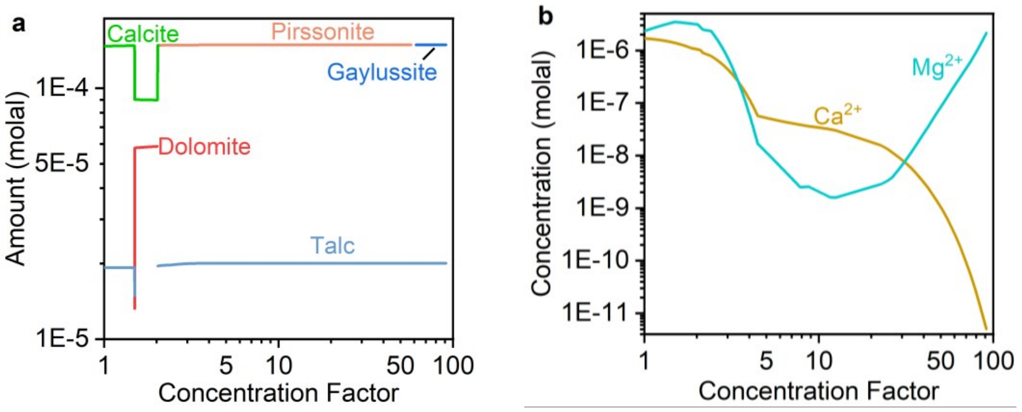

Figure S5. PHREEQC simulation of evaporation and mineral precipitation from Nasikie Engida brine at 30 °C in the absence of phosphate ion. (a) the mineral precipitation sequence of minor phases and the amount precipitated; (b) evolution of minor ions concentrations.

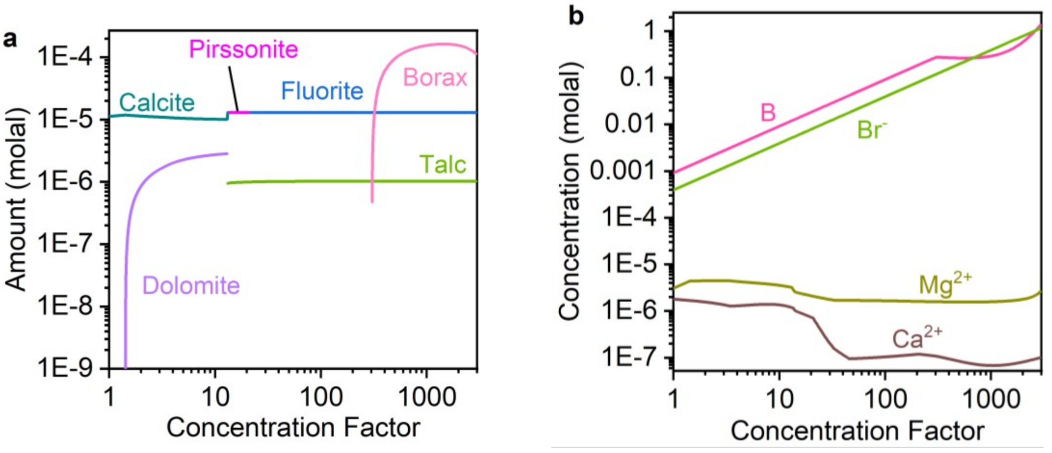

Figure S6. PHREEQC simulation of evaporation and mineral precipitation from Nasikie Engida hot spring at 30 °C. (a) the mineral precipitation sequence of minor phases and the amount precipitated; (b) evolution of minor ions concentrations

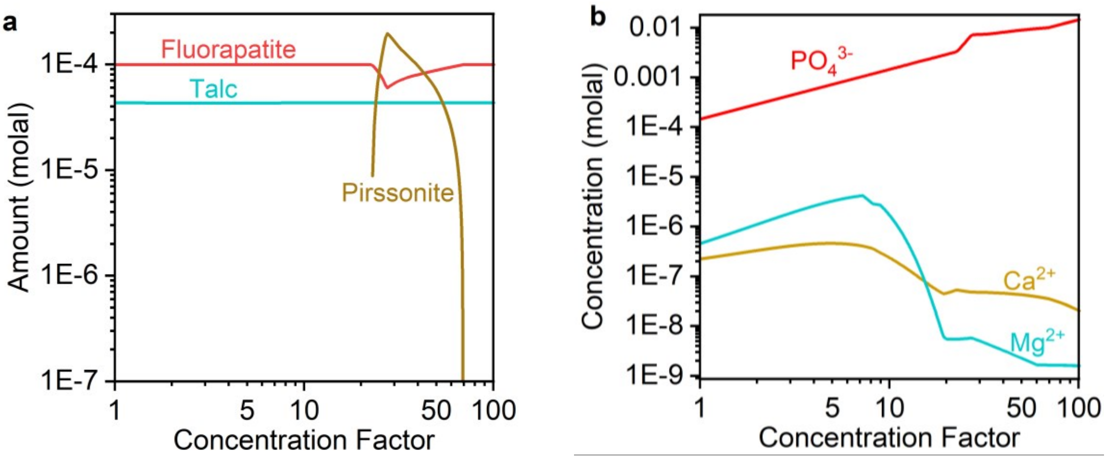

Figure S7. PHREEQC simulation of evaporation and mineral precipitation from Lake Natron brine at 30 °C in the presence of phosphate ions. (a) the mineral precipitation sequence of minor phases and the amount precipitated; (b) evolution of minor ions concentrations.

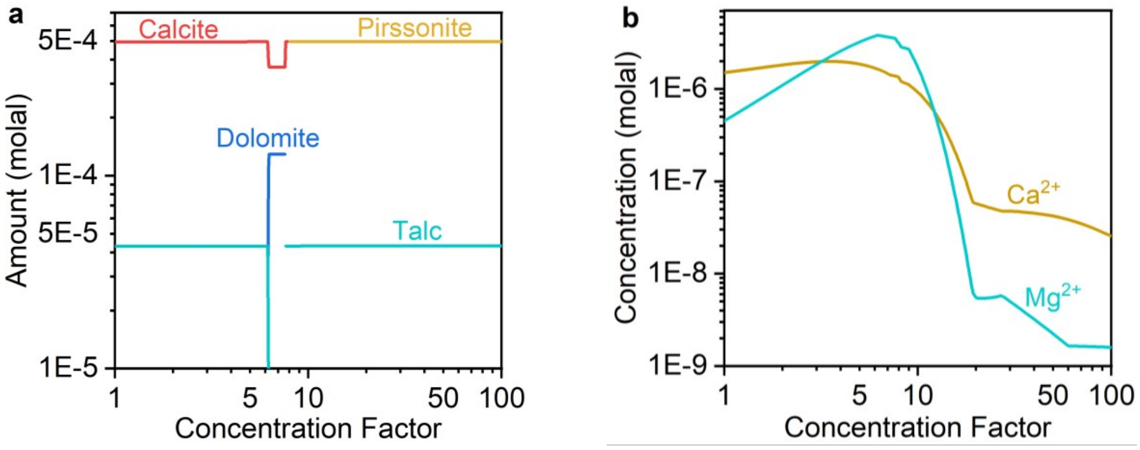

Figure S8. PHREEQC simulation of evaporation and mineral precipitation from Lake Natron brine at 30 °C in the absence of phosphate. (a) the mineral precipitation sequence of minor phases and the amount precipitated; (b) evolution of minor ions concentrations

Chapter 4

4. Mineral Vesicles and Chemical Gardens from Carbonate-Rich Alkaline Brines of Lake Magadi, Kenya [1]

Supplementary Materials for this article are presented at the end of this chapter.

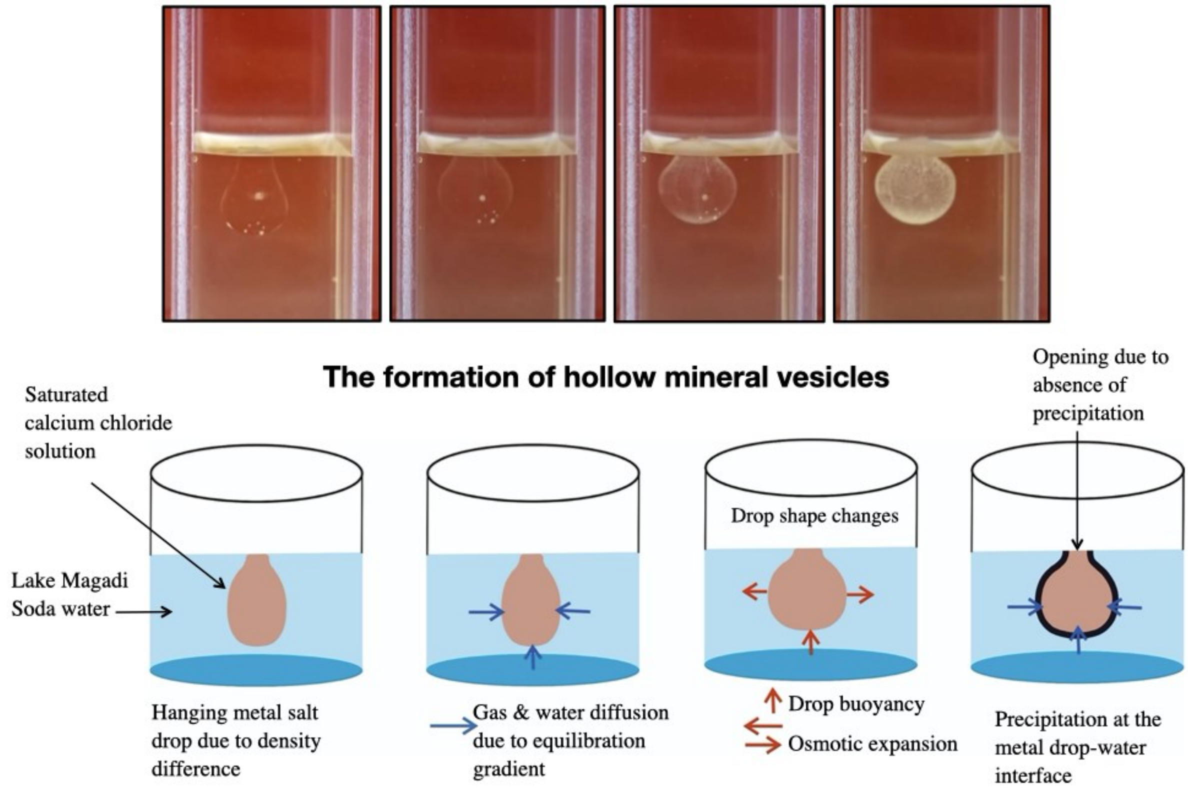

Graphical Abstract

---

[1] This chapter has been published in Getenet, M., García-Ruiz, J.M., Verdugo-Escamilla, C., Guerra-Tschuschke, I. Mineral Vesicles and Chemical Gardens from Carbonate-Rich Alkaline Brines of Lake Magadi, Kenya. Crystals 2020, 10, 467. https://doi.org/10.3390/cryst10060467

Journal metrics:
JCR 2021 (Clarivate Analytics): Impact Factor: 2.67, Q2 in Crystallography Category

crystals

MDPI

Article

Mineral Vesicles and Chemical Gardens from Carbonate-Rich Alkaline Brines of Lake Magadi, Kenya

Melese Getenet [1], Juan Manuel García-Ruiz [1,*], Cristóbal Verdugo-Escamilla [1] and Isabel Guerra-Tschuschke [2]

[1] Laboratorio de Estudios Cristalográficos, Instituto Andaluz de Ciencias de la Tierra (CSIC-UGR), Avenida de las Palmeras 4, Armilla, E-18100 Granada, Spain; dessie.melese@csic.es (M.G.); cristobal.verdugo@csic.es (C.V.-E.)
[2] Centro de Instrumentación Científica, Universidad de Granada (UGR), 18071 Granada, Spain; iguerra@ugr.es
* Correspondence: juanmanuel.garcia@csic.es; Tel.: +34-958-230-000 (ext. 190201)

Received: 28 April 2020; Accepted: 28 May 2020; Published: 1 June 2020

Abstract: Mineral vesicles and chemical gardens are self-organized biomimetic structures that form via abiotic mineral precipitation. These membranous structures are known to catalyze prebiotic reactions but the extreme conditions required for their synthesis has cast doubts on their formation in nature. Apart from model solutions, these structures have been shown to form in serpentinization-driven natural silica-rich water and by fluid-rock interaction of model alkaline solutions with granites. Here, for the first time, we demonstrate that self-assembled hollow mineral vesicles and gardens can be synthesized in natural carbonate-rich soda lake water. We have synthesized these structures by a) pouring saturated metal salt solutions, and b) by immersing metal salt pellets in brines collected from Lake Magadi (Kenya). The resulting structures are analyzed by using SEM coupled with EDX analysis, Raman spectroscopy, and powder X-ray diffraction. Our results suggest that mineral self-assembly could have been a common phenomenon in soda oceans of early Earth and Earth-like planets and moons. The composition of the obtained vesicles and gardens confirms the recent observation that carbonate minerals in soda lakes sequestrate Ca, thus leaving phosphate behind in solution available for biochemical reactions. Our results strengthens the proposal that alkaline brines could be ideal sites for "one-pot" synthesis of prebiotic organic compounds and the origin of life.

Keywords: Lake Magadi; soda lake; mineral self-organization; mineral vesicles; calcite; witherite; rhodochrosite; chemical gardens; early Earth; prebiotic chemistry; origin of life

1. Introduction

Mineral self-organization is an important subject for understanding pattern formation in Earth and Materials Sciences [1]. Among the different self-organized patterns [2], chemical gardens, specifically silica-induced self-organized structures, are thought to be relevant for the earliest stages of the planet, when alkaline silica-rich oceans evolved from methane-rich to CO and CO_2-rich atmosphere and hydrosphere [3]. Under these geochemical conditions of Hadean Earth, it is thought that mineral membranous structures (mineral gardens), and silica/carbonate biomorphs were forming in the alkaline oceans, rich in silica and/or carbonate. Mineral gardens are hollow tubular mineral membranes formed via abiotic precipitation upon the interaction of metal-ion salts with aqueous solutions containing anions such as silicate, carbonate, and phosphates [4,5]. It has been shown that the space-compartmentalized silica membranes are small batteries [6] that selectively catalyze the synthesis of prebiotically relevant compounds such as carboxylic acids, amino acids, and nucleobases in the presence of formamide [7].

So far, mineral gardens have only been synthesized using laboratory model solutions, except for two cases where silica gardens form upon the interaction of model alkaline fluids with granites [8] and the interaction of serpentinization-driven natural alkaline water with metal salt pellets [9].

It has been demonstrated that silica-induced mineral self-assembly could have been a common phenomenon on primitive Earth and Earth-like planets [9], where alkaline environments are thought to be widespread. In addition to serpentinization-driven water [9], soda lakes such as Lake Magadi (Kenya) are proposed as having the naturally high alkalinity and high silica content required to trigger mineral self-organization [3,10]. It has also been suggested that Precambrian oceans were in some way analogous to modern soda lakes such as Lake Magadi [3,11–14]. Recent work [15] has shown that carbonate-rich lakes are highly plausible environments for accumulating phosphate at concentration and pH levels relevant to laboratory syntheses of prebiotic organophosphate compounds. This is due to calcium sequestration in carbonate minerals that prevent apatite precipitation and accumulate phosphate [15]. Therefore, testing the geochemical plausibility of self-organization in one of the early Earth-analogous environments, soda lakes, is important for prebiotic chemistry and life detection. Calcium-based mineral self-organization experiments in carbonate-rich soda lake water have two advantages: testing geochemical plausibility of mineral self-assembly and testing the role of carbonate-rich water in calcium sequestration. Up until now, there have been no reported self-assembled mineral membranes synthesized in natural modern soda lakes.

Therefore, we have tested the precipitation of self-assembled mineral membranes from Lake Magadi brines, in Southern Kenya. Lake Magadi is one of the soda lakes of the East African Rift Valley, with the characteristics of high pH, silica and carbonate concentration [16,17]. It occupies a narrow trough formed by N-S faulting of plateau trachyte during the Pleistocene. The predominant geology of the Lake Magadi area is alkali trachyte lava flows [18,19]. A unique combination of tectonic, volcanic, hydrothermal and climatological settings favor soda lake formation in East Africa [20]. Geochemical studies of closed-basin water in volcanic terrains show that their chemical composition is mainly controlled by silicate hydrolysis and evaporative concentration [21,22]. We have performed two types of membrane precipitation experiments. The first type is mineral garden precipitation by immersing pressed metal (Ba, Ca, Co, Cu, Mg, Mn, Fe (II), Fe (III) and Zn) salt pellets into Lake Magadi water [4,5] (hereafter, Magadi gardens). The second one is mineral vesicle precipitation by adding drops of saturated solutions of the above metal salts onto Lake Magadi water [23] (hereafter, Magadi vesicles). The focus in this article is Ba, Ca and Mn mineral vesicles synthesized by adding drops of saturated salt solutions onto Lake Magadi water. Hence, here we present the macroscopic growth of mineral gardens and Co, Mg, Zn and Fe (II) vesicles to demonstrate the range of mineral self-organization that might form in soda lakes.

2. Materials and Methods

2.1. Geological Setting, Sampling and Hydrochemical Analysis

Lake Magadi is one of the saline and alkaline soda lakes of the East African Rift Valley. It lies in the axial trough of the southern Kenya Rift Valley formed by the N–S faulting of plateau trachyte during the Pleistocene [18,19]. The predominant geology of the Lake Magadi area is alkali trachyte lava flows [18,19] overlain by Holocene bedded trona and trona-bearing muds [16].

Lake Magadi brine is the last stage of the evolution of dilute inflows enriched in Na^+, SiO_2, and HCO_3^- through hydrolysis of weathered volcanic glass and lavas from the rift escarpments. These inflows lose their Ca and Mg content before joining the groundwater system beneath the rift floor due to evaporative precipitation of alkaline Earth carbonate in the rift floor sediments [17,24]. Through a combination of further rock-water interaction, evaporative concentration and solute loss, the initially dilute water produces highly alkaline groundwater characterized by high pH, Na^+, HCO_3^-, Cl^-, CO_3^{2-} and SiO_2 contents [16,17]. This groundwater reservoir discharges warm and hot springs into Lake Magadi lagoons along its shoreline. Upon surface evaporation and mineral precipitation (mainly trona), these lagoons form the most fractioned Lake Magadi brines saturated in trona. The high concentrations of SiO_2 are attributed to the dissolution of silicate-rich volcanic rocks by feeder springs and subsequent evaporative concentration accompanied by pH rise [25]. Hydrothermal input is an important contributor to silica in soda lake waters [20]. The high pH of Lake Magadi brines attributes to trona deposition and subsequent depletion in HCO_3^- and CO_2 degassing [16,17].

The sample used for the experiments was collected from the Lake Magadi evaporation ponds during the field campaign in March 2018. The sample was collected and stored in polyethylene bottles. The sampling point was located at a coordinate of 199441E and 9791457N (UTM) and 602m above sea level. The in-situ pH was measured to be 10.9. The in-situ temperature was 37 °C. The hydrochemistry of the Lake Magadi sample was analyzed by ALS Laboratory Group SL, except for Na^+, K^+, SO_4^{2-}, and F^-. Cl^-, CO_3^{2-}, and HCO_3^- were analyzed by potentiometric titration. Total P and SiO_2 were determined by discrete spectrophotometry. Ca^{2+}, Ba^{2+}, B^+, Sr^{2+}, and total Fe were analyzed using inductively coupled plasma (ICP) atomic emission spectrometry (AES). Al^{3+}, Mg^{2+}, Br^-, and I^- were determined by using inductively coupled plasma (ICP) mass spectrometry (MS). To avoid matrix interference, samples were homogenized and mineralized with nitric acid in an autoclave under high pressure (7.5 atm) and temperature (170 °C) before analysis by ICP-AES and ICP-MS. Na^+ was analyzed by using inductively coupled plasma (ICP) optical emission spectrometry at the Instrumental Technical Services of the Estación Experimental del Zaidín (CSIC) in Granada (Spain). F^- was measured by the ion-selective electrode technique with a pH and ion-meter GLP 22 CRYSON at the Instituto de Catálisis y Petroleoquímica-CSIC, Madrid (Spain). K^+ and SO_4^{2-} was determined by using Varian Cary 1E ultraviolet-visible spectrophotometry at the Laboratorio de Estudios Cristalográficos (LEC) of the Instituto Andaluz de Ciencias de la Tierra (IACT) in Granada, Spain. Total dissolved solids were determined gravimetrically after filtering the water by using glass microfibre filters (Environmental Express, 1.5 µm pore size). The hydrochemical analysis of Lake Magadi water used for the growth of mineral gardens and vesicles is presented in Table 1.

Table 1. Chemical analysis of the Lake Magadi water used for mineral garden and vesicle synthesis. Elemental concentrations are in ppm, conductivity in mS/cm.

pH	T (°C)	Conductivity	TDS	Na^+	K^+	SiO_2	Cl^-	CO_3^{2-}	HCO_3^-	SO_4^{2-}
10.9	37	16,200	440,000	179,460	831	1080	125,000	54,900	8110	2254
F^-	**PO_4^{3-}**	**Mg^{2+}**	**Al^{3+}**	**Ca^{2+}**	**Fe^{tot}**	**B^+**	**Sr^{2+}**	**Ba^{2+}**	**Br^-**	**I^-**
1075	418	0.023	<0.005	<0.5	<0.05	211	0.0767	0.622	725	26.6

2.2. Magadi Gardens and Vesicles Synthesis

Mineral membranes were synthesized by using two types of experimental procedures. The first procedure is a classical method used in silica garden growth experiments [4]. The method consists of the immersion of crystals of soluble salts into a viscous sodium silicate solution, which form tubular structures (Magadi gardens) through a combination of buoyancy and osmosis. Under this setup, crystalline pellets (13 mm diameter) of $CaCl_2{\cdot}2H_2O$ (Sigma Aldrich ≥ 99%), $BaCl_2{\cdot}2H_2O$ (Sigma Aldrich ≥ 99%), $CoCl_2{\cdot}6H_2O$ (Sigma Aldrich)/$Co(NO_3)_2{\cdot}6H_2O$ (PANREAC), $CuSO_4{\cdot}5H_2O$ (PROBUS ≥ 98%), $CuCl_2{\cdot}6H_2O$ (Sigma Aldrich ≥ 99%), $FeCl_2{\cdot}4H_2O$ (Honeywell Fluka)/ $FeSO_4{\cdot}7H_2O$ (Sigma Aldrich), $FeCl_3$ (Honeywell Fluka)/$Fe_2(SO_4)_3{\cdot}9H_2O$ (PROBUS), $MgCl_2{\cdot}6H_2O$ (Sigma Aldrich ≥ 99)/$MgSO_4$ (Sigma Aldrich ≥ 99.5%), $MnCl_2{\cdot}4H_2O$ (Sigma Aldrich), and $ZnSO_4{\cdot}7H_2O$ (PANREAC)/$ZnCl_2$ (Sigma Aldrich ≥ 99) were placed at the bottom of a 10 mL plastic vial by using double-sided tape, and 5 mL of Lake Magadi brine was poured into the vial slowly. The pellets were prepared by grinding the above salts to powder fraction using an agate mortar and then pressing with 3–10 ton pressure.

The second experiment was performed by adding drops of saturated solutions of the metal salts (mentioned above) onto a reservoir of Lake Magadi brine in half-filled Linbro plate wells and plastic cuvettes [23]. This method of membrane growth gives hollow bulb-like and spherical precipitates (Magadi vesicles) hanging on top of the carbonate-rich water and with an opening towards the water-air interface (atmosphere). Saturated metal salt solutions were prepared by dissolving an excess amount of metal salts into Milli-Q membrane-purified water followed by filtration using a 0.45 µm pore size filter. The pH of these metal salts were measured with CRISON GLP 21 pH meter except for $FeCl_3$ and $ZnCl_2$, which are measured with HANNA HI98160 portable pH meter because of their high acidity. Both of the experimental procedures for the membrane growth were performed under ambient lab conditions.

After the completion of the growth, the membranes are cleaned with distilled water and ethanol multiple times before harvesting from the reservoir. In the case of tubular gardens, the water outside the tube was replaced with distilled water and then ethanol to dry the membrane faster. Mineral vesicles were cleaned by removing the metal salt solution inside the vesicles by introducing a syringe through their "mouth" open to the atmosphere. After the removal of the solution inside the vesicle, the outer solution was removed slowly until the hanging vesicle smoothly lands on the bottom of the wells or the cuvettes. The vesicles were cleaned by repeated addition of distilled water and ethanol outside and inside the vesicle using a syringe. Finally, the mineral vesicles and gardens were collected by using a tiny brush and a spatula.

2.3. Membrane Characterization

The growth process of Magadi gardens and vesicles was monitored by time-lapse photography and video using a Nikon optical microscope and camera respectively. Both top view and lateral view were acquired. After drying at ambient temperature and careful isolation from the reservoir, ex-situ characterization of the texture and chemical composition of the tubular and the vesicular membranes were performed by using a Zeiss Supra 40VP field-emission scanning electron microscope (SEM) equipped with an Oxford energy-dispersive X-ray analyzer (EDX) at the Centro de Instrumentación Científica (CIC) of the University of Granada (Spain) operating at 5–20 keV. Determination of the crystalline phases of the membranes was performed by using a high-resolution Bruker D8 Advance X-ray diffractometer with monochromatic Cu $K_{\alpha1}$ radiation, primary Ge(111) monochromator and a Lynxeye PSD detector in our lab. Powder diffraction of samples took place in transmission mode, at 40 kV acceleration voltage, and 40 mA current for one hour from 5° to 80° 2θ with an increment of 0.02° per second. Mineral phases were identified by using Bruker AXS Diffrac EVA software with the ICCD PDF-2 and the Crystallographic Open Database. Raman spectra of fragments of the membranes were recorded by using a HORIBA Jobin Yvon LabRAM high-resolution ultraviolet-visible light spectrometer equipped with an Olympus BX41 optical microscope with binocular and Koehler illumination and a charge-coupled device detector at an excitation wavelength of 532 nm (frequency-doubled neodymium-doped yttrium-aluminium-garnet laser).

3. Results

3.1. The Magadi Gardens Growth Process

We have identified three types of Magadi garden growth processes by immersing metal salt pellets in Lake Magadi water. In less soluble and less acidic salts of Ba^{2+}, Mn^{2+} and Fe^{2+} (Table 2), the pellets remain intact inside the growth medium and there was no membrane formation observed due to the inability of the alkaline water to dissolve the metal salts that upon interaction with the anions would form membranes. In the case of Fe^{3+} ($FeCl_3$ and $Fe_2(SO_4)_3{\cdot}9H_2O$), Cu^{2+} ($CuCl_2{\cdot}6H_2O$ and $CuSO_4{\cdot}5H_2O$) and Zn^{2+} ($ZnCl_2$ and $ZnSO_4{\cdot}7H_2O$), the experiment resulted in a premature bursting of the membrane and sedimentation by gravity due to high acidity and high solubility of the metal salts (Table 2). The bursting of the membrane was accompanied by the bubbling of gases (see Videos S1–S3). Unlike the aforementioned metals, the salts of Ca^{2+} ($CaCl_2{\cdot}2H_2O$) and Co^{2+} ($CoCl_2{\cdot}6H_2O$ and $Co(NO_3)_2{\cdot}6H_2O$) form tubular membranes shown in Figures 1 and 2 respectively. Likewise, Mg^{2+}

($MgCl_2 \cdot 6H_2O$) pellets immersed in Magadi water form mineral gardens (not presented here) that are morphologically similar to Co ($Co(NO_3)_2 \cdot 6H_2O$)) gardens.

Table 2. Metal salts used for the mineral vesicles and gardens experiments, their measured pH and solubility in g/100g of water at 25 °C [26]. Accuracy of pH measurements: ±0.1.

Salt	**$BaCl_2 \cdot 2H_2O$**	**$CaCl_2 \cdot 2H_2O$**	**$MnCl_2 \cdot 4H_2O$**	**$CoCl_2 \cdot 6H_2O$**	**$Co(NO_3)_2 \cdot 6H_2O$**
pH	5.2	4.6	2.3	2.6	3.5
Solubility	37	81.3	77.3	56.2	103
Salt	**$CuCl_2 \cdot 6H_2O$**	**$CuSO_4 \cdot 5H_2O$**	**$FeCl_2 \cdot 4H_2O$**	**$FeSO_4 \cdot 7H_2O$**	**$FeCl_3$**
pH	0.5	3.1	1.0	2.6	−1.7
Solubility	75.7	22	65	29.5	91.2
Salt	**$Fe_2(SO_4)_3 \cdot 9H_2O$**	**$MgCl_2 \cdot 6H_2O$**	**$MgSO_4$**	**$ZnCl_2$**	**$ZnSO_4 \cdot 7H_2O$**
pH	−0.3	5.1	8.1	−1.9	4.7
Solubility	440 [1]	56	35.5	408	57.7

[1] Solubility measured at 20 °C.

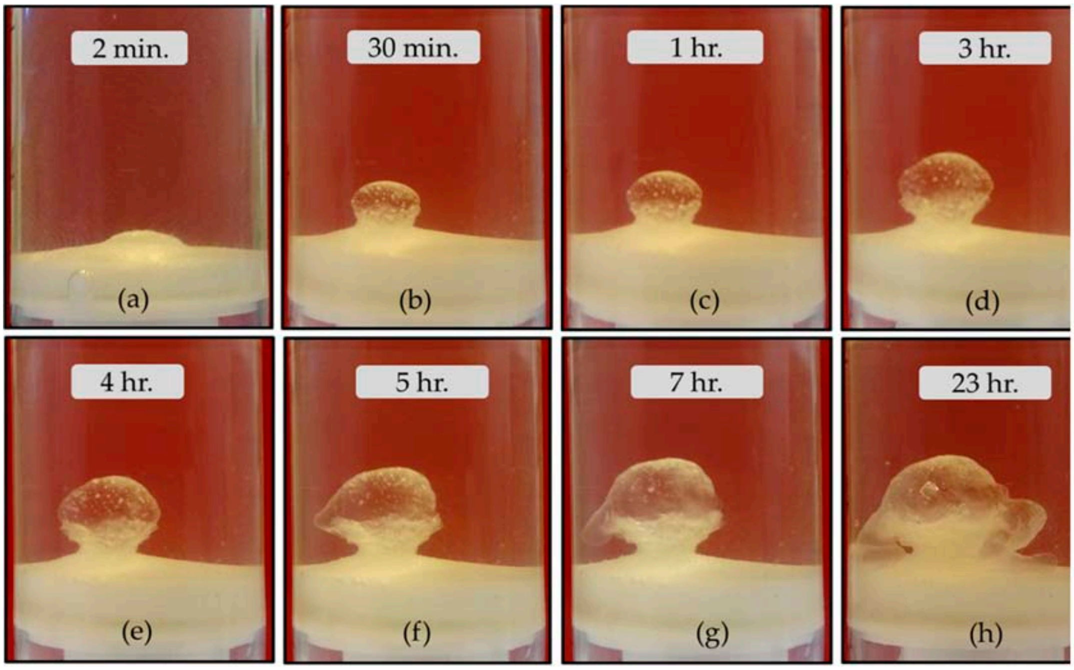

Figure 1. The growth process of calcium carbonate garden. The diameter of the vial is 1.45 cm.

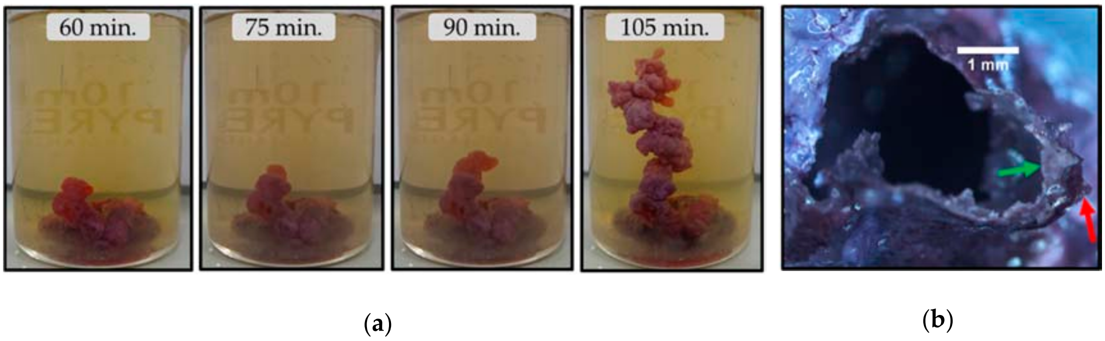

Figure 2. Tubular mineral gardens synthesized by immersing cobalt nitrate pellets in Lake Magadi water. (**a**) Time-lapse images of the growth process (diameter of the beaker is 25 mm); (**b**) cross-section of the tubular membrane.

Figure 1, a set of frames taken from Video S4, shows the macroscopic growth of Ca gardens. Upon the interaction of the calcium chloride pellet with Lake Magadi water, a white dome-shaped structure forms (Figure 1a, and Video S4). The osmotic-driven inflow of water into the dome-shaped structure causes gradual swelling and the formation of the transparent elastic membrane at the interface between the outer Magadi water and the inner salt solution. As shown by the morphology of the calcium gardens (Figure 1f–h), the growth process takes place both in vertical and horizontal directions. After the horizontal growth of the membrane, vertically downward growth follows (Figure 1f–h). The combination of these vertical and horizontal membrane growths gives rise to the tubular structure. These tubular structures have a variable diameter (3–7 mm) because of horizontal expansion and their length can reach 6.5 mm. The powder X-ray diffraction shows calcite, gaylussite, pirssonite and trona phases (Figure S1). The powder X-ray diffraction (Figure S1) and a video (Video S4) showing the macroscopic growth are presented in Supplementary Materials.

After the addition of the Magadi water on the Co pellets, a dome-shaped envelope forms surrounding the pellet in about 30 min (Video S5). Due to osmotic-driven diffusion of water, the membranous envelope swells and finally ruptures. The rupture of the envelope ejects the inner Co solution into the surrounding Magadi water, which upon precipitation forms the tubular mineral gardens (Figure 2a). The growth of the tube continues in periodic pulses that range from 6 s to 3 min with an eventual change of growth direction. The change in growth direction produces rounded and tubular branches connected with the main tubular membrane (Figure 2a at 105 min). These small tubular branches give rise to an elliptical cross-section (Figure 2b). The height of cobalt gardens reach ca. 30 mm. Cobalt gardens have two layers (Figure 2b, red and green arrow). The exterior layer is a very thin film (Figure 2b, red arrow). As a result, these membranes are highly fragile and it must be isolated carefully. The powder X-ray diffraction (Figure S2) shows $Co_2(OH)_3Cl$ phase. The powder X-ray diffraction (Figure S2) and a video (Video S5) showing the macroscopic growth are presented in the Supplementary Materials.

3.2. The Magadi Vesicles Growth Process and Characterization

Drops of saturated Fe^{3+}, Cu^{2+} and $ZnCl_2$ solutions undergo premature bursting when they interact with Lake Magadi water (Videos S6–S8). The bubbling of gases was observed during the bursting of the vesicles. When the metal salt drops of Ca^{2+}, Ba^{2+}, Mg^{2+}, Mn^{2+}, Zn^{2+}, Fe^{2+} and Co^{2+} are placed on Lake Magadi water, hollow bulb-like and spherical vesicles form at the interface between the two solutions.

3.2.1. Calcium Chloride Vesicles

Calcium vesicles were synthesized by adding drops of saturated calcium chloride solutions onto Lake Magadi water in a half-filled cuvette. Figure 3a and Video S9 show the growth process of Ca vesicles. Figure 3a is a set of frames taken from Video S9 in Supplementary Materials. The Ca salt drops placed on the surface of Magadi water remain hanging in the uppermost part of the water throughout the growth process (Figure 3a) due to the lower density of the Ca salt solution. The drops change from bulb-like to spherical shape during the first 10 min. During this morphological change, the bottom of each drop lifts up while expanding radially outward. This morphological evolution is accompanied by a color change from transparent to white. Calcium vesicles are hollow mineral membranes formed by mineral precipitation at the interface between the two solutions. These vesicles have an opening ("mouth") at the water–air interface (Figure 3b).

After washing with distilled water and alcohol, vesicles are dried and powdered for X-ray diffraction. The X-ray diffraction shows halite, calcite, trona, vaterite and gaylussite phases (Figure 4). Raman spectra acquired on vesicle fragments after cleaning with a similar protocol confirmed only calcite (Figure S3). The bands at 153 and 280 cm^{-1} are translational and librational modes (lattice modes) of ${CO_3}^{2-}$ respectively. The bands at 712 and 1085.3 cm^{-1} are assigned to in-plane bending and symmetric stretching (internal modes) of ${CO_3}^{2-}$ group respectively [27,28]. Trona, vaterite and gaylussite did not appear in Raman spectra most likely because of low proportion. However, trona, gaylussite and vaterite were observed in SEM micrographs.

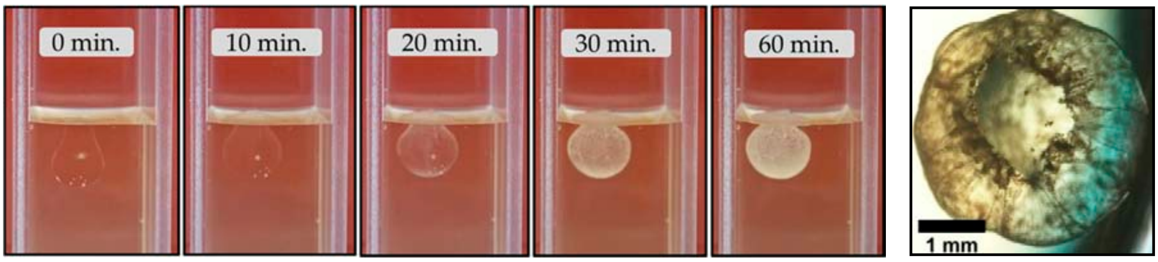

(**a**) (**b**)

Figure 3. (**a**) Temporal evolution of morphology and texture of the calcium mineral vesicles (width of the cuvette is 1.25 cm); (**b**) hollow calcium vesicle with its opening.

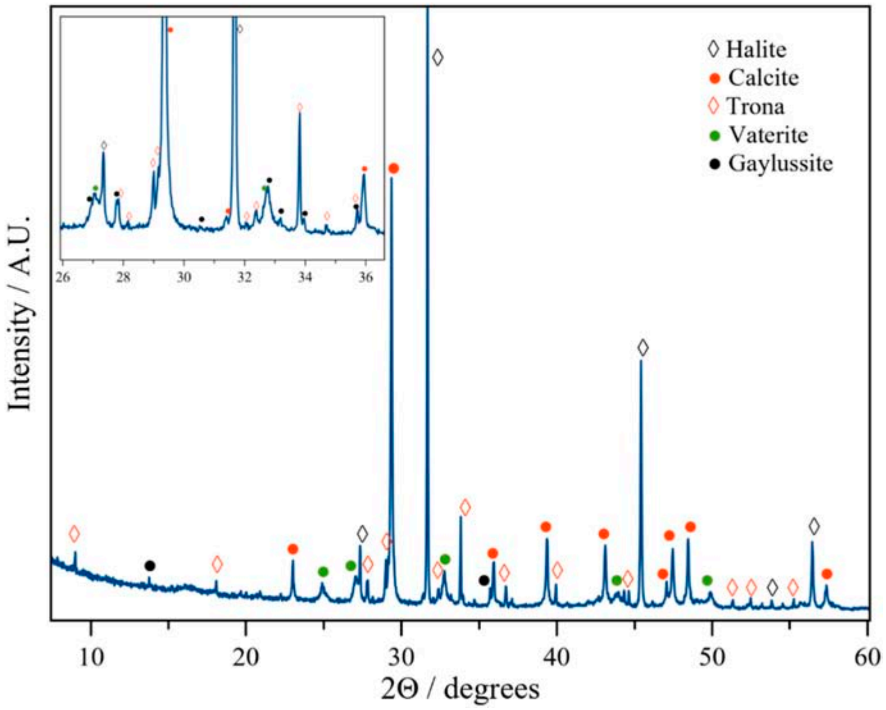

Figure 4. Powder X-ray diffractogram of calcium vesicles.

EDX mapping (Figure 5a and Figure S4) and point analysis (Figure 5b and Figure S5) show that the cross-sections of calcium vesicles are composed of bilayer of calcite with halite core where interlayered calcite precipitate. Figures S4 and S5 in Supplementary Materials show the separate elemental maps of Figure 5a and the EDX analyses of the rectangles in Figure 5b respectively. The calcite bilayers are composed of nano- to few micron-sized spherical aggregates of calcite, which are in turn composed of nano-spherical aggregates. The inner calcite layer is thicker and reach ca. 25 µm thickness (Figure 5a). A thin layer of halite cover the internal wall of calcium vesicles whereas elongated trona crystals precipitate on the external surface of the membranes (Figure 5a). Similar to trona, gaylussite precipitate on the external calcite layer (see Figure 5c and Figure S6 for the point EDX analyses).

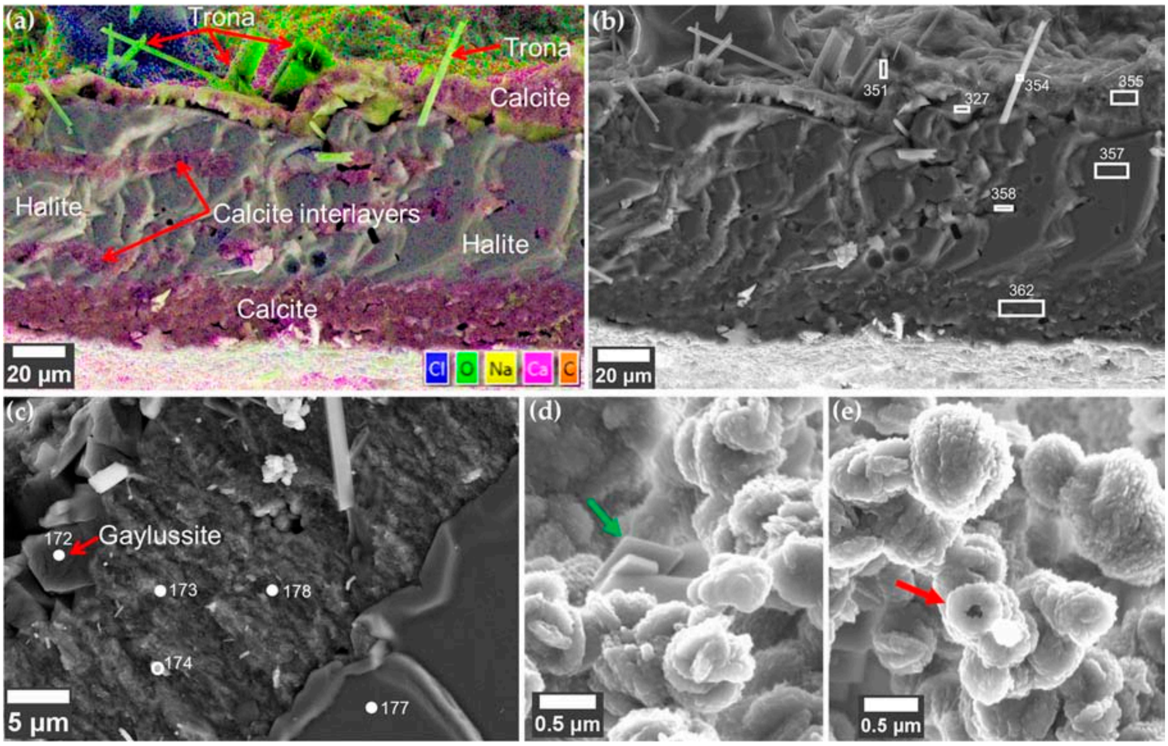

Figure 5. SEM micrographs of calcium vesicles synthesized by adding drops of calcium chloride solution in Magadi water. (**a**) EDX map of the membrane cross-section containing bilayer of calcite, halite core, interlayered calcite and trona on the external surface; (**b**) SEM micrograph of the panel (**a**) with points where EDX analysis was performed (see Figure S5); (**c**) cross-section of the membrane showing gaylussite crystals; (**d**) rhombohedral calcite (green arrow); (**e**) hollow vaterite sphere (red arrow) on the exterior of the membrane.

Aggregates of calcite and vaterite minerals (Figure 5d,e) form small patches on the exterior of the membrane. Due to the fragile nature of calcium vesicles, rupture of the membrane during cleaning may form non-extensive precipitates on the exterior of the membrane when the interior calcium and the exterior carbonate-rich water comes in contact. The dominant minerals in these local patches are spherules of calcite (Figure 5d,e). These local precipitates are also composed of rhombohedral calcite (Figure 5d, green arrow) and vaterite with a hole at the centre (Figure 5e, red arrow).

3.2.2. Barium Chloride Vesicles

Barium vesicles were synthesized by placing drops of saturated barium chloride solution on Magadi water in a half-filled cuvette. Figure 6 and Video S10 show the growth process of Ba vesicles. Figure 6 is a sequence of frames taken from Video S10 (in Supplementary Materials). Upon the interaction of the Ba solution with the Magadi water, barium vesicles immediately precipitate at the interface between the drop and the Magadi water. Consequently, the transparency of the drop changes to white within about a minute. The vesicles remain hanging on the upper part of the water. Later on, these vesicles sink to the bottom of the reservoir (Figure 7a).

After an hour of growth, the lowering and sinking of the opening allow water to enter into the hollow vesicles, which upon interaction with the inner Ba solution form white mineral precipitates inside the vesicles. These white precipitates give rise to sudden and distinct color changes of the vesicles. Following the intrusion of the exterior water, the vesicles sink to the bottom of the cuvettes (Figure 7a). These vesicles develop corrugated surfaces that exist throughout the growth processes (Figures 6 and 7b). Barium vesicles are also hollow mineral membranes with an opening at the air–water interface (Figure 7c).

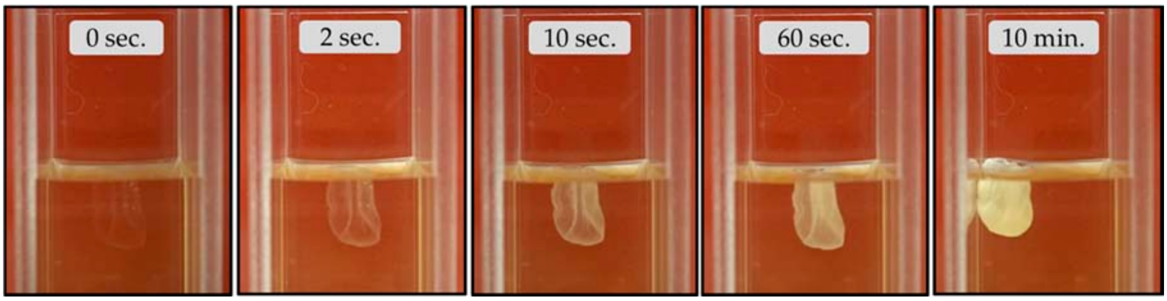

Figure 6. Temporal evolution of the morphology and texture of the barium carbonate Magadi vesicles. The width of the cuvette is 1.25 cm.

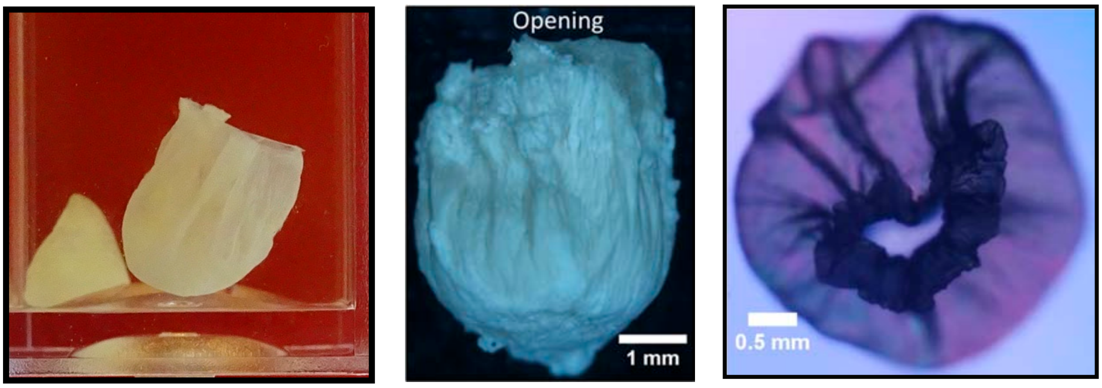

(**a**) (**b**) (**c**)

Figure 7. (**a**) Barium vesicle sinking at the bottom of the cuvette (the width of the cuvette is 1.25 cm); (**b**) corrugated surfaces of isolated barium vesicle; (**c**) hollow barium vesicle with opening.

After washing with distilled water and alcohol, the vesicles are dried and powdered for X-ray diffraction. Witherite and halite appeared in the powder X-ray diffractions (Figure 8e). Raman spectra (Figure 8f) acquired on vesicle fragments after cleaning with a similar protocol confirmed witherite [29,30]. Bands at 137, 152, and 225 cm^{-1} are assigned to lattice (external) modes whereas bands at 691 and 1061 cm^{-1} are symmetric bending and symmetric stretching modes of the carbonate groups respectively [30].

Figure 8a–d shows scanning electron micrographs of the cross-section of barium vesicles. These vesicles are ca. 18 µm thick mineral membranes (Figure 8b) composed of nano-spherical witherite aggregates. EDX analyses (Figure 8c and Figure S7) and mapping (Figure 8d and Figure S8) confirmed that the membranes are witherite, whereas the whiskers covering the inner and the outer surface of the membrane are sodium carbonate minerals (Figure 8d). A thin layer of halite precipitate on the inner and outer wall of these membranes (Figure 8d). The sodium carbonate whiskers grow outward from these halite cover. These whiskers, which appear only in SEM micrographs, could be an artefact formed by capillary evaporation during sample preparation. Figures S7 and S8 in Supplementary Materials show the EDX analyses of Figure 8c and the separate elemental maps of Figure 8d respectively.

3.2.3. Manganese Chloride Vesicles

Manganese vesicles were synthesized by adding drops of saturated manganese chloride solution on top of Magadi water. The evolution of manganese vesicles over time is presented in Figure 9a and Video S11. Figure 9a is a sequence of frames taken from Video S11 (in Supplementary Materials). The Mn salt drops suspend on the top section of the water column by retaining a bulb-like shape. In the beginning, the drops are transparent (Figure 9 at 0 sec.). After a few seconds, the color of the drops changes to white due to mineral precipitation at the interface between the drop and Magadi water, which gives hollow vesicles. These vesicles have an opening at the very top as shown in Figure 9b. Manganese vesicles undergo visible swelling in the first 10 min and later the shape remains the same throughout the growth processes. During the active growth period (about 30 min), the vesicles suspending on the water surface rotate periodically clockwise and anti-clockwise. The opening of manganese vesicles shows corrugated surfaces that intensify from the bottom towards the mouth (Figure 9b). The development of shrinkage surfaces was accompanied by a gradual narrowing of the initially wider opening.

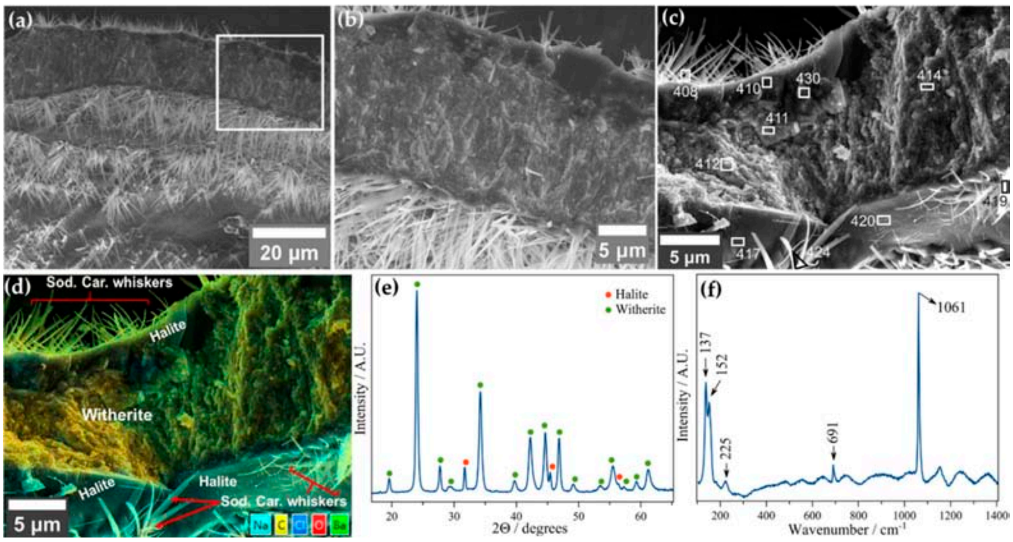

Figure 8. (**a**) Cross-section and the inner surface of Ba vesicle; (**b**) closer look of the cross-section marked by the white square in panel (**a**); (**c**) SEM micrograph of the membrane cross-section with rectangles where EDX analyses performed (see Figure S7 for EDX analyses); (**d**) EDX map of panel (**c**) showing witherite membrane with the inner and outer halite and sodium carbonate whiskers; (**e**) powder X-ray diffractogram of Ba vesicles; (**f**) Raman spectra of Ba vesicles (137, 152, 225 cm^{-1} —lattice modes; 691 cm^{-1} —symmetric bending mode; 1061 cm^{-1} —symmetric stretching mode).

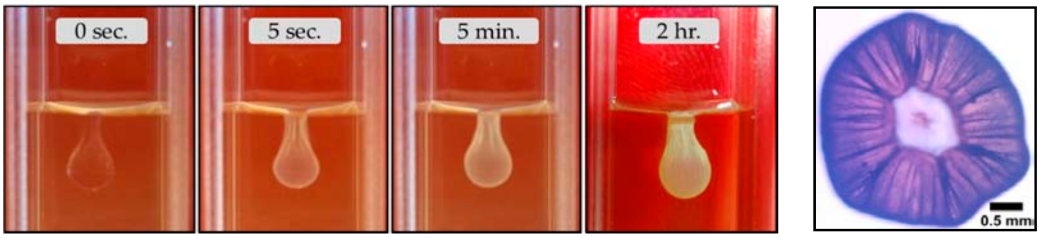

(**a**) (**b**)

Figure 9. Mineral vesicles synthesized by adding manganese chloride on Magadi water. (**a**) Growth process of the vesicles (width of the cuvette is 1.25 cm); (**b**) hollow vesicle with its opening and corrugated surfaces.

After washing with distilled water and alcohol, the vesicles are dried and powdered for X-ray diffraction. The X-ray diffraction shows halite, rhodochrosite, and nahcolite phases (Figure 10a). Raman spectra (Figure 10b) acquired on the vesicles after cleaning with a similar protocol confirmed rhodochrosite. Bands at 182 and 286 cm^{-1} are assigned to translational lattice modes whereas bands at 725 and 1087 cm^{-1} are in-plane bending and symmetric stretching modes of the carbonate groups respectively [30]. Nahcolite did not appear in Raman spectra.

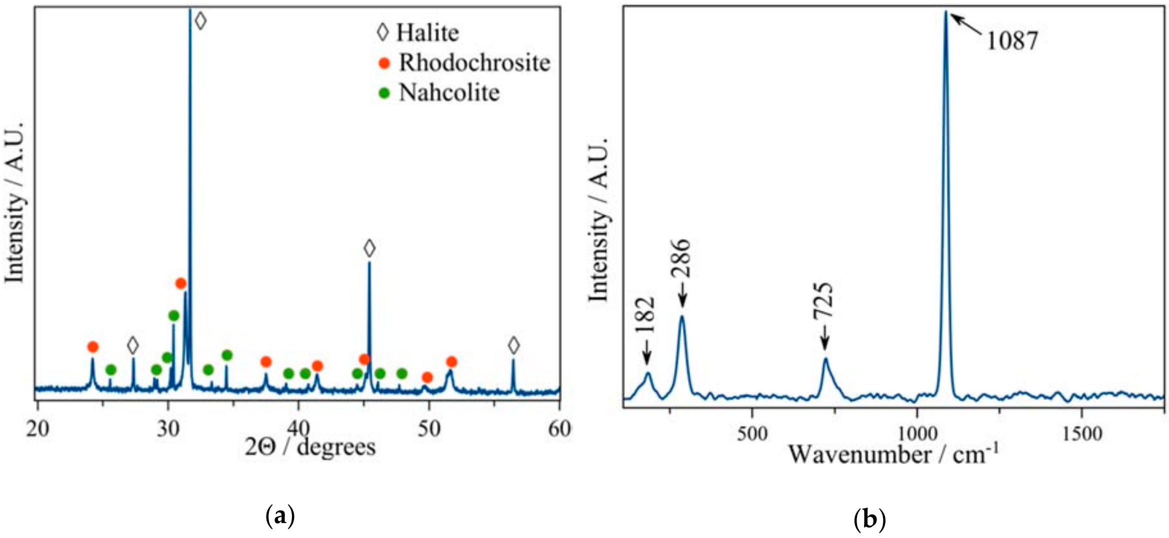

Figure 10. (**a**) Powder X-ray diffractogram; (**b**) Raman spectra of manganese vesicles (182, 286 cm^{-1} —translational lattice modes; 725 cm^{-1} —in-plane bending mode; 1087 cm^{-1} —symmetric stretching mode).

Figure 11 shows the scanning electron micrographs of manganese vesicles. As shown in Figure 11a, manganese vesicles are composed of aggregates of 9–12 µm rhodochrosite spherules. Figure 11b, with its simplified sketch (Figure 11c) shows the cross-section and the exterior of Mn membranes. EDX analysis (Figure S9) has shown that sometimes the cross-section of the manganese vesicles are covered with a smooth undulating layer of halite (Figure 11d). On top of this halite layer, spherical rhodochrosite particles precipitate (Figure 11d). The diameter of these spherules of rhodochrosite varies roughly between 1 and 3.4 µm.

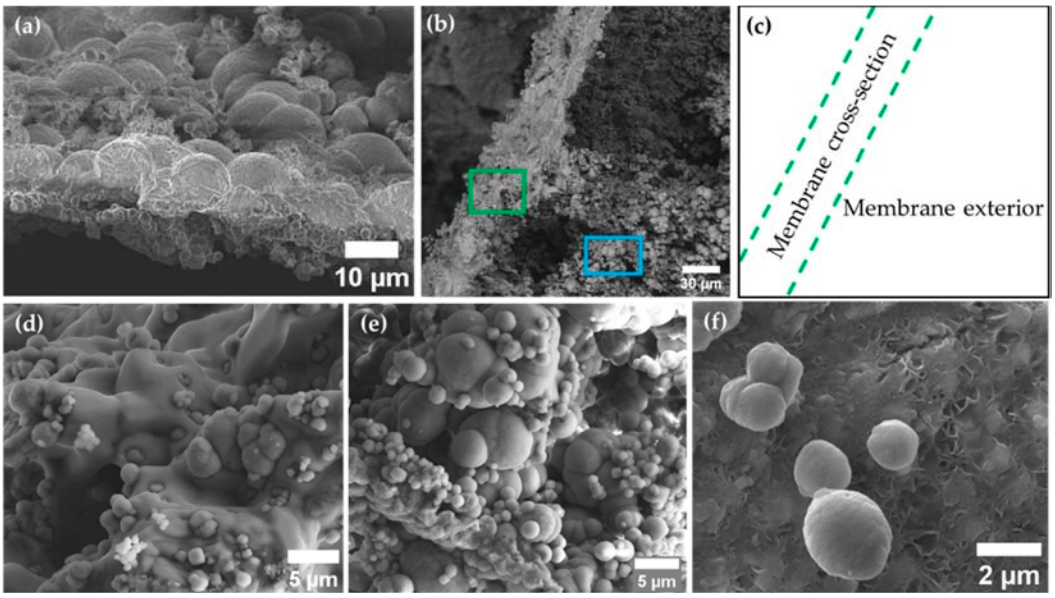

Figure 11. SEM images of manganese vesicles. (**a**) Cross-section of the membrane; (**b**) cross-section of the membrane and its exterior; (**c**) simplified sketch of panel (**b**); (**d**) closer look of the cross-section at the green rectangle in panel (**b**); (**e**) exterior of the membrane at the blue rectangle in panel (**b**); (**f**) interior wall of the membrane.

Rhodochrosite spherules with varying diameter (ca. 1–6 µm) form on the exterior of manganese membranes (Figure 11e). The interior of the membranes are covered by smooth rhodochrosite and nahcolite on which rhodochrosite spherules precipitate (Figure 11f). Point EDX analysis of the interior surface (Figure S10) has shown negligible Cl content. Hence, the relatively higher Na on the interior surface of the membrane could be because of nahcolite that appeared in the X-ray diffractions. The spherical rhodochrosite observed at the interior and exterior section of the membrane has a smoother surface than the spherules that make the membrane.

3.2.4. Cobalt, Magnesium, Zinc, and Iron (II) Mineral Vesicles

Figure 12 and Video S12 show the growth process and morphological evolution of cobalt chloride vesicles. In the beginning, the drop with a smooth surface hangs on the uppermost layer of Magadi water. The exterior of the drop corrugates gradually following the precipitation of minerals at the interface between the Co salt drop and Magadi water, which forms the hollow mineral vesicles. Cobalt vesicles gain the final color and morphology within an hour and fall to the bottom of the cuvette. As shown in the last panel of Figure 12, cobalt vesicles have an opening on top. Hollow mineral vesicles form by using saturated cobalt nitrate solution as well. The powder X-ray diffraction of cobalt nitrate vesicles reveals $Co_2(OH)_3Cl$ and nahcolite (Figure S11).

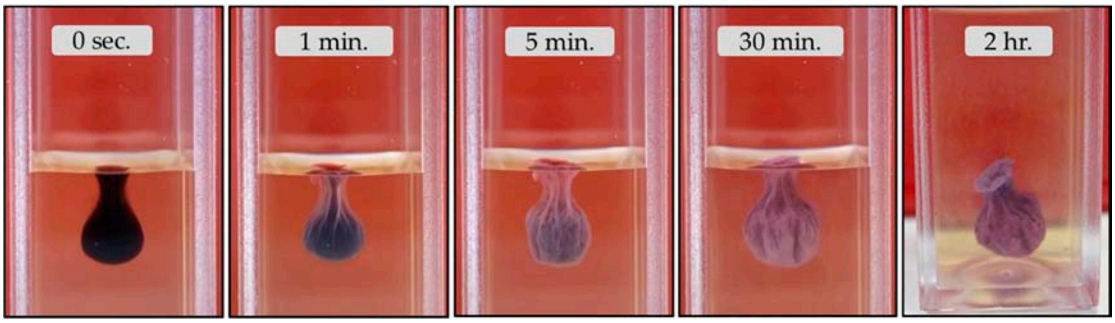

Figure 12. The growth process of cobalt chloride mineral vesicles in Magadi water.

Figure 13a and Video S13 show the growth of magnesium chloride vesicles. Figure 13a is a set of frames from Video S13. The transparent drop changes to white gradually due to mineral precipitation at the interface between the drop and Magadi water. Magnesium vesicles did not undergo visible swelling during the growth process. Osmotic pressure developed inside these vesicles, which was accommodated by the growth of a transparent dome-shaped membrane capping the opening on top as shown in Figure 13a (green arrow). This capping membrane forms when the salt solution trying to overflow out of the vesicle encounters the alkaline solution surrounding the vesicle. The overflow of the inner salt solution could be due to the vesicle's lack of expansion to accommodate the water diffusing into it. Once the membrane cap forms, the later overflow of salt solution ejects into the alkaline water due to its inability to rupture the capping membrane and forms a new vesicle (Figure 13a, blue arrow). The opening of these vesicles, therefore, serves as an osmotic pressure-relieving mechanism and inhibits membrane rupture that would form tubular membranes. Similar hollow vesicles form by using saturated magnesium sulphate drops (Figure 13b). Thenardite, blodite, loweite, and halite appear in the powder X-ray diffraction of magnesium sulphate vesicles (Figure S12).

Zinc sulphate vesicles are initially transparent like those mineral vesicles presented above and are morphologically similar to the manganese vesicles (Figure 14a). Gradually the color changes to white. During the growth process, these vesicles have a wide rupture opening that narrows down with time. The narrowing of the opening is accompanied by corrugation of the membrane (Figure 14b). Gunningite, gordaite and changoite appear in the powder X-ray diffraction of zinc sulphate vesicles (Figure S13).

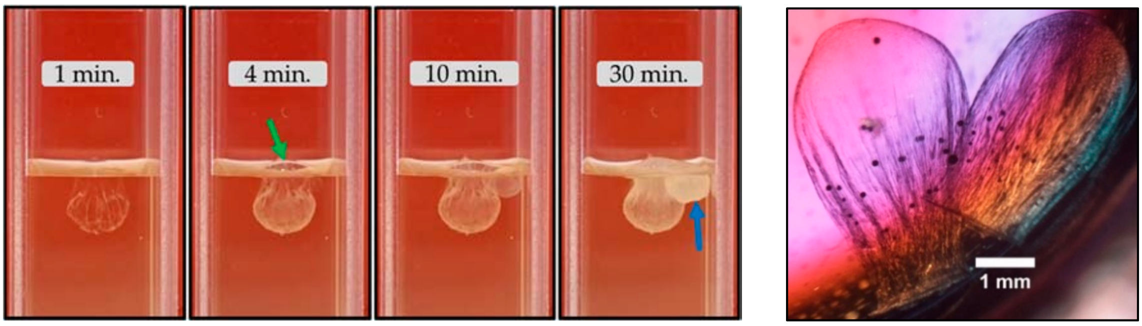

(**a**) (**b**)

Figure 13. (**a**) The growth process of magnesium chloride mineral vesicles in Magadi water (note: two vesicles grow from one drop; the width of the cuvette is 1.25 cm); (**b**) lateral view of magnesium sulphate vesicle.

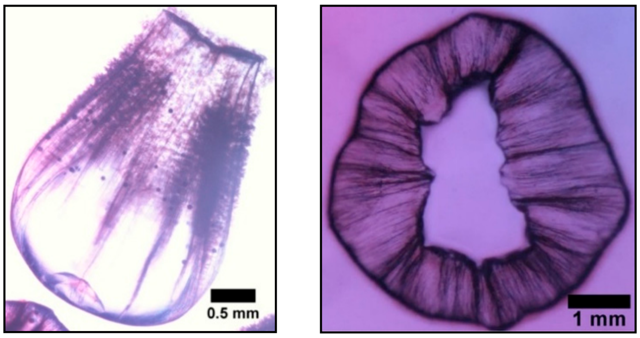

(**a**) (**b**)

Figure 14. Zinc sulphate mineral vesicle: (**a**) lateral view; (**b**) hollow vesicle with its opening.

Unlike Magadi gardens, iron (II) chloride and sulphate form hollow mineral vesicles (Figure 15 and Video S14) due to the free availability of Fe (II) in saturated solutions. These vesicles hang on the upper part of the water. The big vesicle in Figure 15a lies at the bottom because of a very shallow water column. The change in the shape of the vesicles was insignificant. The color changed from yellow to dark green. The dome-like membrane capping the opening of these vesicles is evidence of the overflow of the interior salt solution via the opening to accommodate the diffusion of water into the hollow membrane (Figure 15a, last panel). The overflowing interior solution forms very small vesicles at the bottom of the capping membrane, as in the case of the Mg vesicles (Figure 15a). Fe (II) vesicles are hollow mineral membranes (Figure 15b).

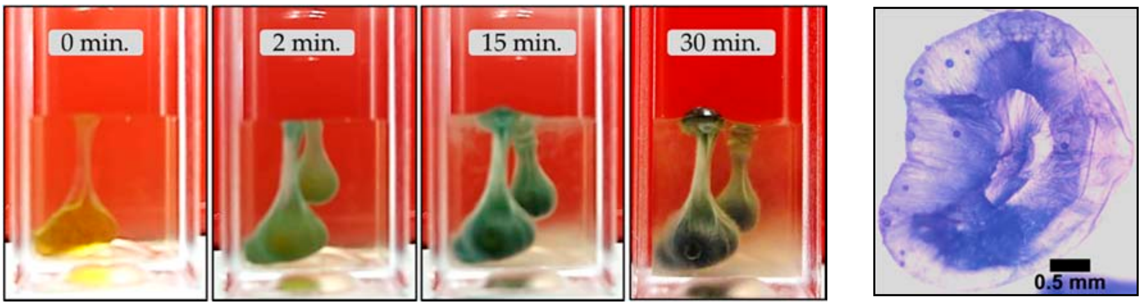

(**a**) (**b**)

Figure 15. (**a**) Growth process of iron (II) chloride vesicles. The small drop was added 25 s later (width of the cuvette is 1.25 cm); (**b**) iron (II) sulphate vesicle with its opening.

4. Discussion

The above results demonstrate that the mixing of high-pH, high-carbonate water from the soda Lake Magadi with metal salts results in the formation of membranous self-assembled structures. For the sake of clarity, we will discuss separately the two main type of experiments performed, namely a) the reactions of metal salt pellets with Magadi water, and b) the interaction of drops of a saturated solution of metal salts with Magadi water.

4.1. The Growth Process of Magadi Mineral Gardens

We have identified three groups of metals with different behavior when immersing pellets of their salt in Lake Magadi water:

1) The pellets of the less soluble and less acidic salts of Ba^{2+}, Mn^{2+} and Fe^{2+} (Table 2) do not react with the Magadi water.
2) In the case of Fe^{3+} ($FeCl_3$ and $Fe_2(SO_4)_3{\cdot}9H_2O$), Cu^{2+} ($CuCl_2{\cdot}6H_2O$ and $CuSO_4{\cdot}5H_2O$) and Zn^{2+} ($ZnCl_2$ and $ZnSO_4{\cdot}7H_2O$), the experiment resulted in the bursting of the initial membrane. The bursting of the membrane was accompanied by the bubbling of gases, and subsequent breaking of the forming mineral membranes in multiple pieces that later sediment (Videos S1–S3).
3) Unlike the aforementioned metals, the salts of Ca^{2+} ($CaCl_2{\cdot}2H_2O$) and Co^{2+} ($CoCl_2{\cdot}6H_2O$) and $Co(NO_3)_2{\cdot}6H_2O$) form tubular membranes, as shown in Figures 1 and 2 respectively. Likewise, Mg^{2+} ($MgCl_2{\cdot}6H_2O$) pellets immersed in Magadi water form mineral gardens (not presented here) that are morphologically similar to Co ($Co(NO_3)_2{\cdot}6H_2O$) gardens.

To interpret the three different behaviors of the metal salts, we should take into account two main variables, the pH of the saturated solution of these salts and their solubility in alkaline water.

The precipitation of tubular and vesicular membranes requires a reaction between the metal ions and the anionic species in the aqueous solutions. This reaction is possible when the metal salt pellets are dissolvable by the aqueous solution containing anionic species. There were no mineral precipitations from the pellets of Ba, Mn and Fe (II). However, when drops of soluble solutions of these salts were injected into the water of Magadi, both solutions react forming a metal carbonate membrane. Therefore, we can explain the absence of precipitation by the inability of the alkaline water of Lake Magadi to dissolve the pellets of the metal salts.

In the case of Fe (III), Cu and Zn, the interaction of the pellets with Magadi water resulted in extraordinary gas bubbling (see Videos S1–S3). This is due to the solubility and the extreme acidity of the solutions of these metals salts (Table 2). The metal pellets interact with the Magadi brines, the pellets dissolve and react with the brine forming a mineral membrane enveloping highly acidic metal solutions. High osmotic pressure develops inside these envelopes following the inflow of water to equilibrate the high pH and concentration gradient between the inner Fe (III), Cu and Zn solution and outer Magadi water [6,31]. The subsequent mixing of the Magadi carbonate brine with the low pH solutions shifts the initial high pH (10.9) to pH values below 8, consequently converting most carbonate and bicarbonate to carbonic acid and CO_2. CO_2 gas escapes from this quickly supersaturated solution, breaking the incipient membranes and disrupting the formation of continuous membranous structures. A similar bursting of metal-silicate hydrate membranes was observed during the growth of silica gardens with pellets of Fe (III), Cu and Zn in alkaline carbonate-rich water of Aqua de Ney springs with characteristic high pH, silica and carbonate content [9]. Note that the concentration of carbonate in Lake Magadi brines is 10-times that of Aqua de Ney water. Hence, there could be more CO_2 production and membrane disruption in Magadi than in Aqua de Ney water.

The interaction of Ca pellets with Magadi water forms a dome-like envelope in the middle of the pellets (Figure 1). This "osmotic envelope" [32] expands vertically and radially outward by a self-renewal precipitation process [32] due to high pressure inside the membranous envelope. The pressure inside the envelope develops due to osmotic-driven diffusion of water to equilibrate the concentration and pH gradient between the solutions inside and outside the envelope [6,31].

The elasticity of the envelope and slow inflow of water inhibit the bursting of the envelope and injection of the interior solution into the Magadi water. The absence of envelope rupture could be due to low CO_2 production as well. This is because of relatively less acidity than Co salts (Table 2) that form tubes by envelope rupture and inner salt jetting. Once the radial expansion ceases, transparent tubes grow horizontally from osmotic envelopes (Figure 1). The change in growth direction is likely due to the gradual rise in the density of the inner metal salt solution, which is evidenced by the vertically downward growth following the horizontal tube growth (see Figure 1g–h). The density rise could be due to further diffusion of water and subsequent dissolution of the salt pellet. For example, the Fe^{2+} concentration in the inner solution of silica garden tubes showed a marked initial increase for 10 h, reflecting the ongoing dissolution of the metal salt pellet [31].

So far, there are no reported Ca carbonate mineral gardens in natural water. However, Cardoso et al. [33] synthesized calcium gardens in commercial sodium carbonate solutions by using calcium chloride salts. The resulting membranes have vesicle forms in high sodium carbonate concentrations (1.33, 2, and 4 M), whereas at low concentration (0.5, 0.8, and 1 M), tubular gardens form [33]. The absence of envelope rupture in Magadi calcium gardens could be due to the high solute content and the high density of the water. The density of Lake Magadi brines varies mainly between 1.2 and 1.33 g/cm^3 [16,17]. The water used for the Magadi garden experiments is more concentrated than the brines reported in [16,17] and it may have a density greater than 1.2. This density is comparable with the density of silica solutions [32] reported to slow reactivity of the calcium salts in Ca-silica garden experiments. High concentration (high viscosity) silicate solution slows down the reaction and allows only a few slow-growing tubes [32]. The composition of Magadi Ca gardens include mainly calcite, gaylussite, pirssonite and minor trona. Cardoso et al. [33] reported calcite and gaylussite in Ca carbonate-hydroxide gardens.

The dissolution of Co pellets and the reaction with Magadi water form an envelope surrounding the pellets. Water diffuses into the membranous envelope to equilibrate the concentration and pH gradient between the two solutions [6,31]. Following water diffusion and a rise in internal pressure, the envelope expands and finally ruptures. At the point of rupture, the Co solution ejects into the Magadi water with the aid of buoyancy force [4,5]. Mineral precipitation at the interface between the ejected Co solution and Magadi water forms tubular membranes (Figure 2a). The tube grows in periodic pulses that give rise to the widening of the vertical tube due to the oscillation of pressure in the osmotic envelope, analogues to the growth process in budding regimes [34,35]. Due to very quick closure of the tubular membrane, osmotic pumping of the Co solution causes slow pressure build-up inside the membrane. Consequently, the growth occurs via repeated rupturing of the membrane and subsequent precipitation [5]. The oscillatory pressure is short-lived at the beginning due to the fast ejection of the inner solution. This results in the growth of small round branches at the lower part of the tube. Later, when the pH and the chemical gradient between the inner and outer solution decrease [6,31], the buoyancy of the inner solution declines and the vertical growth ends. Following the end of vertical growth, repeated rupture at the same location produces small tubes connected with the upper part of the main tubular structure [5]. The viscosity of the water could be another reason for the periodic pulses that may arise from the development of osmotic pressure that ejects the solution periodically when it reaches a critical point for penetrating the water. The buoyancy-driven ejection of Co solution forms longer tubes than Ca gardens, in which diffusion was the main driver for the expansion of the tubular mushroom-like membranes.

4.2. The Growth Process of Magadi Mineral Vesicles

Mineral precipitation triggered by pouring drops of saturated metal salt solutions in Magadi water forms hollow vesicular membranes. The formation of these mineral vesicles follows a general process that is schematically shown in Figure 16. Once the lighter metal salt drop is poured on top of the Magadi brine, the drop remains hanging on the uppermost layer of the water by a combination of buoyancy and surface tension. The shape of the liquid drop, which is controlled by its density, is maintained for the first few seconds to few minutes (Figure 16a), depending on the onset of mineral precipitation in the interface of the metal salt drops with the surrounding Magadi water. A good example of density control over the shape of the drops is observed in Ca vesicles (Figure 3a). Initially, the liquid drop has a transparent bulb-like shape (Figure 3a at 0 min.). Water diffusion (Figure 16b) by osmosis slowly dilutes the concentration of the drop and lowers its density relative to the initial drop at 0 min. Consequently, the bottom of the drop moves upward by buoyancy effect while expanding horizontally outward, and forms a spherical transparent drop (Figure 3a at 10 min. and Figure 16c). Later on, metal carbonate minerals precipitate at the interface, forming hollow vesicles (Figure 16d), which have an opening or mouth at their uppermost edge, i.e., at the place where the metal solution is in contact with the air. This opening eventually facilitates the escape to the atmosphere of the forming CO_2 gas, thus avoiding the bursting of the membrane. The evolution over time of the shape and characteristic of the membranes depends very much of the precipitation rate, which is a function of the supersaturation of the mineral phases, and the rate of equilibration of the inner and outer regions of the vesicle, which is a function of the evolving chemical gradient between the salt solution inside the vesicle and the exterior Magadi water. The porosity and the rigidity of the forming mineral membrane allow different osmosis-driven inflows of water molecules from the alkaline water towards the metal solution inside the membrane (Figure 16d). For instance, the osmotic inflow of water and the resulting internal pressure causes the swelling of the vesicles. During swelling, the shape of the vesicles change from bulb-like to spherical membranes (Figure 16b–d). In quickly precipitating vesicles and rigid membranes, only the size of the membrane increases while retaining the initial bulb-like morphology. In Mg and Fe (II) vesicles, the rigidity of the membrane causes overflow of the interior salt solution via the mouth and precipitation of secondary vesicles upon the interaction of the overflowing interior metal solution with the exterior Magadi water (Figures 13a and 15a). Finally, the combination of the buoyancy of the drop and osmotic diffusion of water forms floating, hollow bulb-like or spherical membranes with an opening at the upper edge.

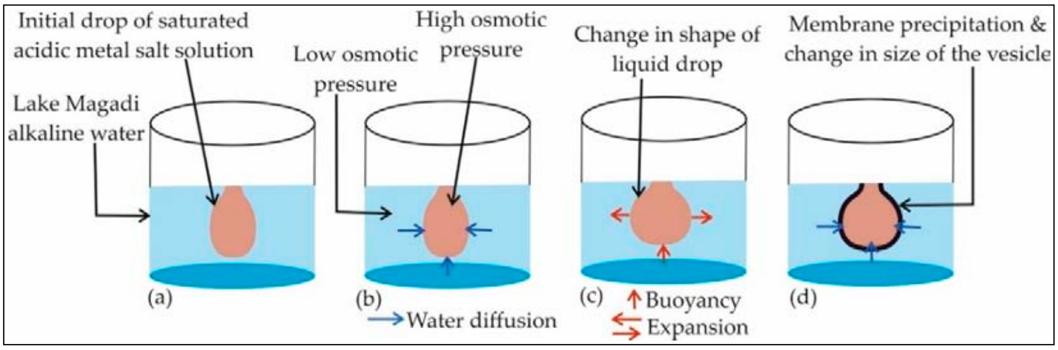

Figure 16. Illustration of the growth process of the Magadi vesicles from metal salt solution drops in Lake Magadi water.

Barium chloride drops float in Magadi water and the membranes precipitate in a few seconds. Unlike in Magadi mineral gardens, Ba vesicles form due to freely available Ba in solution. The vesicles have long-lasting corrugated surfaces and there is little change in the shape of the vesicles (Figure 6), inferring the rigidity of the membrane, unlike calcium vesicles. Among the Magadi vesicles, Ba vesicles were most stable during the preparation of SEM samples. Ba vesicles sink to the bottom in less than an hour following the intrusion of the water via the opening and subsequent rise in density of the inner solution. The density of the mineral (witherite) composing the membranes of Ba vesicles is higher than calcite and rhodochrosite. Hence, the mineral composition may play its role in sinking Ba vesicles. The composition of Ba vesicles was mainly witherite as confirmed from Raman spectra bands [29,36], EDX analysis and X-ray powder diffraction. Barium silica gardens [32] share a similar composition to the Magadi Ba vesicles. The silica garden tubes are composed of $BaCO_3$ and halite forming on the interior wall, evidencing Na+ diffusion across the membrane [32]. In the case of Ba vesicles, the interior halite could be from a combination of Na diffusion and the intruded Na-Cl rich water via the openings, which can form halite that remained uncleaned. Trona forms in Lake Magadi due to lake surface evaporation [16]. Therefore, the minor trona in the X-ray diffraction may form during the drying of the membrane.

After pouring Mn drops onto Magadi water, manganese carbonate precipitates in a few seconds at the interface between the two solutions and forms hanging hollow membranes. Unlike in Magadi gardens, Mn vesicles form due to the availability of free Mn in solution. The swelling and rotation in the clockwise and anti-clockwise direction of Mn vesicles is evidence of the osmotic diffusion of water across the membrane. Fast membrane precipitation changes the transparent drop into a white mineral vesicle. Rapid aggregation of rhodochrosite spheres forms highly fragile vesicles. The thin layer of water near the opening may intensify the shrinkage surface of the vesicles by forming thin membranes towards the opening. The Mn-silica vesicles form by the osmotic expansion of the drop and subsequent jetting of inner salt solution due to buoyancy [23]. The composition of the Mn silica gardens and vesicles [23,37] are mainly manganese oxides and hydroxides due to the absence of CO_3, whereas Magadi Mn vesicles are mainly of rhodochrosite.

In addition to rhodochrosite, nahcolite and halite form in Magadi vesicles. Halite appeared as a smooth layer covering the membrane. The fragile nature of Mn vesicles did not allow intense cleaning and halite could precipitate during the drying of the poorly cleaned membranes. Nahcolite is a mineral predicted to form at elevated pCO_2 [38,39]. In fact, nahcolite precipitate in Little Magadi lake where the direct release of magmatic CO_2 occurs [40,41]. The interaction of acidic Mn solution (Table 2) with carbonate-rich Magadi water may release CO_2 high enough to favor nahcolite formation. CO_2 production has been already reported from the early bursting of membranes in Fe (III), Cu, and Zn silica garden experiments with carbonate-rich Aqua de Ney water [9], which is a phenomenon observed in Fe (III), Cu, and $ZnCl_2$-based Magadi vesicles.

4.3. Calcium Magadi Mineral Self-Organization and the Origin of Life

Upon the addition of Ca salt drops in Magadi water, mainly $CaCO_3$ mineral membranes precipitate at the interface between the two solutions. The evolution of the color of Ca vesicles (Figure 3a) could be due to precipitation of calcium carbonate minerals followed by halite and trona precipitation on the exterior of the membrane as observed in the EDX map of the membranes (Figure 5a). The minimal shrinkage surfaces of Ca vesicles may infer elasticity of the membrane as observed in Ca gardens. These membranous structures are selective barriers between the two distinct solutions forming a chemical gradient across the membranes. A distinct chemical gradient across the membranes [6,31] and subsequent osmotic-driven inflow of water and buoyancy-driven jetting of the acidic metal salt solutions were one of the driving mechanisms for the growth of tubular silica gardens [4,5] and carbonate-hydroxide gardens [33]. Due to the lower density of calcium salt inside the vesicle, the membranes float on the uppermost layer of the water. The chemical and pH gradient across mineral membranes causes osmotic diffusion of water into the Magadi vesicles, as evidenced from the horizontal swelling and morphological evolution from bulb-like to spherical vesicles of calcium (Figure 3a and Video S9). The morphological evolution of the drop at the beginning, while it was transparent, could be due to buoyancy that pushes the bottom of the drop to the surface following dilution of the interior solution and subsequent lowering in density. The opening on the top of the vesicles serves as a pressure-relieving mechanism, which was observed in magnesium and iron (II) chloride vesicles (Figures 13a and 15a).

Calcite, vaterite, and gaylussite minerals observed in Magadi vesicles were reported in calcium carbonate-hydroxide vesicles and gardens synthesized in sodium carbonate solution by using calcium chloride salts [33]. The halite that appeared both in the SEM images and in XRD data could be due to evaporation of Magadi water that remains uncleaned. Trona and halite commonly form during Lake Magadi surface evaporation. The spherical vateritic and calcitic morphology may arise from the transformation of spherical amorphous calcium carbonate via the routes reported in [42,43]. However, it is important to perform time-resolved in-situ X-ray diffraction and Raman spectroscopy of the vesicles to clearly understand the mineralogical evolution during the growth process. Gaylussite is a common authigenic mineral in modern muds of Lake Magadi where local sources of calcium are available [24,44].

A recent study [15] has reported a direct correlation between phosphate and carbonate concentration values in lakes and seas. The reason is most likely due to kinetics-controlled precipitation. The supersaturation value of a given phase in solution can be defined by the equation:

$$\text{Ionic Activity Product/Solubility Product} \tag{1}$$

The solubility product of calcium phosphate is lower than that of calcium carbonate(s). Therefore, in circumneutral solutions, thermodynamically calcium phosphate precipitates first and the remaining solution is devoid of phosphate. However, at the very high carbonate concentration values of soda lakes, the saturation index of calcium carbonate can be much higher than that of calcium phosphate, thus forming gaylussite and/or calcite, sequestering excess calcium and leaving the phosphate as soluble species in the soda lake brines [15]. Similarly, our Magadi calcium mineral vesicles are composed of calcite, vaterite and gaylussite. We have confirmed by X-ray diffraction, EDX and FESEM analysis the total absence of phosphorous and calcium phosphate minerals in the Magadi vesicles and gardens, thus confirming the interesting observation that in soda lakes, carbonate minerals sequestrate Ca and prevent phosphate removal by apatite precipitation [15]. Further work is underway to a deeper exploration of this idea through analysis of phosphate in the residual water that remained after the synthesis of calcium mineral vesicles and gardens.

It has been suggested that soda lakes and alkaline silica-rich environments are analogous to early Earth's oceans [3,11–14]. Lake Magadi is analogous to hydrothermal chert environments on the Archean Earth [45,46]. The geochemical plausibility of mineral self-organization in soda lakes such as Lake Magadi infers that mineral self-assembly may have taken place on the soda oceans of early Earth. It has been reported recently that phosphate, an ion central to the origin of life and metabolism [47,48], accumulates in carbonate-rich soda lakes due to preferential calcium precipitation preventing apatite formation [15]. These phosphate-rich lakes may have preferentially formed on the prebiotic Earth [15]. It is believed that silica gardens, which catalyze the synthesis of prebiotically relevant compounds [7,23], were forming in the alkaline silica and carbonate-rich oceans of Hadean Earth [3]. The high silica, carbonate and phosphate content [3,7,15] and the plausibility of mineral self-assembly in modern soda lakes may imply that alkaline soda oceans of the early Earth could probably be the "one-pot" environments containing the important ingredients for the synthesis of prebiotically relevant molecules and plausible settings for the origin of life.

It should be noted that the contribution of silica to the precipitation of our synthesized Magadi vesicles and gardens is negligible, the membranous mineral structure being mostly made of metal carbonate precipitation. The silica content of the water collected during our field trip was not high enough for the formation of silica gardens and vesicles. The low silica content is due to two reasons. First, the samples were collected in May 2018 after an unanticipated early raining season, but more importantly, because in the last four years, all the soda lakes of the Rift Valley have experienced a raising of the water level by a few meters, the reason for which is unknown. We are performing fluid-rock interaction experiments with Magadi brines and cherts to enrich the concentration of silica to values previously reported in the literature. In addition, we are organizing a new field trip for sampling Lake Magadi during the driest season. Testing the role of silica in inducing mineral self-assembly will increase the potential of modern soda lakes to be considered as "one-pot" geochemical environments for the origin of life.

Supplementary Materials: The following are available online at http://www.mdpi.com/2073-4352/10/6/467/s1, Figure S1: Powder X-ray diffraction of mineral gardens synthesized by immersing $CaCl_2{\cdot}2H_2O$ pellets in Lake Magadi water, Figure S2: Powder X-ray diffraction of mineral gardens produced by immersing $CoCl_2{\cdot}6H_2O$ pellet in Magadi water, Figure S3: Raman spectra of mineral vesicles synthesized by adding drops of saturated $CaCl_2{\cdot}2H_2O$ solution onto Lake Magadi water, Figure S4: EDX mapping of membrane cross-section of vesicles synthesized by adding saturated $CaCl_2 \cdot 2H_2O$ solution onto Lake Magadi water, Figure S5: EDX analysis of membrane cross-section of vesicles synthesized by adding saturated $CaCl_2 \cdot 2H_2O$ solution onto Lake Magadi water, Figure S6: EDX analysis of calcium mineral membrane cross-section containing gaylussite, Figure S7: EDX analysis of membrane cross-section of vesicles synthesized by adding saturated $BaCl_2 \cdot 2H_2O$ solution onto Lake Magadi water, Figure S8: EDX mapping of membrane cross-section of vesicles synthesized by adding saturated $BaCl_2 \cdot 2H_2O$ solution onto Lake Magadi water, Figure S9: EDX analysis of the cross-section of mineral vesicles synthesized by adding saturated $MnCl_2 \cdot 4H_2O$ solution onto Magadi water, Figure S10: EDX analysis of the interior surface of mineral vesicles synthesized by adding saturated $MnCl_2 \cdot 4H_2O$ solution onto Magadi water, Figure S11: Powder X-ray diffraction of mineral vesicles synthesized by adding saturated $Co(NO_3)_2 \cdot 6H_2O$ solution onto Lake Magadi water, Figure S12: Powder X-ray diffraction of mineral vesicles synthesized by adding saturated $MgSO_4$ solution onto Lake Magadi water, Figure S13: Powder X-ray diffraction of mineral vesicles synthesized by adding saturated $ZnSO_4 \cdot 7H_2O$ solution onto Lake Magadi water, Video S1: Gas bubbling and bursting of reaction products of the $FeCl_3$ pellet and Magadi water, Video S2: Gas bubbling and bursting of reaction products of the $CuCl_2 \cdot 6H_2O$ pellet and Magadi water, Video S3: Gas bubbling and bursting of reaction products of the $ZnCl_2$ pellet and Magadi water, Video S4: Growth process of mineral gardens by the interaction of the $CaCl_2 \cdot 2H_2O$ pellet with Magadi water, Video S5: Growth process of mineral gardens by the interaction of the $Co(NO_3)_2 \cdot 6H_2O$ salt pellet with Magadi water, Video S6: Gas bubbling and bursting upon the reaction of drops of saturated $FeCl_3$ solution and Magadi water, Video S7: Gas bubbling and bursting upon the reaction of drops of saturated $CuCl_2 \cdot 6H_2O$ solution and Magadi water, Video S8: Gas bubbling and bursting upon the reaction of drops of saturated $ZnCl_2$ solution and Magadi water, Video S9: Synthesis of mineral vesicles by adding saturated $CaCl_2 \cdot 2H_2O$ solution onto Magadi water, Video S10: Synthesis of mineral vesicles by adding saturated $BaCl_2 \cdot 2H_2O$ solution onto Magadi water, Video S11: Synthesis of mineral vesicles by adding saturated $MnCl_2 \cdot 4H_2O$ solution onto Magadi water, Video S12: Synthesis of mineral vesicles by adding saturated CoCl2·6H2O solution onto Magadi water, Video S13: Synthesis of mineral vesicles by adding saturated $MgCl_2 \cdot 6H_2O$ solution onto Magadi water, Video S14: Synthesis of mineral vesicles by adding saturated $FeCl_2 \cdot 4H_2O$ solution onto Magadi water.

Author Contributions: M.G. performed the experiments, characterized the materials and analyzed the results; J.M.G.-R. conceived and designed the experiments and analyzed the results; C.V.-E. performed X-ray diffraction experiments and mineral phase identification; I.G.-T. performed the SEM study and EDX analyses; M.G. and J.M.G.-R. wrote the paper. All authors have read and agreed to the published version of the manuscript.

Funding: The authors thank the European Research Council under the European Union's seventh Framework Program (FP7/2007-2013)/ERC grant agreement no. 340863 and the Spanish "Ministerio de Educacion y Ciencia" for the financial support to the project CGL2016-78971-P. MG. acknowledges Grant No. BES-2017-081105 of the "Ministerio de Ciencia, Innovacion y Universidades" of the Spanish government.

Acknowledgments: The authors thank Alicia González Segura for help with the scanning electron microscope, Francisca Espinosa, Raquel Fernandez-Penas, and Joaquín Criado-Reyes for technical help in the laboratory. We also thank National Commission for Science Technology and Information, National Environmental Management Authority and Kenya Wildlife Services for research permissions. Magadi Tata Chemicals Ltd. and National Museums of Kenya provide logistic help. Finally, we also acknowledge very much Patricia Gitari, Lukas Sossoika, and Tara Barwa for their assistance in fieldwork.

Conflicts of Interest: The authors declare no conflict of interest.

References

1. García-Ruiz, J.M.; Otálora, F. Crystal Growth in Geology: Patterns on the Rocks. In *Handbook of Crystal Growth*; Nishinaga, T., Rudolph, P., Eds.; Elsevier: Amsterdam, The Netherlands, 2015; Volume II, pp. 1–43. [CrossRef]
2. Nakouzi, E.; Steinbock, O. Self-organization in precipitation reactions far from the equilibrium. *Sci. Adv.* **2016**, *2*, e1601144. [CrossRef] [PubMed]
3. García-Ruiz, J.M.; van Zuilen, M.; Bach, W. Mineral self-organization on a lifeless planet. *Phys. Life Rev.* **2020**. (in press). [CrossRef]
4. Kellermeier, M.; Glaab, F.; Melero-García, E.; García-Ruiz, J.M. Experimental Techniques for the Growth and Characterization of Silica Biomorphs and Silica Gardens. In *Methods in Enzymology*; De Yoreo, J.J., Ed.; Academic Press: Cambridge, MA, USA, 2013; Volume 532, pp. 225–256. [CrossRef]
5. Barge, L.M.; Cardoso, S.S.S.; Cartwright, J.H.E.; Cooper, G.J.T.; Cronin, L.; De Wit, A.; Doloboff, I.J.; Escribano, B.; Goldstein, R.E.; Haudin, F.; et al. From Chemical Gardens to Chemobrionics. *Chem. Rev.* **2015**, *115*, 8652–8703. [CrossRef] [PubMed]
6. Glaab, F.; Kellermeier, M.; Kunz, W.; Morallon, E.; García-Ruiz, J.M. Formation and Evolution of Chemical Gradients and Potential Differences Across Self-Assembling Inorganic Membranes. *Angew. Chemie* **2012**, *124*, 4393–4397. [CrossRef]

7. Saladino, R.; Di Mauro, E.; García-Ruiz, J.M. A Universal Geochemical Scenario for Formamide Condensation and Prebiotic Chemistry. *Chem. A Eur. J.* **2019**, *25*, 3181–3189. [CrossRef]
8. Satoh, H.; Tsukamoto, K.; Garcia-Ruiz, J.M. Formation of chemical gardens on granitic rock: A new type of alteration for alkaline systems. *Eur. J. Mineral.* **2014**, *26*, 415–426. [CrossRef]
9. García-Ruiz, J.M.; Nakouzi, E.; Kotopoulou, E.; Tamborrino, L.; Steinbock, O. Biomimetic mineral self-organization from silica-rich spring waters. *Sci. Adv.* **2017**, *3*, e1602285. [CrossRef]
10. García-Ruiz, J.M. Carbonate precipitation into alkaline silica-rich environments. *Geology* **1998**, *26*, 843–846. [CrossRef]
11. Kempe, S.; Degens, E.T. An early soda ocean? *Chem. Geol.* **1985**, *53*, 95–108. [CrossRef]
12. Kempe, S.; Kazmierczak, J.; Degens, E.T. The Soda Ocean Concept and Its Bearing on Biotic Evolution. In *Origin, Evolution, and Modern Aspects of Biomineralization in Plants and Animals*; Crick, R.E., Ed.; Springer: Boston, MA, USA, 1989; pp. 29–43.
13. García-Ruiz, J.M. Geochemical Scenarios for the Precipitation of Biomimetic Inorganic Carbonates. In *Carbonate Sedimentation and Diagenesis in the Evolving Precambrian World*; Grotzinger, J.P., James, N.P., Eds.; SEPM Society for Sedimentary Geology: Tulsa, OK, USA, 2000; Volume 67, pp. 75–89.
14. Kempe, S.; Kazmierczak, J. Soda Ocean Hypothesis. In *Encyclopedia of Geobiology*; Reitner, J., Thiel, V., Eds.; Springer: Dordrecht, The Netherlands, 2011; pp. 829–833.
15. Toner, J.D.; Catling, D.C. A carbonate-rich lake solution to the phosphate problem of the origin of life. *Proc. Natl. Acad. Sci. USA* **2020**, *117*, 883–888. [CrossRef]
16. Eugster, H.P. Chemistry and origin of the brines of Lake Magadi, Kenya. *Miner. Soc. Amer. Spec. Pap.* **1970**, *3*, 213–235.
17. Jones, B.F.; Eugster, H.P.; Rettig, S.L. Hydrochemistry of the Lake Magadi basin, Kenya. *Geochim. Cosmochim. Acta* **1977**, *41*, 53–72. [CrossRef]
18. Baker, B.H. *Geology of the Magadi Area*; Geological Survey of Kenya: Nairobi, Kenya, 1958; Volume 42, p. 81.
19. Baker, B.H. *Geology of the Area south of Magadi*; Geological Survey of Kenya: Nairobi, Kenya, 1963; Volume 61, p. 27.
20. Deocampo, D.M.; Renaut, R.W. Geochemistry of African Soda Lakes. In *Soda Lakes of East Africa*; Schagerl, M., Ed.; Springer: Cham, Switzerland, 2016; pp. 77–93.
21. Garrels, R.M.; Mackenzie, F.T. Origin of the Chemical Compositions of Some Springs and Lakes. In *Equilibrium Concepts in Natural Water Systems*; Stumm, W., Ed.; ACS: Washington, DC, USA, 1967; pp. 222–242. [CrossRef]
22. Hardie, L.A.; Eugster, H.P. The Evolution of Closed-Basin Brines. *Miner. Soc. Amer. Spec. Pap.* **1970**, *3*, 273–290.
23. Mattia Bizzarri, B.; Botta, L.; Pérez-Valverde, M.I.; Saladino, R.; Di Mauro, E.; García-Ruiz, J.M. Silica Metal Oxide Vesicles Catalyze Comprehensive Prebiotic Chemistry. *Chem. A Eur. J.* **2018**, *24*, 8126–8132. [CrossRef]
24. Eugster, H.P. Lake Magadi, Kenya, and Its Precursors. In *Developments in Sedimentology*; Nissenbaum, A., Ed.; Elsevier: Amsterdam, The Netherlands, 1980; Volume 28, pp. 195–232. [CrossRef]
25. Jones, B.F.; Rettig, S.L.; Eugster, H.P. Silica in Alkaline Brines. *Science* **1967**, *158*, 1310–1314. [CrossRef]
26. Haynes, W.M. (Ed.) *CRC Handbook of Chemistry and Physics*, 97th ed.; CRC Press: Boca Raton, FL, USA, 2016; ISBN 978-1-4987-5429-3.
27. Bischoff, W.D.; Sharma, S.K.; MacKenzie, F.T. Carbonate ion disorder in synthetic and biogenic magnesian calcites: A Raman spectral study. *Am. Mineral.* **1985**, *70*, 581–589.
28. Urmos, J.; Sharma, S.K.; Mackenzie, F.T. Characterization of some biogenic carbonates with Raman spectroscopy. *Am. Mineral.* **1991**, *76*, 641–646.
29. Burgio, L.; Clark, R.J. Library of FT-Raman spectra of pigments, minerals, pigment media and varnishes, and supplement to existing library of Raman spectra of pigments with visible excitation. *Spectrochim. Acta Part. A Mol. Biomol. Spectrosc.* **2001**, *57*, 1491–1521. [CrossRef]
30. Frezzotti, M.L.; Tecce, F.; Casagli, A. Raman spectroscopy for fluid inclusion analysis. *J. Geochemical Explor.* **2012**, *112*, 1–20. [CrossRef]
31. Glaab, F.; Rieder, J.; García-Ruiz, J.M.; Kunz, W.; Kellermeier, M. Diffusion and precipitation processes in iron-based silica gardens. *Phys. Chem. Chem. Phys.* **2016**, *18*, 24850–24858. [CrossRef]
32. Cartwright, J.H.E.; Escribano, B.; Khokhlov, S.; Sainz-Díaz, C.I. Chemical gardens from silicates and cations of group 2: A comparative study of composition, morphology and microstructure. *Phys. Chem. Chem. Phys.* **2011**, *13*, 1030–1036. [CrossRef]

33. Cardoso, S.S.S.; Cartwright, J.H.E.; Sainz-Díaz, C.I. Carbonate-hydroxide chemical-garden tubes in the soda ocean of Enceladus: Abiotic membranes and microtubular forms of calcium carbonate. *Icarus* **2019**, *319*, 337–348. [CrossRef]
34. Thouvenel-Romans, S.; Steinbock, O. Oscillatory growth of silica tubes in chemical gardens. *J. Am. Chem. Soc.* **2003**, *125*, 4338–4341. [CrossRef]
35. Thouvenel-Romans, S.; Van Saarloos, W.; Steinbock, O. Silica tubes in chemical gardens: Radius selection and its hydrodynamic origin. *Europhys. Lett.* **2004**, *67*, 42–48. [CrossRef]
36. Lafuente, B.; Downs, R.T.; Yang, H.; Stone, N. The power of databases: The RRUFF project. In *Highlights in Mineralogical Crystallography*; Armbruster, T., Danisi, R.M., Eds.; De Gruyter: Berlin, Germany, 2016; pp. 1–29.
37. Cartwright, J.H.E.; Escribano, B.; Sainz-Díaz, C.I. Chemical-Garden Formation, Morphology, and Composition. I. Effect of the Nature of the Cations. *Langmuir* **2011**, *27*, 3286–3293. [CrossRef]
38. Lowenstein, T.K.; Demicco, R.V. Elevated Eocene Atmospheric CO_2 and Its Subsequent Decline. *Science* **2006**, *313*, 1928. [CrossRef]
39. Jagniecki, E.A.; Lowenstein, T.K. Evaporites of the Green River Formation, Bridger and Piceance Creek Basins: Deposition, Diagenesis, Paleobrine Chemistry, and Eocene Atmospheric CO_2. In *Stratigraphy and Paleolimnology of the Green River Formation, Western USA*; Smith, M.E., Carroll, A.R., Eds.; Springer: Dordrecht, The Netherlands, 2015; pp. 277–312.
40. Lee, H.; Muirhead, J.D.; Fischer, T.P.; Ebinger, C.J.; Kattenhorn, S.A.; Sharp, Z.D.; Kianji, G. Massive and prolonged deep carbon emissions associated with continental rifting. *Nat. Geosci.* **2016**, *9*, 145–149. [CrossRef]
41. Lowenstein, T.K.; Jagniecki, E.A.; Carroll, A.R.; Smith, M.E.; Renaut, R.W.; Owen, R.B. The Green River salt mystery: What was the source of the hyperalkaline lake waters? *Earth-Science Rev.* **2017**, *173*, 295–306. [CrossRef]
42. Rodriguez-Blanco, J.D.; Shaw, S.; Benning, L.G. The kinetics and mechanisms of amorphous calcium carbonate (ACC) crystallization to calcite, via vaterite. *Nanoscale* **2011**, *3*, 265–271. [CrossRef]
43. Bots, P.; Benning, L.G.; Rodriguez-Blanco, J.-D.; Roncal-Herrero, T.; Shaw, S. Mechanistic Insights into the Crystallization of Amorphous Calcium Carbonate (ACC). *Cryst. Growth Des.* **2012**, *12*, 3806–3814. [CrossRef]
44. Surdam, R.C.; Eugster, H.P. Mineral reactions in the sedimentary deposits of the Lake Magadi region, Kenya. *Geol. Soc. Am. Bull.* **1976**, *87*, 1739. [CrossRef]
45. Eugster, H.P.; Jones, B.F. Gels Composed of Sodium-Aluminium Silicate, Lake Magadi, Kenya. *Science* **1968**, *161*, 160–163. [CrossRef]
46. Reinhardt, M.; Goetz, W.; Duda, J.-P.; Heim, C.; Reitner, J.; Thiel, V. Organic signatures in Pleistocene cherts from Lake Magadi (Kenya) – implications for early Earth hydrothermal deposits. *Biogeosciences* **2019**, *16*, 2443–2465. [CrossRef]
47. Pasek, M.A.; Gull, M.; Herschy, B. Phosphorylation on the early earth. *Chem. Geol.* **2017**, *475*, 149–170. [CrossRef]
48. Plattner, H.; Verkhratsky, A. Inseparable tandem: Evolution chooses ATP and Ca^{2+} to control life, death and cellular signalling. *Philos. Trans. R. Soc. B Biol. Sci.* **2016**, *371*, 20150419. [CrossRef]

Supplementary Materials

Mineral vesicles and chemical gardens from carbonate-rich alkaline brines of Lake Magadi, Kenya

Melese Getenet, Juan Manuel García-Ruiz, Cristobal Verdugo-Escamilla and Isabel Guerra-Tschuschke

This document includes legends for the videos and the following figures:

Other Supplementary Material for this manuscript includes the following videos under https://doi.org/10.6084/m9.figshare.12652319.v2

Video S1: Gas bubbling and bursting of reaction products of the $FeCl_3$ pellet and Magadi water

Video S2: Gas bubbling and bursting of reaction products of the $CuCl_2·6H_2O$ pellet and Magadi water

Video S3: Gas bubbling and bursting of reaction products of the $ZnCl_2$ pellet and Magadi water

Video S4: Growth process of mineral gardens by the interaction of the $CaCl_2·2H_2O$ pellet with Magadi water

Video S5: Growth process of mineral gardens by the interaction of the $Co(NO_3)_2·6H_2O$ salt pellet with Magadi water

Video S6: Gas bubbling and bursting upon the reaction of drops of saturated $FeCl_3$ solution and Magadi water

Video S7: Gas bubbling and bursting upon the reaction of drops of saturated $CuCl_2·6H_2O$ solution and Magadi water

Video S8: Gas bubbling and bursting upon the reaction of drops of saturated $ZnCl_2$ solution and Magadi water

Video S9: Synthesis of mineral vesicles by adding saturated $CaCl_2·2H_2O$ solution onto Magadi water

Video S10: Synthesis of mineral vesicles by adding saturated $BaCl_2·2H_2O$ solution onto Magadi water

Video S11: Synthesis of mineral vesicles by adding saturated $MnCl_2·4H_2O$ solution onto Magadi water Video S12: Synthesis of mineral vesicles by adding saturated CoCl2·6H2O solution onto Magadi water

Video S13: Synthesis of mineral vesicles by adding saturated $MgCl_2·6H_2O$ solution onto Magadi water

Video S14: Synthesis of mineral vesicles by adding saturated $FeCl_2·4H_2O$ solution onto Magadi water

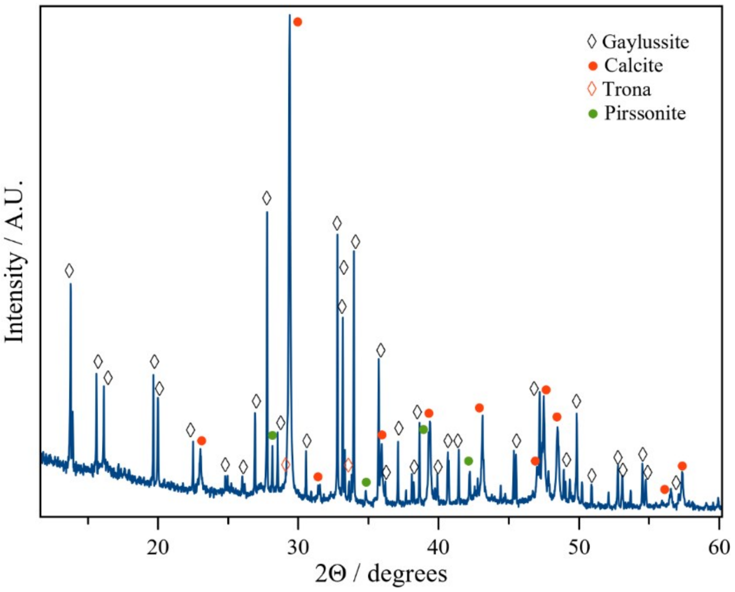

Figure S1: Powder X-ray diffraction of mineral gardens synthesized by immersing $CaCl_2·2H_2O$ pellets in Lake Magadi water

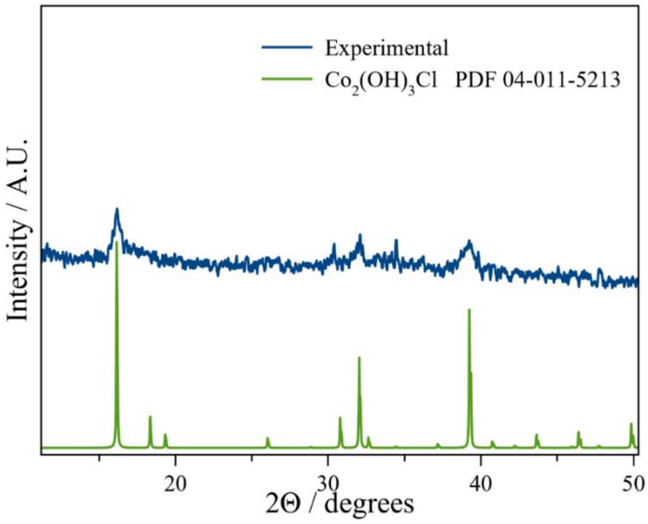

Figure S2: Powder X-ray diffraction of mineral gardens produced by immersing $CoCl_2 \cdot 6H_2O$ pellet in Magadi water

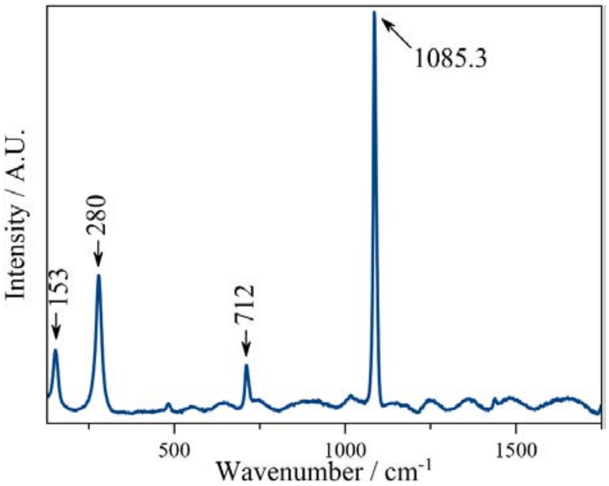

Figure S3: Raman spectra of mineral vesicles synthesized by adding drops of saturated $CaCl_2 \cdot 2H_2O$ solution onto Lake Magadi water (153, 280, 712, and 1085.3 cm^{-1} are translational, librational, in-plane bending and symmetric stretching modes respectively)

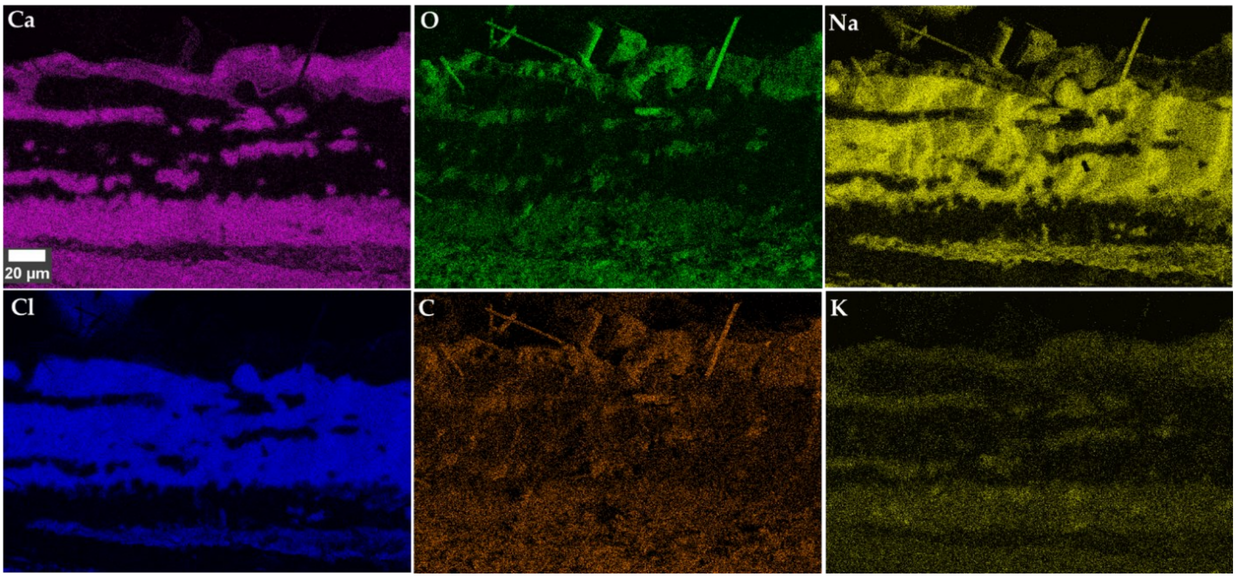

Figure S4: EDX mapping of membrane cross-section of vesicles synthesized by adding saturated $CaCl_2 \cdot 2H_2O$ solution onto Lake Magadi water

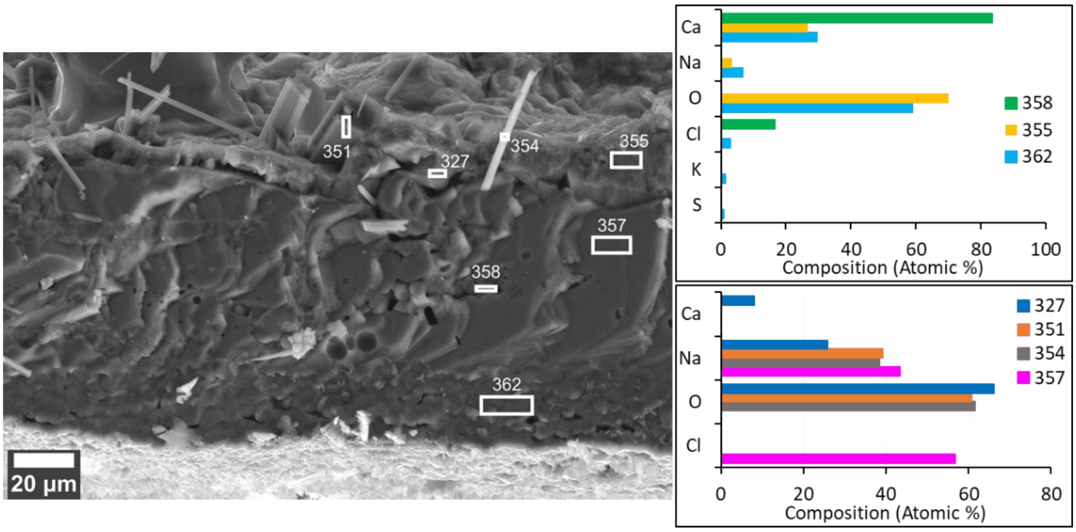

Figure S5: EDX analysis of membrane cross-section of vesicles synthesized by adding saturated $CaCl_2 \cdot 2H_2O$ solution onto Lake Magadi water

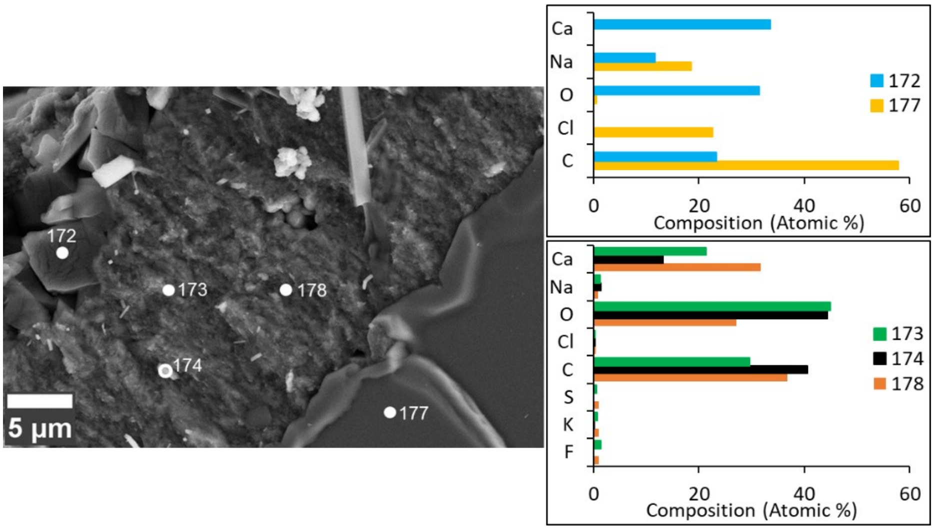

Figure S6: EDX analysis of calcium mineral membrane cross-section containing gaylussite

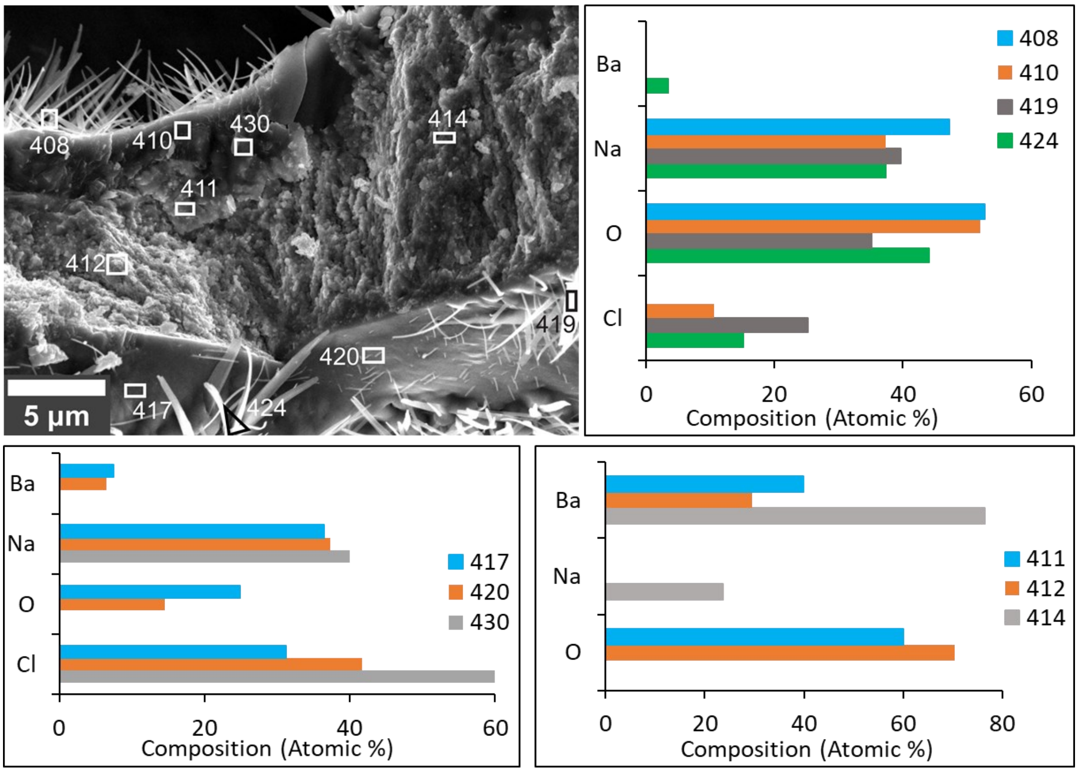

Figure S7: EDX analysis of membrane cross-section of vesicles synthesized by adding saturated $BaCl_2 \cdot 2H_2O$ solution onto Lake Magadi water

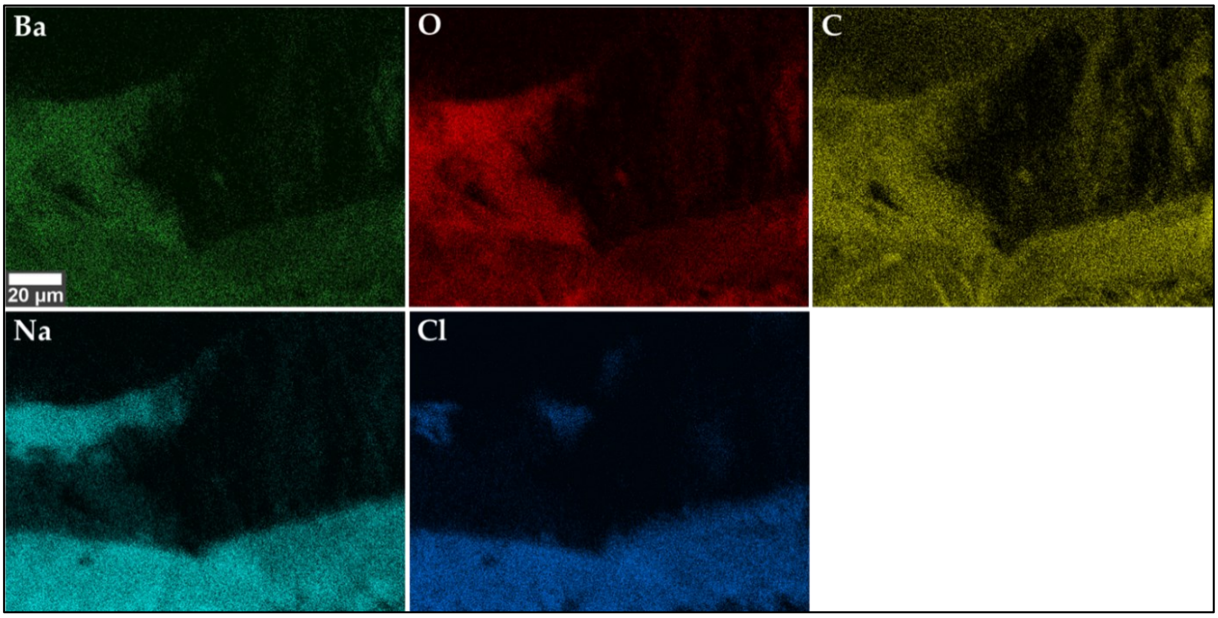

Figure S8: EDX mapping of membrane cross-section of vesicles synthesized by adding saturated $BaCl_2 \cdot 2H_2O$ solution onto Lake Magadi water

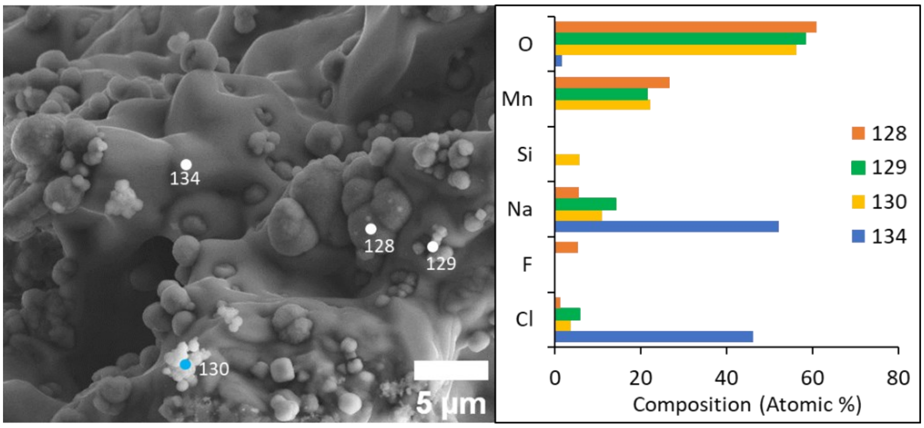

Figure S9: EDX analysis of the cross-section of mineral vesicles synthesized by adding saturated $MnCl_2 \cdot 4H_2O$ solution onto Magadi water

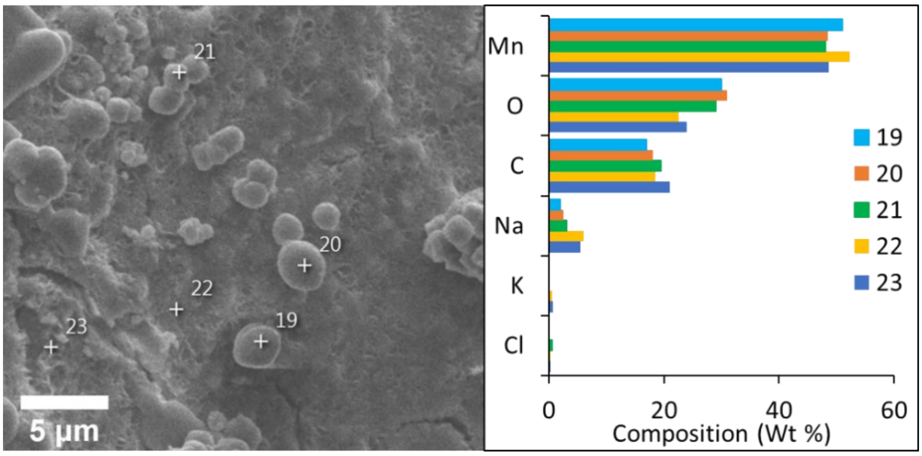

Figure S10: EDX analysis of the interior surface of mineral vesicles synthesized by adding saturated $MnCl_2 \cdot 4H_2O$ solution onto Magadi water

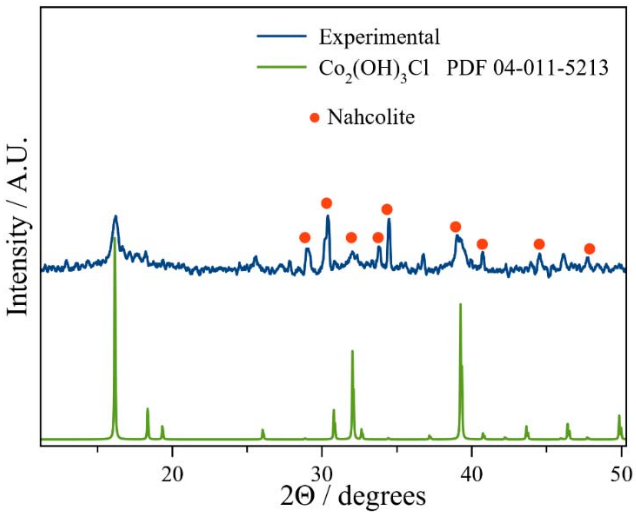

Figure S11: Powder X-ray diffraction of mineral vesicles synthesized by adding saturated $Co(NO_3)_2{\cdot}6H_2O$ solution onto Lake Magadi water

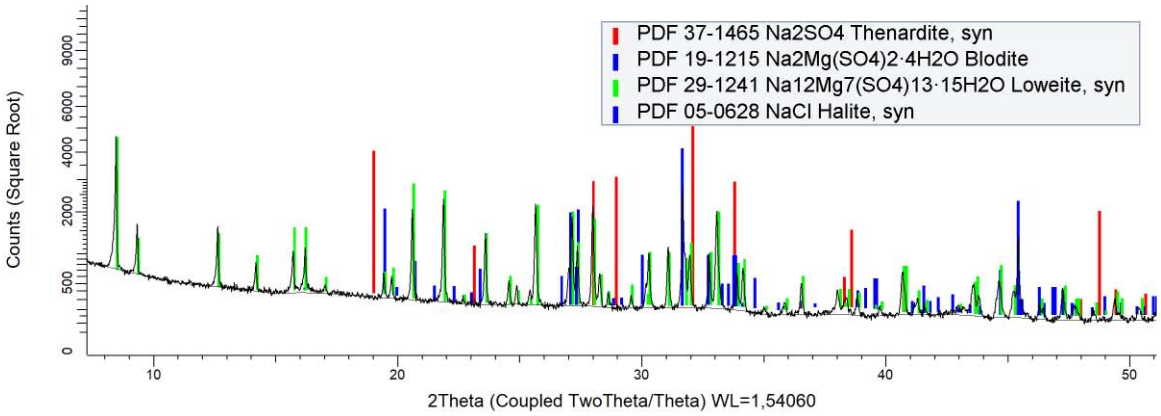

Figure S12: Powder X-ray diffraction of mineral vesicles synthesized by adding saturated $MgSO_4$ solution onto Lake Magadi water

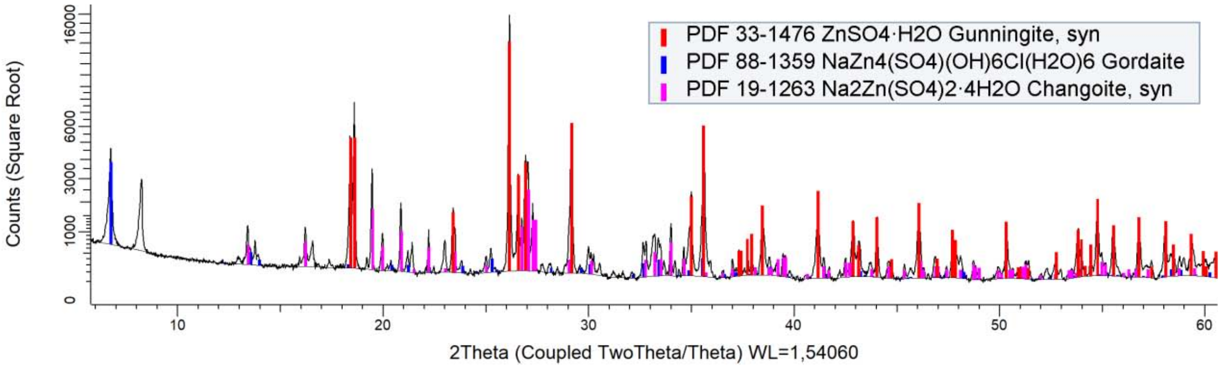

Figure S13: Powder X-ray diffraction of mineral vesicles synthesized by adding saturated $ZnSO_4{\cdot}7H_2O$ solution onto Lake Magadi water

Chapter 5

5. Tubular Structures of Calcium Carbonate: Formation, Characterization, and Implications in Natural Mineral Environments [1]

Supporting Information for this article is found at the end of this chapter.

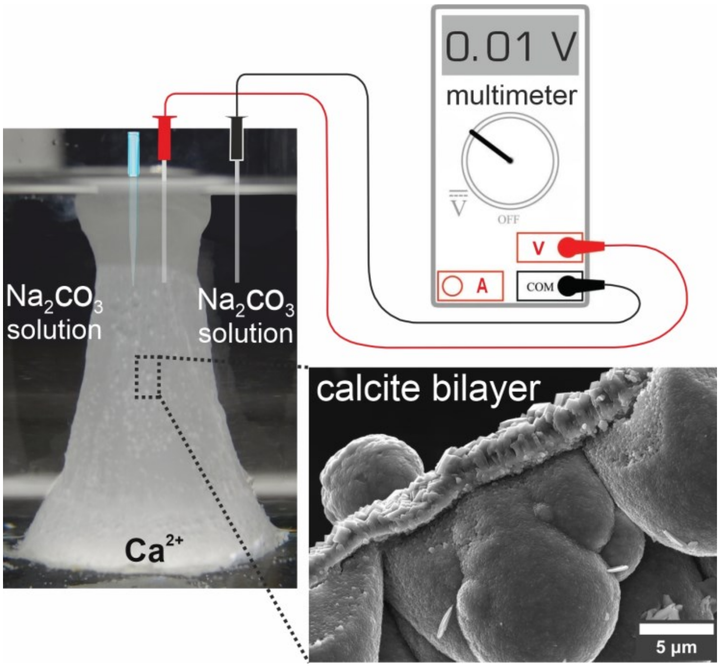

Prebiotic barriers? Calcium carbonate chemical gardens are self-assembled mineral membranes that form upon contact of a solid calcium salt with an alkaline carbonate-rich solution. In-situ studies on solution speciation and ex-situ membrane characterization show that the tube walls are highly crystalline materials with complex texture that impede ion exchange and prevent transmembrane electrochemical potentials from being generated. These findings have important implications for the relevance of such structures as microreactors for chemical conversions and as catalysts in prebiotic chemistry.

---

[1] This chapter has been published in Getenet, M., Rieder, J., Kellermeier, M., Kunz, W., García-Ruiz, J.M. Tubular structures of calcium carbonate: formation, characterization, and implications in natural mineral environments. Chemistry – A European Journal 2021, 27, 16135. https://doi.org/10.1002/chem.202101417

Journal metrics:
JCR 2021 (Clarivate Analytics): Impact Factor: 5.02, Q2 in Chemistry, Multidisciplinary Category

WILEY-VCH

Chemistry—A European Journal

Tubular structures of calcium carbonate: formation, characterization, and implications in natural mineral environments

Melese Getenet+,[a] Julian Rieder+,[b] Matthias Kellermeier,*[c] Werner Kunz[b] and Juan Manuel García-Ruiz*[a]

[a] Mr. M. Getenet, Prof. Dr. J.M. García-Ruiz
Laboratorio de Estudios Cristalográficos
Instituto Andaluz de Ciencias de la Tierra (CSIC-UGR)
Avenida de las Palmeras 4, Armilla, E-18100 Granada (Spain)
E-mail: juanmanuel.garcia@csic.es
[b] Mr. J. Rieder, Prof. Dr. W. Kunz
Institute of Physical and Theoretical Chemistry
University of Regensburg, Regensburg (Germany)
[c] Dr. M. Kellermeier
Material Physics, BASF SE, RAA/OS – B007, Carl-Bosch-Strasse 38, D-67056 Ludwigshafen am Rhein (Germany)
E-mail: matthias.kellermeier@basf.com

[+] These authors contributed equally to this work

Abstract:
Chemical gardens are self-assembled tubular precipitates formed by a combination of osmosis, buoyancy, and chemical reaction, and thought to be capable of catalyzing prebiotic condensation reactions. In many cases, the tube wall is a bilayer structure with the properties of a diaphragm and/or a membrane. The interest of silica gardens in materials science as microreactors has increased over the past decade because of their ability to create long-lasting electrochemical potential. In this study, we have grown single macroscopic tubes based on calcium carbonate and monitored their time-dependent behavior by in-situ measurements of pH, ionic concentrations inside and outside the tubular membranes, and electrochemical potential differences. Further, we have characterized the composition and structure of the tubular membranes by using ex-situ X-ray diffraction, infrared and Raman spectroscopy, as well as scanning electron microscopy. Based on the collected data, we propose a physicochemical mechanism for the formation and ripening of these peculiar $CaCO_3$ structures and compare the results to those of other chemical garden systems. We find that the wall of the macroscopic calcium carbonate tubes is a bilayer of texturally distinct but compositionally similar calcite showing high crystallinity. The resulting high density of the material prevents macroscopic calcium carbonate gardens to develop significant electrochemical potential differences. In the light of these observations, possible implications in materials science and prebiotic (geo)chemistry are discussed.

Introduction

Chemical gardens are self-assembled membranous structures formed upon the interaction of metal salts with aqueous solutions containing anions such as silicate, carbonate, and phosphates [1,2]. The mechanism underlying the growth of the typically resulting hollow tubes is known to be a complex interplay of osmosis, buoyancy, and chemical reaction [1–3]. These peculiar structures – once wrongly thought to be remainders of living organisms [4–7] – have recently attracted growing attention, because of multiple coupled chemical fluxes occurring across the tubular membrane upon ripening. Detailed insights into these processes could be gained through the design of a novel procedure [3,8] allowing the growth of single macroscopic tubes, in which both the inner and outer solutions could readily be sampled for time-dependent concentration measurements, and microelectrodes could be immersed for in-situ monitoring of pH and potential differences. It was shown that chemical gardens operate far from equilibrium and relieve the initially generated gradients only slowly through a cascade of coupled diffusion and precipitation processes [3]. Furthermore, it was demonstrated that the concentration gradients caused by spontaneous compartmentalization during the early stages of tube growth induce long-lasting electrochemical potential differences [2,3,9–11]. Consequently, the interest in chemical gardens in the context of self-fueled microreactors has also increased in the last years [12–16]. Clearly, the idea of having a “battery” of hundreds of millivolts for at least several hours is worth to be explored with respect to synthetic chemistry. Indeed, recent work could show that tubular chemical gardens and osmosis-driven mineral vesicles catalyze the conversion of formamide into nucleobases and amino acids [17–19]. Furthermore, experimental evidence suggesting that chemical gardens are geochemically plausible structures [20–22] triggers a new view of the likely relevance of these self-assembled microreactors in the context of the origin of life [17–19].

While chemical gardens can be grown with various anions such as aluminate [12,23,24], oxalate [25], carbonate [13,26,27], phosphate [28,29], hydroxide [16], or oxometallate [30,31], most research efforts have been devoted to systems based on silicate solutions, the so-called silica gardens. These structures are typically made by soaking small solid particles of soluble metal salts in a concentrated, strongly alkaline silicate solution. The interaction of the acidic metal ion solution arising from the dissolution of the solid particles with the strongly basic silicate solution creates tubular membranes separating an inner acidic solution from an outer alkaline solution with a substantially dissimilar composition. Electrochemical potential develops across these membranes due to spontaneous compartmentalization and the generation of considerable concentration gradients [2,3,10,11]. The overall measured potential difference depends on the type of salt used and seems to be the result of three terms, namely diffusion (ΔE_{diff}) and membrane (ΔE_m) potentials as well as a third pH-induced contribution (ΔE_{pH}). So far, such electrochemical potentials have been measured for silica gardens made with soluble salts of cobalt, ferrous, and ferric ions [3,9–11] as well as calcium [32]. Among the other anions known to produce chemical gardens, carbonate is of particular interest, because the existence of Na_2CO_3-rich oceans on the early Earth has been postulated [33–37], in which carbonate-based chemical gardens might have developed. Tubular structures and mineral vesicles consisting of iron, cobalt, manganese, magnesium, zinc, barium, and calcium carbonate have been confirmed to form with waters of the Magadi lake (Kenya) [22], which is considered a modern analogue of the early soda oceans. Several previous studies have reported the formation and ex-situ characterization of calcium carbonate-based tubular structures synthesized by immersion of Ca^{2+}-containing salts pellets in Na_2CO_3 solutions[13,26,27], or by growth on cation-exchange membranes [38,39] and gel/liquid interfaces [40]. However, dynamic diffusion and precipitation processes occurring during the growth and subsequent ripening have not been studied yet in this system. In the present work, we have applied the approaches previously developed for silica gardens [3,10] to monitor time-dependent chemical gradients across tubular $CaCO_3$ membranes. To this end, we have performed in-situ measurements of ion concentrations, pH, and electrochemical potentials across the membrane. In addition, we also report results of detailed ex-situ characterization of the morphology and the composition of the tubular $CaCO_3$ membranes at different stages of the growth and ripening process.

Results and Discussion

Growth of macroscopic calcium carbonate tubes

Hollow vertical tubes, up to a few centimeters long and several millimeters in diameter, were obtained by controlled addition of sodium carbonate solution (2 M, pH 10.8) to a pressed pellet of $CaCl_2 \cdot 2H_2O$ (Figure 1). These tubes grow vertically over time with the ascending air-solution interface as the sodium carbonate solution is added continuously. This technique was previously developed by Glaab et al. [3,8,10,41] for studying the dynamic behavior of macroscopic silica gardens based on different metal cations. It allows access to the solution inside the tubes for sample drawing and continuous monitoring of ionic concentration, pH, and electrochemical potential across the formed membrane.

Time-dependent changes of ion concentrations

Results of elemental analysis of samples collected from the outer and inner solutions of the tubular structures at different times are presented in Figure 2. Here we assume that any concentration gradients within each of the two compartments are negligible (as suggested by experiments where samples were drawn at different positions relative to the tube wall within one compartment), although local gradients may exist on short length scales (especially near the tube wall). Throughout the entire monitored period (72 h), the concentration of Ca^{2+} in the exterior solution was limited to a few millimolar (Figure 2a) due to the excess volume and high concentration of the external carbonate solution and the poor solubility of calcium under these conditions. During the first 8 hours, $[Ca^{2+}]_{ext}$ rises from 0.8 mM to 2.2 mM and gradually decreases back to 0.8 mM in the following 60 hours. In contrast to calcium, the concentration of sodium in the exterior solution declines over the first 8 hours.

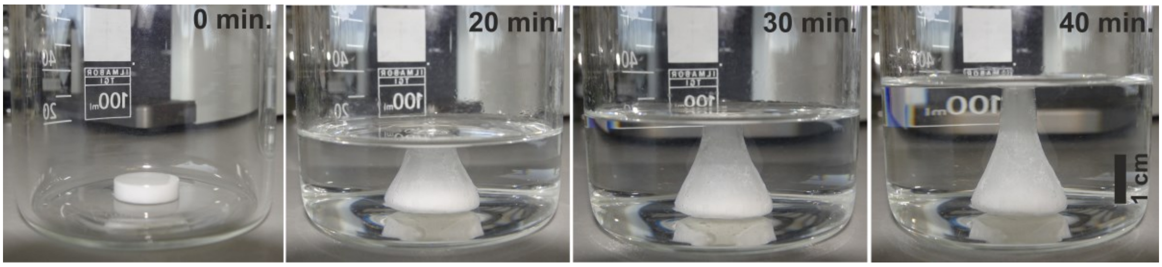

Figure 1. Growth of a single macroscopic chemical garden tube based on $CaCO_3$ by controlled addition of sodium carbonate solution (2 M, pH 10.8) to a pressed pellet of $CaCl_2 \cdot 2H_2O$. In the given setup, the volumes of the inner and outer solution compartments are ~2.7 and 50 mL, respectively.

This is clear evidence for the counter-diffusion of calcium and sodium ions across the tubular structures during this early stage of ripening. Between 10 and 15 hours, there is another stepwise drop in $[Na^+]_{ext}$ from *ca.* 4.0 to 3.8 M, which roughly coincides with the maximum in the outer calcium concentration. Subsequently, the concentration of sodium in the outer reservoir changes only slightly, indicating that Na^+ diffusion substantially slowed down. In turn, the exterior calcium concentration continues decreasing until the end of the monitored period, indicating progressive precipitation of all Ca^{2+} ions that have entered the outer reservoir during the first 10 hours onto the outer surface of the tubular membrane (as calcite and/or gaylussite as described below, see Figure 6 and Figure 7). It is worth emphasizing at this point that although the calcium concentrations detected in the outer reservoir are rather low on an absolute level, the expected nominal supersaturation of the solution with respect to various $CaCO_3$ (and other) phases is high (see Figure S1 in the Supplementary Information), due to the large amounts of carbonate present at high pH. In principle, this should lead to immediate precipitation especially during the first 10 hours. Possibly, amorphous nanoparticles of calcium carbonate (ACC) are nucleated in the solution but remain finely dispersed and thus are detected by $[Ca^{2+}]$ measurements after acidification [32]. Such particles (which did not cause any visual turbidity) could become incorporated into the outer surface of the membrane during the later stages when the total detected concentration of calcium decreases.

The trends in $[Ca^{2+}]$ and $[Na^+]$ observed in the outer reservoir are partially mirrored in the time-dependent concentrations measured in the interior solution (Figure 2b). The internal Ca^{2+} concentration decreases from 1.16 M to 0.88 M between 0 and 3 hours, inversely reflecting the observed increase in $[Ca^{2+}]_{ext}$ (see Figure 2a). However, this initial decline turns into a pronounced increase up to a maximum concentration of *ca.* 1.37 M after 20 hours. Subsequently, the calcium concentration inside the membrane decreases continuously down to values around 1.15 M after 60 hours (Figure 2b). The decline in $[Ca^{2+}]_{int}$ during the first 3 hours can be attributed to i) the ongoing tube growth nourished by calcium carbonate precipitation onto its inner surface and ii) diffusion of calcium ions into the outer reservoir. Mass balance considerations (see Figure S2 in the Supplementary Information) suggest that after 3 hours, about 76 % of the released calcium ions remain dissolved in either the inner (~75 %) or outer (~1 %) solution, while the rest has precipitated into the tube wall (which would correspond to a net mass of *ca.* 100 mg if $CaCO_3$ was the only formed phase). This distribution indicates that precipitation is the major cause for the decline in $[Ca^{2+}]_{int}$ during the first 3 hours, while diffusion only plays a minor role in this context.

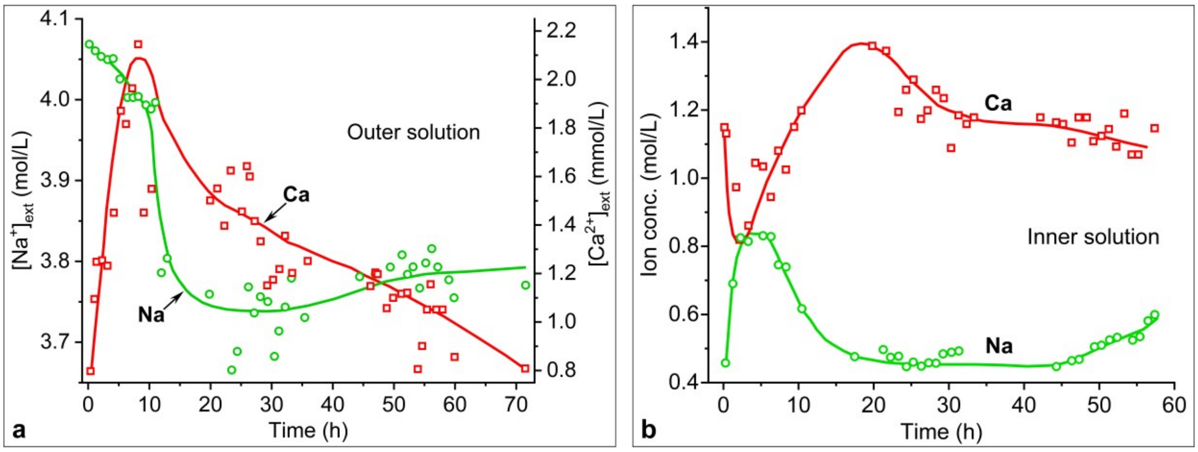

Figure 2. Spatiotemporal distribution of ionic species in macroscopic calcium carbonate gardens. Calcium (squares) and sodium (circles) ion concentrations measured (a) in the outer sodium carbonate reservoir and (b) in the interior solution of the formed tube at different times of ripening after completed preparation. Note that the full lines are only meant to serve as a guide for the eye and do not rely on a distinct physical model.

The subsequent rise in the inner Ca^{2+} concentration between 3 and 20 hours can be explained by two different scenarios: first, dissolution of the original $CaCl_2{\cdot}2H_2O$ pellet may not be completed after 3 hours (when the macroscopic structure has already been fully developed) and could become dominant when the rate of $CaCO_3$ precipitation onto the tube wall has lowered. This process may be supported by continued osmosis-driven inflow of water from the outer reservoir, dissolving the remaining calcium salt until it reaches its maximum concentration. In a second, perhaps more plausible scenario, the observed re-increase of the internal calcium concentration may be ascribed to the dissolution of an initially precipitated metastable phase (vaterite, as discussed below) in the course of its solution-mediated transformation into more stable polymorphs (like calcite). This second explanation is supported by mass balance considerations (see Figure S2 in the Supplementary Information, ruling out the first scenario) and would furthermore be consistent with results from ex-situ characterizations, which revealed that vaterite was a major component of the membranes isolated within the first 24 hours of ripening (see Figure 5). Indeed, such co-existence of vaterite and calcite as well as possible transformation of vaterite into calcite has also been observed for tubular $CaCO_3$ grown on cation-exchange membranes [38]. In the present case, this suggests that vaterite formation was the primary cause for the removal of Ca^{2+} ions from the inner solution via precipitation on the interior surface of the tube wall during the early stages of ripening. After 20 hours, the inner calcium concentration has reached its maximum and subsequently declines continuously due to completed transformation into calcite (and gaylussite, see below) and ongoing growth of the stable phase on the membrane. Notably, previous studies on silica gardens reported that metal cations were removed from the internal solution by incorporation into the inner surface of the membrane through precipitation as hydroxides [3,10,41–44]. However, due to the higher solubility of calcium hydroxide compared to other metal cations (Table 1), it seems safe to conclude that precipitation of $Ca(OH)_2$ does not play a significant role in the evolution of calcium carbonate-based chemical gardens as prepared in the present work (a notion that is further corroborated by the results of the ex-situ analyses discussed below).

The concentration of sodium detected inside the tubular $CaCO_3$ membranes is quite high (*ca.* 0.45 M) already at the beginning (Figure 2b), most likely because some Na^+ ions have entered the interior volume together with water during the onset of tube formation [3,10,32]. During the subsequent 4 hours, $[Na^+]_{int}$ further increases until it reaches a maximum concentration of about 0.83 M. This continued rise in the sodium concentration is likely caused by diffusion from the outer solution and accompanied by the gradual decrease in calcium concentration, due to precipitation as calcium carbonate into the tube wall. Interestingly, the concentration of sodium inside the tube decreases in the following (between 3 and 20 hours), while in parallel the concentration of calcium increases significantly. This opposite trend in sodium and calcium concentrations could be due to dilution of the inner volume due to ongoing osmosis, which lowers the sodium content while raising the interior calcium concentration by dissolving the remaining salt pellet (although mass balance considerations argue against this scenario, cf. Figure S2 in the Supplementary Information). Similar trends have also been observed for sodium and metal cations in the inner solutions of iron- and cobalt-based silica gardens [3,10], although at much shorter time scales. Another possible explanation for the observed decrease in $[Na^+]_{int}$ again refers to ongoing mineral phase transformations: as shown by ex-situ analyses (see below), increasing fractions of gaylussite ($Na_2Ca(CO_3)_2{\cdot}5H_2O$) are found in the membrane after prolonged periods of ripening. Indeed, the drop in the inner sodium concentration could be related to the onset of gaylussite formation in the tube wall – a notion that is consistent with calculated supersaturation indexes (see Figure S1 in the Supplementary Information) and may also explain the observed drop in the outer sodium concentration occurring between 10 and 15 hours (see Figure 2a). This process reduces the inner sodium concentration to levels of about 0.43 M after *ca.* 20 hours, which are maintained for the following 25 hours, most probably because in-diffusion and precipitation into the tube establish a steady state. Finally, after *ca.* 45 hours, the inner sodium concentration starts to increase again, evidencing that the membrane is still permeable for Na^+ at this stage and suggesting that gaylussite precipitation has come to an end – leaving (slow) diffusion as the only active process.

pH measurements

The pH of the inner solution was measured continuously for a period of 43 hours after the completed addition of sodium carbonate solution. The resulting time-dependent profile is shown in Figure 3, together with data collected in the same way for macroscopic silica garden tubes based on different metal cations [3,10,32]. The pH of the external carbonate solution (*ca.* 10.8) does not vary significantly because of its large volume and the excess of CO_3^{2-} present in this compartment. The initial pH of the inner solution was found to be around 9.5 and slowly declined to 9.3 through the first 8 hours. Subsequently, a continuous rise of the pH towards the value of the outer carbonate solution was observed. The evolution of pH inside the tubular membrane has a strong correlation with the ionic concentrations and the ongoing processes of dissolution, diffusion, and precipitation. At the beginning of tube formation, certain amounts of hydroxide (and (hydrogen) carbonate) ions enter the interior volume along with water and result in the alkaline initial value. In the following 8 hours, any still ongoing dissolution of the calcium salt pellet and precipitation of $CaCO_3$ on the tube wall cause the pH to decline. Finally, the continuous pH rise after 8 hours can be explained by inward transport of hydroxide ions and concurrent decelerated calcium carbonate formation and/or ongoing $CaCO_3$ phase transformation via dissolution-reprecipitation processes, which lead to a parallel increase in the concentration of interior Ca^{2+} ions up to around 20 hours (cf. Figure 2b).

Compared to calcium-based silica garden tubes (magenta-colored curve in Figure 3) [32], the initial and long-term pH inside the calcium carbonate tubes was significantly lower, because of the lower pH of the used sodium carbonate solution in the outer reservoir (*ca.* 10.8 compared to 11.9) and slower equilibration. On the contrary, the initial pH of the solution inside the $CaCO_3$-based tubes was significantly higher than that reported for cobalt- (purple) and iron-based (orange and green) silica garden systems [3,10]. This can be ascribed to the lower acidity of the Ca^{2+} ions compared to Co^{2+}, $Fe^{2+,}$ and Fe^{3+} (as shown in Table 1), as well as the buffering ability of the bicarbonate/carbonate equilibrium. A second main difference between the carbonate- and the silica-based chemical gardens was the time required for the pH gradient across the membranes to be eliminated. Indeed, the rate of pH gradient decline across calcium carbonate membranes (*ca.* 0.03/h) is considerably slower than for Fe(III) (*ca.* 1.4/h), Fe(II) (*ca.* 0.13/h) Co(II) (*ca.* 0.4/h) and Ca(II) (*ca.* 0.2/h) silica gardens. The reasons for the slow rate of pH progression in $CaCO_3$-based chemical gardens relate to the slow precipitation kinetics of carbonate minerals due to lower expected levels of supersaturation compared to calcium silicates as well as cobalt or iron hydroxides, which generally have much lower solubility (cf. Table 1). Moreover, the initial higher pH gradient across Fe(III)/silica, Fe(II)/silica, and Co(II)/silica membranes accelerates counter-diffusion of reactants and thus raises the pH of the interior solution more rapidly.

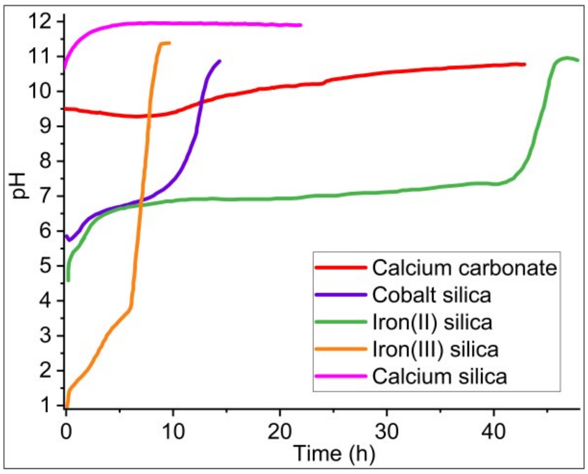

Figure 3. Temporal evolution of the pH in the inner solutions of macroscopic chemical garden tubes based on $CaCO_3$ (red) and silica with different metal cations as indicated. Data for calcium-based [32], cobalt-based [3], iron(II)-based and iron(III)-based [10] silica gardens are reproduced from the literature with permission from the publishers.

Table 1. Acidity of metal ions [45] and solubility products of mineral phases [46–52] presumed to precipitate during the formation and ripening of macroscopic carbonate and silica garden tubes.

Cations	Acidity (pK_a)	Possible minerals and their solubility products
Ca^{2+}	12.9 (pK_1)	calcite (3.4×10^{-9}), vaterite (1.2×10^{-8}), aragonite (4.6×10^{-9}), hydrated / anhydrous amorphous calcium carbonate (ACC) (9.1×10^{-7} / 9.9×10^{-8}), gaylussite (3.8×10^{-10}) calcium-silicate-hydrate ($6CaO\cdot5SiO_2\cdot6H_2O$) ($5.5\times10^{-49}$), wollastonite ($CaSiO_3$) ($2.5\times10^{-8}$), $Ca(OH)_2$ (5.0×10^{-6})
Co^{2+}	9.6 (pK_1)	$Co(OH)_2$ (5.9×10^{-15})
Fe^{2+}	9.5 (pK_1)	$Fe(OH)_2$ (4.9×10^{-17})
Fe^{3+}	2.2 (pK_1) 5.7 (pK_2)	$Fe(OH)_3$ (2.8×10^{-39})

According to Glaab et al. [10,41], the relatively slow progression of pH in Fe(II)-based silica garden systems (as compared to Fe(III) and Co(II)) can further be attributed to high crystallinity and low porosity/permeability. Similar arguments can be put forward for the $CaCO_3$ case: the higher crystallinity of forming calcium carbonate minerals may lead to densely packed membrane structures (as shown below, cf. Figure 5 and Figure 7), which inhibit diffusion processes and retard the pH equilibration in this system.

Electrochemical potential differences

For comparison, the time-dependent electrochemical potential differences measured across calcium carbonate tubes in this work and different types of silica-based tubes in previous studies [3,10,32] are plotted together in Figure 4. The potential difference detected for the $CaCO_3$ system immediately after completed tube formation was close to zero, whereas silica gardens based on Fe(II), Fe(III), and Co(II) developed initial ΔE_h values of as high as 190, 650, and 120 mV, respectively. In the case of macroscopic tubes based on calcium salts and silica, the potential difference measured during the early stages was slightly positive (*ca.* 20 mV). Although ΔE_h values of around 10 mV were observed during the first 10 hours of aging in the $CaCO_3$ system, the absence of more distinct electrochemical potential differences across the membrane is striking and can be explained by two factors: first, the pH gradient across the membrane – identified as one major contribution to the overall ΔE_h in previous work [3]– is rather low from the very beginning, as compared to other chemical garden systems. Second, the tube wall appears to be too thick and/or dense to allow for actual diffusion and membrane potential terms to be measured in the $CaCO_3$ system [32], so that the (low) pH gradients represent the sole contributions to the overall potential difference in this case. Probably, the absence or minimal contribution of membrane and diffusion potentials in calcium carbonate gardens is due to slower precipitation kinetics of $CaCO_3$ (and gaylussite) species as compared to metal oxy/hydroxides in the case of iron and cobalt silica-based chemical gardens, leading to more crystalline and less permeable membranes that inhibit diffusion and counter-diffusion processes.

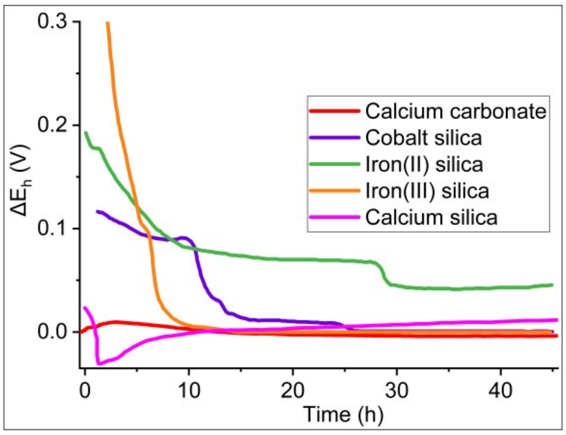

Figure 4. Temporal evolution of electrochemical potential differences (ΔE_h) measured across macroscopic chemical gardens tubes based on calcium carbonate and silica with different metal cations as indicated. Data for calcium-based [32], cobalt-based [3], iron(II)-based and iron(III)-based silica [10] are reproduced from the literature with permission from the publishers.

Membrane characterization

The formed tubular $CaCO_3$ membranes were characterized in detail using different methods, namely X-ray diffraction, Raman spectroscopy, IR spectroscopy, and scanning electron microscopy. All these methods were applied ex-situ, i.e. after isolation of the tube material at different times of aging to better understand the temporal evolution of the system. Powder X-ray diffraction patterns (Figure 5) reveal that membranes isolated immediately after completed tube preparation (0 h) as well as after 4 and 8 hours of ripening were composed of mainly calcite with minor amounts of vaterite and gaylussite, a hydrated form of sodium-calcium carbonate, which is usually unstable in both water and air [53], but predicted to form in solutions at high pH and sodium content (such as the outer Na_2CO_3 reservoir in the present case) [54]. In membranes isolated after 24 hours, significantly higher fractions of both gaylussite and vaterite were found next to calcite as the three major phases (see Table S1 in the Supplementary Information for quantitative values), indicating enhanced precipitation of vaterite and gaylussite on the exterior and interior surfaces of the tube walls, respectively. After 48 hours, progressive vaterite and gaylussite dissolution and re-precipitation cause calcite to become the dominant solid phase again. Moreover, trace amounts of halite were also detected at all sampled time points, which likely formed during isolation and drying of the membranes (possibly in the course of partial gaylussite decomposition) and were not removed despite extensive rinsing with water – a phenomenon also observed in calcium-based silica gardens [32]. Based on these observations, we note that the procedure used for isolation of the tubular membranes may also induce partial transformation of some of the other originally present metastable phases (e.g. vaterite and/or ACC into calcite), thus increasing to a greater or lesser extent the fraction of the more stable phase(s) detected by XRD as well as the Raman and IR analyses discussed below.

Figure 6 shows Raman and IR spectra recorded from tubular $CaCO_3$ membranes isolated after different periods of ripening. Raman spectra (Figure 6a) acquired immediately after completed preparation (0 h) reveal the presence of calcite and vaterite on the interior tube surface (green curve in Figure 6a), whereas only calcite was detected on the exterior surface (black curve). After 4 and 8 hours of aging, calcite was the only mineral detected on both the inner and the outer surfaces of the tube (red and orange curves in Figure 6a). Finally, for membranes isolated after 24 and 48 hours, calcite and gaylussite were identified on the exterior surface (blue curve), whereas only calcite was detected on the interior surface (data not shown). This is consistent with the XRD data, which showed that only minor amounts of metastable gaylussite and vaterite were present in tubes isolated during the first 8 hours of aging (cf. Figure 5).

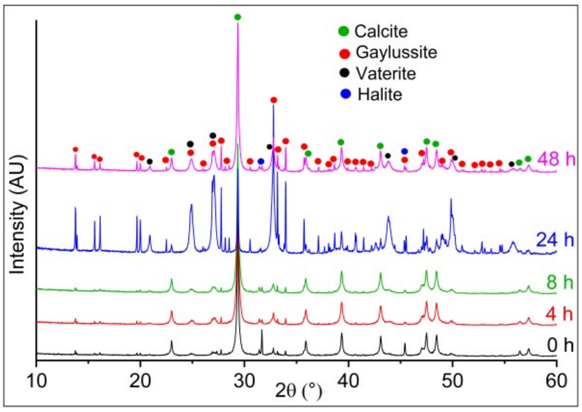

Figure 5. Powder X-ray diffraction patterns of tubular calcium carbonate structures isolated after different periods of ripening as indicated. Reflections are assigned to the different detected mineral phases by colored circles.

Figure 6b shows IR spectra of powdered membranes that were isolated after different periods of ripening. Essentially, the data confirm the formation and relative amounts of the distinct mineral phases already identified by X-ray diffraction and Raman spectroscopy, but it also suggests the presence of traces of ACC especially during the earlier stages of ripening, as evident from a more or less pronounced splitting of the asymmetric stretching modes of carbonate ions occurring between 1400 and 1500 cm^{-1} (with a second peak or shoulder near 1490 cm^{-1} indicating ACC) [62]. Some of the infrared modes of gaylussite observed in membranes isolated after 50 and 72 hours (647, 804, 896, and 1657 cm^{-1}) did not appear for tubes aged for less than 24 hours, probably due to the relatively small amounts of gaylussite present during the earlier stages, in line with results from XRD (Figure 5) and Raman spectroscopy (Figure 6a).

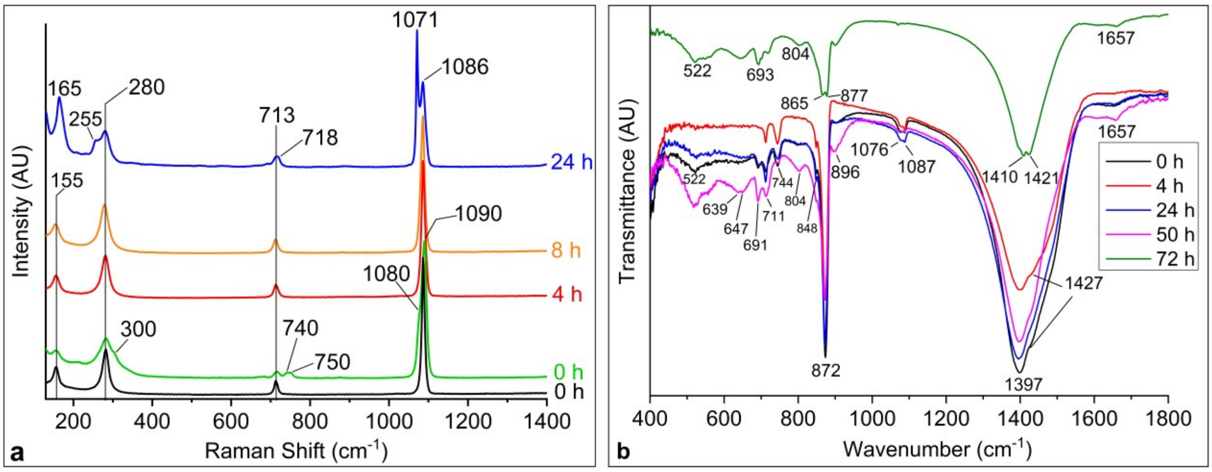

Figure 6. Spectroscopic characterization of macroscopic $CaCO_3$ tubes after different times of maturation. (a) Raman spectra acquired on the interior (0 h – green, 4 h – red, 8 h – orange) and exterior (0 h – black, 24 h – blue) surfaces of the tubular membranes. The observed Raman bands can be assigned to lattice, in-plane bending, and symmetric stretching modes of the CO_3^{2-} groups in different mineral phases as follows: calcite – 155/280, 713, and 1086 cm^{-1} [55]; vaterite – 300, 740/750, and 1080/1090 cm^{-1} [56]; gaylussite –165/255, 718, and 1071 cm^{-1} [57]. (b) IR spectra collected from $CaCO_3$ tubes at distinct times of aging (as indicated) after grinding to a fine powder. The observed vibrational bands correspond to in-plane bending, out-of-plane bending, and asymmetric stretching modes of the CO_3^{2-} groups in different mineral phases as follows: calcite – 711, 848/877, and 1421/1427 cm^{-1} [58–60]; vaterite –744, 872/877, and 1087 cm^{-1} [58,59]; gaylussite – 522/647/693, 804/877, and 896/1397 cm^{-1}, with further bands at 1421 and 1657 cm^{-1} [57,60,61].

Selected SEM views of macroscopic calcium carbonate tubes are shown in Figure 7. The collected data confirm the mineral identification made with X-ray diffraction as well as Raman and IR spectroscopy and allows a better understanding of membrane formation. Our SEM studies show that after prolonged ripening, the tubular calcium carbonate structures are in fact bilayered membranes (Figure 7a-c), consisting of a rather dense external layer made of aggregated rhombohedral calcite crystals, and an internal layer comprising a base of adjacent cone-like calcite structures that are decorated by spherical as well as dumbbell-shaped precipitates. To some extent, the latter structures are reminiscent of textures observed in the mammillary core layer of eggshells [63] especially when viewed from below (Figure 7e). Interestingly, the cones – which likely form at the very beginning of tube growth (cf. Figure 7a vs. 7b) – are composed of nano-spherical subunits (Figure 7f) that aggregated into bunches of elongated columnar crystals (Figure 7g), suggesting growth by an accretion-based mechanism [64]. Alternatively, these conical structures may result from a precipitation process that involves radially inward propagating reaction-diffusion fronts [65]. The dumbbell-like and spherical structures covering the inner surface of the cone layer (Figure 7e) likewise seem to be composed of smaller subunits and/or have formed by progressive non-crystallographic branching [66] (Figure 7h), and probably consist of vaterite. The outer surface of the cone layer initially has a wavy topography (Figure 7a), similar to membrane structures that were reported to form at the interface between $MnCl_2$ and NaOH solutions after injection into two parallel fluid channels of a 2D microfluidic device [67]. With time, the wavy surface becomes covered with faceted rhombohedral calcite crystals (Figure 7i) that grow and interlock to form a thick (*ca.* 3 µm) outer layer (Figure 7b). Finally, flat crystals of gaylussite, up to more than 100 microns in size, grow on top of this outer calcite layer (Figure 7d).

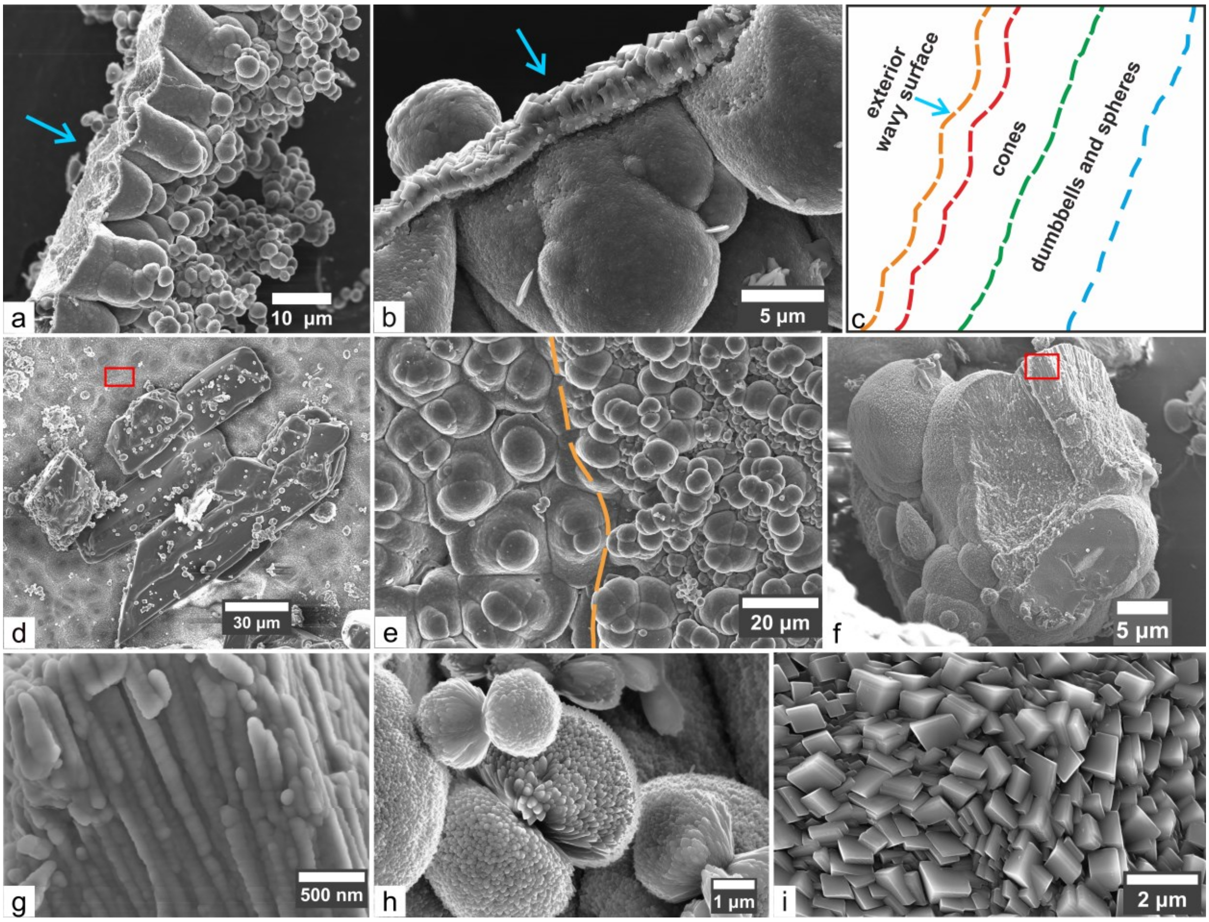

Figure 7. Scanning electron micrographs of macroscopic calcium carbonate gardens. (a-b) Cross-sectional views of the tube wall after (a) 4 and (b) 24 hours of ripening, showing an exterior wavy surface (indicated by blue arrows) composed of a dense layer of interlocked and co-aligned rhombohedral calcite crystals, and a less dense interior surface formed by calcite cones, on which open networks of spheres and dumbbells have grown. (c) Sketch illustrating the multilayered cross-section of the formed $CaCO_3$ membranes. (d) Gaylussite crystals observed on top of the exterior wavy surface of the membranes after 24 hours of ripening. (e) Top view of the interior surface of tubes aged for 8 hours, showing apexes of the calcite cones and loosely aggregated dumbbells/spheres on the left and right of the dashed line, respectively. (f) Close-up view of a fractured cone on the interior surface as shown in (a). (g) High-magnification micrograph of the area marked by the red rectangle in (f), showing that the cone-like microstructures consist of aggregated nano-spherical subunits. (h) Close-up view of dumbbells and spheres on the interior surface, similar to those observed to the right of the dashed line in panel (e). (i) Zoom onto the exterior wavy surface of the membrane in the area marked by the red rectangle in (d), revealing multiple interlocked crystallites of rhombohedral calcite.

Figure 8 shows a summary of the observed time-dependent changes of pH and ionic concentrations in the inner solution of the tubular $CaCO_3$ structures (cf. Figures 2 and 3), along with the mineral precipitation sequence deduced from the SEM images (Figure 7). Based on the collected data, a phenomenological explanation of the series of events leading to the formation and ripening of single macroscopic $CaCO_3$ tubes can be proposed. During the first 3 hours, the decrease of the interior calcium concentration indicates ample precipitation of calcium carbonate, enough to (over)compensate any possible increase of concentration due to still ongoing dissolution of the $CaCl_2$ pellet and/or $CaCO_3$ phase transformation processes. Consequently, the inner pH also decreases due to the removal of basic CO_3^{2-} ions and the slightly acidic character of the released Ca^{2+} ions. At this stage, calcium carbonate precipitates mainly in the form of cone-like calcitic structures as well as spherical and dumbbell-shaped microparticles, which presumably consist of vaterite. Amorphous calcium carbonate may form in minor amounts during this period, but will only occur during the very early stages of the process and quickly transform into vaterite and calcite via routes reported in detail elsewhere [68,69]. After 3 hours, precipitation of calcite/vaterite is slowed down, and the calcium concentration and the pH inside the tube re-increase due to dissolution of any possible remainders of the $CaCl_2$ pellet and, more importantly, the transformation of vaterite polycrystals (spheres and dumbbells) into calcite (cones) via a dissolution-recrystallization pathway. Almost simultaneously, gaylussite crystals start to nucleate and grow on the outer surface of the tube wall, which is reflected in a clear decrease in the concentration of sodium dissolved in both the interior and exterior solution. Precipitation of calcium carbonate becomes dominant again after about 18 hours, resulting in a slow decrease of the calcium concentration. During this stage, slow growth at low supersaturation leads to the formation of faceted rhombohedral calcite crystals on the outer surface of the tube wall. On top of this calcite layer, the growth of gaylussite is continued in the presence of the high sodium concentrations of the outer Na_2CO_3 solution, yielding large (single) crystals that cover the exterior surface of the tubular structure.

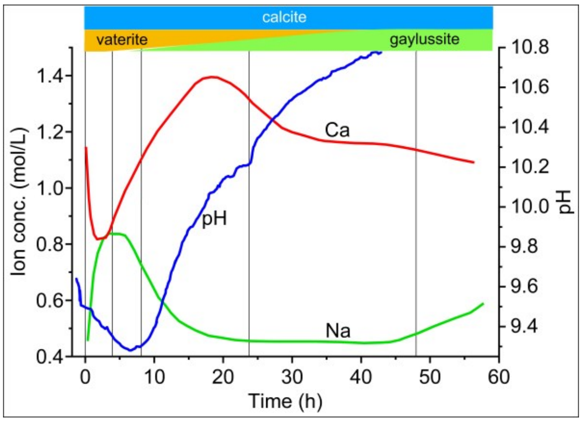

Figure 8. Plot showing the temporal evolution of the pH and ion concentrations in the inner solution of a macroscopic $CaCO_3$ tube, together with the mineral phases constituting the membrane at the different stages of ripening.

Conclusions

In this work, we have prepared single macroscopic chemical garden tubes made from calcium carbonate and monitored their dynamic evolution by time-dependent measurements of pH, ion concentrations, and electrochemical potential in the two solutions on both sides of the forming membrane. Complementarily, the sequence of mineral precipitation into the tube wall was elucidated by ex-situ analyses of membrane composition and structure using X-ray diffraction, IR and Raman spectroscopy, as well as scanning electron microscopy. Combining the results of all our studies, we have revealed the phenomenology of $CaCO_3$ membrane formation and proposed a mechanism rationalizing the different processes of dissolution, diffusion, and precipitation occurring in the system. It was shown that in the end, the formed calcium carbonate membranes are actually bilayers of texturally distinct but compositionally similar crystalline calcite: while the interior surface of the membrane consists of numerous adjacent cone-like structures that are decorated with spherical and dumbbell-like polycrystals, the outer surface eventually becomes covered by a dense layer of interlocked calcite rhombohedra, formed during slow growth at low supersaturation. These textures of multiple crystalline calcite layers dramatically reduce the exchange and interaction of ionic species between the inner and outer volume, which prevents gradients in ion concentrations to be fully eliminated in the long term. Another important consequence is the absence of significant electrochemical potential differences across the $CaCO_3$ membrane – in contrast to macroscopic tubes of silica gardens based on different transition metal cations such as Fe(II), Fe(III), and Co(II) [3,10,41]. This finding is relevant for studies aiming at the use of chemical gardens or similar structures as microreactors for electrochemically enhanced synthesis. It also has implications for the suggested role of chemical gardens as catalyzers of prebiotic chemistry, in particular in soda lakes and soda oceans likely to have formed on the primitive Earth, as well as Earth-like planets and moons [19,27,37,70]. Carbonate vesicles and gardens were shown to form under the conditions prevailing in modern soda lakes, considered to be analogues of soda oceans on the early Earth. Structures obtained with calcium, barium, and manganese cations were composed of highly crystalline metal carbonate minerals, whereas cobalt(II)- and iron(II)-based vesicles and gardens proved to be less crystalline materials [22]. Hence, it may be inferred that $CaCO_3$, $BaCO_3$, and $MnCO_3$ vesicles and chemical gardens formed in soda oceans of the early Earth might not have developed significant electrochemical voltage, whereas the lower crystallinity of corresponding cobalt- and iron-based structures could have permitted the build-up of higher voltages, facilitating chemical conversions. However, further investigations are required to better understand the nature of these membranes and their potential role in prebiotic chemistry.

Experimental Section

Tubular calcium carbonate membranes were synthesized by slow and controlled addition of sodium carbonate solution (2 M, pH 10.8) to pressed pellets (diameter: 13 mm) of calcium chloride dihydrate, which were fixed by double-sided adhesive tape at the bottom of 120 mL plastic beaker. The pellets were prepared by grinding 0.7 g $CaCl_2 \cdot 2H_2O$ (Carl Roth, ≥ 99 %) to a fine powder using an agate mortar and then pressing this powder using a Perkin-Elmer/Specac hydraulic press. Sodium carbonate solutions were obtained by dissolving appropriate amounts of anhydrous Na_2CO_3 (Carl Roth, ≥ 99.5 %) in purified water, which was taken from a Millipore system and decarbonated by purging with nitrogen gas prior to use.

For controlled growth of the $CaCO_3$ tubes, 9 mL sodium carbonate solution was added instantly at the beginning before another 41 mL were dosed at a rate of 0.55 mL/min using a Metrohm Dosimat 665. Samples were collected at different times from the interior and exterior solutions by means of a volumetric pipette, in order to determine calcium and sodium ion concentrations. The drawn aliquots were first diluted with 0.01 M HNO_3 and subsequently analyzed by inductively coupled plasma atomic emission spectroscopy (ICP-AES).

For continuous pH measurements, a glass microelectrode (Mettler-Toledo InLab Micro; tip diameter: 3 mm) was immersed into the inner solution at a depth of 5 mm. The electrode was connected to a digital laboratory pH meter (Schott CG 843), which was read out by custom-designed software at intervals of 5 s for 43 hours. Electrochemical potential differences were monitored using a pair of identical Pt stick electrodes, which were immersed at a depth of 2 mm into both the inner and outer solution. Data were recorded every 0.4 s over a period of 120 h using a multimeter (Metex M-3890D USB) linked to a PC.

The formed tubular membranes were isolated after different times of ripening for ex-situ compositional and structural characterization. For this purpose, the exterior and interior solutions were removed carefully using a syringe and replaced with deionized water multiple times to remove soluble salts. After final rinsing of the membrane material with water and ethanol, it was dried at ambient temperature in a nitrogen atmosphere and parts of the obtained dry tube were ground to a fine powder. The tubular structures were subsequently characterized using powder X-ray diffraction (PXRD), Raman and infrared (IR) spectroscopy, as well as scanning electron microscopy (SEM). Most of the PXRD measurements were performed on a high-resolution Bruker D8 Advance X-ray diffractometer using Cu-$K_{\alpha1}$ radiation provided by a primary Ge(111) monochromator and a Lynxeye PSD detector. Diffraction data were collected in transmission mode at 40 kV acceleration voltage and 40 mA current for 1 h, covering a 2θ range of $5-80^0$ with an increment of 0.02^0 per second. Further XRD analyses were carried out in transmission mode using a Huber G670 Guinier Camera, which produced diffraction patterns over a 2Θ range of 4-86° with a step resolution of 0.005° based on Cu-$K_{\alpha1}$ radiation. Mineral phases present in the powders were identified by using Malvern Panalytical HighScore software (version 4.8) with the ICCD PDF-4+ database. Raman spectra were recorded on the exterior and interior wall of intact tubular structures by using a HORIBA Jobin Yvon LabRAM high-resolution UV-Vis spectrometer, which was equipped with an Olympus BX41 optical microscope (with binocular and Koehler illumination) and a charge-coupled device (CCD) detector. Excitation at a wavelength of 532 nm was achieved with frequency-doubled, neodymium-doped yttrium-aluminum-garnet laser. IR spectra of ground powders were acquired on a Varian FT-IR 670 spectrometer equipped with a GladiATR package (PIKE), covering wavenumbers of 400-4000 cm^{-1} in 100 accumulated scans. Assignments of observed vibrational modes were made with the Varian Resolutions Pro 4.1.0.101 software. All Raman and IR analyses were performed in air at ambient conditions. Studies on the texture and chemical composition of intact tubular membranes were performed by using field-emission scanning electron microscopy (FESEM) on an AURIGA instrument from Carl Zeiss SMT, which was operated at 3-10 kV.

Acknowledgments

The authors thank Alicia González Segura for support during the scanning electron microscopy analyses at the Centro de Instrumentación Científica (CIC) of the University of Granada, Cristóbal Verdugo Escamilla for his guidance in quantitative phase analysis, and Raquel Fernandez-Penas for her technical assistance. M.G. and J.M.G.R. thank the European Research Council under the European Union's Seventh Framework Program (FP7/2007-2013)/ERC grant agreement no. 340863, the Spanish Ministerio de Economía y Competitividad for the financial support to the project CGL2016-78971-P and Junta de Andalucía for financing the project P18-FR-5008. M.G. acknowledges Grant No. BES-2017-081105 of the Ministerio de Ciencia, Innovacion y Universidades of the Spanish government.

Conflicts of Interest

The authors declare no conflict of interest.

Keywords: calcium carbonate • chemical gardens • electrochemical potential • membranes • prebiotic chemistry

[1] M. Kellermeier, F. Glaab, E. Melero-García, J. M. García-Ruiz, in *Methods Enzymol.*, Elsevier, **2013**, pp. 225–256.

[2] L. M. Barge, S. S. S. Cardoso, J. H. E. Cartwright, G. J. T. Cooper, L. Cronin, A. De Wit, I. J. Doloboff, B. Escribano, R. E. Goldstein, F. Haudin, D. E. H. Jones, A. L. Mackay, J. Maselko, J. J. Pagano, J. Pantaleone, M. J. Russell, C. I. Sainz-Díaz, O. Steinbock, D. A. Stone, Y. Tanimoto, N. L. Thomas, *Chem. Rev.* **2015**, *115*, 8652–8703.

[3] F. Glaab, M. Kellermeier, W. Kunz, E. Morallon, J. M. García-Ruiz, *Angew. Chem.* **2012**, *124*, 4393–4397.

[4] R. Buick, *PALAIOS* **1990**, *5*, 441–459.

[5] M. D. Brasier, O. R. Green, A. P. Jephcoat, A. K. Kleppe, M. J. Van Kranendonk, J. F. Lindsay, A. Steele, N. V. Grassineau, *Nature* **2002**, *416*, 76–81.

[6] F. Stalport, P. Coll, M. Cabane, A. Person, R. N. González, F. Raulin, M. J. Vaulay, P. Ausset, C. P. McKay, C. Szopa, J. Zarnecki, *Geophys. Res. Lett.* **2005**, *32*, L23205.

[7] S. McMahon, *Proc. R. Soc. B Biol. Sci.* **2019**, *286*, 20192410.

[8] F. Glaab, In-Situ Examination of Diffusion and Precipitation Processes during the Evolution of Chemical Garden Systems, PhD Thesis, Universität Regensburg, **2011**.

[9] L. M. Barge, I. J. Doloboff, L. M. White, G. D. Stucky, M. J. Russell, I. Kanik, *Langmuir* **2012**, *28*, 3714–3721.

[10] F. Glaab, J. Rieder, J. M. García-Ruiz, W. Kunz, M. Kellermeier, *Phys. Chem. Chem. Phys.* **2016**, *18*, 24850–24858.

[11] L. M. Barge, Y. Abedian, M. J. Russell, I. J. Doloboff, J. H. E. Cartwright, R. D. Kidd, I. Kanik, *Angew. Chem. Int. Ed.* **2015**, *54*, 8184–8187.

[12] C. Collins, R. Mokaya, J. Klinowski, *Phys. Chem. Chem. Phys.* **1999**, *1*, 4669–4672.

[13] J. Maselko, P. Strizhak, *J. Phys. Chem. B* **2004**, *108*, 4937–4939.

[14] J. J. Pagano, T. Bánsági, O. Steinbock, *Angew. Chem. Int. Ed.* **2008**, *47*, 9900–9903.

[15] T. S. Sørensen, *J. Colloid Interface Sci.* **1981**, *79*, 192–208.

[16] B. C. Batista, O. Steinbock, *Chem. Commun.* **2015**, *51*, 12962–12965.

[17] R. Saladino, G. Botta, B. M. Bizzarri, E. Di Mauro, J. M. Garcia Ruiz, *Biochemistry* **2016**, *55*, 2806–2811.

[18] B. Mattia Bizzarri, L. Botta, M. I. Pérez-Valverde, R. Saladino, E. Di Mauro, J. M. García-Ruiz, *Chem. – Eur. J.* **2018**, *24*, 8126–8132.

[19] R. Saladino, E. Di Mauro, J. M. García-Ruiz, *Chem. - Eur. J.* **2019**, *25*, 3181–3189.

[20] J. M. García-Ruiz, E. Nakouzi, E. Kotopoulou, L. Tamborrino, O. Steinbock, *Sci. Adv.* **2017**, *3*, e1602285.

[21] H. Satoh, K. Tsukamoto, J. M. Garcia-Ruiz, *Eur. J. Mineral.* **2014**, *26*, 415–426.

[22] M. Getenet, J. M. García-Ruiz, C. Verdugo-Escamilla, I. Guerra-Tschuschke, *Crystals* **2020**, *10*, 467.

[23] R. D. Coatman, N. L. Thomas, D. D. Double, *J. Mater. Sci.* **1980**, *15*, 2017–2026.

[24] C. Collins, G. Mann, E. Hoppe, T. Duggal, T. L. Barr, J. Klinowski, *Phys. Chem. Chem. Phys.* **1999**, *1*, 3685–3687.

[25] A. Baker, Á. Tóth, D. Horváth, J. Walkush, A. S. Ali, W. Morgan, Á. Kukovecz, J. J. Pantaleone, J. Maselko, *J. Phys. Chem. A* **2009**, *113*, 8243–8248.

[26] J. Maselko, P. Borisova, M. Carnahan, E. Dreyer, R. Devon, M. Schmoll, D. Douthat, *J. Mater. Sci.* **2005**, *40*, 4671–4673.

[27] S. S. S. Cardoso, J. H. E. Cartwright, C. I. Sainz-Díaz, *Icarus* **2019**, *319*, 337–348.

[28] J. Maselko, A. Geldenhuys, J. Miller, D. Atwood, *Chem. Phys. Lett.* **2003**, *373*, 563–567.

[29] Á. Tóth, D. Horváth, R. Smith, J. R. McMahan, J. Maselko, *J. Phys. Chem. C* **2007**, *111*, 14762–14767.

[30] C. Ritchie, G. J. T. Cooper, Y.-F. Song, C. Streb, H. Yin, A. D. C. Parenty, D. A. MacLaren, L. Cronin, *Nat. Chem.* **2009**, *1*, 47–52.

[31] H. N. Miras, D.-L. Long, L. Cronin, in *Adv. Inorg. Chem.* (Eds.: R. van Eldik, L. Cronin), Academic Press, **2017**, pp. 1–28.

[32] J. Rieder, L. Nicoleau, F. Glaab, A. E. S. Van Driessche, J. M. Garcia-Ruiz, W. Kunz, M. Kellermeier, *submitted* **2021**.

[33] S. Kempe, E. T. Degens, *Chem. Geol.* **1985**, *53*, 95–108.

[34] S. Kempe, J. Kazmierczak, E. T. Degens, in *Orig. Evol. Mod. Asp. Biominer. Plants Anim.* (Ed.: R.E. Crick), Springer US, Boston, MA, **1989**, pp. 29–43.

[35] S. Kempe, J. Kazmierczak, in *Encycl. Geobiol.* (Eds.: J. Reitner, V. Thiel), Springer Netherlands, Dordrecht, **2011**, pp. 829–833.

[36] J. M. García-Ruiz, in *Carbonate Sediment. Diagenesis Evol. Precambrian World* (Eds.: J.P. Grotzinger, N.P. James), SEPM Society For Sedimentary Geology, **2000**, pp. 75–89.

[37] J. M. García-Ruiz, M. A. van Zuilen, W. Bach, *Phys. Life Rev.* **2020**, S1571064520300014.

[38] M. Takiguchi, K. Igarashi, M. Azuma, H. Ooshima, *Cryst. Growth Des.* **2006**, *6*, 1611–1614.

[39] K. Igarashi, M. Takiguchi, H. Ooshima, *J. Ceram. Soc. Jpn.* **2008**, *116*, 111–114.

[40] C. J. Steenbjerg Ibsen, B. F. Mikladal, U. Bjørnholt Jensen, H. Birkedal, *Chem. - Eur. J.* **2014**, *20*, 16112–16120.

[41] F. Glaab, J. Rieder, R. Klein, D. Choquesillo-Lazarte, E. Melero-Garcia, J.-M. García-Ruiz, W. Kunz, M. Kellermeier, *ChemPhysChem* **2017**, *18*, 338–345.

[42] C. Collins, W. Zhou, J. Klinowski, *Chem. Phys. Lett.* **1999**, *306*, 145–148.

[43] J. J. Pagano, S. Thouvenel-Romans, O. Steinbock, *Phys Chem Chem Phys* **2007**, *9*, 110–116.

[44] E. Kotopoulou, M. Lopez-Haro, J. J. C. Gamez, J. M. García-Ruiz, *Angew. Chem. Int. Ed.* **2020**, *59*, DOI https://doi.org/10.1002/anie.202012059.

[45] C. F. Baes, R. E. Mesmer, *The Hydrolysis of Cations*, John Wiley & Sons, New York, **1976**.

[46] L. N. Plummer, E. Busenberg, *Geochim. Cosmochim. Acta* **1982**, *46*, 1011–1040.

[47] K. Suzuki, T. Nishikawa, S. Ito, *Cem. Concr. Res.* **1985**, *15*, 213–224.

[48] T. Ogino, T. Suzuki, K. Sawada, *Geochim. Cosmochim. Acta* **1987**, *51*, 2757–2767.

[49] N. Plummer, D. L. Parkhurst, G. W. Fleming, S. A. Dunkle, *A Computer Program Incorporating Pitzer's Equations for Calculation of Geochemical Reactions in Brines*, U.S. Geological Survey, **1988**.

[50] J. R. Clarkson, T. J. Price, C. J. Adams, *J. Chem. Soc. Faraday Trans.* **1992**, *88*, 243.

[51] C. Rodriguez-Navarro, K. Kudłacz, Ö. Cizer, E. Ruiz-Agudo, *CrystEngComm* **2015**, *17*, 58–72.

[52] H. Sun, S. He, P. Wu, C. Gao, P. Feng, T. Xiao, Y. Deng, C. Shuai, *Materials* **2016**, *9*, 287.

[53] J. W. Anthony, R. A. Bideaux, K. W. Bladh, M. C. Nichols, *Handbook of Mineralogy*, Mineralogical Society Of America, Chantilly, VA 20151-1110, USA, **1990**.

[54] R. Firdous, T. Hirsch, D. Klimm, B. Lothenbach, D. Stephan, *Miner. Eng.* **2021**, *165*, 106849.

[55] J. Urmos, S. K. Sharma, F. T. Mackenzie, *Am. Mineral.* **1991**, *76*, 641–646.

[56] U. Wehrmeister, A. L. Soldati, D. E. Jacob, T. Häger, W. Hofmeister, *J. Raman Spectrosc.* **2010**, *41*, 193–201.

[57] R. L. Frost, M. Dickfos, *Polyhedron* **2007**, *26*, 4503–4508.

[58] F. A. Andersen, L. Brečević, G. Beuter, D. B. Dell'Amico, F. Calderazzo, N. J. Bjerrum, A. E. Underhill, *Acta Chem. Scand.* **1991**, *45*, 1018–1024.

[59] E. Loste, R. M. Wilson, R. Seshadri, F. C. Meldrum, *J. Cryst. Growth* **2003**, *254*, 206–218.

[60] N. V. Chukanov, in *Infrared Spectra Miner. Species Ext. Libr.* (Ed.: N.V. Chukanov), Springer Netherlands, Dordrecht, **2014**, pp. 21–1701.

[61] H. H. Adler, P. F. Kerr, *Am. Mineral.* **1963**, *48*, 839–853.

[62] F. A. Andersen, L. Brečević, G. Beuter, D. B. Dell'Amico, F. Calderazzo, N. J. Bjerrum, A. E. Underhill, *Acta Chem. Scand.* **1991**, *45*, 1018–1024.

[63] Y. Nys, M. T. Hincke, J. L. Arias, J. M. García-Ruiz, S. E. Solomon, *Avian Poult. Biol. Rev.* **1999**, *10*, 143–166.

[64] A. Gal, K. Kahil, N. Vidavsky, R. T. DeVol, P. U. P. A. Gilbert, P. Fratzl, S. Weiner, L. Addadi, *Adv. Funct. Mater.* **2014**, *24*, 5420–5426.

[65] L. Roszol, O. Steinbock, *Phys. Chem. Chem. Phys.* **2011**, *13*, 20100–20103.

[66] J.-P. Andreassen, E. M. Flaten, R. Beck, A. E. Lewis, *Chem. Eng. Res. Des.* **2010**, *88*, 1163–1168.

[67] Y. Ding, B. Batista, O. Steinbock, J. H. E. Cartwright, S. S. S. Cardoso, *Proc. Natl. Acad. Sci.* **2016**, *113*, 9182–9186.

[68] J. D. Rodriguez-Blanco, S. Shaw, L. G. Benning, *Nanoscale* **2011**, *3*, 265–271.

[69] P. Bots, L. G. Benning, J.-D. Rodriguez-Blanco, T. Roncal-Herrero, S. Shaw, *Cryst. Growth Des.* **2012**, *12*, 3806–3814.

[70] G. Angelis, G. G. Kordopati, E. Zingkou, A. Karioti, G. Sotiropoulou, G. Pampalakis, *Chem. – Eur. J.* **2020**, *26*, DOI https://doi.org/10.1002/chem.202004018.

Supporting Information

Tubular structures of calcium carbonate: formation, characterization, and implications in natural mineral environments

Melese Getenet, Julian Rieder, Matthias Kellermeier, Werner Kunz and Juan Manuel García-Ruiz

Figure S1. Saturation indexes (SI) predicted for different possible mineral phases in the exterior solutions surrounding single macroscopic tubes of calcium carbonate as a function of ripening time. Calculations were performed using the PHREEQC software package [1] with the Thermoddem [2] (left) and Pitzer [3] (right) geochemical databases, utilizing the time-dependent concentration shown by Figure 2a in the main text and assuming the pH (10.8) and the Na_2CO_3 concentration (2 M) to be constant throughout the entire monitored period (i.e. the depletion of the outer reservoir in CO_3^{2-} due to precipitation of calcium and/or sodium carbonate phases was neglected). The data clearly shows that the outer solution is nominally supersaturated with respect to all carbonate-containing phases detected in/on the membrane by ex-situ characterization (cf. Figures 5-7 in the main text). The experimentally confirmed formation of vaterite, despite its lower levels of supersaturation compared to calcite or gaylussite, suggests that phase selection is governed by kinetic effects during the early stages of ripening.

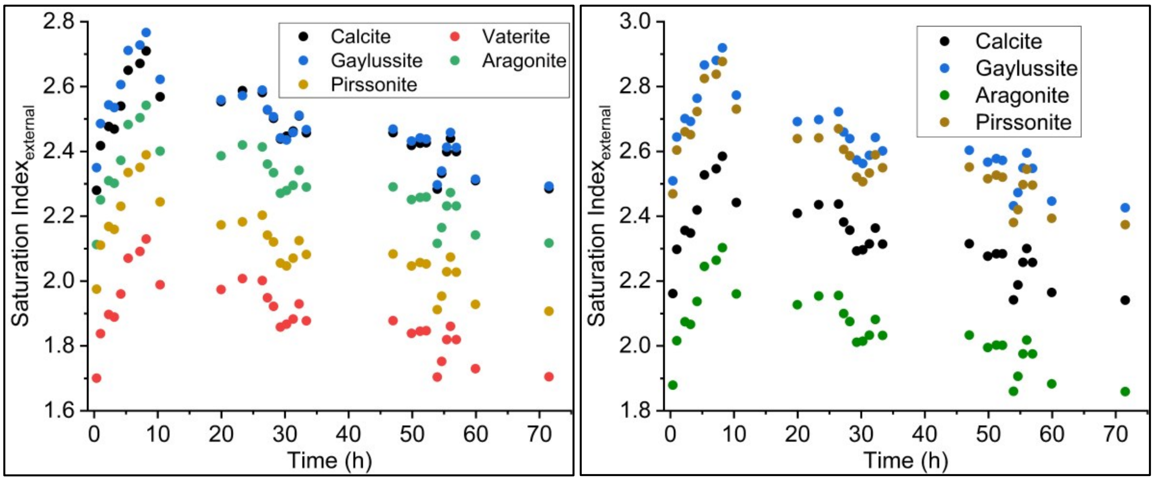

Figure S2. Time-dependent distribution of calcium ions in macroscopic chemical gardens of calcium carbonate. The plot shows the total fraction of Ca^{2+} dissolved at different times (black) and its relative occurrence in the interior (red) and exterior (blue) solutions (as derived from concentration measurements in the two compartments, cf. Figure 2 in the main text). 100 wt% corresponds to the total amount of calcium ions present in the system, as given by the mass of the originally employed $CaCl_2 \cdot 2H_2O$ pellet. Consequently, the difference between the black line and 100 wt% represents the fraction of calcium ions bound in the solid state, which at all times can be considered as the sum of contributions from incomplete dissolution of the original pellet and precipitation into the forming tube wall. The fact that the highest concentration of total dissolved calcium ions (>95 wt%) is observed at the very beginning of the ripening process suggests that pellet dissolution is rather fast and the variations observed in the following are mainly caused by ongoing precipitation and phase transformation processes.

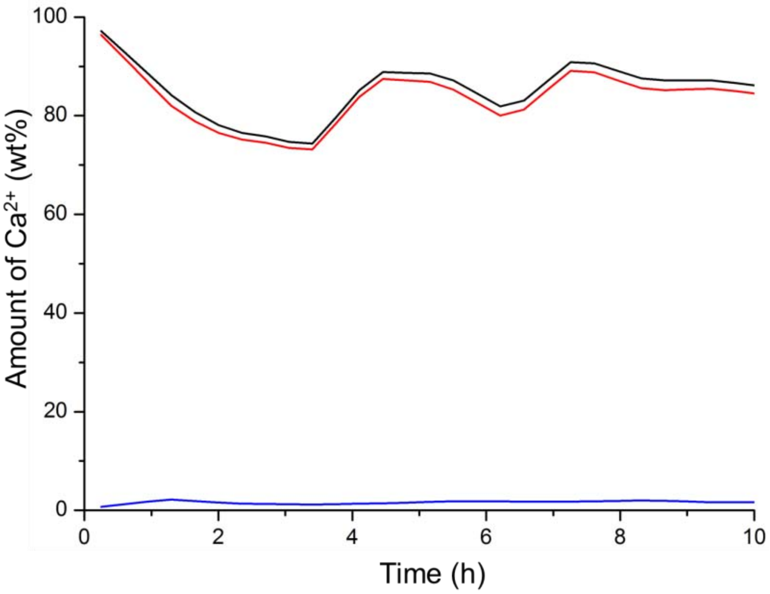

Table S1. Results of quantitative analyses of mineral phase composition in macroscopic calcium carbonate tubes after different periods of ripening, as derived from the powder diffraction patterns shown by Figure 5 in the main text.

	Phases (wt%)			
Time (h)	Calcite	Vaterite	Gaylussite	Halite
0	85.2	3.0	8.4	3.4
4	78.4	13.9	7.0	0.7
8	80.3	13.5	5.6	0.7
24	9.9	59.8	30.3	0
48	52.1	30.5	16.8	0.6

References

[1] D. L. Parkhurst, C. A. J. Appelo, Description of Input and Examples for PHREEQC Version 3: A Computer Program for Speciation, Batch-Reaction, One-Dimensional Transport, and Inverse Geochemical Calculations, Reston, VA, **2013**.

[2] Ph. Blanc, A. Lassin, P. Piantone, M. Azaroual, N. Jacquemet, A. Fabbri, E. C. Gaucher, Appl. Geochem. **2012**, 27, 2107–2116.

[3] K. S. Pitzer, J. Phys. Chem. **1973**, 77, 268–277.

Cover Feature: Tubular Structures of Calcium Carbonate: Formation, Characterization, and Implications in Natural Mineral Environments

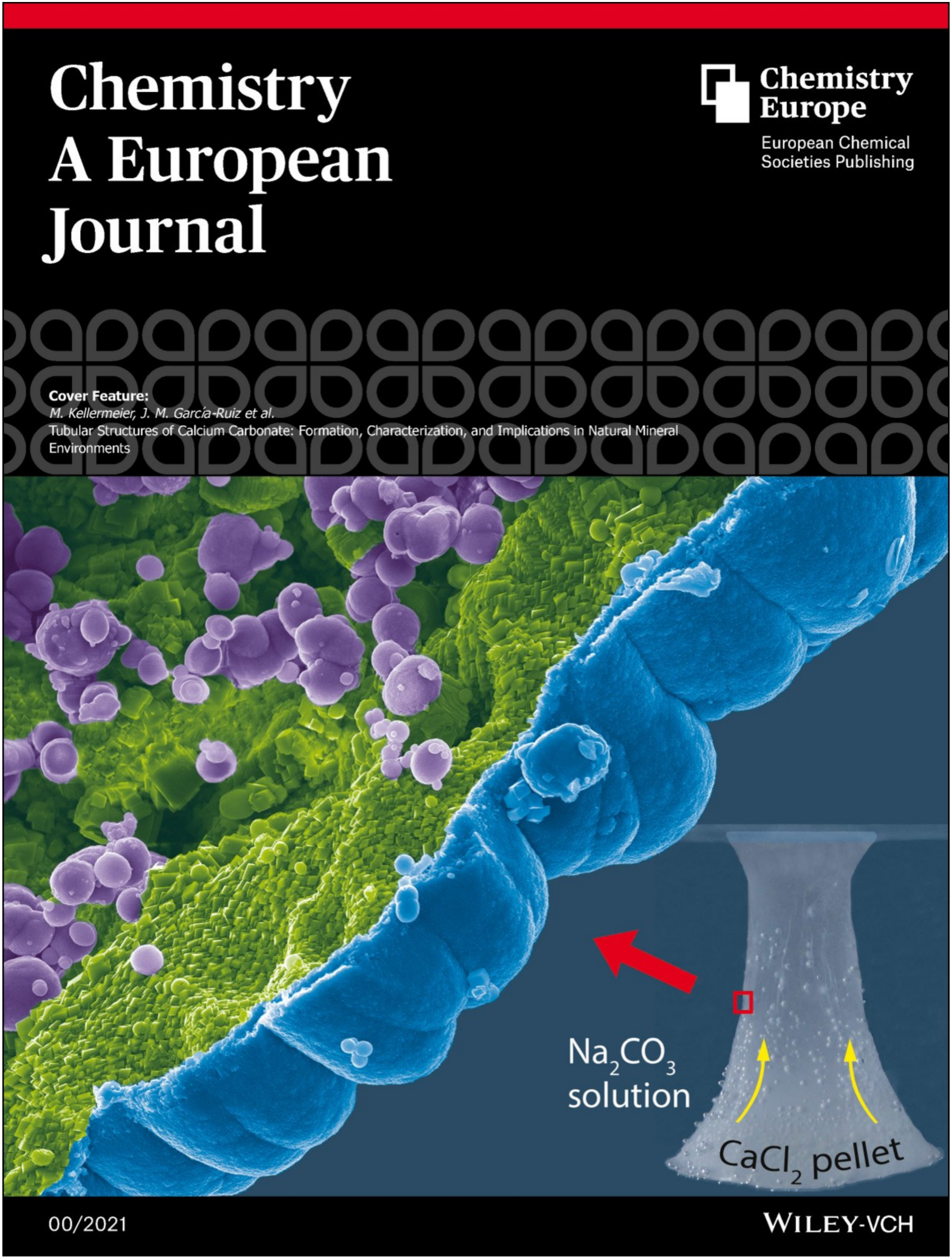

Chemistry
A European Journal

Chemistry
Europe
European Chemical
Societies Publishing

Cover Feature:
M. Kellermeier, J. M. García-Ruiz et al.
Tubular Structures of Calcium Carbonate: Formation, Characterization, and Implications in Natural Mineral Environments

00/2021

WILEY-VCH

Chapter 6

6. Calcium Carbonate Tubular Structures from Natural Alkaline Soda Lakes: Growth, Characterization, and Implication to Prebiotic Geochemistry [1]

This chapter is a manuscript prepared for submission to Chemistry – A European Journal.

Supporting Information is found at the end of the chapter.

Chemistry—A European Journal

Calcium Carbonate Tubular Structures from Natural Alkaline Soda Lakes: Formation, Characterization, and Implication to Prebiotic Geochemistry

Melese Getenet, Juan Manuel García-Ruiz*

[a] M. Getenet, Prof. Dr. J.M. García-Ruiz
Laboratorio de Estudios Cristalográficos
Instituto Andaluz de Ciencias de la Tierra (CSIC-UGR)
Avenida de las Palmeras 4, Armilla, E-18100 Granada (Spain)
E-mail: juanmanuel.garcia@csic.es

Abstract: Chemical gardens are self-assembled tubular precipitates formed by a combination of osmosis, buoyancy, and chemical reaction, and are thought to be capable of catalyzing prebiotic condensation reactions. In many cases, the tube wall is a bilayer structure with the properties of a diaphragm and/or a membrane. Chemical gardens gained great attention in materials science and origin of life research as microreactors to catalyze chemical reactions. Here, we present, for the first time, the in-situ monitoring of the time-dependent evolution of pH, ionic concentrations, and electrochemical potential differences in single macroscopic calcium carbonate tubular structures synthesized in “natural” soda lake water. Furthermore, we have characterized the composition and structure of the tubular membranes by using ex-situ X-ray diffraction, infrared, and Raman spectroscopy, as well as scanning electron microscopy. Based on these data, we discussed the mechanisms of dynamic diffusions and precipitation processes of these unique natural $CaCO_3$ structures and compare the results to those of synthetic chemical garden systems. We find that the wall of natural calcium carbonate tubes is a bilayer of texturally different but compositionally similar calcite with high crystallinity. The resulting high density of the material prevents these tubes to develop significant electrochemical potential differences compared to silica gardens. Yet, the voltages in these tubes were three times that of synthetic $CaCO_3$ tubes. We have discussed these observations to shed light on the possible implications in materials science and prebiotic (geo)chemistry.

Introduction

Chemical gardens are self-assembled membranous structures formed upon the interaction of metal salts with aqueous solutions containing anions such as silicate, carbonate, and phosphates. These structures are typically hollow tubes that grow due to a complex interplay of chemical reactions, osmosis, and buoyancy [1–3]. Owing to their plant-like tubular morphology, these structures were wrongly thought as remnants of living organisms [4–6]. Chemical gardens gained growing attention because of the presence of chemical and mineralogical gradients across these membranes [7–9]. Detailed insights into these gradients could be gained through a novel procedure [7] allowing the growth of single macroscopic tubes, in which both the inner and outer solutions could readily be sampled for time-dependent concentration measurements, and microelectrodes could be immersed for in-situ monitoring of pH and potential differences. Chemical gardens operate far from equilibrium and relieve the initially generated gradients slowly through a cascade of coupled diffusion and precipitation processes. The concentration and pH gradients during the early stages of the tube growth induce long-lasting electrochemical potential differences [7–11]. Consequently, the interest in chemical gardens has also increased in recent years in the context of self-fueled microreactors [12–16]. Indeed, recent work has shown that tubular silica gardens and osmosis-driven mineral vesicles catalyze the condensation of formamide [17–19] and pyruvate [20] into nucleobases and amino acids. Furthermore, experimental evidence, suggesting that chemical gardens are geochemically plausible structures [21–23], triggers a new view of the plausible role of self-assembled microreactors in origin of life [17–19,24].

Even though chemical gardens can grow in various anions, most research efforts have been devoted to systems based on silicate solutions, the so-called silica gardens. These structures are typically tubular membranes separating an inner acidic solution from an outer alkaline solution with a markedly different composition that led to the generation of significant pH, concentration, and electrochemical potential gradients [7–10,25]. The overall measured potential difference depends on the type of salt used and seems to be the result of three terms, namely diffusion (ΔE_{diff}), membrane (ΔE_m), and pH-induced potential (ΔE_{pH}) [9,26].

Among the other anions known to produce chemical gardens, carbonate is of particular interest because the existence of Na_2CO_3-rich oceans on the early Earth and other planets and moons has been postulated [24,27–30], in which carbonate-based chemical gardens might have developed [23,24,31]. Indeed, tubular and vesicular mineral structures consisting of iron, cobalt, manganese, magnesium, zinc, barium, and calcium carbonate have been confirmed to form in Lake Magadi water (Kenya)[23], which is considered a modern analogue of the early Earth soda oceans and other planets and moons such as Enceladus and Europa [27–29,32,30]. More importantly, carbonate-based iron chemical gardens were shown to catalyze the polymerization of simple organic molecules to kerogenous products, suggesting the plausible role of self-assembled carbonate structures in the emergence of prebiotic organic chemistry [33].

Several other studies have reported the formation and ex-situ characterization of calcium carbonate-based tubular structures synthesized by immersion of Ca^{2+} containing salt pellets in commercial Na_2CO_3 solutions [13,31,34,35]. Recently, we have discussed dynamic diffusions and precipitation processes occurring during the growth and subsequent ripening of calcium carbonate gardens synthesized in commercial sodium carbonate solutions [36]. The wall of these tubes was texturally distinct bilayers but compositionally similar crystalline calcite. The resulting high-density layers prevented the tubes from developing significant pH gradients and electrochemical potential differences [36]. In an earlier study, we confirmed that calcium carbonate tubular and vesicular mineral structures could form in natural soda lake water, suggesting the plausibility of these structures in early Earth soda oceans [23]. However, dynamic diffusion and precipitation processes occurring during the growth and subsequent ripening of these natural tubes are yet unknown. Here, we have applied the approaches previously developed for silica gardens [7,9] to monitor time-dependent chemical gradients across tubular $CaCO_3$ membranes synthesized in “natural” soda lake water (Lake Magadi, Kenya) for the first time. The tubular structures were synthesized by the controlled addition of Magadi water onto $CaCl_2$ salt pellets. We have performed in-situ measurements of ion concentrations, pH, and electrochemical potentials across these tubular structures. In addition, we have presented a detailed ex-situ characterization of the morphology and the composition of the natural $CaCO_3$ tubes at different stages of the growth and ripening process by comparing them with synthetic silica and carbonate gardens.

Results and Discussion

Hydrochemistry of Magadi Soda Lake

Lake Magadi is one of the extreme alkaline and saline soda lakes of the East African Rift Valley, occupying faulted alkali trachyte [37,38]. Lake Magadi brine is the last stage of the evolution of dilute inflows enriched in Na^+, SiO_2, and HCO_3^- but depleted in Ca^{2+} and Mg^{2+} [39,40]. Through a combination of rock-water interaction, evaporative concentration, and solute loss, the dilute water produces highly alkaline groundwater beneath the rift valley floor characterized by high pH, Na^+, Cl^-, CO_3^{2-}, HCO_3^-, and SiO_2 contents [40,41]. This groundwater discharge into Lake Magadi as warm and hot springs which, upon surface evaporation and mineral precipitation (mainly trona), evolve into highly alkaline and saline sodic brines (Table 1). The high pH of Lake Magadi brines results from trona deposition and subsequent depletion in HCO_3^- and CO_2 degassing [40,41]. The high concentrations of SiO_2 are the result of the dissolution of silicate-rich volcanic rocks by feeder hot springs and subsequent evaporative concentration [42]. Owing to their high pH, carbonate, and silica content, soda lakes were proposed as one of the plausible geochemical settings for the synthesis of self-assembled mineral structures [32,43]. We proved this claim by synthesizing mineral gardens and vesicles of various metals by using Lake Magadi water [23]. In this work, we have performed a detailed study of calcium-based tubular structures formed in Lake Magadi water. The chemistry of the water used for the experiments is shown in Table 1.

Table 1. Chemical analysis of the Lake Magadi water used for tubular mineral gardens synthesis. Elemental concentrations are in ppm, EC: electrical conductivity, IS: ionic strength

pH[a]	T (°C)[a]	EC (mS/cm)	IS (M)	Na^+	K^+
9.9	37.5	14300	5.7	104000	1939
Cl^-	CO_3^{2-}	HCO_3^-	F^-	SO_4^{2-}	SiO_2
103000	52400	20200	1670	988	388
PO_4^{3-}	Ca^{2+}	Mg^{2+}	Fe	Al^{3+}	
171	1.98	0.121	0.392	<0.02	

[a] measured in situ during sampling

Growth of macroscopic calcium carbonate tubes

Hollow tubular carbonate membranes were grown first by manually pipetting about 40 ml of Lake Magadi water at a rate of *ca.* 1 mL/s. This method is chosen to shed light on the processes underlying the growth of these tubular structures by comparing them with synthetic silica and carbonate gardens grown with similar methods. This method resulted in a transparent dome-shaped tubular mineral structure surrounded by air bubbles that could be CO_2 gases (Figure 6a). During the growth process, the domes expand both vertically and horizontally and the color changes to white upon gradual mineral precipitation and wall thickening. The growth of the tube took a relatively long time when compared with the synthetic silicate and carbonate gardens. In synthetic chemical gardens, the typical morphology is longer tubes due to osmotic-driven membrane rupture followed by buoyancy-driven vertically upward injection of the interior acidic solution into the exterior alkaline solution [1–3]. In Magadi tubes, the elasticity of the membrane and slow diffusion of water inhibits the rupturing of the envelope and injection of the interior solution into Magadi water, resulting in limited growth in the vertical direction. The absence of envelope rupture in Magadi tubes could be due to the high solute content and the high density of the water [23]. The density of Lake Magadi brines varies mainly between 1.2 and 1.33 g/cm^3 [40,41]. The water used for the Magadi garden experiments is more concentrated than the brines reported in ref. [40,41] and it may have a density greater than 1.2. This density is comparable with the density of silica solutions [44] reported to slow reactivity of the calcium salts in Ca-silica garden experiments. High concentration (high viscosity) silicate solution slows down the reaction and allows only a few slow-growing tubes [44]. Similarly, synthetic calcium carbonate vesicles were shown to form in high sodium carbonate concentrations while tubular gardens form at low concentrations (≤ 1 M) [31]. The sum of carbonate and bicarbonate ions alone is higher than 1.2 M in Magadi water. These observations evidence that slow diffusion and the high density of the water reduced buoyancy-driven vertical growth in Magadi tubes compared with synthetic silica and carbonate gardens.

To be able to monitor the pH, ionic concentration, and electrochemical potential, tubular structures with an opening on top (Figure 6b) were synthesized by controlled addition of Lake Magadi water (Table 1) on top of calcium chloride salt pellets using the technique developed elsewhere [7,9]. The lake brine was added in two steps. First, 5 mL was quickly pipetted manually and waited for about 10 minutes until a gelatinous membrane formed around the pellet (cf. the first panel of Figure 6a). After *ca.* 10 minutes, automatic dosing of 35 mL began at a rate of 0.15 mL/minute. These tubes are a few centimeters in length (up to *ca.* 3 cm) and several millimeters in diameter (*ca.* 20 mm) with an opening on top, allowing access to the solution inside the tubes to take samples and to continuously monitor pH, and electrochemical potential across the formed membranes. The faster dosing ratios used in synthetic chemical gardens [7,9,10,25,36] resulted in malformed tubular structures in Magadi gardens, likely because the dissolution rate of calcium chloride was very slow in Magadi water. Consequently, the dosing rate was reduced to 0.15 mL/minute, causing the tube growth to take about 4 hours for completion. The tubes are very fragile and transparent at the beginning and gradually change to white in a similar manner shown in Figure 6a. The macroscopic growth terminates when the dosing of the Lake Magadi brine stopped. However, the diffusion of water towards the interior of the tubes led to an overflow of the interior solution via the opening of the tubes on top (Figure 6b). As a result, further membrane precipitation took place along the water-air interface in the horizontal direction forming an umbrella-shaped precipitate around the opening. A similar phenomenon was observed in iron and cobalt silica gardens [9].

Immediately after terminating the addition of the lake brine, the tubes were extremely fragile to introduce pipette tips and pH and potential electrodes. Hence, sampling of the interior solution and monitoring of the pH and electrochemical voltage was commenced 2 h after terminating the addition of Lake Magadi brine. At this point, the tubes were rigid enough to support the displacement of the interior solution caused by the immersion of pipette tips and pH and potential electrodes. Hence, the reference time (0 h) for measurements and ripening is the time of termination of water addition.

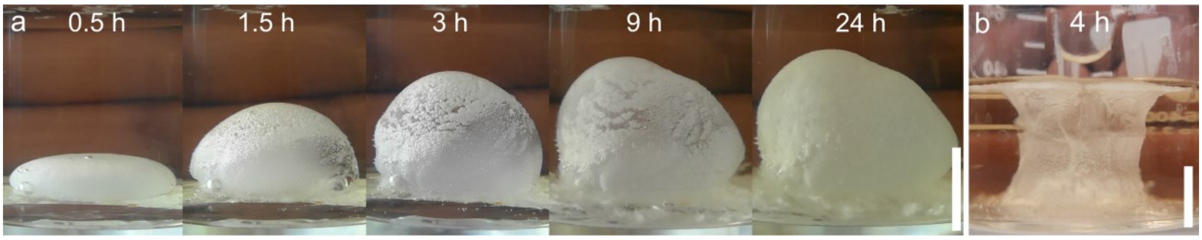

Figure 1. Growth of macroscopic calcium garden tube by manual (a) and controlled (b) addition of Lake Magadi water to a pressed pellet of $CaCl_2 \cdot 2H_2O$. Time refers to since the beginning of the addition of lake water. Scale bar: 1 cm

Time-dependent changes in ion concentrations

The results of the chemical analysis of the samples collected from the interior solutions are presented in Figure 2. The concentration of Ca^{2+} in the interior solution steeply rises from 1.67 to 2.45 M between 2 and 3.5 h of the growth time. Between 3.5 and 10.5 h, Ca^{2+} steeply declines from its maximum to its minimum value (1.36 M). Between 10.5 and 21 h, Ca^{2+} concentration rises a little bit to 1.6 M. From this point onward, Ca^{2+} decline very slightly to 1.4 M after ripening of 56 h. The general trend observed in Ca^{2+} ions is similar to the metal ions evolutions in iron and cobalt silicate gardens [7,9]. The initial pronounced increase in Ca^{2+} reflects the still ongoing dissolution of calcium chloride salt pellets, probably aided by the osmotic-driven inflow of water, until it reaches a maximum value followed by a steep decrease to a minimum and nearly constant values, evidencing progressive precipitation of the Ca^{2+} into the tube wall.

The concentration of Na^+ (0.54 M) and K^+ (7.4 mM) ions inside the tubes was already high after 2 h of ripening, suggesting the influx of Na^+ and K^+ ions together with the exterior Magadi water towards the tubular structures during the addition of Magadi water and/or the first 2 hours of ripening. Owing to the higher amount of Na^+ in Magadi water (see Table 1), the amount of Na^+ observed in the interior solution was significantly higher than K^+. In contrast to Ca^{2+}, Na^+ and K^+ concentrations rise continuously throughout the monitoring period, suggesting the continuous diffusion of these ions towards the interior solution. The rate of Na^+ and K^+ rise seems relatively rapid between 2 and 9 h whereas, after 9 h, these ions rise relatively slower. The coincidence of steep Ca^{2+}, $Na^{+,}$ and K^+ rise at the beginning may imply that Na^+ and K^+ were introduced to the interior solution with the water that dissolve the pellet, resulting sharp rise in Ca^{2+} concentration. The slowdown of the rate of Na^+ and K^+ rise occurred after Ca^{2+} concentration reach its minimum value upon precipitation of calcium carbonate minerals on the tube wall. This implies that tube thickening could have slowed down the diffusion of these ions after 9 h of ripening. The continuous rise of Na^+ and K^+ evidence the absence of removal mechanisms such as precipitation on the interior wall. These membranes seem permanently permeable for Na^+ and K^+ as observed in Co-silica gardens for Na^+ ions [7].

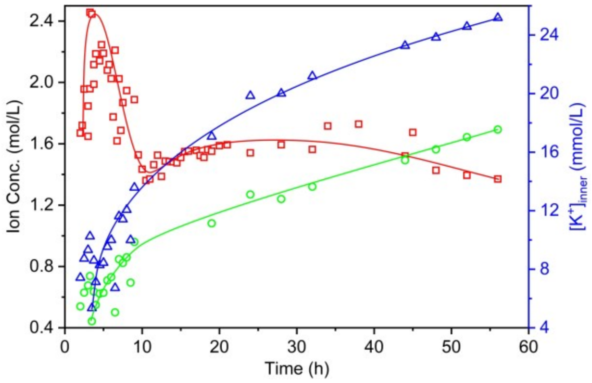

Figure 2. Temporal distribution of ionic species in the interior solution of macroscopic calcium-based Magadi gardens measured at different times of ripening after completed preparation. Calcium (□), sodium (○), and potassium (△) ion concentrations. Blue y-axis on the right is for potassium (△). Note that the lines are only meant to serve as a guide for the eye and do not rely on a distinct physical model.

pH measurements

The pH of the inner solution was measured continuously for 100 h after the addition of Lake Magadi water was completed. The resulting time-dependent profile of the pH of the interior solution is shown in Figure 3 (blue), together with data collected in the same way for macroscopic synthetic silica and carbonate garden tubes based on different metal cations [7,9,10,25]. The pH of Magadi water (9.9) does not vary significantly because of its large volume and the excess of CO_3^{2-} and HCO_3^- present in this compartment (see Table 1). The pH of the interior solution was basic (8.6) after 2 h of ripening. The pH steeply falls to a minimum value of 4.2 after 3.7 h of ripening. This value is the third acidic pH measured inside chemical gardens following aluminium and iron (III) silica gardens [7,9] (see Figure 3). Between 3.7 and 11 h, the pH gently rises to 5.8 followed by a steep increase to 8.9 between 11 and 15 h. Hereafter, the pH rises quite slowly, taking about 84 h to attain equilibrium with the pH of the exterior Magadi water (9.9). Regardless of the rate of pH rise and fall, the interior pH of Magadi carbonate gardens behaves similarly to the pH of the interior solution of synthetic calcium carbonate gardens, which initially decreases and later increases until it reaches equilibrium. Unlike in natural and synthetic carbonate gardens, the pH in silicate gardens never experiences a decline which instead continuously rises until equilibrium. The pH disequilibrium in Magadi gardens could sustain for a very long time (95 h), which is the longest compared to synthetic tubes.

The evolution of pH inside Magadi gardens has a strong correlation with the ionic concentrations and the ongoing processes of dissolution, diffusion, and precipitation, as observed in synthetic silicate and carbonate gardens [7,9,10,25,36]. During the growth process of Magadi gardens, hydroxide ions enter the interior solution along with water and result in alkaline pH of 8.6 after 2 h. Between 2 and 3.7 h, the ongoing dissolution of the calcium salt pellet causes the pH to decline due to the rise in the acidic Ca^{2+} concentration (Figure 2). The gentle pH rise between 3.7 and 11 h can be explained by the accelerated precipitation of $CaCO_3$ on the tube wall, which led to a parallel steep decline in Ca^{2+} ions up to 11 h (see Figure 2). Finally, the pH rise after 11 h can be explained by the continued inward transport of hydroxide ions and simultaneous decelerated calcium carbonate precipitation and/or ongoing $CaCO_3$ phase transformation via dissolution-reprecipitation processes [36], which led to a slight increase in Ca^{2+} ions between 10.5 and 21 h followed by a slight decline (Figure 2).

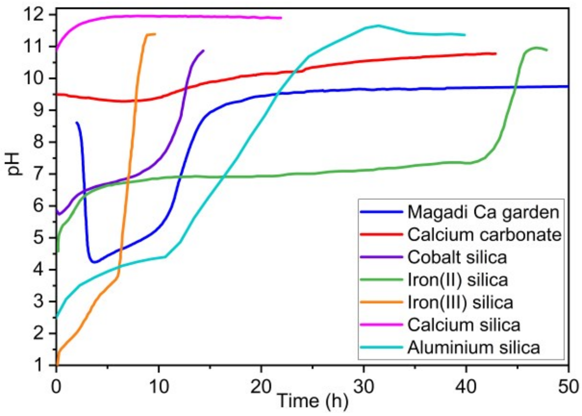

Figure 3. Temporal evolution of the pH in the inner solutions of macroscopic chemical garden tubes based on Magadi water (black), carbonate (red), and silicates with different metals as indicated. Data for calcium-[11], cobalt-[7], aluminium-[10], iron(II)- and iron(III)-based silicate [9] and calcium-based carbonate[12] are reproduced from the literature with permission from the publishers.

Compared to the synthetic Ca-based tubes [25,36], the long-term pH inside Magadi tubes was lower because of the lower pH of Magadi water in the outer reservoir (9.9 compared to 10.8 and 11.9). On the contrary, the pH of the solution inside the Magadi tubes (at 2 h) was higher than that of cobalt (purple), iron (orange and green), and aluminium (cyan) silicate-based systems [7,9,10]. This can be ascribed to the lower acidity of the Ca^{2+} ions compared to Co^{2+}, Fe^{2+}, Fe^{3+}, and Al^{3+} as shown in Table 2[36]. Despite this fact, Magadi tubes attained lower pH than Co and Fe^{2+} silica gardens due to the slow progression of Magadi tubes towards equilibrium. Magadi tubes were still dissolving the pellet and releasing acidic Ca^{2+} ions between 2 and 3.7 h leading to pH decline whereas Co and Fe^{2+} ions were being consumed through metal hydroxide precipitation on the tube walls, leading to continuous pH rise [7,9].

The second difference between Magadi and synthetic chemical gardens was the time required for the pH gradient across the membranes to be eliminated. The rate of pH gradient decline across Magadi gardens (*ca.* 0.013/h) is slower than that of Ca carbonate (*ca.* 0.03/h), Fe(III) (*ca.* 1.4/h), Fe(II) (*ca.* 0.13/h), Co(II) (*ca.* 0.4/h), Ca (*ca.* 0.2/h), and Al (*ca.* 0.23/h) silicate gardens[10,25,36]. The reasons for the overall slow rate of pH progression in $CaCO_3$-based chemical gardens relate to the slow precipitation kinetics of carbonate minerals due to lower expected levels of supersaturation compared to calcium silicates and hydroxides of cobalt, iron, and aluminium, which generally have much lower solubility (cf. Table 2) [36]. Moreover, the initial higher pH gradient across Fe(II), Fe(III), Co, and Al silicate membranes accelerates the counter-diffusion of reactants and thus raises the pH of the interior solution more rapidly[7,9,10]. The effect of a high pH gradient on pH progression towards equilibrium was evident in Magadi tubes between 3.7 and 15 h (see Figure 3). Once these tubes attain the minimum pH of 4.2 at 3.7 h (i.e., the highest pH gradient), subsequent accelerated diffusion of hydroxide ions and precipitation of calcium carbonate minerals raise the pH rapidly to 8.9 at the rate of *ca*. 0.4/h between 3.7 and 15 h.

According to Glaab et al. [9,55], the relatively slow progression of pH in Fe(II)-based silica garden systems (as compared to Fe(III) and Co) can further be attributed to high crystallinity and low porosity/permeability. Similarly, the higher crystallinity of calcium carbonate minerals led to densely packed membrane structures, which inhibit diffusion processes and retard the pH equilibration in synthetic $CaCO_3$ tubes [36]. The slow progression of pH in Magadi tubes could be explained by densely packed highly crystalline $CaCO_3$ minerals and their low porosity-permeability (see Figure 5 and Figure 7).

Table 2. Acidity of metal ions [60] and solubility products of mineral phases [61–69] presumed to precipitate during the formation and ripening of macroscopic carbonate and silicate garden tubes.

Cations	Acidity (pK_a)	Possible minerals and their solubility products
Ca^{2+}	12.9 (pK_1)	calcite ($3.4×10^{-9}$), vaterite ($1.2×10^{-8}$), aragonite ($4.6×10^{-9}$), hydrated/ anhydrous amorphous calcium carbonate (ACC) ($9.1×10^{-7}$ / $9.9×10^{-8}$), gaylussite ($3.8×10^{-10}$) calcium-silicate-hydrate ($6CaO·5SiO_2·6H_2O$) ($5.5×10^{-49}$), wollastonite ($CaSiO_3$) ($2.5×10^{-8}$), $Ca(OH)_2$ ($5.0×10^{-6}$), fluorite ($3.45×10^{-11}$)
Co^{2+}	9.6 (pK_1)	$Co(OH)_2$ ($5.9×10^{-15}$)
Fe^{2+}	9.5 (pK_1)	$Fe(OH)_2$ ($4.9×10^{-17}$)
Fe^{3+}	2.2 (pK_1) 5.7 (pK_2)	$Fe(OH)_3$ ($2.8×10^{-39}$)
Al^{3+}	5.0 (pK_1) 9.3 (pK_2)	$Al(OH)_3$ ($3.2×10^{-34}$)

Electrochemical potential differences

Time-dependent electrochemical potential differences measured across Magadi calcium carbonate tubes are shown in Figure 4 together with different synthetic metal carbonate and silicate tubes from previous studies [7,9,10,25,36] for comparison. The potential difference measured across Magadi tubes after 2 h of ripening was 30 mV which is higher than the maximum voltage across synthetic Ca-based carbonate (10 mV) and silica (20 mV) garden tubes, whereas it's much lower than Fe(II), Fe(III), Co, and Al silica tubes which developed initial ΔE_h values as high as 190, 650, 120, and 90 mV, respectively. The potential difference across Magadi tubes quickly drops to 6 mV until 3.5 h. Subsequently, ΔE_h decline continuously and eventually reaches zero at about 40 h. The overall electrochemical potential of metal silicate gardens was shown to be a combination of contributions originating from diffusion and membrane potentials, and a third component caused by the pH gradient between the two reservoirs [7,9]. The absence of distinct electrochemical potential differences across calcium carbonate and calcium silicate tubes was explained by the absence of distinct pH gradients and diffusions due to bilayered highly crystalline calcite and dense homogeneous calcium silicate walls, respectively [25,36].

In Magadi tubes, the voltage at 2 h (30 mV) seems to arise mainly from the contribution of membrane and/or diffusion potentials since the initial pH gradient of the Magadi tube seems relatively small (1.3), compared to later stages, to explain the observed high voltage. This is evident from the active diffusion of water with Ca^{2+} (causing pH decline) up to 3.7 h. Moreover, the transparency (see Figure 1) and fragile nature of the tubes at the beginning reflect high porosity-permeability that may permit significant diffusion of water and ions. The maximum pH gradient across these tubes was achieved after 3.7 h. Based on the analogy with synthetic silicate and carbonate gardens [7,9,10,25,36], the potential difference was expected to rise considerably at this time. Nonetheless, ΔE_h shows a very little rise (in 3 mV) between 3.5 and 4.5 h and continues to decline until the pH equilibrates with the external reservoir. This reflects the counterbalance between pH-induced ΔE_h rise and decline in diffusion and/or membrane potential following the onset of calcium carbonate mineral precipitation and tube densification as evidenced by continuous Ca^{2+} decline after 3.5 h (see Figure 2). Hence, the initial high voltage observed in natural Magadi carbonate tubes seems to be dominated by diffusion- and/or membrane-induced potential contrary to synthetic silicate gardens with an initial high ΔE_h dominated by pH-induced contribution. Based on the transparent and crumbling nature of the tubes and the very steep decline of potential at the beginning, Magadi tubes may have developed higher voltage (> 30 mV) immediately after the water addition stopped. This suggestion can be supported by the observations that transparent calcium carbonate gardens and vesicles synthesized in Magadi water have shown significant changes in morphology owing to significant inward water diffusion [23] that may result diffusion-induced electrochemical potential differences.

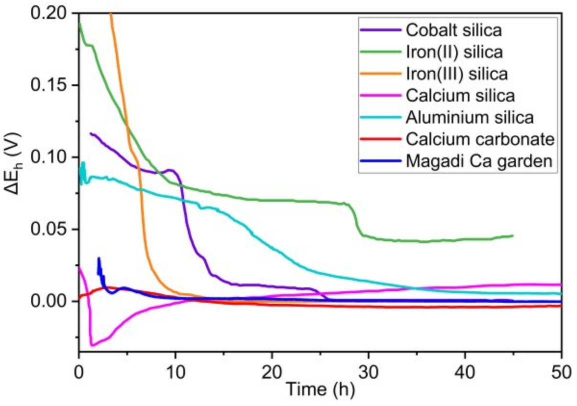

Figure 4. Temporal evolution of electrochemical potential differences (ΔE_h) measured across macroscopic chemical gardens tubes based on Magadi water (black), carbonate (red), and silicates with different metals as indicated. Data for calcium-[11], cobalt-[7], aluminium-[10], iron(II)- and iron(III)-based silicate [9] and calcium-based carbonate [12] are reproduced from the literature with permission from the publishers.

On the other hand, cobalt silicate and Magadi tubes have shown an overall comparable pH gradient (Figure 3). Nevertheless, the sum of all potential contributions (membrane, diffusion, and pH gradient induced) in Magadi tubes is significantly smaller than the potential difference induced only by the pH gradient of cobalt silicate gardens (see ref. [7]). This shows that the pH gradient (whether high or low) doesn't seem to produce significant electrochemical potential difference unless the membrane is porous and permeable. The absence or minimal contribution of membrane and diffusion potentials in synthetic calcium carbonate gardens is due to slower precipitation kinetics of $CaCO_3$ (and gaylussite) species as compared to metal oxy/hydroxides in the case of iron and cobalt silicate-based chemical gardens, leading to more crystalline and less permeable membranes that inhibit diffusion and counter-diffusion processes [36]. Consequently, the low pH gradients represent the sole contributions to the overall potential difference. Despite the presence of a significantly higher pH gradient in Magadi tubes than in synthetic carbonate tubes, the crystalline and densely packed carbonate minerals of both tubes led to a potential difference that doesn't differ a lot (10 vs 30 mV).

Membrane characterization

Magadi calcium carbonate gardens have been characterized by using X-ray diffraction, Raman spectroscopy, FTIR-ATR (attenuated total reflectance) spectroscopy, and scanning electron microscopy. These methods of characterization were performed ex-situ, after isolating the tubes at different periods of aging, to reveal the evolution of the tubes over time. Powder X-ray diffraction patterns of Magadi tubes (Figure 5) reveal that membranes isolated after 4h of ripening were composed of mainly calcite with minor amounts of gaylussite. In membranes isolated after 8 hours and later, the tubes are composed of calcite and minor fluorite, indicating precipitation of fluorite on the interior surfaces of the tube walls. Owing to the presence of high amount of fluoride in Magadi water (see Table 1) and its low solubility (Table 2), fluorite precipitation is expected upon the interaction of the interior Ca-rich solution with the exterior reservoir. Gaylussite and fluorite have been forming in both modern and ancient Lake Magadi and Nasikie Engida when Na^+, CO_3^{2-} and F^--rich lake brines mix with Ca^{2+}-rich groundwater or via reaction of calcite with Na^+, CO_3^{2-} and F^--rich lake brines [39,56–58]. In the case of the natural setting, lake brines serve as a source of Na^+ and F^- whereas groundwater and calcite serve as a source of Ca^{2+}. Calcite was the dominant phase in most of the synthetic carbonates with some vaterite and gaylussite [31,36]. The proposed route of transformation from amorphous calcium carbonate to calcite via vaterite [59,60] may have happened in Magadi tubes earlier than 4 hours.

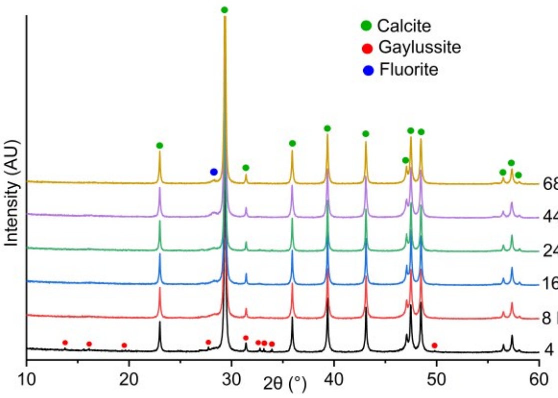

Figure 5. Powder X-ray diffraction patterns of tubular calcium carbonate structures isolated after different periods of ripening as indicated. Reflections are assigned to the different detected mineral phases by coloured circles.

Figure 6 shows Raman and IR spectra recorded from Magadi calcium carbonate tubes isolated after different periods of ripening. Raman spectra (Figure 6a) acquired after 4, 8, 16 h, and later up to 68 h revealed the presence of only calcite both on the interior and exterior of the tubes, whereas spectra acquired after 12 h of ripening on the exterior of the tubes have shown calcite, vaterite, gaylussite, and fluorite (see Figure S1 for fluorite). Spectra (data not shown) collected on the exterior surface after 4, 8, 16, 24, 44, and 68 h of aging have shown only calcite. Gaylussite detected on the interior tube isolated after 12 h could be an artifact formed during isolation when the two solutions come in contact. Gaylussite was observed only on the exterior surfaces in scanning electron microscopic studies (see Figure 7, S2). In synthetic calcium gardens, gaylussite wasn't observed on the interior surfaces [36]. The dominance of calcite at most of the ages of the tubes is consistent with the XRD data, which showed calcite and fluorite with gaylussite in tubes isolated after 12 hours of aging. Fluorite has one prominent peak at 322 cm^{-1} [61,62] but its intensity in Magadi tubes (see Figure S1) is very small, implying that fluorite may have been precipitating but it is obscured due to its small quantity and low intensity peaks relative to calcite. This is in line with the X-ray diffraction that shows fluorite with the appearance of its most intense diffraction peak at 2θ of 28.34°.

Figure 6b shows IR spectra of powdered membranes that were isolated after different periods of ripening. The data confirm the presence of calcite and vaterite as identified by X-ray diffraction and Raman spectroscopy, but gaylussite and fluorite were not detected, probably due to the relatively small amounts, in line with results from XRD (Figure 5) and Raman spectroscopy (Figure 6a). X-ray diffractions and IR spectra of tubes isolated after 12 h (not shown) didn't show the gaylussite detected by Raman spectroscopy (Figure 6a magenta curve), implying that gaylussite could have formed locally in a small quantity inside the tube during isolation.

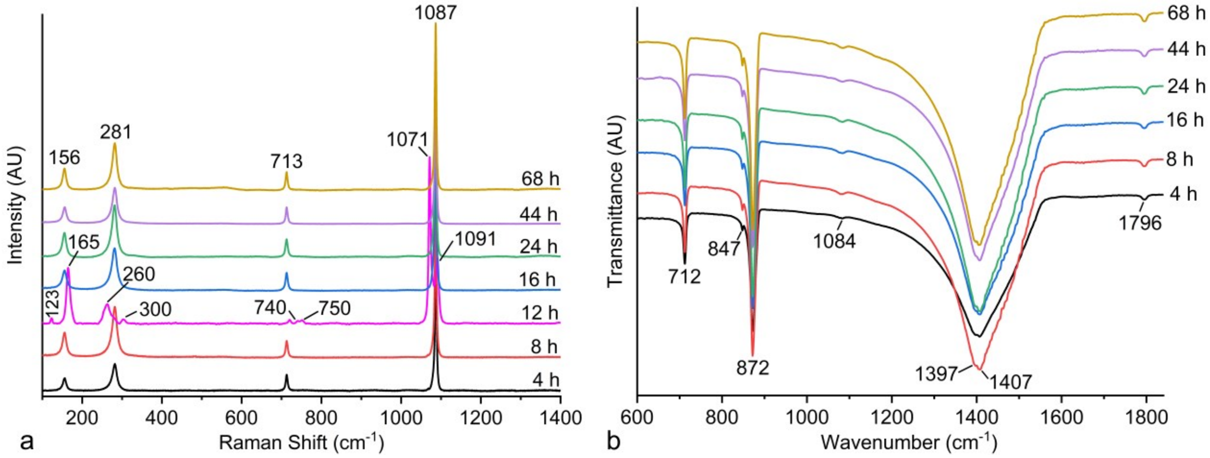

Figure 6. Spectroscopic characterization of Magadi $CaCO_3$ gardens after different times of ripening. (a) Raman spectra acquired on the interior (4 h – black, 12 h – magenta, 16 h – blue, 44 h – violet, 68 – orange) and exterior (8 h – red, 24 h – green) surfaces of the tubular membranes. The observed Raman bands can be assigned to lattice, in-plane bending, and symmetric stretching modes of the CO_3^{2-} groups in different mineral phases as follows: calcite – 156/281, 713, and 1087 cm^{-1} [78]; vaterite – 123/260/300, 740/750, and 1091 cm^{-1} [79]; gaylussite – 165 and 1071 cm^{-1} [80]. (b) IR spectra collected from Magadi $CaCO_3$ tubes at distinct times of aging (as indicated) after grinding to a fine powder. The observed vibrational bands correspond to in-plane bending, out-of-plane bending, and asymmetric stretching modes of the CO_3^{2-} groups in different mineral phases as follows: calcite – 712, 847, 1397 and 1796 cm^{-1} [81–84]; vaterite – 872, 1084, and 1407 cm^{-1} [81,82,84].

Scanning electron micrographs of macroscopic Magadi carbonate tubes are shown in Figure 7. The collected data confirm the mineral identification made with X-ray diffraction, Raman, and IR spectroscopy. The SEM studies show that tubular Magadi carbonate structures are bilayered membranes (Figure 7a-c). The external wavy surfaces (Figure 7b) are covered with a densely packed layer (ca. 40 µm thick) composed of aggregates of nanospherical subunits organized in a random and columnar fashion (Figure 7b,c). When we move from the interior of the tubes towards the exterior surface across this layer, the randomly packed nanospherical units gradually change to columnar aggregates forming bunches of columnar crystals (Figure 7c) that appear on the outer surface as interlocked rhombohedral calcite (Figure 7d,e). Gaylussite crystals were observed on the exterior surfaces of Magadi tubes (Figure 7d, S2). Sheet-like and filamentous silica precipitates were also observed covering the wavy interlocked calcite surfaces on the exterior of the tubes after 24 h of ripening (Figure S2). In synthetic calcium carbonate gardens, wavy external surfaces were observed at the early stage of the tube growth that appeared later as a dense layer of rhombohedral calcite aggregates [36]. Wavy membranes have been reported to form at the interface between $MnCl_2$ and NaOH solutions injected into two parallel fluid channels of a 2D microfluidic device [70].

The internal layer of Magadi tubes is composed of adjacent cone-like calcite structures (Figure 7a) that are covered by complex textures such as hollow spherical, cauliflower-, bowl- and prismatic precipitates (Figure 7h-i, Figure S3). The cones are composed of nanospherical subunits that aggregate randomly and as elongated columnar crystals that appeared on the interior surface as interlocked calcite crystals (Figure S4), like the external layer. However, the direction of the textural gradient is the opposite. The columnar crystals in cones are found towards the interior of the tubes whereas the randomly aggregated nanospheres are away from the interior surface of the tubes. In other term, the textural gradient moves from random aggregation to euhedral crystalline texture towards the solutions inside and outside the tubes, implying rather slow crystallization. Cone-shaped calcite interior surfaces were observed in synthetic calcium carbonate gardens [36]. However, the apexes of these cones appeared on the surface as nanospherical aggregates [36] whereas in Magadi tubes the apexes are interlocked rhombohedral calcite (Figure 7g, S4) due to the slow progression of tube formation.

When viewed from below (Figure 7f), the cones are reminiscent of textures observed in the mammillary core layer of eggshells [71]. The columnar nanospherical subunits in both layers may suggest growth by an accretion-based mechanism [72]. Alternatively, these inward pointing conical structures may infer a precipitation process via a radially inward propagating reaction-diffusion front[73]. However, the radial textural gradient from the core towards the interior and the exterior surface of the tubes (i.e., from randomly aggregated nanospheres to interlocked rhombohedral calcite via columnar nanospherical aggregates) suggests, most likely, a slow transformation from amorphous calcium carbonate to calcite via vaterite through two-step crystallization processes of calcium carbonates[51,59,60].

Hollow spherical, cauliflower- and bowl-shaped precipitates were observed covering the apexes of the cones on the interior surfaces of the tubes that ripened for 12 hours and above whereas they are absent in tubes that ripened for 4 and 8 hours. The hollow spherical and bowl-shaped precipitates are bilayered, composing an interior smooth shell covered by an external cauliflower-shaped interlocked rhombohedral calcite aggregate (Figure S3a-c). The crushed hollow spheres appear as bowls (Figure 7h-i). EDX elemental analysis has shown that the interior smooth shell contains a high amount of fluoride which is absent on the faceted cauliflowers (see Figure S5).

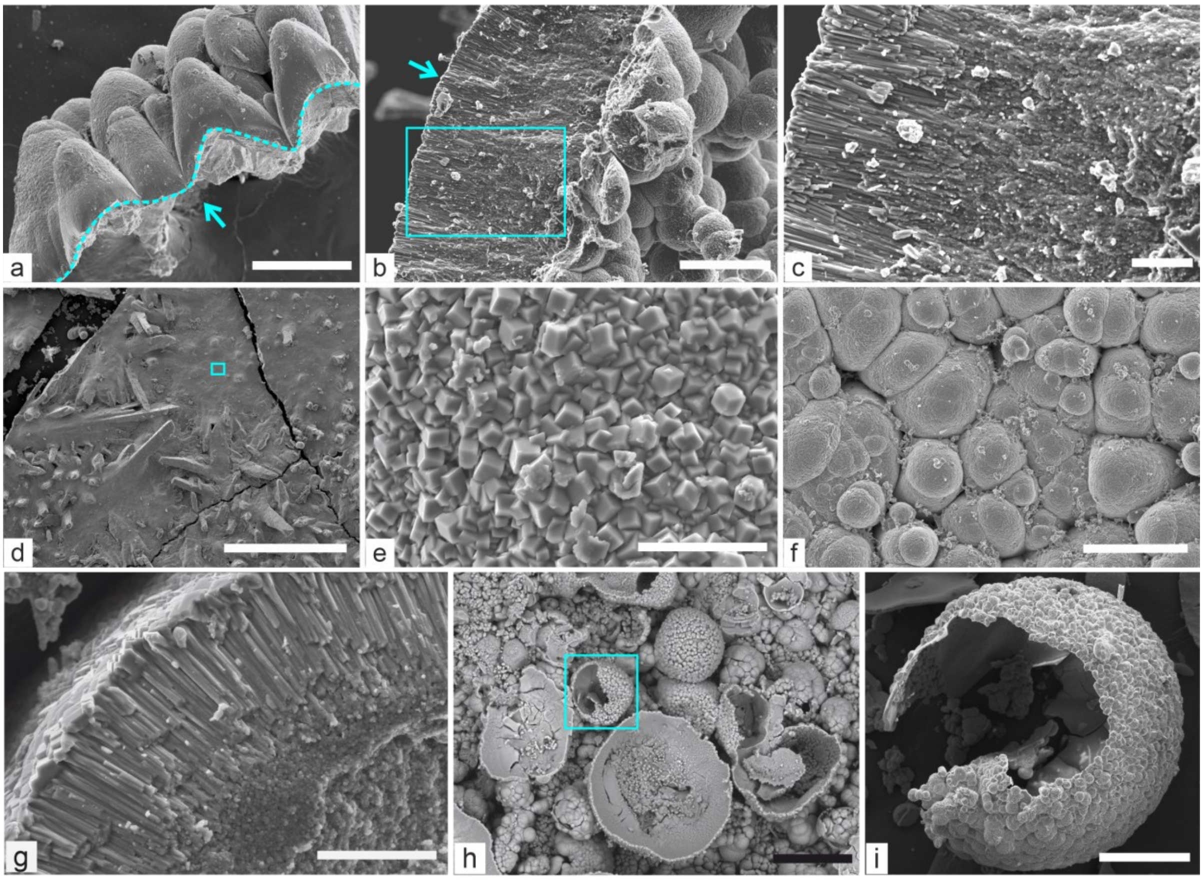

Figure 7. Scanning electron micrographs of macroscopic Magadi carbonate gardens. (a-c) Cross-sectional views of the tube wall after a) 44 and b) 24 hours of ripening, showing an exterior wavy surface (indicated by dashed line and arrows) composed of a dense layer of co-aligned rhombohedral calcite crystals, and a less dense interior surface formed by calcite cones. (c) Close-up view of the area marked by the cyan rectangle in (b) showing a textural gradient from nanosphere to columnar texture composed of nano-spherical subunits. (d) Gaylussite crystals observed on the exterior surface of the membranes after 4 hours of ripening. (e) High-magnification micrograph of the exterior surface marked by the cyan rectangle in (d), revealing multiple interlocked crystallites of rhombohedral calcite. (f) Top view of the interior surface of tubes aged for 16 hours, showing apexes of the calcite cones like (a). (g) Close-up view of a fractured cone on the interior surface as shown in (f). (h) Spherical and bowl-shaped calcite precipitates on top of the interior surface of the tubes after 12 hours of aging. (i) Zoom into the area marked by the cyan rectangle in (h), showing a partially broken hollow spherical bilayered structure composed of exterior faceted calcite aggregates on the smooth inner layer. Scale bars in µm: (a, h) 100, (b) 20, (c, e, g) 5, (d) 400, (f) 10, and (i) 50

Hollow spherical vaterites have been synthesized using bubble templating [74–76]. Amorphous calcium carbonates (ACC) [77] and vaterite hollow structures [78,79] were reported to form in the presence of additives. These structures form through ACC precipitation on CO_2 bubbles followed by dissolution and recrystallization to vaterite [74–76]. Hollows also form through a dissolution of the core of ACC microspheres after its exterior transformation to a vaterite shell [76]. However, elemental analysis of the smooth shells on Magadi tubes shows fluorite instead of $CaCO_3$ (see Figure S5). This may imply that either fluorite has precipitated on CO_2 bubble templates owing to the buildup of fluoride concentration in the interior solution or transformation of hollow vaterite shells, formed via the mechanism presented in ref. [74–76], to fluorite or fluoride surface absorption on $CaCO_3$ shells [80]. The outer faceted calcite aggregates may form on the interior fluorite/vaterite by secondary nucleation when supersaturation is low, and crystallization is slow [81]. The formation of hollow spherical fluorite/$CaCO_3$ agrees with the CO_2 bubbles observed on macroscopic tubular structures (Figure 1a) which could form when the acidic interior solution encounters the CO_3^{2-}-rich Magadi water. In contrast to Magadi tubes, hollow spherical carbonate minerals were not observed in synthetic calcium carbonate tubes [36]. The surfaces of the prismatic precipitates on the interior of the tubes show stepped patterns whereas the tips are three (probably pentagonal or rhomboid {104} faces) to multifaceted calcite crystals (Figure S3d), suggesting transformation from hexagonal vaterite to calcite [82].

Conclusions

For the first, we have monitored the dynamic time-dependent evolution of pH, ion concentrations, and electrochemical potential differences in calcium carbonate gardens synthesized in natural water. In addition, mineral precipitation into the tube walls was explained by ex-situ analyses of membrane composition and structure using X-ray diffraction, IR, and Raman spectroscopy as well as scanning electron microscopy. The results revealed that the natural calcium carbonate membranes are bilayers of texturally distinct but compositionally similar crystalline calcite. The interior surface of the membrane consists of numerous adjacent cone-like structures that are decorated with hollow spherical, cauliflower-, bowl-shaped, and prismatic crystals whereas the outer surface is a thick layer of interlocked calcite rhombohedra. Both the outer and the inner layers initially precipitate as randomly aggregated nanospheres followed by columnar crystals containing nanospherical units that manifest both on the interior and exterior surfaces as interlocked rhombohedral calcite. This textural gradient from the core of the membranes towards the surface shows the gradual slowing down of the crystallization process. These multiple crystalline calcite layers permit slow diffusion of Na^+ and K^+ ions from the outer reservoir towards the interiors of the tubes for more than two days. Gradually reduced exchange and interaction of ionic species between the inner and outer solutions caused concentration gradients to sustain for days.

The other important observation is the existence of high pH gradient comparable to Co and Fe(II) silica gardens[9,26] – in contrast to synthetic calcium-based silica and carbonate gardens[25,36]. Low electrochemical potential differences across these tubes are in contrast with the findings that pH-induced electrochemical potential differences were significant in silica gardens [9,10,26]. These observations revealed that pH gradient contributes to electrochemical potential differences only if it co-exists with permeable membranes. Owing to the very fragile and transparent nature of the tubes immediately after tube preparation that inhibits monitoring from the beginning, Magadi tubes may have attained a voltage higher than 30 mV which is measured after 2 h. Still, Magadi tubes generated an electrochemical potential three times those obtained in synthetic carbonate gardens, and they seem to be more permeable at the earlier stages. This finding is relevant for studies aiming at using chemical gardens for electrochemically enhanced synthesis and the suggested role of chemical gardens as catalyzers of prebiotic chemistry in soda oceans of primitive Earth, and Earth-like planets and moons.

Cobalt(II)- and iron(II)-based vesicles and gardens synthesized in Magadi water were shown to be less crystalline materials[23]. Hence, it may be inferred that these vesicles and chemical gardens formed in soda oceans of the early Earth might have developed significant electrochemical voltage, allowing chemical conversions. Indeed, synthetic carbonate-based iron chemical gardens were shown to catalyze the polymerization of simple organic prebiotic molecules to kerogens [33]. A recent study has shown that, in addition to electrochemical voltage, the structure and nano-mineralogy control the catalytic function of iron silica membranes [83]. This implies that catalytic properties inherited from the mineralogy of natural calcium carbonate tubes may have played roles in prebiotic chemistry and origin of life. Hence, it’s crucial to elucidate the nano-mineralogy of these membranes to better understand their potential role in prebiotic chemistry. In addition, we suggest that origin of life research should utilize natural self-assembled structures instead of synthetic ones to obtain a better picture of prebiotic geo(bio)chemistry on early Earth soda oceans.

The role of silica in the formation of the observed tubular gardens was not significant due to its small amount in Magadi water because of the recent dilution of the rift valley lakes by unusually high rainfall in the region. To enrich the concentration of silica to values reported before the recent dilution of Lake Magadi, fluid-rock interaction experiments between Magadi brines and cherts are underway. Future studies will focus on testing the formation of silica-based self-assembled mineral structures and elucidating their dynamic precipitation process by using the silica-enriched brine.

Experimental Section

The sample used for the experiments was collected from the Lake Magadi evaporation ponds (sampling point located at a coordinate of 36.29° E, 1.88° S, and 607m above sea level) during the field campaign in March 2018. The in-situ pH was measured to be 9.9 whereas the temperature was 37.5 °C. The hydrochemistry of Lake Magadi sample was analyzed by ALS Laboratory Group (Czech Republic), except for K^+ and SO_4^{2-}. Na^+, Ca^{2+}, Mg^{2+}, Al^{3+}, and Fe were analyzed using inductively coupled plasma (ICP) atomic emission spectrometry (AES). To avoid matrix interference, samples were homogenized and mineralized with nitric acid in an autoclave under high pressure (7.5 atm) and temperature (170 °C) before analysis by ICP-AES. CO_3^{2-} and HCO_3^- were analyzed by potentiometric titration. Cl^- and F^- ions were determined using ion liquid chromatography. Total P and SiO_2 were determined by discrete spectrophotometry. K^+ and SO_4^{2-} were determined by using Varian Cary 1E ultraviolet-visible spectrophotometry in our lab. Total dissolved solids were determined gravimetrically after filtering the water by using glass microfibre filters (Environmental Express, 1.5 μm pore size). The hydrochemical analysis of Lake Magadi water used for the growth of mineral gardens and vesicles is presented in Table 1.

Magadi calcium carbonate membranes were synthesized using the method developed elsewhere [7,9,12]. Tubular carbonate gardens were synthesized by slow and controlled addition of Lake Magadi water (pH 9. 9) to pressed pellets of calcium chloride dihydrate, which were fixed by double-sided adhesive tape at the bottom of a 120 mL plastic beaker. The pellets (20 mm diameter) were prepared by grinding $CaCl_2 \cdot 2H_2O$ (Sigma Aldrich, ≥ 99 %) to a fine powder using an agate mortar. Then, 1.2 g of the powdered $CaCl_2 \cdot 2H_2O$ was pressed with 7 ton pressure by using a Specac hydraulic press. For controlled growth of the tubes, 5 mL of Magadi water (see Table 1) was pipetted manually at the beginning and an additional 35 mL was dosed at a flow rate of 0.15 mL/min using an Ismatec Reglo digital peristaltic pump (Antylia Scientific, USA). For the determination of ion concentrations, samples were collected at different times from the interior (20 μL) and exterior (100 μL) solutions by using a volumetric pipette. The samples were diluted with 10 mL distilled Milli-Q water and analyzed by inductively coupled plasma optical emission spectroscopy (ICP-OES) on a Varian ICP 720-ES instrument (Agilent Technologies, USA). For continuous pH measurements, a glass microelectrode (Mettler-Toledo InLab Micro; tip diameter: 3 mm) was immersed into the inner solution at a depth of *ca*. 5 mm. The electrode was connected to a digital laboratory pH meter (CRISON GLP 21), which was read out by ComLabo Easy software (CRISON, Spain) at intervals of 5 s for 100 hours. Electrochemical potential differences were monitored using a pair of identical platinum stick electrodes, which were immersed at a depth of about 2 mm into both the inner and outer solution. Data were recorded every 1 s for 120 h using a multimeter (PeakTech® 3430) linked to a computer. The tubes were extremely fragile to introduce pipette tips and electrodes immediately after terminating the addition of Magadi water. Hence, sampling of the interior solution and monitoring of the pH and electrochemical potential difference was commenced after two hours of ripening. The reference time (0 h) for pH, electrochemical voltage, ionic concentration measurements, and membrane isolation refers to the time after the addition of the water was stopped, which takes about 4 hours.

The formed tubular membranes were isolated after different times of ripening for ex-situ compositional and structural characterization. For this purpose, the exterior and interior solutions were removed carefully using a syringe and replaced with deionized water multiple times to remove soluble salts. After the final rinsing of the membrane material with water and ethanol, it was dried in an ambient atmosphere, and parts of the obtained dry tube were ground to a fine powder. The tubular structures were subsequently characterized using powder X-ray diffraction (PXRD), Raman and infrared (IR) spectroscopy, as well as scanning electron microscopy (SEM). PXRD measurements were performed on a high-resolution Bruker D8 Advance X-ray diffractometer using Cu-Kα1 radiation provided by a primary Ge(111) monochromator and a Lynxeye PSD detector. Diffraction data were collected in transmission mode at 40 kV acceleration voltage and 40 mA current for 1 hour, covering a 2θ range of 5-80° with an increment of 0.02° per second. Mineral phases present in the powders were identified by using Malvern Panalytical HighScore software (version 4.8) with the ICCD PDF-4+ database. Raman spectra were recorded on the exterior and interior walls of intact tubular structures by using a HORIBA Jobin Yvon LabRAM high-resolution UV-Vis spectrometer, which was equipped with an Olympus BX41 optical microscope (with binocular and Koehler illumination) and a charge-coupled device (CCD) detector. Excitation at a wavelength of 532 nm was achieved with a frequency-doubled, neodymium-doped yttrium-aluminum-garnet laser. FTIR spectra of ground powders were recorded by a Bruker INVENIO FTIR spectrometer with a Bruker Platinum ATR accessory. The spectra were analyzed using the OPUS software with 80 scans in a spectral range of 4000–400 cm^{-1}, at 2 cm^{-1} resolution. A background spectrum was collected on the clean diamond crystal before each sample measurement. Studies on the texture and chemical composition of tubular membranes were performed by using FEI field emission environmental scanning electron microscope (FEG-ESEM QUEMSCAN 650F) equipped with Bruker XFlash 6-30 EDX analyzer, which was operated at 5-20 kV with a working distance of 6-10 mm.

Acknowledgments

The authors thank Isabel Sánchez Almazo for support during the scanning electron microscopy analyses at the Centro de Instrumentación Científica (CIC) of the University of Granada and Cristóbal Verdugo Escamilla, Joaquín Criado-Reyes, Raquel Fernandez-Penas, and Francisca Espinosa for their technical assistance. We acknowledge Miryam Rojas Gómez for the ICP-OES analyses carried out at the Instrumental Technical Services of the Estación Experimental del Zaidín (CSIC), Granada, Spain. We thank Fabian Glaab and Enrique Castillo for their technical help with a multimeter and custom-made Pt electrodes. We acknowledge the European Research Council under the European Union's Seventh Framework Program (FP7/2007-2013)/ERC grant agreement no. 340863, the Spanish Ministerio de Economía y Competitividad for the financial support to the project CGL2016-78971-P and Junta de Andalucía for financing the project P18-FR-5008. M.G. acknowledges Grant No. BES-2017-081105 of the Ministerio de Ciencia, Innovacion y Universidades of the Spanish government.

Keywords: calcium carbonate • natural mineral gardens • soda lake • electrochemical potential • prebiotic chemistry

[1] L. M. Barge, S. S. S. Cardoso, J. H. E. Cartwright, G. J. T. Cooper, L. Cronin, A. De Wit, I. J. Doloboff, B. Escribano, R. E. Goldstein, F. Haudin, D. E. H. Jones, A. L. Mackay, J. Maselko, J. J. Pagano, J. Pantaleone, M. J. Russell, C. I. Sainz-Díaz, O. Steinbock, D. A. Stone, Y. Tanimoto, N. L. Thomas, *Chem. Rev.* **2015**, *115*, 8652–8703.

[2] M. Kellermeier, F. Glaab, E. Melero-García, J. M. García-Ruiz, in *Methods in Enzymology*, Elsevier, **2013**, pp. 225–256.

[3] J. H. E. Cartwright, J. M. García-Ruiz, M. L. Novella, F. Otálora, *Journal of Colloid and Interface Science* **2002**, *256*, 351–359.

[4] R. Buick, *PALAIOS* **1990**, *5*, 441–459.

[5] M. D. Brasier, O. R. Green, A. P. Jephcoat, A. K. Kleppe, M. J. Van Kranendonk, J. F. Lindsay, A. Steele, N. V. Grassineau, *Nature* **2002**, *416*, 76–81.

[6] F. Stalport, P. Coll, M. Cabane, A. Person, R. N. González, F. Raulin, M. J. Vaulay, P. Ausset, C. P. McKay, C. Szopa, J. Zarnecki, *Geophysical Research Letters* **2005**, *32*, L23205.

[7] F. Glaab, M. Kellermeier, W. Kunz, E. Morallon, J. M. García-Ruiz, *Angew. Chem.* **2012**, *124*, 4393–4397.

[8] L. M. Barge, Y. Abedian, M. J. Russell, I. J. Doloboff, J. H. E. Cartwright, R. D. Kidd, I. Kanik, *Angew. Chem. Int. Ed.* **2015**, *54*, 8184–8187.

[9] F. Glaab, J. Rieder, J. M. García-Ruiz, W. Kunz, M. Kellermeier, *Phys. Chem. Chem. Phys.* **2016**, *18*, 24850–24858.

[10] J. Rieder, M. Nützl, W. Kunz, M. Kellermeier, *Langmuir* **2022**, *38*, 10392–10399.

[11] L. M. Barge, I. J. Doloboff, L. M. White, G. D. Stucky, M. J. Russell, I. Kanik, *Langmuir* **2012**, *28*, 3714–3721.

[12] C. Collins, R. Mokaya, J. Klinowski, *Phys. Chem. Chem. Phys.* **1999**, *1*, 4669–4672.

[13] J. Maselko, P. Strizhak, *J. Phys. Chem. B* **2004**, *108*, 4937–4939.

[14] J. J. Pagano, T. Bánsági, O. Steinbock, *Angewandte Chemie International Edition* **2008**, *47*, 9900–9903.

[15] T. S. Sørensen, *Journal of Colloid and Interface Science* **1981**, *79*, 192–208.

[16] B. C. Batista, O. Steinbock, *Chem. Commun.* **2015**, *51*, 12962–12965.

[17] R. Saladino, G. Botta, B. M. Bizzarri, E. Di Mauro, J. M. Garcia Ruiz, *Biochemistry* **2016**, *55*, 2806–2811.

[18] B. M. Bizzarri, L. Botta, M. I. Pérez-Valverde, R. Saladino, E. Di Mauro, J. M. García-Ruiz, *Chemistry – A European Journal* **2018**, *24*, 8126–8132.

[19] R. Saladino, E. Di Mauro, J. M. García-Ruiz, *Chem. Eur. J.* **2019**, *25*, 3181–3189.

[20] L. M. Barge, E. Flores, M. M. Baum, D. G. VanderVelde, M. J. Russell, *Proceedings of the National Academy of Sciences* **2019**, *116*, 4828–4833.

[21] J. M. García-Ruiz, E. Nakouzi, E. Kotopoulou, L. Tamborrino, O. Steinbock, *Sci. Adv.* **2017**, *3*, e1602285.

[22] H. Satoh, K. Tsukamoto, J. M. Garcia-Ruiz, *ejm* **2014**, *26*, 415–426.

[23] M. Getenet, J. M. García-Ruiz, C. Verdugo-Escamilla, I. Guerra-Tschuschke, *Crystals* **2020**, *10*, 467.

[24] J. M. García-Ruiz, M. A. van Zuilen, W. Bach, *Physics of Life Reviews* **2020**, *34–35*, 62–82.

[25] J. Rieder, L. Nicoleau, F. Glaab, A. E. S. Van Driessche, J. Manuel Garcia-Ruiz, W. Kunz, M. Kellermeier, *Journal of Colloid and Interface Science* **2022**, *618*, 206–218.

[26] F. Glaab, M. Kellermeier, W. Kunz, E. Morallon, J. M. García-Ruiz, *Angew. Chem.* **2012**, *124*, 4393–4397.

[27] S. Kempe, E. T. Degens, *Chemical Geology* **1985**, *53*, 95–108.

[28] S. Kempe, J. Kazmierczak, E. T. Degens, in *Origin, Evolution, and Modern Aspects of Biomineralization in Plants and Animals* (Ed.: R.E. Crick), Springer US, Boston, MA, **1989**, pp. 29–43.

[29] S. Kempe, J. Kazmierczak, in *Encyclopedia of Geobiology* (Eds.: J. Reitner, V. Thiel), Springer Netherlands, Dordrecht, **2011**, pp. 829–833.

[30] C. R. Glein, J. A. Baross, J. H. Waite, *Geochimica et Cosmochimica Acta* **2015**, *162*, 202–219.

[31] S. S. S. Cardoso, J. H. E. Cartwright, C. I. Sainz-Díaz, *Icarus* **2019**, *319*, 337–348.

[32] J. M. García-Ruiz, in *Carbonate Sedimentation and Diagenesis in the Evolving Precambrian World* (Eds.: J.P. Grotzinger, N.P. James), SEPM Society For Sedimentary Geology, **2000**, pp. 75–89.

[33] G. Angelis, G. G. Kordopati, E. Zingkou, A. Karioti, G. Sotiropoulou, G. Pampalakis, *Chemistry – A European Journal* **2021**, *27*, 600–604.

[34] J. Maselko, P. Borisova, M. Carnahan, E. Dreyer, R. Devon, M. Schmoll, D. Douthat, *J Mater Sci* **2005**, *40*, 4671–4673.

[35] S. S. S. Cardoso, J. H. E. Cartwright, A. G. Checa, C. I. Sainz-Díaz, *Acta Biomaterialia* **2016**, *43*, 338–347.

[36] M. Getenet, J. Rieder, M. Kellermeier, W. Kunz, J. M. García-Ruiz, *Chemistry – A European Journal* **2021**, *27*, 16135–16144.

[37] B. H. Baker, *Geology of the Magadi Area*, Geol. Surv. Kenya, Nairobi, Kenya, Rep. 42. Pp 81, **1958**.

[38] B. H. Baker, *Geology of the Area South of Magadi*, Geol. Surv. Kenya, Nairobi, Kenya, Rep. 61. Pp 27, **1963**.

[39] H. P. Eugster, in *Developments in Sedimentology* (Ed.: A. Nissenbaum), Elsevier, **1980**, pp. 195–232.

[40] B. F. Jones, H. P. Eugster, S. L. Rettig, *Geochimica et Cosmochimica Acta* **1977**, *41*, 53–72.

[41] H. P. Eugster, *Mineral. Soc. Amer. Spec. Pap.* **1970**, *3*, 213–235.

[42] B. F. Jones, S. L. Rettig, H. P. Eugster, *Science* **1967**, *158*, 1310–1314.

[43] J. M. García-Ruiz, *Geology* **1998**, *26*, 843–846.

[44] J. H. E. Cartwright, B. Escribano, S. Khokhlov, C. I. Sainz-Díaz, *Phys. Chem. Chem. Phys.* **2011**, *13*, 1030–1036.

[45] C. F. Baes, R. E. Mesmer, *The Hydrolysis of Cations*, John Wiley & Sons, New York, **1976**.

[46] L. N. Plummer, E. Busenberg, *Geochimica et Cosmochimica Acta* **1982**, *46*, 1011–1040.

[47] K. Suzuki, T. Nishikawa, S. Ito, *Cement and Concrete Research* **1985**, *15*, 213–224.

[48] T. Ogino, T. Suzuki, K. Sawada, *Geochimica et Cosmochimica Acta* **1987**, *51*, 2757–2767.

[49] N. Plummer, D. L. Parkhurst, G. W. Fleming, S. A. Dunkle, *A Computer Program Incorporating Pitzer's Equations for Calculation of Geochemical Reactions in Brines*, U.S. Geological Survey, **1988**.

[50] J. R. Clarkson, T. J. Price, C. J. Adams, *Faraday Trans.* **1992**, *88*, 243.

[51] C. Rodriguez-Navarro, K. Kudłacz, Ö. Cizer, E. Ruiz-Agudo, *CrystEngComm* **2015**, *17*, 58–72.

[52] H. Sun, S. He, P. Wu, C. Gao, P. Feng, T. Xiao, Y. Deng, C. Shuai, *Materials* **2016**, *9*, 287.

[53] C. R. Frink, M. Peech, *Soil Science Society of America Journal* **1962**, *26*, 346–347.

[54] W. M. Haynes, *CRC Handbook of Chemistry and Physics*, CRC Press, **2016**.

[55] F. Glaab, J. Rieder, R. Klein, D. Choquesillo-Lazarte, E. Melero-Garcia, J.-M. García-Ruiz, W. Kunz, M. Kellermeier, *ChemPhysChem* **2017**, *18*, 338–345.

[56] R. W. Renaut, R. B. Owen, T. K. Lowenstein, G. D. Cort, E. Mcnulty, J. J. Scott, A. Mbuthia, *Sedimentology* **2020**, *68*, 108–134.

[57] R. C. Surdam, H. P. Eugster, *GSA Bulletin* **1976**, *87*, 1739–1752.

[58] H. P. Eugster, *Geological Society, London, Special Publications* **1986**, *25*, 177–189.

[59] P. Bots, L. G. Benning, J.-D. Rodriguez-Blanco, T. Roncal-Herrero, S. Shaw, *Crystal Growth & Design* **2012**, *12*, 3806–3814.

[60] J. D. Rodriguez-Blanco, S. Shaw, L. G. Benning, *Nanoscale* **2011**, *3*, 265–271.

[61] Z. Čermáková, P. Bezdička, I. Němec, J. Hradilová, V. Šrein, J. Blažek, D. Hradil, *Journal of Raman Spectroscopy* **2015**, *46*, 236–243.

[62] R. Srivastava, H. V. Lauer, L. L. Chase, W. E. Bron, *Physics Letters A* **1971**, *36*, 333–334.

[63] J. Urmos, S. K. Sharma, F. T. Mackenzie, *American Mineralogist* **1991**, *76*, 641–646.

[64] U. Wehrmeister, A. L. Soldati, D. E. Jacob, T. Häger, W. Hofmeister, *Journal of Raman Spectroscopy* **2010**, *41*, 193–201.

[65] R. L. Frost, M. Dickfos, *Polyhedron* **2007**, *26*, 4503–4508.

[66] F. A. Andersen, L. Brečević, G. Beuter, D. B. Dell'Amico, F. Calderazzo, N. J. Bjerrum, A. E. Underhill, *Acta Chem. Scand.* **1991**, *45*, 1018–1024.

[67] E. Loste, R. M. Wilson, R. Seshadri, F. C. Meldrum, *Journal of Crystal Growth* **2003**, *254*, 206–218.

[68] N. V. Chukanov, in *Infrared Spectra of Mineral Species: Extended Library* (Ed.: N.V. Chukanov), Springer Netherlands, Dordrecht, **2014**, pp. 21–1701.

[69] G. C. Jones, B. Jackson, *Infrared Transmission Spectra of Carbonate Minerals*, Springer Netherlands, Dordrecht, **1993**.

[70] Y. Ding, B. Batista, O. Steinbock, J. H. E. Cartwright, S. S. S. Cardoso, *PNAS* **2016**, *113*, 9182–9186.

[71] Y. Nys, M. T. Hincke, J. L. Arias, J. M. García-Ruiz, S. E. Solomon, *Avian and Poultry Biology Reviews* **1999**, *10*, 143–166.

[72] A. Gal, K. Kahil, N. Vidavsky, R. T. DeVol, P. U. P. A. Gilbert, P. Fratzl, S. Weiner, L. Addadi, *Advanced Functional Materials* **2014**, *24*, 5420–5426.

[73] L. Roszol, O. Steinbock, *Phys. Chem. Chem. Phys.* **2011**, *13*, 20100–20103.

[74] G. Hadiko, Y. S. Han, M. Fuji, M. Takahashi, *Materials Letters* **2005**, *59*, 2519–2522.

[75] Christopher. J. Grimes, T. Hardcastle, M. S. Manga, T. Mahmud, D. W. York, *Crystal Growth & Design* **2020**, *20*, 5572–5582.

[76] T. Tomioka, M. Fuji, M. Takahashi, C. Takai, M. Utsuno, *Crystal Growth & Design* **2012**, *12*, 771–776.

[77] A.-W. Xu, Q. Yu, W.-F. Dong, M. Antonietti, H. Cölfen, *Advanced Materials* **2005**, *17*, 2217–2221.

[78] S. Kim, J. W. Ko, C. B. Park, *J. Mater. Chem.* **2011**, *21*, 11070–11073.

[79] A. Cai, X. Xu, H. Pan, J. Tao, R. Liu, R. Tang, K. Cho, *J. Phys. Chem. C* **2008**, *112*, 11324–11330.

[80] B. D. Turner, P. Binning, S. L. S. Stipp, *Environ. Sci. Technol.* **2005**, *39*, 9561–9568.

[81] N. Loges, K. Graf, L. Nasdala, W. Tremel, *Langmuir* **2006**, *22*, 3073–3080.

[82] D. Liu, M. Z. Yates, *Langmuir* **2006**, *22*, 5566–5569.

[83] E. Kotopoulou, M. Lopez-Haro, J. J. Calvino Gamez, J. M. García-Ruiz, *Angewandte Chemie International Edition* **2021**, *60*, 1396–1402.

Supporting Information

Calcium Carbonate Tubular Structures from Natural Alkaline Soda Lakes: Formation, Characterization, and Implication for Prebiotic Geochemistry

Melese Getenet, Juan Manuel García-Ruiz

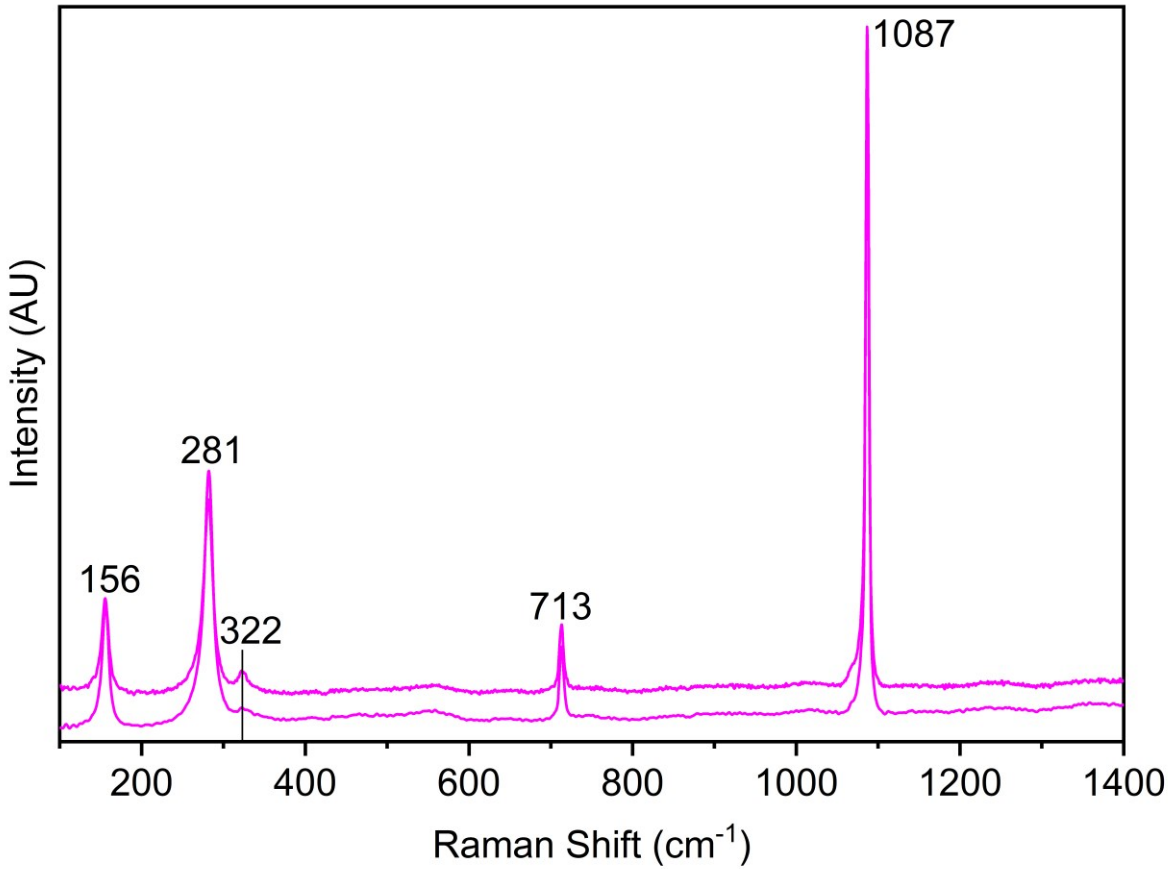

Figure S1. Raman spectra collected on the interior surface of the tubes collected after 12 hours of ripening showing calcite and fluorite. 322 cm^{-1} is Raman mode of fluorite

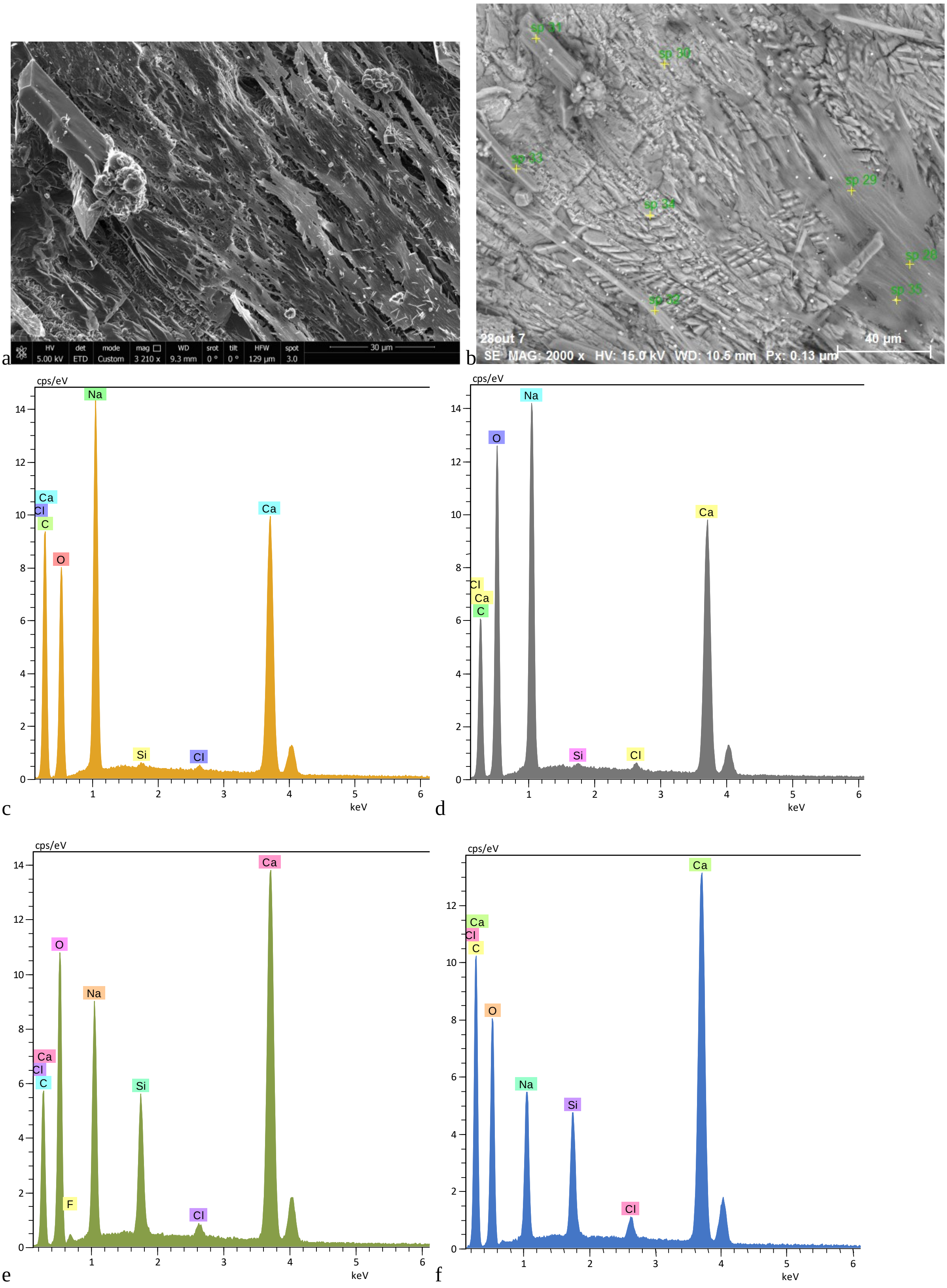

Figure S2. (a) SEM micrographs of gaylussite and silica precipitates covering the exterior surfaces of tubes ripened for 24 h, (b) points where elemental microanalysis performed, composition of sp31 (c) and sp33 (d) showing gaylussite, sp29 (e) and sp32 (f) showing mixture of gaylussite and silica precipitates

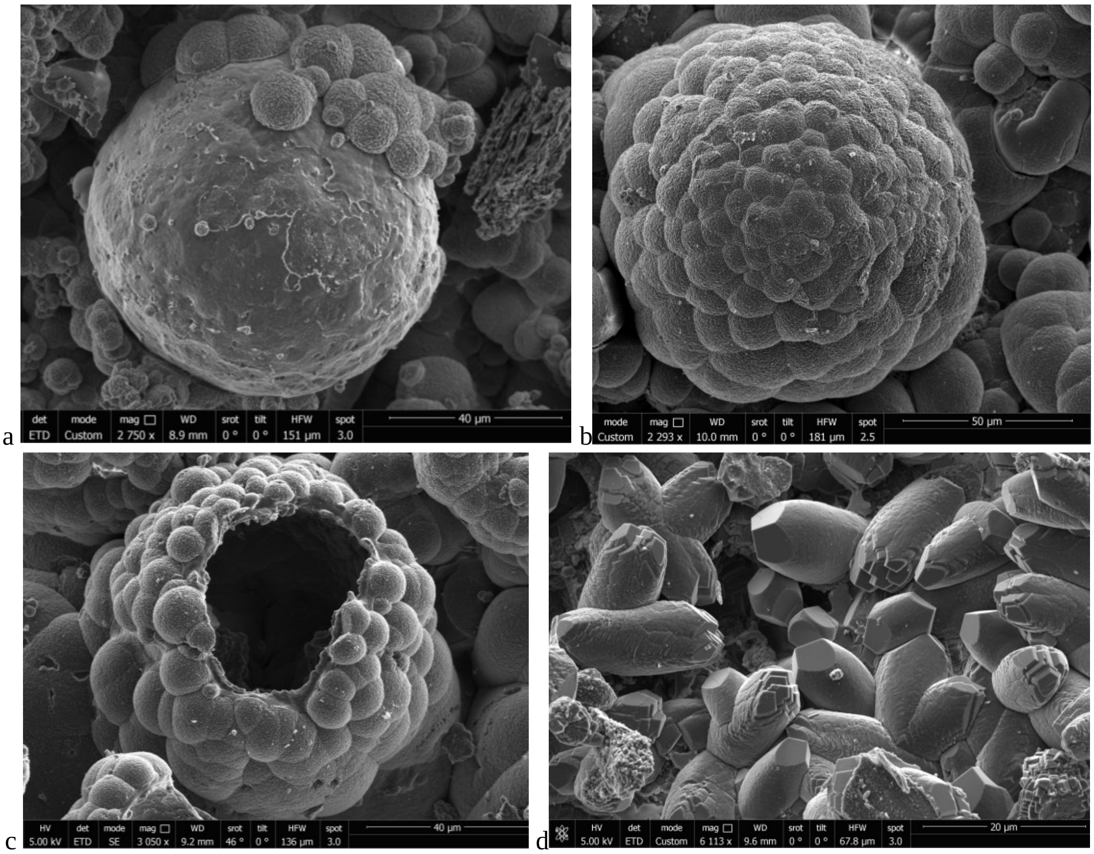

Figure S3. Mineral patterns observed covering the apexes of the cones: (a) fluorite/vaterite smooth shell partly covered by secondary faceted calcite precipitate (24 h ripening), (b) cauliflower-shaped calcite aggregate covering the shells shown in (a) (16 h), (c) bowl-shaped aggregate forming after breaking of the cauliflower shown in (b) (20 h), (d) prismatic vaterite with stepped surface and three to multifaceted apexes (8 h)

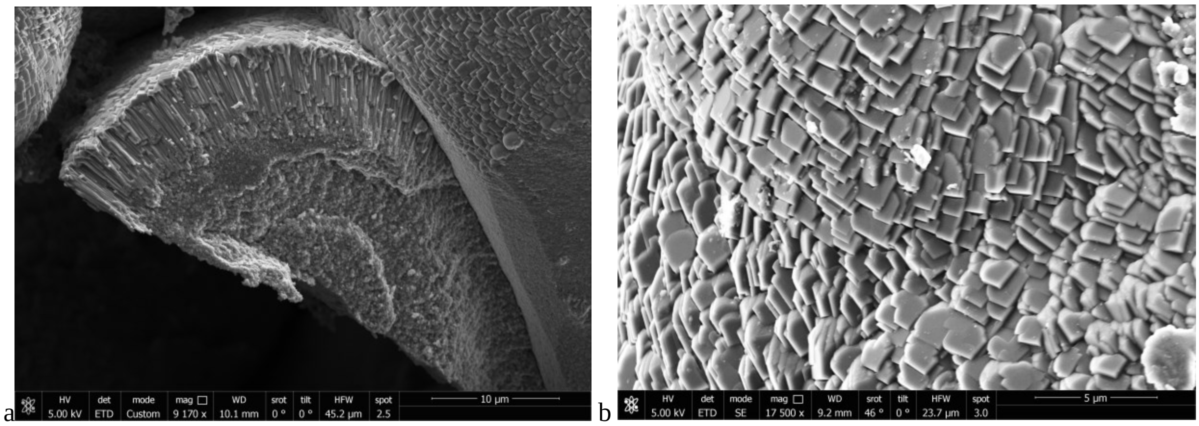

Figure S4. The columnar patterns of the interior of the cones (a) (16 h) manifest as interlocked rhombohedral calcite when viewed from top (b) (44 h)

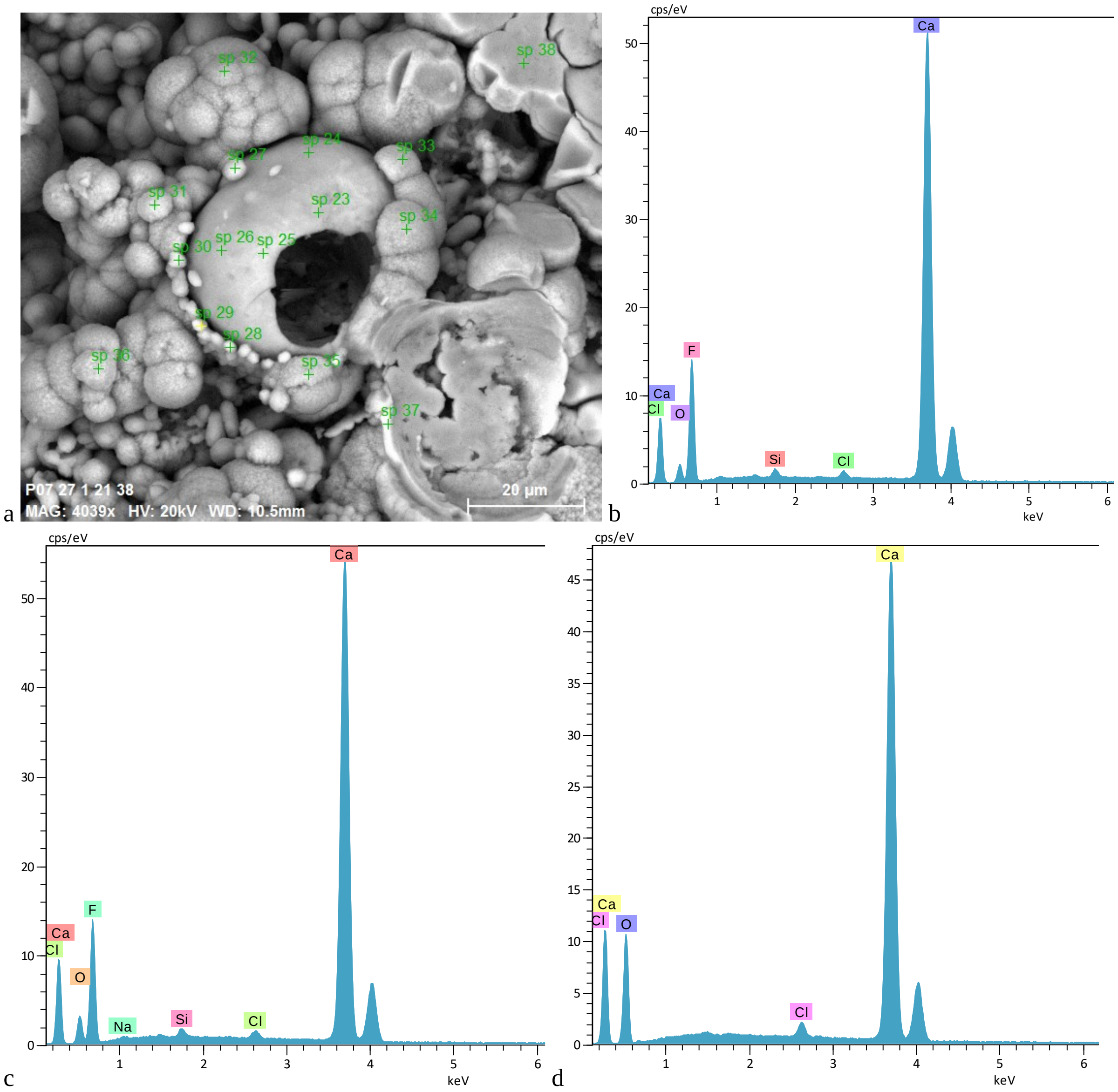

Figure S5. (a) Back scattered electron micrographs of void fluorite sphere partly covered by faceted calcite aggregates (24 h ripening), microanalysis of spots sp23 (b), sp24 (c) showing mainly fluorite composition of the smooth shell and sp34 (d) showing secondary calcite aggregates covering the interior shell

Chapter 7

Conclusions

7. Conclusions

As all chapters contain an individual summary of the corresponding publication or manuscript, this chapter provides a summary of all chapters in the context of each other.

Chapter 2: A comprehensive methodology for monitoring evaporitic mineral precipitation and hydrochemical evolution of saline lakes: the case of Lake Magadi soda brine (East African Rift Valley, Kenya). Getenet, M., García-Ruiz, J.M., Otálora, F., Emmerling, F., Al-Sabbagh, D., Verdugo-Escamilla, C. Crystal Growth & Design 2022, 22, 2307 − 2317. https://doi.org/10.1021/acs.cgd.1c01391

This chapter presented the synergy of multiple methodologies that allowed the accurate determination of mineral precipitation sequence during laboratory evaporation of Lake Magadi soda brines. The proposed combination of in-situ methods has shown a high potential to evaluate hydrochemical models that can be used in explaining current depositional environments, interpreting the evaporitic deposits appearing in sedimentary records in terms of paleoclimatic indicators, and proposing the applied methods for the industrial use of these brines at the optimal time during their natural hydrochemical evolution. This methodology can be improved by simultaneously using synchrotron diffraction and Raman spectroscopy of levitated droplets if additional in-situ information is required from minor, short-lived metastable or amorphous minerals.

Chapter 3: Mineral Precipitation and Hydrochemical Evolution Through Evaporitic Processes in Soda Brines (East African Rift Valley). Getenet, M., Otálora, F., Emmerling, F., Al-Sabbagh, D, García-Ruiz, J.M. Chemical Geology, 2022, under review.

In this chapter, the methodology presented in chapter two was expanded to Lake Nasikie Engida, Lake Natron, and tributary springs to highlight the geochemical and sedimentological perspective of evaporitic sediments. The results have shown that pH and CO_3^{2-}/HCO_3^- ratios are the major factors determining the precipitation order, relative quantity, and resulting mineral paragenesis in the East African Rift Valley hyperalkaline, hypersaline lakes, and springs. The precipitation of sodium carbonates/bicarbonates phases increases the pH of the brines causing hyperalkaline character while the high solubility of Na-CO_3^{2-}/HCO_3^- salts cause the hypersaline character of soda lakes.

The sequence of precipitating minerals depends on the starting composition of the brine. Nahcolite form only from the northern segment of Nasikie Engida and its feeder hot springs due to the lower pH and excess HCO_3^-. However, in southern Nasikie Engida, Magadi, and

Natron lakes, nahcolite precipitates only for a short, transient period during evaporation and re-dissolves when pH increases, leading to the precipitation of trona as the main phase. Thermonatrite and halite form dominantly in local pools and efflorescent crust subjected to intense and fast evaporation that limits the dissolution of atmospheric CO_2. Silica precipitate during the first stages of evaporation at a relatively lower pH but gets redissolved due to the pH increase. Silica accumulation in the stratigraphic sequence require either relatively lower evaporation levels or lower pH of the brines.

This work has shown the full range of evaporation up to complete dryness, showing the full landscape of plausible evaporitic scenarios. Yet only a fraction of this range has been achieved by the actual perennial lake brines due to the amplitude of seasonal dry/rainy periods, which regulate the balance between dilution by fresh water and concentration by evaporation of the brines. The development of hydrochemical models predicting, within this window of conditions, the precipitation sequence, and the relative abundance of evaporitic minerals in the resulting paragenesis is expected to be a novel tool in explaining modern depositional settings and in reconstructing paleoclimatic and hydrochemical conditions during the deposition of ancient evaporite deposits. This approach could be adapted to investigate the industrial crystallization of economic minerals from natural brines or even the conditions for the formation of evaporites in extraterrestrial environments using model and analogue brines.

Chapter 4: Mineral Vesicles and Chemical Gardens from Carbonate-Rich Alkaline Brines of Lake Magadi, Kenya. Getenet, M., García-Ruiz, J.M., Verdugo-Escamilla, C., Guerra-Tschuschke, I. Crystals 2020, 10, 467. https://doi.org/10.3390/cryst10060467

After explaining, in chapters two and three, the drivers of high pH, and high carbonate and silica content required for self-assembly, chapter four explored for the first time self-assembled mineral structures from natural soda lakes. These results have shown that mineral self-assembly could have been a common phenomenon in soda oceans of early Earth and Earth-like planets and moons such as Enceladus and Europa. Tubular and vesicular Ca, Ba, Mn, Co, Mg, Zn, and Fe (II) have shown the range of mineral self-organization that might form in early Earth soda oceans. Particularly, the composition of $CaCO_3$ mineral vesicles and gardens confirms the recent observation that carbonate minerals in soda lakes sequestrate Ca, leaving phosphate behind in solution for biochemical reactions. The high silica, carbonate, and phosphate content and the plausibility of mineral self-assembly in modern soda lakes may imply that alkaline soda oceans of the early Earth could probably be the “one-pot” environments containing the important ingredients for the synthesis of prebiotically relevant molecules and plausible settings for the origin of life.

Chapter 5: Tubular structures of calcium carbonate: formation, characterization, and implications in natural mineral environments. Getenet, M., Rieder, J., Kellermeier, M., Kunz, W., García-Ruiz, J.M. Chemistry – A European Journal 2021, 27, 16135. https://doi.org/10.1002/chem.202101417

Chapter 5 highlighted the time-dependent dissolution, diffusion, and precipitation processes occurring during the growth of tubular calcium carbonate structures. These structures were shown to be bilayers of texturally distinct but compositionally similar crystalline calcite, containing adjacent cone-like structures on the interior surfaces and a dense exterior layer of interlocked calcite rhombohedra. These dense and crystalline calcite layers dramatically reduce the exchange and interaction of ionic species between the inner and outer solutions, preventing ionic gradients from eliminating for long periods. Moreover, these dense layers cause the absence of significant electrochemical potential differences – in contrast to Fe(II), Fe(III), Co(II), and Al silica gardens. This finding is relevant for the use of chemical gardens as microreactors for electrochemically enhanced synthesis and catalysis of prebiotic reactions.

Chapter 6: Calcium Carbonate Tubular Structures from Natural Alkaline Soda Lakes: Growth, Characterization, and Implication to Prebiotic Geochemistry. Getenet, M., García-Ruiz, J.M., Manuscript to be submitted to Chemistry – A European Journal.

This chapter presented for the first time the evolution of pH, ion concentrations, and electrochemical potential differences in natural calcium carbonate gardens synthesized from soda lake water. Ex-situ characterization has shown that these membranes are bilayers of texturally distinct but compositionally similar crystalline calcite, like model calcium carbonate tubes. The reduced exchange of ionic species between the inner and outer solutions caused concentration gradients sustainable for days. In natural $CaCO_3$ tubes, high pH gradient comparable to Co and Fe(II) silica gardens was observed – in contrast to synthetic calcium-silica and carbonate gardens. Nevertheless, these tubes have low voltage (~ 30 mV), evidencing that pH gradient contributes to electrochemical potential differences only if permeable membranes co-exist. The fragile and transparent nature of these tubes immediately after preparation may have permitted voltage higher than 30 mV which is measured after 2 h of tube densification.

Ultimately, the thesis demonstrated the capabilities of the synergies between multitechnical approaches to accurately monitor evaporitic mineral precipitation and hydrochemical evolution of extreme evaporite settings. These methodologies were shown to be novel approaches to explain depositional settings and paleoclimatic conditions, with a potential applicability to explore industrial crystallization of economic minerals from extreme saline settings and the formation conditions of evaporites in extraterrestrial environments. In addition, the thesis demonstrated for the first time the plausibility of mineral self-organization in alkaline soda lakes which are considered as analogue to early Earth soda oceans. Calcium carbonate tubes in early Earth soda oceans may have developed significant pH gradient but probably lower voltage comparably to silica based self-assembled structures.

Appendix 1: Abstracts Presented at Conferences

AGU FALL MEETING
Online Everywhere | 1–17 December 2020

Mineral Precipitation from Soda Brines, Lake Magadi, Rift Valley (Kenya)

M. Getenet, J.M. Garcia-Ruiz, F. Otálora and C. Verdugo-Escamilla

Laboratorio de Estudios Cristalográficos, Instituto Andaluz de Ciencias de la Tierra, Consejo Superior de Investigaciones Científicas–Universidad de Granada, Granada, Spain.

Lake Magadi is a saline soda lake in East African Rift Valley (Kenya). It is fed by perennial warm and hot saline springs. Na^+-HCO_3^- type dilute inflows evolve into Lake Magadi brines rich in Na^+, CO_3^{2-}, Cl^-, HCO_3^- and SO_4^{2-} and depleted in Ca^{2+} and Mg^{2+}. The pH, CO_3^{2-} and SiO_2 content of these brines reach 11.5, 109000 ppm and 1440 ppm respectively. Evaporative concentration coupled with mineral precipitation and fractional dissolution are thought to be the main processes responsible for the stepwise evolution between dilute inflows and brines. In order to understand the details of the precipitation kinetics, we have performed simulations of mineral precipitation sequences and the resulting hydrochemical evolution during evaporation under different partial pressure of CO_2 (pCO_2) and temperature by using EQL-EVP program. In addition, we have performed laboratory precipitation experiments. The crystallization sequence was monitored by using in situ video microscopy and in situ and ex situ X-ray diffraction and Raman spectroscopy. The precipitation sequence was also monitored by scanning electron microscopy coupled with energy dispersive x-ray analysis. Trace amounts of magnesite, calcite and pirssonite precipitate at the beginning. Magnesium silicate precipitate at low pCO_2 (<-2.5) by redissolution of magnesite. Pirssonite forms from calcite dissolution at low pCO_2. The rise in temperature highly delayed amorphous silica precipitation. Trona was the second precipitate. At low temperature-high pCO_2, nahcolite precipitates at the second place whereas at high temperature-low pCO_2, thermonatrite forms instead of trona. Halite is the third in precipitation sequence. Burkeite (pCO_2 of -3 to -4.5) and thenardite (pCO_2 of -2 to -2.5) are the fourth in the sequence, which upon redissolution form glaserite. Sylvite, kalicinite and villiaumite forms at the end. Evaporation linearly raises the solute concentration until saturation of Na-CO_3-HCO_3 minerals and halite, which upon precipitation deplete solute content. Glaserite is the major phase depleting K^+ and SO_4^{2-}. The combination of modelling based on a kinetic approach and in situ mineralogical analysis is a powerful tool to understand mineral assemblages and kinetic precipitation pathways in soda lakes.

Acknowledgments: We acknowledge funding from the European Research Council under grant agreement no. 340863 and from the Ministerio de Economía y Competitividad of Spain through the project CGL2016-78971-P. M.G. acknowledges grant no. BES-2017-081105 of the “Ministerio de Ciencia, Innovacion y Universidades” of the Spanish government.

[1] Eugster (1970) Mineral. Soc. Amer. Spec. Pap. 3, 213-235. [2] Jones et al. (1977) Geochim. Cosmochim. Acta. 41, 53–72. [3] Eugster (1980) In Developments in Sedimentology 28, 195–232, [4] Risacher and Clement (2001) Comput. Geosci. 27, 191-201.

https://doi.org/10.1002/essoar.10505653.2

IN SITU MONITORING OF MINERAL PRECIPITATION SEQUENCE FROM ACOUSTICALLY LEVITATED DROPLETS OF LAKE MAGADI BRINE, EAST AFRICAN RIFT VALLEY

M. Getenet[1], J.M. García-Ruiz*[1], F. Emmerling[2], D. Al-Sabbagh[2], F. Otálora[1], and C. Verdugo-Escamilla[1]

[1] Laboratorio de Estudios Cristalográficos, Instituto Andaluz de Ciencias de la Tierra, Consejo Superior de Investigaciones Científicas–Universidad de Granada, Granada, SPAIN.
dessie.melese@csic.es, juanmanuel.garcia@csic.es, otalora@iact.ugr-csic.es, cristobal.verdugo@csic.es
[2] BAM Federal Institute of Materials Research and Testing, Berlin, GERMANY
franziska.emmerling@bam.de, dominik.al-sabbagh@bam.de

Abstract: Lake Magadi is a saline soda lake in East African Rift Valley (Kenya). Perennial saline hot and warm springs fed the lagoons of lake Magadi. These springs discharging into the lagoons evolve into lake Magadi brines enriched in Na^+, CO_3^{2-}, Cl^-, HCO_3^- and SO_4^{2-}. Evaporative concentration, mineral precipitation and fractional dissolution are thought to be the main processes responsible for the saline and soda chemistry of the lake. As a result of evaporation, different minerals precipitate in the lake. Understanding the kinetics of mineral precipitation have a paramount importance to understand the geochemical evolution of the brines. Therefore, we have envisaged an experimental study of the precipitation sequence of evaporating brines from lake Magadi. We have performed in situ X-ray diffraction of levitated droplets of the brine to monitor the mineral precipitation sequence during evaporation. A droplet of the brine was injected into an acoustic levitator and in situ X-ray diffraction were performed until complete evaporation of the droplet in the µSpot beamline at BESSY II synchrotron (Helmholtz Centre Berlin for Materials and Energy, Berlin, Germany). A monochromatized (Si 111) X-ray beam with a wavelength of 0.72929 Å and a beam size of 100 µm was used. Scattered intensities were collected with a two-dimensional X-ray detector (Eiger9M, CCD 3072 × 3072). Trona was the first mineral to precipitate. Halite precipitation began shortly after trona whereas thermonatrite was the last phase to appear. The results are compared with video monitored precipitation sequences and in situ Raman spectroscopy and ex-situ FESEM and EDX analysis. The combination of these techniques is a powerful tool for revealing actual precipitation sequences during evaporation of brines that are near saturation with respect to multiple minerals. We highlight in this work X-ray diffraction levitation experiments and discuss the power of this technique in understanding the geochemistry of evaporative environments.

Key words: Lake Magadi, soda lake, trona, evaporation, mineral precipitation kinetics

Acknowledgments: We acknowledge funding from the European Research Council under grant agreement no. 340863 and from the Ministerio de Economía y Competitividad of Spain through the project CGL2016-78971-P. M.G. acknowledges Grant No. BES-2017-081105 of the "Ministerio de Ciencia, Innovacion y Universidades" of the Spanish government.

References:

Eugster, H.P. (1970). Chemistry and origin of the brines of Lake Magadi, Kenya. Mineralogical Society of America Special Papers, 3, 213–235.

Jones, B.F., Eugster, H.P. and Rettig, S.L. (1977). Hydrochemistry of the Lake Magadi basin, Kenya. Geochimica et Cosmochimica Acta, 41, 53–72.

Surdam, R.C. and Eugster, H.P. (1976). Mineral reactions in the sedimentary deposits of the Lake Magadi region, Kenya. GSA Bulletin, 87 (12), 1739-1752.

Eugster, H.P. (1986). Lake Magadi, Kenya: a model for rift valley hydrochemistry and sedimentation?. Geological Society of London Special Publications, 25, 177-189.

Renaut, R.W., Owen, R.B., Lowenstein, T.K., De Cort, G., Mcnulty, E., Scott, J.J., and Mbuthia, A., (2020). The role of hydrothermal fluids in sedimentation in saline alkaline lakes: Evidence from Nasikie Engida, Kenya Rift Valley. Sedimentology.

Paris, O., Li, C., Siegel, S., Weseloh, G., Emmerling, F., Riesemeier, H., Erko, A., and Fratzl, P., (2006). A new experimental station for simultaneous X-ray microbeam scanning for small- and wide-angle scattering and fluorescence at BESSY II. J. Appl. Crystallogr. 40, s466–s470.

EGU21-4392, updated on 17 Aug 2022
https://doi.org/10.5194/egusphere-egu21-4392 EGU
General Assembly 2021

Monitoring mineral precipitation sequence of Lake Magadi soda lake: A multi-technical approach

Melese Getenet[1], Juan Manuel García-Ruiz[1], Franziska Emmerling[2], Dominik Al-Sabbagh[2], Fermín Otálora[1], and Cristóbal Verdugo-Escamilla[1]
[1]Laboratorio de Estudios Cristalográficos, Instituto Andaluz de Ciencias de la Tierra, Consejo Superior de Investigaciones Científicas–Universidad de Granada, Granada, Spain
[2]BAM Federal Institute of Materials Research and Testing, Berlin, Germany

Lake Magadi is a saline soda lake in East African Rift Valley, occupying the axial trough of Southern Kenyan Rift. It's fed by perennial saline hot/warm springs, which evolve into the soda and saline chemistry of the lake. The main processes thought to cause the enrichment of the lake in Na^+, CO_3^{2-}, Cl^-, HCO_3^- and SO_4^{2-} are evaporative concentration, mineral precipitation and fractional dissolution [1]. Lake Magadi is considered an analogous environment to the early Earth [2]. The high pH, silica and carbonate content of Lake Magadi allows the formation of silica and carbonate induced self-assembled mineral structures [3,4]. Revealing the mineral precipitation sequence of Lake Magadi have implications in understanding the geochemistry of evaporative rift settings and soda oceans. We have experimentally investigated the mineral precipitation sequence during evaporation at 25 °C. The sequence of mineral precipitation was recorded by using in-situ video microscopy. The mineral patterns observed in video microscopies were identified by spectroscopic, diffraction and electron microscopy techniques. The mineralogy and elemental composition of the precipitates were determined by using Raman spectroscopy, powder X-ray diffractions and scanning electron microscopy coupled with energy dispersive X-ray analyser. The results of the ex-situ analyses were compared with the in-situ X-ray diffraction. In-situ X-ray diffractions were performed on acoustically levitated droplets in the µSpot beamline at BESSY II synchrotron (Berlin, Germany). Finally, thermodynamic evaporation simulation was performed by using PHREEQC code with Pitzer database. Ex-situ and in-situ experiments revealed that mineral precipitation begins with trona, followed by halite and finally thermonatrite. In PHREEQC simulations, natron was observed instead of thermonatrite, suggesting the role of kinetics in the mineral assemblages. This multi-technical approach of in-situ monitoring and ex-situ characterization is a powerful approach to unveil mineral precipitation patterns and the resulting geochemical evolution in evaporative rift settings.

Acknowledgments: We acknowledge funding from the European Research Council under grant agreement no. 340863, from the Ministerio de Economía y Competitividad of Spain through the project CGL2016-78971-P and Junta de Andalucía for financing the project P18-FR-5008. M.G. acknowledges Grant No. BES-2017-081105 of the Ministerio de Ciencia, Innovacion y Universidades of the Spanish government.

References:

[1] Eugster, H.P. (1970). Chemistry and origin of the brines of Lake Magadi, Kenya. Mineralogical Society of America Special Papers, 3, 213–235.

[2] Kempe, S.; Degens, E.T. (1985). An early soda ocean?. Chem. Geol. 53, 95–108

[3] Getenet, M.; García-Ruiz, J.M.; Verdugo-Escamilla, C.; Guerra-Tschuschke, I (2020). Mineral Vesicles and Chemical Gardens from Carbonate-Rich Alkaline Brines of Lake Magadi, Kenya, Crystals, 10, 467.

[4] García-Ruiz J.M., van Zuilen M.A., Bach W. (2020) Mineral self-organization on a lifeless planet. Phys Life Rev, 34–35,62–82

Goldschmidt 2021 Abstract
https://doi.org/10.7185/gold2021.5047

Searching for mineral self-organization in soda lakes

MELESE GETENET, JUAN MANUEL GARCÍA-RUIZ, FERMÍN OTÁLORA AND CRISTÓBAL VERDUGO-ESCAMILLA

Laboratorio de Estudios Cristalográficos, Instituto Andaluz de Ciencias de la Tierra, Consejo Superior de Investigaciones Científicas–Universidad de Granada

Presenting Author: dessie.melese@csic.es

Mineral self-organization is an important subject to understand pattern formation in geology [1]. Among mineral self-organized phenomena [2], silica-induced structures such as silica-carbonate biomorphs and silica gardens are thought to be relevant for the earliest stages of the planet. They were likely forming during the evolution of silica-rich Hadean alkaline oceans from methane-rich to CO and CO_2-rich atmosphere and hydrosphere [3]. The precipitation of silica gardens generates electrochemical potentials [4] and selectively catalyse the synthesis of prebiotically relevant compounds such as carboxylic acids, amino acids, and nucleobases by condensation of formamide [5]. So far, silica gardens have been synthesized using laboratory solutions except for two cases where silica gardens form upon the interaction of model alkaline fluids with granites [6] and the interaction of serpentinization-driven natural alkaline water with metal salt pellets [7]. Here, we demonstrated that self-assembled mineral membranes form from carbonate-rich soda lake water (Lake Magadi, Southern Kenyan). Mineral vesicles and tubular membranes are obtained respectively by adding drops of barium, calcium, cobalt, magnesium, manganese, and zinc solutions or by immersing pressed pellets of these metal salts into high pH and high silica brine of Lake Magadi. The structures were studied by SEM-EDX, Raman microscopy and X-ray diffraction. We found that mineral membranes synthesized from carbonate-rich brine lack phosphorous in its structure. This confirms the interesting observation made recently that the high phosphate level of carbonate-rich soda lakes is due to the sequestration of calcium into carbonate minerals preventing phosphate removal by apatite precipitation [8]. Our result suggests that mineral self-organization could have been a geochemically plausible phenomenon in carbonate-rich closed basin environments of the early Earth.

[1] García-Ruiz & Otálora (2015) *Handbook of Crystal Growth, Vol. II*. 1-43. Elsevier.

[2] Nakouzi & Steinbock (2016) *Sci. Adv*. 2, e1601144.

[3] García-Ruiz et al. (2020) *Phys Life Rev*. 34-35, 62

[4] Glaab et al. (2012) *Angew. Chem*. 124, 4393.

[5] Saladino et al. (2019) *Chem. Eur. J*. 25, 3181.

[6] Satoh et al., (2014) *Eur. J. Mineral.* 26, 415.

[7] García-Ruiz et al. (2017) *Sci. Adv*. 3, e1602285.

[8] Toner & Catling (2020) *Proc. Natl. Acad. Sci.* 117, 883.

IUCr 2021 Abstract
https://doi.org/10.1107/S010876732109276X

MS-62-3 **Microsymposium**

Crystal texture of mineral self-organized structures from soda lake water and their implication to early Earth and prebiotic chemistry

M. Getenet, J.M. García-Ruiz

Laboratorio de Estudios Cristalográficos, Instituto Andaluz de Ciencias de la Tierra, Consejo Superior de Investigaciones Científicas–Universidad de Granada, Granada, Spain

juanmanuel.garcia@csic.es

The ability of minerals to precipitate into complex shapes and textures creates fascinating patterns that has not been enough explored in natural scenarios. Among them, silica induced mineral self-organized structures have been suggested to be relevant for the earliest stages of the planet, when alkaline silica-rich oceans evolve from methane-rich to CO and CO_2-rich atmosphere and hydrosphere [1]. Under these geochemical conditions of the Hadean Earth, it is thought that silica-carbonate biomorphs and silica-metal hydr(oxide) gardens were actually forming in the alkaline oceans, rich in silica and in carbonate. In this work, we focus on chemical gardens, which are hollow membranes formed via abiotic precipitation when metal salts immerse into aqueous solutions containing anions such as silicate, carbonate, or phosphates [2]. It has been shown that these space-compartmentalized membranes are small batteries [3] that selectively catalyse the synthesis of prebiotically relevant compounds such as carboxylic acids, amino acids, and nucleobases by condensation of formamide [4]. Here, we experimentally demonstrate the formation of carbonate gardens using carbonate-rich alkaline soda lake water (Lake Magadi, Southern Kenyan rift valley). We have studied in detail the mineral composition and crystallinity of these “natural” carbonate gardens by SEM-EDX, Raman microscopy, infrared spectroscopy and X-ray diffraction, and compared to other silica and carbonate gardens made from laboratory solutions. Our result suggests that mineral self-organization could have been a geochemically plausible phenomenon in carbonate-rich closed basin environments of the early Earth, and Earth-like planets. We also discuss the implications of the textural properties of the mineral membranes to develop electrochemical potential that could catalyze prebiotic reactions.

[1] García-Ruiz, J.M., van Zuilen, M. & Bach, W. (2020). Phys Life Rev. **34-35**, 62-82.

[2] Kellermeier, M., Glaab, F., Melero-García, E., & García-Ruiz, J. M. (2013). Research Methods in Biomineralization Science, edited by J.J. De Yoreo, pp. 225-256. San Diego: Academic Press.

[3] Glaab, F., Kellermeier, M., Kunz, W., Morallon, E. & Garcia-Ruiz, J. M. (2012). Angew. Chem. **124**, 4393.

[4] Saladino, R., Di Mauro, E. & García-Ruiz, J. M. (2019). Chem. Eur. J. **25**, 3181.

Keywords: chemical gardens; self-organization; biomorphs; early Earth; Soda lakes

Acknowledgments: *We acknowledge funding from the European Research Council under grant agreement no. 340863, from the Ministerio de Economía y Competitividad of Spain through the project CGL2016-78971-P and Junta de Andalucía for financing the project P18-FR-5008. M.G. acknowledges Grant No. BES-2017-081105 of the Ministerio de Ciencia, Innovacion y Universidades of the Spanish government.*

AGU FALL MEETING
New Orleans, LA & Online Everywhere
13–17 December 2021

Calcium Carbonate Tubular Structures from Soda Lake Water: Growth Process, Characterization, and Implications to Prebiotic Chemistry and Origin of Life

Melese Getenet and Juan Manuel García-Ruiz

Laboratorio de Estudios Cristalográficos, Instituto Andaluz de Ciencias de la Tierra, Consejo Superior de Investigaciones Científicas–Universidad de Granada, Granada, Spain.

dessie.melese@csic.es, juanmanuel.garcia@csic.es

Chemical gardens are self-assembled tubular structures formed via abiotic precipitation upon the interaction of metal-ion salts with aqueous solutions of anionic species such as silicate, carbonate, or phosphate. These tubular structures have been suggested to be relevant for the early Earth and Earth-like planets and moons where alkaline silica and carbonate rich soda oceans are thought to be widespread. Carbonate and silica gardens are believed to be forming under the geochemical conditions of these soda oceans. Silica gardens are self-compartmentalized compositionally distinct bilayered mineral membranes. These membranes are small batteries that selectively catalyze the synthesis of prebiotically relevant organic compounds such as carboxylic acids, amino acids, and nucleobases by condensation of formamide. Recently, we have grown chemical gardens and mineral vesicles by immersing different metal salts in soda lake water and inferred that mineral self-organization could be a plausible scenario on soda oceans of early Earth and extraterrestrial planets and moons such as Enceladus.

In this work, we have performed in-situ monitoring of the chemical gradient, pH and electrochemical potential differences across macroscopic calcium carbonate tubular structures grown by immersing calcium chloride salt pellets in carbonate-rich soda lake water (Lake Magadi, Southern Kenyan Rift Valley). To understand the temporal evolution of the growth process, we have performed ex-situ X-ray diffraction, Raman and infrared spectroscopy, and scanning electron microscopy of the tubular structures isolated after different periods of growth. We have also compared our results with calcium carbonate and silica gardens grown in model laboratory solutions. The walls of calcium carbonate tubular structures are composed of bilayers of texturally different but mineralogically similar crystalline calcite. We have observed that pH gradients across these “natural” calcium carbonate tubes are comparable to that of silica gardens and higher than that of synthetic carbonate gardens. We have discussed the implications of the texture, ionic gradient, pH and electrochemical potential differences across the tubes to material sciences, prebiotic chemistry, and origin of life.

https://doi.org/10.1002/essoar.10509574.1

Mineral Precipitation and Hydrochemical Evolution Through Evaporitic Processes in Soda Brines

Melese Getenet (1), Juan Manuel García-Ruiz (1*), Fermín Otálora (1), Franziska Emmerling (2), Dominik al-Sabbagh (2)

(1) Laboratorio de Estudios Cristalográficos, Instituto Andaluz de Ciencias de la Tierra (CSIC-UGR), Avenida de las Palmeras 4, Armilla, E-18100 Granada, Spain
(2) Federal Institute for Materials Research and Testing (BAM), Richard-Willstätter-Straße 11, 12489 Berlin, Germany
* corresponding author: juanmanuel.garcia@csic.es

Palabras Clave: Evaporitas, Lagos alcalinos, Carbonato de sodio. **Key Words:** Evaporites, Soda Lakes, Sodium Carbonate.

INTRODUCCIÓN

Soda lakes are saline lakes mostly typically fed by volcanic terrains. They are characterized by high pH and a large concentration of Na^+, Cl^-, CO_3^{2-} and HCO_3^-, leading to active evaporite precipitation. Lakes Magadi, Nasikie Engida and Natron (MNN), are among the highly saline and alkaline soda lakes in the tectonic depressions of the East African Rift valley. Precipitation in MNN lakes follows a complex, recurrent cycle of undersaturation, evaporative concentration, and desiccation. During the evaporative concentration, trona grows as thin sheet-like rafts on the surface and as upward radiating needles at the bottom of the lake. After complete evaporation (desiccation stage), continued evaporation of interstitial brines causes expansion and buckling of the crust and precipitation of a variety of efflorescent crusts and inter-crystallite cement. During the undersaturation stage (flooding of the lake), dilute inflows partially dissolve the preexisting trona or nahcolite, creating layered deposits of upward radiating trona crystals (in Lake Magadi) or nahcolite crystals (in Nasikie Engida) with thin mud layers on top of the dissolution surfaces. The investigation of this complex hydro-chemical evolution, is relevant to geological and paleo-environmental studies of the area. Identifying the chemical and climatological factors controlling the precipitation sequence would simplify the decoding of the stratigraphic record and allow an efficient use of the mineral resources (evaporites are currently exploited by TATA Chemicals). To this end, we have performed ex-situ and in-situ (drop levitation) diffraction experiments during evaporation as well as hydrochemical modeling of the evaporation/precipitation sequences. The methodology for these studies is described in Getenet et al. (2022).

RESULTS AND DISCUSSION

Figure 1 shows the precipitation sequence during evaporation of levitated drops of (a) Lake Magadi brine, (b) Lake Nasikie Engida brine, (c) Nasikie Engida hot spring and (d) Lake Natron brine (left column) along with the output of the evaporative precipitation sequence modeled using the hydrochemical code PHREEQC (mineral phases in the center column and solution species in the right column). Trona and halite were observed to precipitate from all brines except the Nasikie Engida hot spring, where nahcolite is the first precipitate. Thermonatrite was observed to precipitate in all cases except Lake Nasikie Engida brine. The time (and therefore concentration factor) at which these phases start precipitating changes for different brine composition. The mineral precipitation sequences predicted by hydrochemical modeling agree for sodium carbonate phases with the outcome of evaporation experiments, with the only exception of natron, predicted to precipitate from Lake Nasikie Engida brine but not observed and trona, predicted to precipitate from Lake Nasikie Engida spring while thermonatrite is observed instead. The absence of natron in the evaporation experiments can be due to the thermal transformation of the mineral into trona (Eugster, 1980). The differences in the relative amount of the minerals among the experiments, the simulations and the natural setting arise mainly from the differences in partial CO_2 pressure (pCO_2) and in biogenic activity, leading to the dissolution of the early precipitated nahcolite. In the case of hot springs, the initial brine was dominated by HCO_3^- over CO_3^{2-}, allowing the precipitation of significant amount of nahcolite even though CO_2 input was minimal. In a later stage, nahcolite partially convert to trona. The precipitation of a significant amount of thermonatrite and halite in artificial pans exploited by TATA Chemicals is also explained by our results: the company pumps the HCO_3^- depleted lake brine (after trona precipitation) into shallow evaporation ponds where evaporation is very rapid and organic production of CO_2 is negligible.

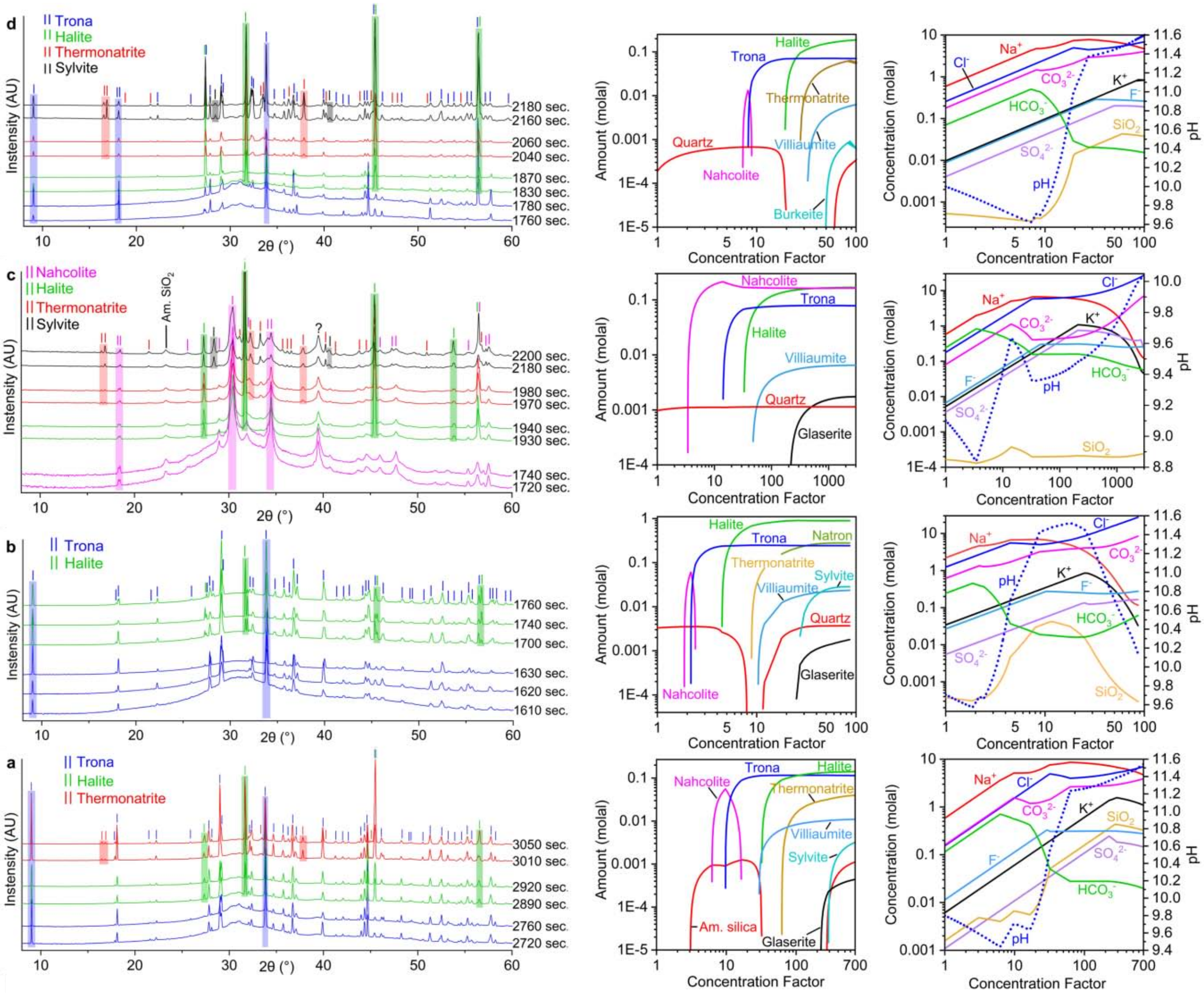

Fig 1. Powder X-ray diffraction data from in-situ (levitated drop) evaporation /precipitation experiments of (a) Lake Magadi brine, (b) Lake Nasikie Engida brine, (c) Nasikie Engida hot spring and (d) Lake Natron brine (left column). Simulation of the same process by hydrochemical modeling; precipitated mineral phase amounts and solution species concentrations are represented as a function of the concentration factor (initial solution weight divided by the current solution weight).

These results also reproduce the hydrochemical evolution observed in natural settings. In Lake Magadi, and in southern Nasikie Engida, trona precipitates currently at the bottom as a firm mesh of vertical acicular crystals and on the surface as crusts of smaller crystal aggregates. The successive growth of these crystals forms a layered trona deposits of 2-5 cm annual bands. The evaporite sediments of the northern Nasikie Engida are dominated by nahcolite. Drill cores on the lake bed revealed that the uppermost sediments are composed of intercalations of laminated mud with scattered nahcolite crystals and distinct beds of nahcolite resulting from abrupt precipitation at the sediment–water interface or within the water column. In Lake Natron, trona was reported both in ancient and modern evaporite deposits. The modern surface of Lake Natron is composed of 10-20 cm thick trona, thermonatrite and halite crust with alternating layers of black clay and trona. Thermonatrite and halite form only in the modern evaporite sequence of MNN lakes as efflorescent crusts and some local pools where there is intense evaporation.

REFERENCES

Eugster, H. P. (1980): Lake Magadi, Kenya, and Its Precursors. in "Developments in Sedimentology", A. Nissenbaum, ed. Elsevier, Amsterdam, 195–232

Getenet M., García-Ruiz J. M., Otálora F., Emmerling F., Al-Sabbagh D. and Verdugo-Escamilla C. (2022): A Comprehensive Methodology for Monitoring Evaporitic Mineral Precipitation and Hydrochemical Evolution of Saline Lakes: The Case of Lake Magadi Soda Brine (East African Rift Valley, Kenya). Crystal Growth & Design.

Appendix 2: Hydrochemical data of Lake Magadi, Nasikie Engida, Natron and Tributary Springs and Rivers

Lakes	Sample ID	Sample type	Location		Temp.	pH	EC	Al	Ca	Fe	K
			Easting	Northing	°C		mS/cm	ppm	ppm	ppm	ppm
Magadi	P07-02-01	River	191548	9797832	21.50	8.93	0.126	0	16.7	0	6.2
Magadi	P07-03-02	Spring	191499	9795000	26.2	9.39	22.57	0	2.7	0	61.6
Magadi	P07-03-03	Spring	191450	9794986	23.8	9.52	31.46	0	17.5	0	116.4
Magadi	P07-06-01	Spring	195255	9779852	38.90	9.57	24.78	0	0.0	0	125.0
Magadi	P07-07-01	Spring	195549	9779519	37.87	9.44	18.8	0	7.3	0	64.5
Magadi	P07-13-01	Spring	192069	9778554	43.4	9.6	4100	<0.04	<1.00	0.0321	194
Magadi	P07-14-01	Spring	192000	9778432	43.1	9.59	3980	<0.02	0.637	0.0224	163
Magadi	P07-15-01	Spring	192001	9778394	44.2	9.59	4090	<0.02	0.659	0.0268	323
Magadi	P07-19-01	Spring	199903	9790716	32.4	9.82	2820	<0.02	0.684	<0.02	133
Magadi	P07-20-01	Spring	199918	9790708	34.5	9.81	2770	<0.02	<0.50	<0.02	152
Magadi	P07-21-01	Spring	199937	9790669	34.4	9.81	2760	<0.02	<0.50	<0.02	108
Magadi	P07-22-01	Spring pool	199926	9790750	26.3	7.96	38.9	0.0913	10.8	0.0058	4.5
Magadi	P07-24-01	Spring pool	199970	9791189	34.2	9.77	2890	<0.02	0.507	<0.04	251
Magadi	P07-25-01	Evaporation pond	199442	9790877	39.8	10.4	16100	0.123	<2.50	0.241	1052
Magadi	P07-26-01	Evaporation pond	199441	9791457	41.7	10.6	16200	<0.005	<0.500	<0.050	831
Magadi	P07-27-01	Evaporation pond	199498	9791804	37.5	9.89	14300	<0.020	1.98	0.392	1939
Magadi	P07-28-02	Evaporation pond	199208	9791838	33.0	10.4	16800	0.0242	2.03	0.227	1811
Magadi	P07-29-01	Spring	200032	9787948	32.7	9.82	1530	<0.02	0.586	<0.020	109
Magadi	P07-30-01	Spring	200037	9787990	32.4	9.86	1840	<0.020	0.532	<0.020	98
Nasikie Engida	P07-31-01	Lake	197412	9803273	24.7	9.71	10600	0.615	5.06	0.163	1145
Nasikie Engida	P07-32-01	Spring	196358	9809772	24.1	9.17	3420	<0.02	0.744	<0.02	201
Nasikie Engida	P07-33-01	Spring	196309	9809855	37.0	9.46	2480	<0.02	4.08	0.0244	250
Nasikie Engida	P07-34-01	Hot spring	196334	9809666	81.3	9.17	3490	0.0212	0.632	0.0847	240
Nasikie Engida	P07-35-01	Hot spring	196253	9809520	81.1	9.28	3740	<0.02	<0.5	0.0379	189
Nasikie Engida	P07-37-01	Hot spring	197181	9809012	79.4	9.09	3940	<0.02	0.501	0.0487	196
Nasikie Engida	P07-38-01	Hot spring	197431	9809211	82.9	8.9	3480	<0.02	0.668	0.0694	68
Magadi	P07-39-01	Spring	190346	9795083	44.4	9.01		0	0.0	0	129.7

Magadi	P07-40-01	Spring	190337	9795154	42.5	8.89		0	16.4	0	126.9
Magadi	P07-41-01	Lake	196660	9796055	29.2	9.89		0	0.0	0	263.1
Magadi	P07-42-01	Lake	196358	9796125	29.2	9.8	68.6	<0.05	4.54	0.10	228.5
Magadi	P07-43-01	Lake	196386	9796926	29.3	9.91	4460	<0.02	5.46	0.249	186
Magadi	P07-44-01	Lake	196329	9797617	28.6	9.93		0	0	0	231
Magadi	P07-46-01	Lake	196641	9797321	29.4	9.9		0	0	0	297
Magadi	P07-47-01	Lake	196301	9795729	28.2	9.9	5100	<0.02	6.11	0.4	253
Magadi	P07-48-01	Lake	196281	9795262	26.8	9.88		0	0	0	308
Magadi	P07-49-01	Lake	196342	9795000	27.8	9.88		0	0	0	346
Magadi	P07-50-01	Lake	195881	9796078	31.2	9.87	5600	<0.02	9.08	0.496	400
Magadi-Natron	P07-59-01	Swamp	184669	9769232	23.7	8.12	25.2	2.23	17.7	2.46	25
Magadi-Natron	P07-60-01	River	173472	9765275	26.3	7.84	31.9	16.1	23.8	29.2	27
Natron	P07-61-01	Spring	172445	9763097	32.3	9.82	2820	0.0238	0.982	<0.02	264
Natron	P07-62-01	Spring	172449	9762736	31.6	9.82	3040	0.0254	0.54	<0.02	116
Natron	P07-63-01	Spring	173608	9761244	31.5	9.84	5460	<0.02	0.745	0.0494	342
Natron	P07-63-02	Lake-spring mix	173608	9761244	32.6	10.1	4470	20.9	15.5	18.8	272
Natron	P07-64-01	Spring	174608	9760022	38.4	9.43	1180	0.208	1.5	<0.02	40
Natron	P07-64-02	Lake	174608	9760022	40.1	10	4310	8.48	19	7.3	364
Magadi-Natron	P07-65-01	River	176619	9768304	28.1	7.77	27.2	13.9	23.1	25.5	22
Magadi-Natron	P07-66-01	Tap water	197810	9787708	30.3	8.08	41.1	0.0554	9.59	<0.004	10
Magadi	P07-73-01	Lake	197485	9791794	30.5	9.84	6590	1.5	12.8	1.12	404
Magadi	P07-74-01	Spring	191879	9780285	30.0	9.67	3310	<0.04	1.09	<0.04	250
Magadi	P07-76-02	Spring	191866	9780213	32.7	9.77	4160	<0.02	3.99	0.0519	270
Nasikie Engida	P04-01-01	Hot spring	01° 43.272'S	036° 16.200'E	83	9.21	35.80	1.29	0.98		191.86
Nasikie Engida	P04-01-02	Hot spring	01° 43.280'S	036° 16.206'E	84	9.30	38.00	0.48		0.01	201.76
Nasikie Engida	P04-01-08	Hot spring	01° 43.623'S	036° 16.848'E	85.3	8.98	36.20	17.06	1.73	36.20	221.82
Nasikie Engida	P04-01-09	Hot spring	01° 43.653'S	036° 16.852'E	85.9	8.88	34.80	0.46		0.22	203.60
Magadi	P04-03-01	Spring	02° 00.067'S	036° 13.926'E	45.8	9.61	42.10		0.60	0.45	148.41
Magadi	P04-03-03	Spring	02° 00.046'S	036° 13.927'E	45.3	9.61	39.10	0.05	0.15		136.24

Magadi	P04-03-04	Spring	02° 00.062'S	036° 13.927'E	45.8	9.57	41.00	0.12	1.37	0.13	142.23
Magadi	P04-03-05	Spring	02° 00.135'S	036° 13.889'E	45.4	9.63	40.40	0.82	0.29		136.8
Magadi	P04-04-01	Spring	01° 53.483'S	036° 18.167'E	36.6	9.81	27.50	0.07	0.23	0.21	95.16
Magadi	P04-04-03	Spring	01° 53.505'S	036° 18.167'E	36.4	9.90	27.00	1.46			82.95
Magadi	P04-04-05	Spring	01° 53.982'S	036° 18.167'E	36.1	9.80	15.97	0.75	0.14	0.40	64.82
Magadi	P04-04-12	Evaporation pond	01° 53.860'S	036° 17.456'E		10.47	148.40	1.33	0.84		3286.8
Magadi	P04-04-12E	Evaporation pond	01° 53.860'S	036° 17.456'E		10.50	150.30		0.23		3128.2

Table continued.

Sample ID	Mg	Na	SiO$_2$	F	Cl	CO$_3^{2-}$	HCO$_3^-$	SO$_4^{2-}$	PO$_4^{3-}$	B	Sr	Ba	Br	I	TDS
	ppm	ppm	ppm	ppm	ppm	ppm	ppm	ppm	ppm	ppm	ppb	ppb	ppm	ppm	ppm
P07-02-01	2.2	4.2	23.7	0.589	<1	1.6	79.7	<5	0						
P07-03-02	0.0	3820	66	38.237	2160	1560	3477	83.4	0						
P07-03-03	1.0	7121.5	68.3	62.382	4020	3300	4057	118	7.7						
P07-06-01	0.0	13688	58.4	95.373	6250	6930	8540	177	10						
P07-07-01	0.0	5297	61.4	42.668	2760	1890	4911	159	2.8						
P07-13-01	0.0306	12000	58.9	97	6420	7390	10600	201	14.3						
P07-14-01	0.0368	12500	65		5940	6530	10600	95	13.3						
P07-15-01	<0.03	12300	57.3		8660	7860	8920	25	14.3						
P07-19-01	0.0579	8840	24.4	64	5720	5980	4880	81	8.89						
P07-20-01	0.0442	8300	27.6		5420	5740	4180	52	7.4						
P07-21-01	0.0455	8020	26.6	59.7	5200	4780	5240	42	6.68						
P07-22-01	3.83	57.1	13.1	0.4	6.34	0	61.6	96	<0.15						
P07-24-01	<0.06	8615	22.1	62.6	3870	4920	6410	74	7.53						
P07-25-01	<0.150	147703	527	555.6	107000	67200	7320	620	226	121	73.4	644	358	12.8	318000
P07-26-01	0.023	179460	1080	1074.9	125000	54900	8110	2254	418	211	76.7	622	725	26.6	440000

P07-27-01	0.121	104000	388	1670	103000	52400	20200	988	171						
P07-28-02	0.0434	156438	714	1202.3	184000	29400	12500	254	259						
P07-29-01	<0.03	4250	26	32.9	1990	1870	3900	55	3.56	2.32	36.8	<0.002	8.47	0.348	13200
P07-30-01	<0.030	5115	24		2400	2870	4160	21	4.46	2.53	35.8	3.19	9.96	0.412	13100
P07-31-01	1.25	43300	193	434.6	37600	30500	15200	451	26.5						
P07-32-01	0.0659	12400	71.7	103.8	5170	3430	12900	625	7.28	8.57	124	266	29	0.767	29100
P07-33-01	1.32	12900	72.3	112.7	6750	5620	10500	499							
P07-34-01	0.0502	12600	79.8		7040	3440	13100	462							
P07-35-01	<0.03	11700	81.7	114.6	5430	4740	13600	113		8.85	106	270	24	0.771	28300
P07-37-01	0.0716	12700	65.8	120.5	6060	3910	15700	334		9.54	129	313	30.2	0.882	28900
P07-38-01	0.0539	10800	69.2		4730	4940	27700	97		8.29	159	371	27.2	0.664	41300
P07-39-01	0.0	10311	120.4	69.4	4820	2640	11651	199	4.7						
P07-40-01	1.5	10291	129.7	68.7	4650	2520	11529	201	4.9						
P07-41-01	1.2	16760	84.8	192.36	5660	12810	3416	99.6	19.6						
P07-42-01	12.0	12850	91.4	208	5250	9600	6100	100.5	19.5	5.2	41.5	3.44	23.25	0.830	
P07-43-01	1.47	13800	66.4		7800	12000	6730	23							
P07-44-01	1.1	12976	86.3	148.4	4630	9100	3843	78.1	17.5						
P07-46-01	0.9	19743	96.1	224	5830	13020	5978	100	23						
P07-47-01	1.76	17200	66.2	220.1	6280	14200	7760	376	21.5						
P07-48-01	1.3	20305	96.1	231	6030	12810	7152	103	22.8						
P07-49-01	1.0	24375	105.2	254.54	6940	15750	7473	121	25.7						
P07-50-01	1.58	21200	68.2	246.4	9760	16400	9200	32	26.6						
P07-59-01	2.49	26.8	28.4	1.1	4.92	0	147	0	1.11						
P07-60-01	4.29	65.2	32.4	2	12.3	5.09	141	1	0.662						
P07-61-01	0.116	8290	13.9	158.4	3960	4670	5520	152	42.3						
P07-62-01	0.0893	8940	8.56		4280	5970	4950	196	45.6						
P07-63-01	0.065	17600	14.8	244.2	8600	12400	9310	409	83.2						
P07-63-02	3.91	13800	27.6	166.7	5890	23600	10900	518	65						
P07-64-01	0.139	2930	15.4	63.8	1340	2080	7610	79	7.85						

P07-64-02	3.02	13000	51.2	163.2	8700	9710	5340	375	40.1						
P07-65-01	3.95	40.75	31.9	1.8	7.81	0	125	1	0.608						
P07-66-01	3.66	66.4	12.8	0.6	8.86	0	108	14	<0.15						
P07-73-01	2.73	27200	50.2	309.4	9620	19700	11500	623	30.4						
P07-74-01	<0.06	10000	67.4	89.2	5100	5280	8130	164	12.8	8.33	76.6	44.8	29.1	0.828	
P07-76-02	0.18	13300	77.5	170.2	6440	8070	8760	172	13.5						
P04-01-01	0.16	10971.80	81.60	67.3	5328.5	5040	11102	149.3			50				
P04-01-02	0.04	12007.80	87.35	66.8	5750	6120	10980	141			60				
P04-01-08	8.10	9490.80	189.39	74.3	5359	4440	14457	163.7			220				
P04-01-09		9882.20	70.63	76.1	5224.5	3660	13237	226.2			80				
P04-03-01	0.05	13559.80	60.67	56.9	6443.5	8520	7930	196.5							
P04-03-03	0.05	12462.60	63.34	47.9	6123	7980	7747	201.8							
P04-03-04		12840.00	64.93	52.0	6202.5	8460	7686	202.8			0				
P04-03-05	0.01	12722.40	62.55	56.2	6164.5	7920	7869	199							
P04-04-01		8192.00	22.69	36.6	3687	6000	3599	69.8			30				
P04-04-03	0.02	7430.60	20.56	33.4	3667	5700	3721	60.7			20				
P04-04-05		4088.40	26.48	22.4	1989.75	3060	2196	80							
P04-04-12	0.11	133274.00	616.99	213.8	151291.5	87429	0	2091							
P04-04-12E	0.02	143754.00	851.10	94.2	141320			2018.3							

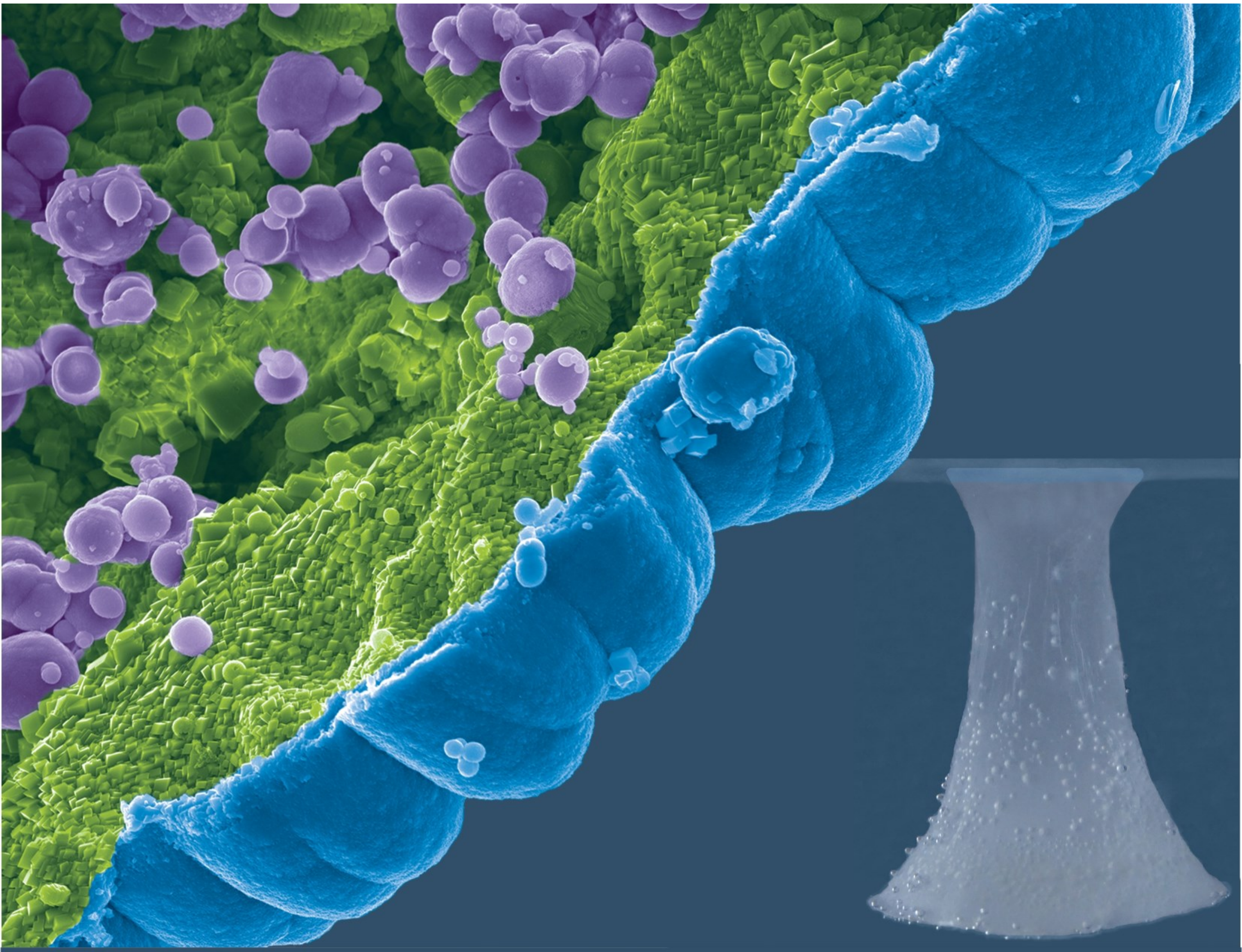

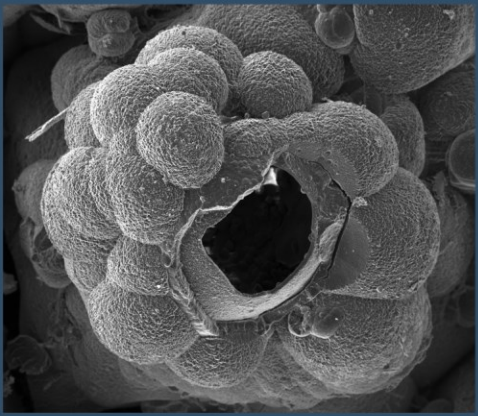

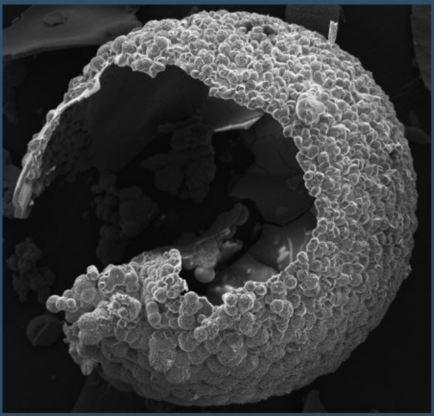

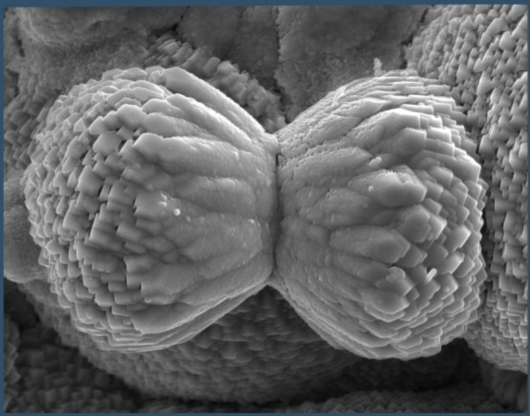

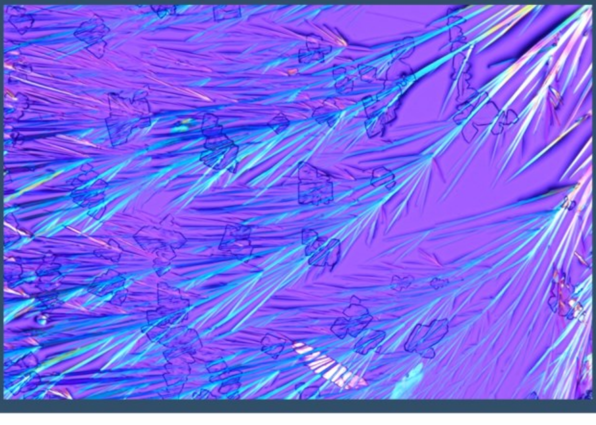

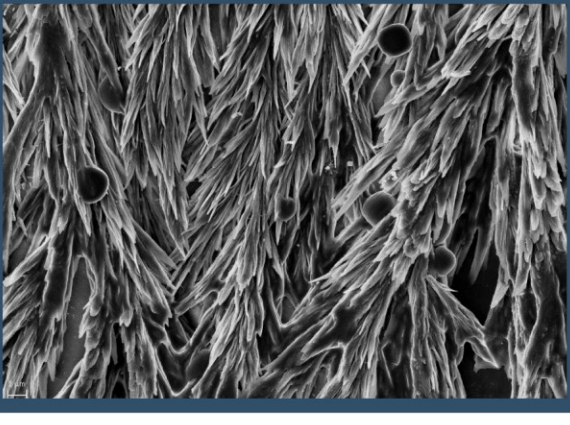

UNIVERSIDAD DE GRANADA

CSIC
Consejo Superior de Investigaciones Científicas

IACT
Instituto Andaluz de Ciencias de la Tierra

lec
Laboratorio de Estudios Cristalográficos